University of
Strathclyde
Glasgow

Department of Pure and Applied Chemistry

The Characterisation and Optimisation of the Zinc Bromine Hybrid Redox Flow Battery

Declan Bryans

Degree of Doctor of Philosophy

April 2018

‘This thesis is the result of the author’s original research. It has been composed by the author and has not been previously submitted for examination which has led to the award of a degree.’

‘The copyright of this thesis belongs to the author under the terms of the United Kingdom Copyright Acts as qualified by University of Strathclyde Regulation 3.50. Due acknowledgement must always be made of the use of any material contained in, or derived from, this thesis.’

Signed:

Date:

Acknowledgements

The experience I have gained throughout my period of study has been very rewarding and enjoyable. This was in no small part due to the support and kindness of others whom I wish to thank. The supervision I have received from Dr Leonard Berlouis was exemplary, I will forever be grateful to your never-ending support and friendship throughout this PhD. I also extend my gratitude to Dr Mark Spicer and Dr John Reglinski whose knowledge and experiences were greatly appreciated.
I wish to thank Professor Hubert Girault, Dr Véronique Amstutz, Dr Christopher Dennison, Dr Heron Vrubel, Dr Alberto Battistel, Mr Yorick Ligen, Ms Patricia Byron, and everyone else I met during my time in Switzerland working at the EPFL-LEPA. I was made to feel very welcome and enjoyed learning from every one of you.

I also wish to thank Dr Jawwad Zafar and all the other research staff and students from the Power Network Demonstration Centre whom welcomed and supported me during my time working with them also.

Additionally, I am thankful to all the other staff and students I have worked with at the University of Strathclyde, particularly Paul, Billy, Lindsay, Margaret, Neil, John, Kate and Muir. I also thank the undergraduate students who I have worked with over the last three and a half years.

I also gratefully acknowledge the funding from the University of Strathclyde, Energy Technology Partnership (ETP) and Lotte Chemical for supporting this studentship. Additionally, I also would like to acknowledge the Royal Society of Chemistry, University of Strathclyde and ETP for additional funding to support the conferences and exchange I was able to undertake.

I would like to extend the utmost gratitude to Dr Brian McMillan and Dr Leung Tang for their support, guidance and friendship.

I would like to extend my heartfelt appreciation to my girlfriend, Nataliya Vasylyeva, for her support and encouragement throughout my PhD.

Finally, I would like to say the biggest thank you to my mother, Karen Bryans, for her never-ending belief and support for my entire duration at University. Without this, I would never have made it this far.

Abbreviations

acac	Acetylacetonate
acacen	Acetylacetone
A	Area
Bpy	2,2-Bipyridine
BAC 2	Biological Activated Carbon Composite Electrode
Q	Charge
α	Charge Transfer Coefficient
R_{CT}	Charge Transfer Resistance
CMPB	*N*-chloromethyl-*N*-methylpyrrolidinium bromide
CAES	Compressed Air Energy Storage
$c_{O/R}^{*}$	Concentration of Oxidant/Reductant in Bulk Solution
$c_{O/R(0,t)}$	Concentration of Oxidant/Reductant at Electrode Surface
CE	Counter Electrode
I	Current
CV	Cyclic Voltammetry
2-EMP	diethylmethylpropylammonium bromide
2-MEP	dimethylethylpropylammonium bromide
C_{dl}	Double Layer Capacitance
D	Diffusion Coefficient
DPS	Double Potential Scan
i	Electrode Current Density
E	Electrode Potential
ES	Energy Storage
EMMB	*N*-ethyl-*N*-methylmorpholinium bromide
i_0	Exchange Current Density
F	Faraday Constant
ω	Frequency
g	Grams
GFA	Graphitised Rayon Felt Electrode
GFD	Graphitised PAN Felt Electrode
Hz	Hertz
h	Hours
IEA	International Energy Agency
MOPB	*N*-methoxymethyl-*N*-methylpiperidinium bromide
MEP	*N*- methyl-*N*-ethylpyrrolidinium bromide
min	Minutes
M	Molar
mol	Mole
E_{eq}	Nernst Potential
n	Number of Electrons
η	Overpotential

ϕ	Phase Angle
BPP4	Phenolic Resin Carbon Composite Electrode
PAN	Polyacrylonitrile
PPG86	Polypropylene Carbon Composite Electrode
PVE	Polyvinyl Ester Carbon Composite Electrode
BMA 5	Polyvinylidene Fluoride Carbon Composite Electrode
PS	Potential Scan
QBr	Quaternary Ammonium Complexing Agent
RE	Reference Electrode
k_0	Rate Constant
RFB	Redox Flow Battery
RDE	Rotation Disc Electrode
s	Seconds
S	Siemens
E_0	Standard Electrode Potential
SCE	Standard Calomel Electrode
SHE	Standard Hydrogen Electrode
SOC	State of Charge (%)
T	Temperature
t	Time
TBABr	tetrabutylammonium bromide
TEABr	tetraethylammonium bromide
TPABr	tetrapropylammonium bromide
R_u	Uncompensated Resistance
R	Universal Gas Constant
WE	Working Electrode
QBr1	*N*-(carboxymethyl)pyridinium bromide
QBr2	*N*-(2-carboxyethyl)- *N* -methylmorpholinium bromide
QBr3	*N*-(2-carboxyethyl)- *N* -methylpyrrolidinium bromide
MO1	*N*-(ethanediyl)bis(*N* -methylmorpholinium) dibromide
MO2	*N*-(propanediyl)bis(*N* -methylmorpholinium) dibromide
MO3	*N*-(butanediyl)bis(*N* -methylmorpholinium) dibromide
PSO	*N*-(sulfanomethyl)pyridinium dibromide
MOSO	*N*-(sulfinomethyl)- *N* -methylmorpholinium bromide
MPSO	*N*-(sulfinomethyl)- *N* -methylpyrrolidinium bromide

Abstract

The zinc-bromine hybrid redox flow battery (RFB) is one of the few battery systems that have seen implementation on the medium to large scale energy storage. However, there still exist financial barriers to allow this technology to be fully utilised on the market. To improve this system, several potential areas could be improved from cell design, additive chemistries and electrode materials.

Throughout this study, work was carried out on identifying new novel additives with the objective to complex the bromine without forming an immiscible phase. This work identified the use of a variety of ammonium- and phosphonium-based additives with appropriate carboxylic, sulphonate and hydroxyl functional groups to aid in the solubility of the complex. These additives were analysed in terms of their electrochemical response and on their physical characteristics. The data obtained were compared the industry standard complex, *N*-methyl-*N*-ethylpyrrolidinium.

Carbon felt electrode materials and activated carbon electrode coatings were also investigated to examine their potential applications in this flow battery. The felt electrodes although providing a greater surface area, caused the immiscible phase to become trapped within it which led to an increase in flow pressure which ultimately was detrimental to the performance of the battery. This shows an even greater need to develop the additive chemistries to make use of the large surface areas offered by the felts. The activated carbon coating was found to be preferable with improved electrode kinetics and ease of the immiscible phase removal once charged.

Finally, experience was gained on two large scale batteries which were characterised in terms of performance optimisation as part of this work. The $ZnBr_2$ 25 kW/ 50 kWh RFB was characterised at the Power Network Demonstration Centre, Scotland, and the all-vanadium 200 kW/ 400 kWh RFB was characterised at the École Polytechnique Fédérale de Lausanne – Laboratory of Physical and Analytical Electrochemistry, Switzerland. This has led to a better understanding of potential complications and differences that occur from scaling up redox chemistries from a lab bench to an industrial level.

Contents

1. Introduction

Energy resources have been crucial for human existence since the very beginning. These key sources are natural gas, oil, coal, nuclear power and energy generated from renewable sources, such as energy of tides, ocean currents, wind, solar, geothermal and biomass.

They have enabled the industrial revolution and shaped the structure of the global economy. However, the availability and use of these energy resources have recently become a focal point of much debate. In modern times, the reliance on fossil fuels is not a sustainable solution to meet global energy demands. Whether it is due to the negative impact these have on the global and local environment or the economic stress from the resources becoming scarcer or even the need to diversify energy resources in general to ensure energy security of the countries, there has been significant investment and time allocated to discovering a feasible low-carbon solution to replace fossil fuels with.

There are three recognised uses of energy, *viz.* heat, electricity, and transport. Commonly, heat is provided from the burning of natural gas although there are instances where electricity or coal are also used to provide the heat. However, there is a question on the efficiency of each of the energy sources in terms of their calorific value. Electricity can be derived from a range of energy sources, such as fossil-fuel based power plants (usually on coal and natural gas), nuclear, and renewable energy. Transport, for many years, has been powered through consumption of petrol and diesel, produced from oil products and to a small extent from biofuels, with a small minority of cars being powered from either electric batteries or hydrogen fuel cells.

Coal, natural gas and oil have played an important role in the global economy. These three types of energy sources are classified as fossil fuels. These fuels are extracted, processed and used to generate energy. Typically, fossil fuel production and utilisation results in the emission of various pollutants and greenhouse gases (GHGs). Coal and natural gas are perceived as a type of the fossil fuel having the most negative impact on the environment in terms of the emission of pollutants and GHGs. It is typically used for production of heat and power with natural gas also being partially used in the transport industry. Oil is predominately used the most in the transportation sector.

Nuclear power plays an important role in generation of electricity: globally 9% of electrical energy supply is provided through this type of energy[1]. Generating energy in this manner is widely considered as a safe process and ‘carbon free’. However, nuclear power divides public opinion and one of the key issues is the generation of nuclear waste. The process of generating nuclear energy revolves around nuclear fission which is where the nucleus of an atom splits into smaller fragments[2]. This process is a highly exothermic reaction which releases large amounts of energy in the form of kinetic and electromagnetic energy. There are currently many variations to the fuel and cycle which offer advantages such as less harmful waste, longer lifecycles and by-products that can be used in other industries therefore decreasing the overall waste produced[3,4,5]. However, the cycle still stands in that a finite source of material is mined, utilised to generate energy and then produce harmful waste. The current solution to the disposal of this material is to bury it in areas considered derelict, usually regions of desert such as parts of Mexico, in special containers to help minimise the radiations effect on the local environment[6]. This leaves the predicament that the ecosystem is inevitably going to be affected by radiation as, for instance, plutonium-240 (240 being the atomic mass of the isotope for this element) has a half-life of 6,580 years[7]. What this means is that for a given mass of material, only half of that mass of radioactive material will have decayed in that period of time. Note that this does not mean all the material will decompose after 13,160 years but rather it decomposes to a quarter of the remainder material as another half-life is required to decompose to half of that and so on. This therefore leads to an accumulation of waste that will take an incredible period to fully decay. Furthermore, the power plants have relatively short life spans due to the radioactive degradation of material, requiring any given site to be decommissioned after around 40-60 years of use[8]. This now leaves France in the situation that a vast number of their plants are now being decommissioned and the relocation and construction of new plants are required to ensure they meet the energy requirements and this is causing some economic concern[9].

Renewable energy sources are recognised as the cleanest and, potentially, the safest technologies producing energy. Their distinct feature is that the energy from – wind, solar energy, energy of waves and tides, geothermal and energy from biomass – is constantly replenished and will never run out. Furthermore, comparing to other energy sources, the process of energy generation from renewables leads to significantly smaller amount of GHGs or pollutants. Currently, the share of renewable energy sources in total global primary energy supply is quite low and is just over 2%[10]. The most common methods of renewable energy generation are from solar and wind. Solar energy uses the light and heat from the sun through varying technologies including photovoltaics, artificial photosynthesis and solar heating. The photovoltaic technique utilises semiconducting materials that allow the transfer of energy from "light" to become an electrical signal. Currently solar energy is expected to produce 300 GW by 2030, although issues relating to the cost of photovoltaic electricity production will need to be resolved in order to allow this to become competitive with nuclear or oil and gas energy production[11].

Wind energy is another well-known source of renewable energy. Wind technologies have gone through tremendous improvements and developments culminating in a reduction in costs over the years and consequently, a widespread deployment of the technology[12, 13, 14]. The current and IEA forecasted levels of electricity generation from solar and wind are presented in Figure 1.1.

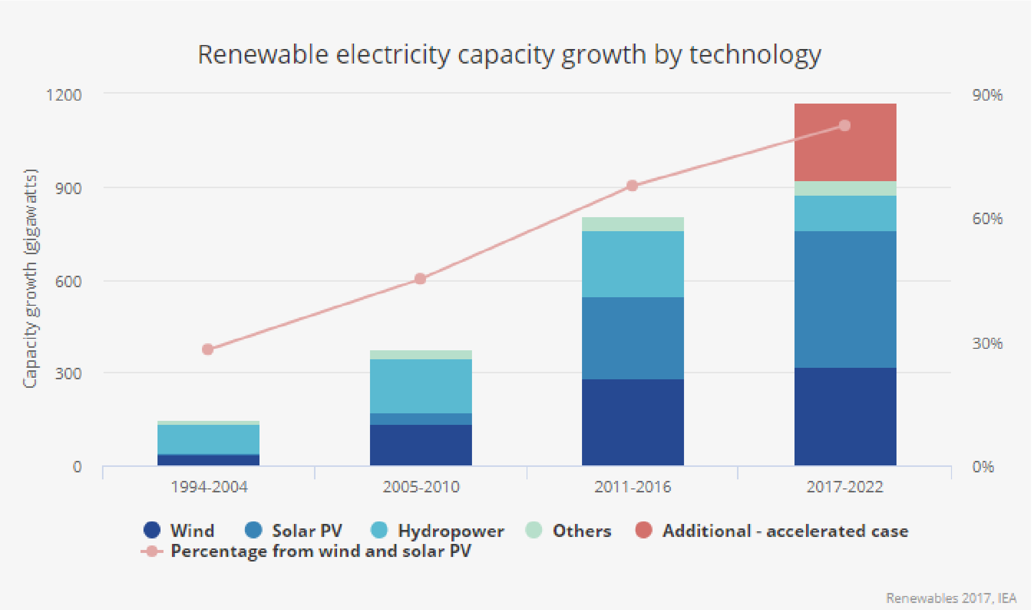

Figure 1.1 Renewable electricity capacity growth by technology. Source: IEA, 2017[15]

Another low carbon technology is using hydrogen as an energy vector and this has been proposed for vehicular power as well as for stationary energy generation. Hydrogen can be produced from many sources ranging from current fossil fuels, *e.g.*

thermal cracking of ethane, to the electrolysis of water. Once hydrogen has been produced, the energy generation comes from reacting the H_2 either in an electrochemical fuel cell or an internal combustion engine[16]. Regardless of the reaction, the product it forms is H_2O. However, the use of hydrogen as an energy vector has several challenges that require to be addressed. One of these is the storage of the hydrogen. Despite hydrogen having a very high energy density due to its low molecular weight, the energy density by volume is very low: hence the need for compression to high pressures. Issues of transportation and subsequent storage at the site then also become problematic, as the pipework currently used would become embrittled, meaning new polymer-based pipes would need to be installed in major cities. Additionally, due to its small molecular mass and therefore size, it is also inevitable that the hydrogen will leak from any containment vessel. Nevertheless, this has not stopped the development of hydrogen networks in some major cities such as Aberdeen and Leeds[17, 18].

One of the major inhibiting factors of the renewable energy sources penetration to the global market is the cost and time required to change the infrastructure from a fossil fuel dependent scheme to one that would utilise these newer technologies. To support this, environmental impact has become an indispensable part of the political agenda, thus, leading to development and adoption of an energy strategy by many countries. For example, the nuclear incidents at Chernobyl and Fukushima have created very negative attitudes in the public's eye which has led to strong opposition from local regions whenever nuclear power plants are attempted to be set up. One country which has moved away from nuclear energy is Germany, once the 5th largest user of nuclear energy for electricity generation in 2012 but now aiming to go nuclear-free by 2022[19]. However, other countries as France, Germany's neighbour, has a massive dependence on nuclear energy which delivers 76% of the electrical domestic energy and this has allowed France to enjoy many years of low fixed energy prices[20].

Renewable energy features strongly in a large number of countries' energy agendas, with Germany aiming to supply 80% of its energy demand through renewables by the year 2050 and Scotland aiming to produce 100% electrical energy through renewables by 2020[21, 22]. It is without doubt that there is a strong global tendency to increase the share of renewable energy sources in the primary energy supply as driven by international political agendas from the Kyoto Protocol and recent Paris Agreement. It is widely accepted that human activity, based on vast consumption of fossil fuels, have caused significant damage to the environment affecting human health (lowering living standards in certain areas of the world and can contributing to certain diseases) and environmental health (contributing significantly to climate change and its associated impact)[23]. Thus, the Paris Agreement, signed by 197 and ratified by 170 countries, emphasised the need to move from use of fossil fuels to alternative energy sources and low carbon technologies that cause less negative impact on environment in general and climate change in particular[24].

Renewable energy seems a likely solution to a problem of the climate change. However, there is a difficulty since most of the renewable technologies generate energy at varying amounts/rates, depending on the location and weather conditions. This leaves the issue of energy being generated in an excess at times and in a deficit at other times in relation to demand. This challenge can be solved with energy storage which is essential to balance these peaks and shortfalls and so to stabilise the energy provided to the electrical grid network and meet electricity demand.

1.1 Energy Storage Systems

Energy storage is the process of converting electrical energy from a power network into a form that can be stored and later converted back to electricity at a time when it is needed. Such a process makes efficient use of the excess energy at times of low demand or from intermittent energy sources to be more efficiently used at time of high demand or when no source of electricity generation is available (most common in isolated rural communities at night where PV is used).

A vast number of storage methods exist, either in development or already very mature technologies. There is no one solution to energy storage to fit all needs as a variety of applications and geographical locations will require different technologies. Power quality in a network, for example, requires high power output over a short period of time whereas energy management will utilise the stored energy over much longer periods. Figure 1.2 shows a number of technologies with their power and energy capacity ranges and so where their applications lie[25–27].

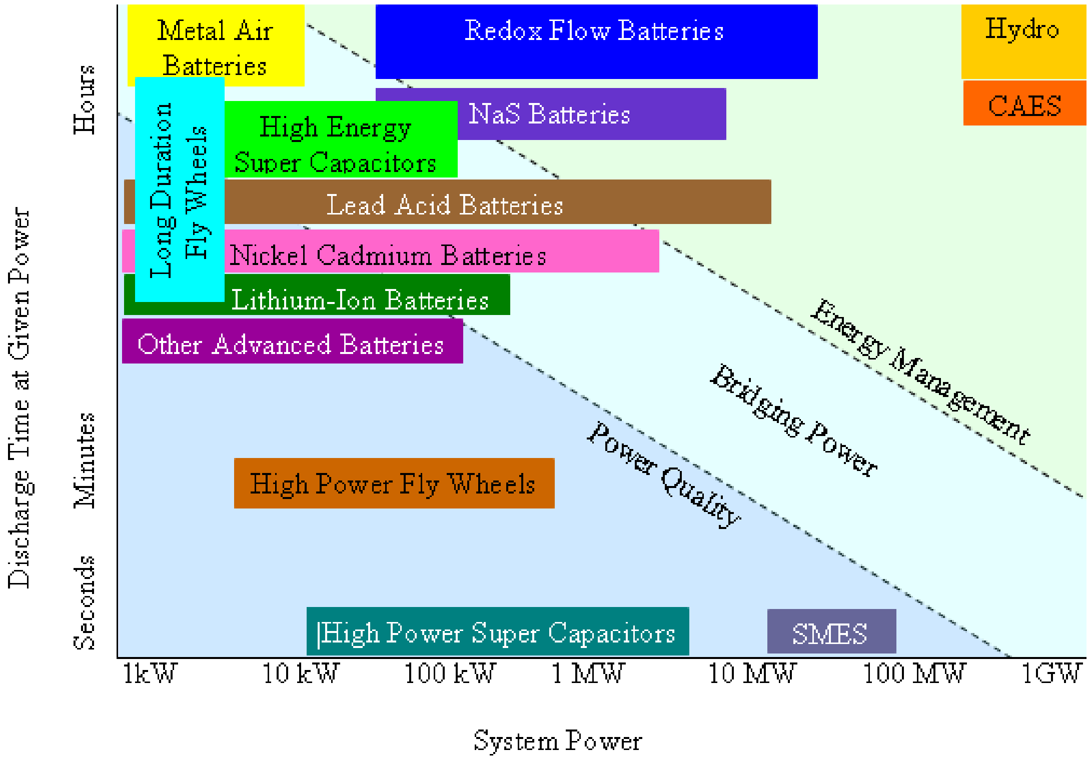

Figure 1.2 Range of energy storage methods and their accompanying applications

This section will briefly review some of the technologies in Figure 1.2 before focussing on redox flow batteries.

1.1.1 Pumped Hydroelectric ES

On the top right corner of Figure 1.2 can be seen the pumped hydropower and the compressed air systems. Pumped hydropower is a method which stores energy in the form of gravitational potential energy of water[28]. The way in which this is carried out is that during off peak times, when generated power from other sources is in excess, this excess power is used to run the turbines that take water from one reservoir to another at higher elevation. Then during periods of high electrical demand, the stored water is released through the same turbines to produce electricity, as illustrated in Figure 1.3.

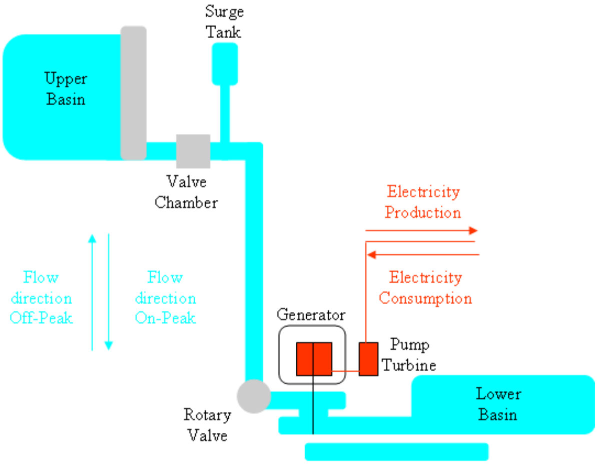

Figure 1.3 Pumped Hydro Energy Storage

Although this process has a net overall consumption of energy due to the energy required by the turbines, it is currently the largest grid energy storage available and had a worldwide generating capacity of 1,064 GW in 2016[29]. Currently this form of hydropower represents 4.3% generation capacity within the EU but is expected to level out due to being limited by geological location[30].

There have been several developments however to either try and make current systems more efficient or more versatile with location. One example of this can be seen in Japan where they have developed a 30 MW hydropower plant in Okinawa, which uses pumped seawater[31,32]. Since then, numerous projects across America and Europe have been proposed[32–34]. There has also been a development to use the excess power generated by solar and wind to power the pumps for this hydroelectric system which is expected to improve the overall efficiency of the process while also resolving the issue with the variability of energy output from the wind or sun[32].

1.1.3 Compressed Air ES

Compressed air energy storage (CAES) is a very similar process to the previously discussed pumped hydropower plants in terms of applications, output and energy capacity. Unlike pumped hydro however, CAES uses ambient air which is compressed and stored in underground caverns during off-peak times and once electrical demand is required, the process generates electricity by releasing the pressurised air (causing expansion) within a turbine which generates the power to meet the demand, as illustrated in Figure 1.4[28].

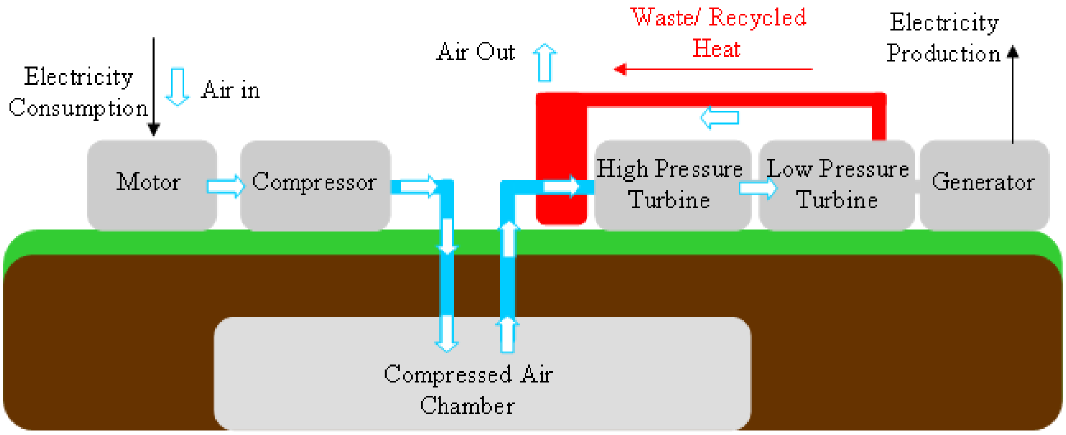

Figure 1.4 Compressed Air Energy Storage

The compression of the air generates heat and the process used to expand the gas cools the gas and so requires heating before the turbine. If the heat generated during compression can be stored and used for heating the expansion process, this will improve the overall efficiency considerably. However, there are currently two proposed methods in which the CAES system utilises the heat generated through compression: adiabatic and conventional.

- Adiabatic storage is the method that stores this heat energy generated from the compression and uses it to expand the air during the generation of power. The heat is stored in solids such as concrete or stone, or more feasible within liquids such as oils or molten salt solutions which can reach temperatures of 600°C[35].

There are currently no utility scale plants but a pilot plant is scheduled to undergo construction in 2018 in Germany[36].

- Conventional CAES storage removes much of the heat generated through compression through use of intercoolers to dispose of it to the atmosphere. Therefore, since the air temperature on expansion is low, a natural gas burner is used to heat this air to ambient. However, this is the only approach so far to have seen commercial implementation[37].

1.1.4 Supercapacitors/ Capacitors

At the bottom left corner of Figure 1.2 is where the supercapacitors/capacitors and flywheels can be found. These capacitors are the most direct method of storing electrical energy. Essentially a capacitor is two metal, conducting plates separated by a non-conducting layer known as a dielectric[28]. When one of these metal plates is charged with electricity the other metal plate will have the opposite charge induced upon it, as shown in Figure 1.5.

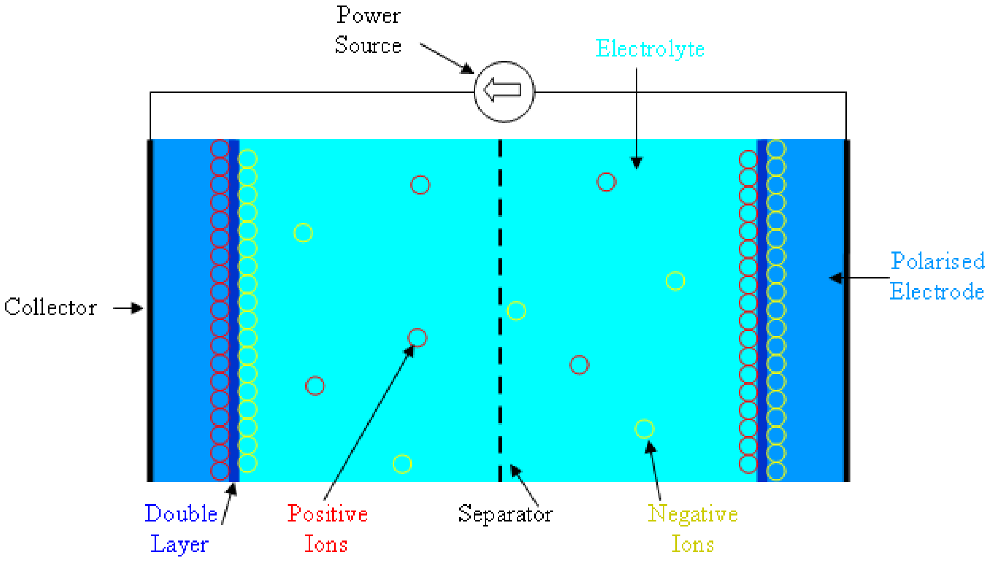

Figure 1.5 Supercapacitor

These capacitors can be charged much faster than that of batteries and maintain a higher cycle lifetime with high efficiencies, going into the tens of thousands of cycles. However, these devices are often only used to for short periods of time at high power. For these capacitors to be considered commercially, the power storage required to be used within the grid would require a large dielectric area which is too expensive.

This is where the development of the supercapacitors has been targeted to challenge this issue with the proposed capacitance and energy density vastly increasing, therefore leading to smaller, more economically feasible designs. These supercapacitors have an electrolyte solution between two solid conductors rather than the previous solid dielectric. The electrodes used are a carbon material which have a high porosity to increase the overall surface area of the conductor. Couple this with a very small separation between the two electrodes leads to the capacitance and the stored energy capabilities to be vastly superior to that of the original capacitors by roughly two orders of magnitude.

Nevertheless, there are still major issues present with this technology in that the durations remain to be at short times and there is also high energy dissipation due to self-discharge loss. However, since this technology is like combustion turbine systems it can be easily integrated into existing power grids. Since this system has a ramp rate similar to gas plants it makes it an ideal application for meeting peak load[28].

1.1.5 Flywheel

Flywheels have been used for a considerable time, dating back to German artisan, Theophilus Presbyter, who recorded using them on numerous machines between 1070-1125 where they store energy in the angular momentum of a spinning mass[22, 28]. During their charge cycle, conventional flywheels are spun by a motor; whilst during discharge this motor is then used as a generator to convert the kinetic energy into electrical energy. This therefore means the total energy output of a flywheel is dependent on the size and speed of its rotor whereas the power rating will come down to the motor/generator.

Figure 1.6 shows a typical energy storage flywheel and its basic components which consist of a flywheel which spins at high velocities to maximise the potential energy it can store through rotational kinetic energy. However, there are several parameters that can constrain this, such as external influences and “windage” losses (common term to describe frictional loss). These are minimised by the containment system which provides a vacuum environment.

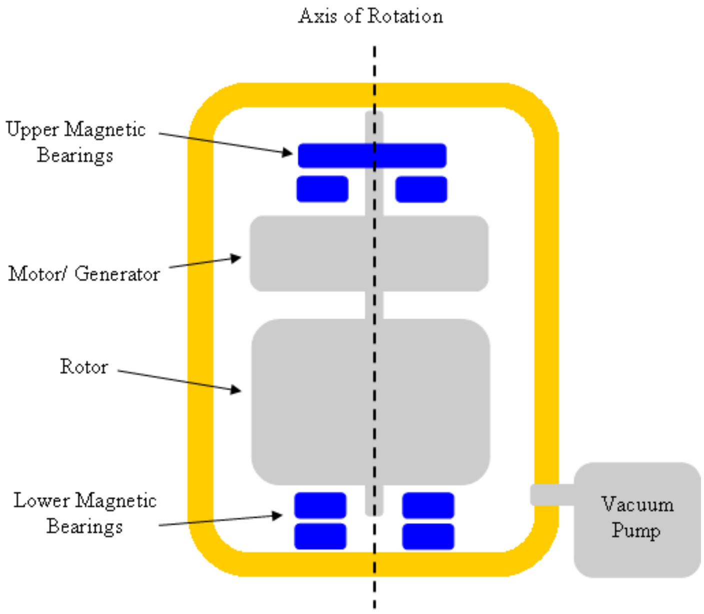

Figure 1.6 Flywheel

The main advantage flywheels have over several other technologies is that they have long life spans which can provide several hundreds of thousands of full charge/ discharges cycles with efficiencies typically in the region of 90-95%. However, much like the supercapacitors they can only provide short durations restricting their applications to that of systems requiring high power over a short time frame. These applications lie within the power quality region for uses such as ride-through of interruptions or as a bridge for one power source to another. Flywheels have also seen use for demand reductions and energy recovery in electrical powered transit systems. There have also been associations of the flywheel providing a smoothing service to wind turbine systems and stabilise small scale power networks[38].

1.2 Electrochemical Energy Storage

Rechargeable (secondary) batteries which store electrical energy in the form of chemical energy have been around for many years. A battery consists of one or more electrochemical cells which have a liquid, paste or solid electrolyte with a positive electrode (cathode during discharge) and a negative electrode (anode during discharge), as seen in Figure 1.7.

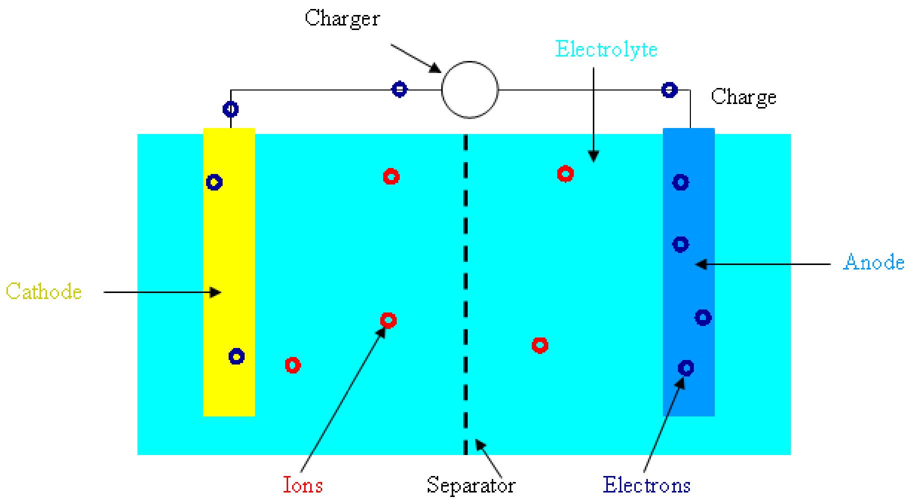

Figure 1.7 Basic components of a rechargeable secondary battery

As discharge occurs, electrochemical reactions take place at the electrodes (*e.g.* $Cu^{2+} + 2e^{-} \rightarrow Cu$ and $Zn \rightarrow Zn^{2+} + 2e^{-}$) providing a flow of electrons through an external circuit. These reactions are reversible allowing the battery to be recharged by applying an external voltage across the electrodes. Secondary batteries have generally fast responses to load changes. Furthermore, they also experience low standby losses and can have efficiencies between 60-95% depending on the battery type and application. However, most batteries can also suffer from low energy densities, small power outputs, and short life cycles making large scale applications unsuitable, however, with notable exceptions such as the Li-ion battery. Additionally, since most batteries contain toxic materials, the potential ecological impact also needs to be taken into consideration. Nevertheless, there are currently utility scale batteries in use for energy storage as backup power supply in niche applications.

1.2.1 Lead Acid Battery

The lead acid battery is one of the oldest and most widely used batteries dating back to its invention in 1860[27]. The lead acid battery consists of electrodes of lead metal and lead dioxide in an electrolyte of ~37% sulphuric acid in the charged state. During discharge this battery loses some of the sulphuric acid due to the electrodes turning this into lead sulphate causing the electrolyte to become more dilute. The reactions for the discharge are:

Anode

$$Pb + SO_4^{2-} \rightarrow PbSO_4 + 2e^- \quad E^0 = 0.356\, V\ vs. SHE \qquad \text{Eq. 1.1}$$

Cathode

$$PbO_2 + SO_4^{2-} + 4H^+ + 2e^- \rightarrow PbSO_4 + 2H_2O\ E^0 = 1.685\, V\ vs. SHE \qquad \text{Eq. 1.2}$$

Overall

$$Pb + PbO_2 + 2H_2SO_4 \rightarrow 2PbSO_4 + 2H_2O\ E^0 = 2.04\, V\ vs. SHE \qquad \text{Eq. 1.3}$$

This type of battery has the advantage of being low cost, at roughly \$300-\$600 per kWh, with high efficiency (70-90%) and high reliability[27,39]. Its applications so far have mainly been for power quality and some spinning reserves. However, in terms of energy management there have been very few implemented due to its short life cycle (500 –1000 cycles) and a low energy density (30 – 50 Wh/ kg) due to high density of the lead[39].

1.2.2 Lithium ion battery

Commercially introduced in the 1990's by SONY this battery consists of a lithiated metal oxide cathode and a graphitic carbon anode with the electrolyte comprises of lithium salts dissolved in carbonates (such as diethyl carbonate or ethylene carbonate)[25]. As the battery is charged, these lithium ions intercalated in the cathode move from the layered metal oxide, through the electrolyte to form an intercalated layer in the graphite, as shown below. The reverse of this occurs during discharge[27]:

Anode

$$LiCoO_2 \rightarrow Li_{1-x}CoO_2 + xLi^+ + xe^- \qquad \text{Eq. 1.4}$$

Cathode

$$xLi^{+} + xe^{-} + xC_6 \rightarrow xLiC_6 \qquad \text{Eq. 1.5}$$

Overall

$$LiCoO_2 + xC_6 \rightarrow Li_{1-x}CoO_2 + xLiC_6 \quad E^0 = 3.7\,V \qquad \text{Eq. 1.6}$$

Lithium ion batteries have been massively improved since their first commercial launch. One key change has been the metal oxide used, from cobalt to manganese and iron oxides. The development of these materials has led to the energy density being improved from 90 Wh/ kg to 400 Wh/ kg and the cycle life up to 2000 cycles with an efficiency almost reaching 100%[40,41].

Currently, lithium ion batteries dominate the small portable device industry. However, there remains some major challenges for making it into any large-scale applications. The main issue focussed upon by many is the high cost (greater than $600 per kW0h) due to the packaging and protection circuits required to operate this battery to lower the risk of flammability[40].

1.2.3 Sodium Sulphur Battery

The sodium sulphur (NaS) battery consists of liquid sulphur at the positive electrode and liquid sodium at the negative electrode separated by a solid alumina ceramic electrolyte, as shown in Figure 1.8[25].

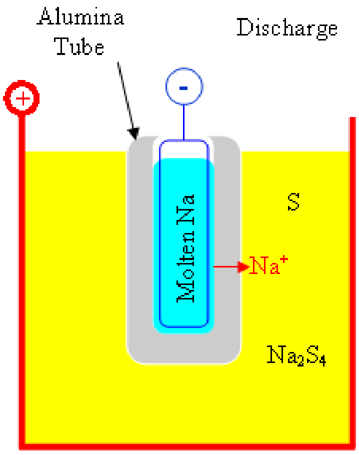

Figure 1.8 Basic structure of a NaS battery

The electrolyte only allows the Na^+ ions to pass through to combine with the sulphur to form sodium polysulphides. As the cell discharges the transfer of this sodium ion from the negative electrode to the positive one within the cell causes electrons to flow in the external circuit. The cell pair has a cell voltage ~2.0 V). On charging the sodium polysulphide releases the sodium ion to transfer through the electrolyte again. The entire system is run at a temperature between at 270-350 °C[42]. The NaS battery has energy densities of 150-240 W/kg and a typical life span of ~1,500 cycles. Additionally the battery has a high efficiency (85-90%) enabling the applications this battery to be used for power quality and peak shaving[41].

The main disadvantage to this system is the temperature at which it is required to be maintained which consumes the own battery's stored energy, effectively reducing the overall performance. Furthermore, the battery is very expensive to build and to operate, costing roughly $2000 / kW and $350 / kWh respectively.

1.2.4 Nickel Cadmium Battery

Nickel-cadmium batteries (NiCd) have been around as long as the lead acid batteries and have seen numerous developments over the years. In the charged state, the NiCd battery contains a nickel oxy-hydroxide positive plate and a cadmium negative plate separated by an alkaline electrolyte held in a porous separator and rolled into a spiral shape, shown in Figure 1.9.

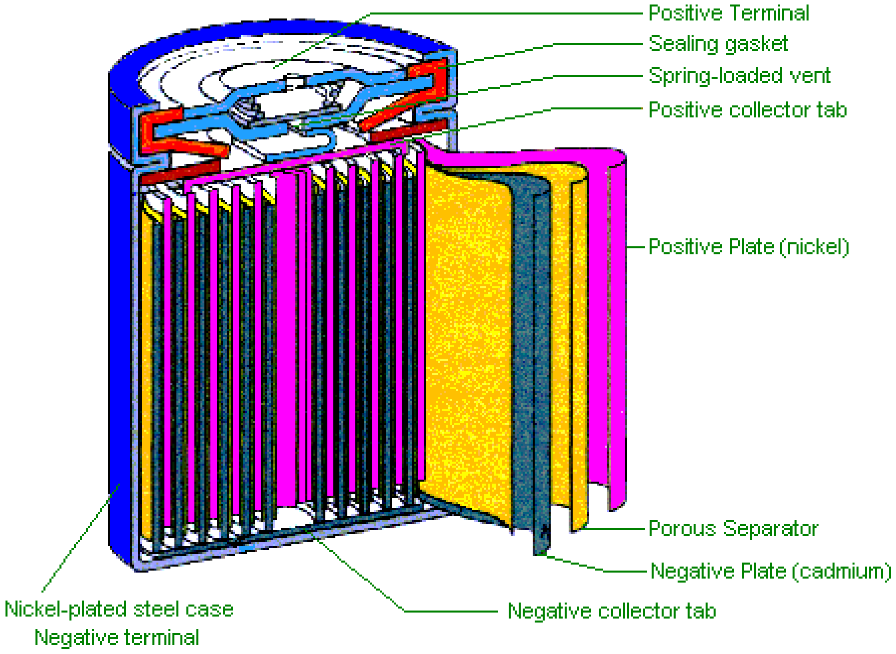

Figure 1.9 NiCd battery [43]

The chemical reaction for the discharge process is:

Anode

$$Cd + 2OH^- \rightarrow Cd(OH)_2 + 2e^- \qquad \text{Eq. 1.7}$$

Cathode

$$2NiO(OH) + 2H_20 + 2e^- \rightarrow 2Ni(OH)_2 + 2OH^- \qquad \text{Eq. 1.8}$$

Overall

$$2NiO(OH) + Cd + 2H_2O \rightarrow 2Ni(OH)_2 + Cd(OH)_2\ E^0 = 1.2\,V vs. SHE \qquad \text{Eq. 1.9}$$

These batteries have high energy densities (35 Wh/kg) with very low maintenance requirements. However, they also have a relatively low life time (1,000 cycles) [41]. Despite this, they are popular in power tools, emergency lighting, telecoms and generator starting. Latterly however, the portable market has been taken over by the lithium ion battery. The reasons for this are the relatively expensive cost associated with this battery ($1000/ kWh) due to the manufacture process. In addition, the cadmium is a toxic heavy metal causing disposal issues.

1.2.5 Metal Air Battery

Metal air batteries can be regarded as a unique form of fuel cell where the metal can be considered as the fuel and the air as the oxidant, as shown in Figure 1.10. These batteries are the smallest and least expensive of the batteries discussed with little impact on the environment. However, there are a few issues surrounding this technology in that the recharging of this battery is both difficult and very inefficient.

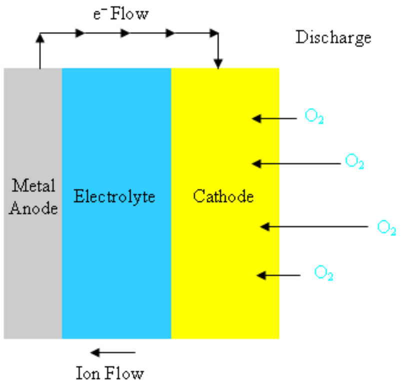

Figure 1.10 Basic structure of a metal air battery during discharge

This technology can be regarded as being in its infancy as major developments are still taking place to improve the overall impact this battery will have. However, metal air batteries at the moment only have a lifetime of a few hundred cycles and efficiency between 40% – 60% due to the difficulty in replenishing the bifunctional catalyst[44].

The current set up is the anode being an energy dense metal which releases electrons upon oxidation, such as zinc or aluminium, with the cathode (or air) electrode often being a porous carbon structure or material with similar properties. The electrolytes are hydroxide ion conductors either in a liquid form or solid polymer membrane saturated with the electrolyte. For example the zinc-air battery; the anode reaction would be[45]:

$$Zn + 4OH^- \rightarrow Zn(OH)_4^{2-} + 2e^- \quad E^0 = 1.25\,V\ vs.SHE \qquad \text{Eq. 1.10}$$

A reaction occurring in the fluid phase:

$$Zn(OH)_4^{2-} \rightarrow ZnO + H_2O + 2OH^- \qquad \text{Eq. 1.11}$$

Cathode reaction:

$$O_2 + 2H_2O + 4e^- \rightarrow 4OH^- \quad E^0 = 0.4\,V\ vs.SHE \qquad \text{Eq. 1.12}$$

This leads to an overall reaction:

$$2Zn + O_2 \rightarrow 2ZnO \quad E^0 = 1.65\,V\ vs.SHE \qquad \text{Eq. 1.13}$$

Though these air batteries have high energy densities and low costs, making them ideal for most primary battery applications, the rechargeability of the overall system battery must be further developed to enable its much commercialisation in energy storage.

1.3 Redox Flow Battery

Redox flow batteries (RFBs), of particular interest in this study, can provide a solution to large scale energy storage a more efficient link between energy production and energy demand[27,46,47]. This type of battery system has the advantage of lower cost, rapid response, low level of self-discharge and is considered to have a much safer operation compared to other battery systems such as the sodium sulphur and lithium ion batteries[48,49]. Additionally, as with all battery systems, it has the advantage of being more flexible and mobile in relation to none electrochemical technologies, such as pumped hydro and compressed air storage. The latter large scale energy management technologies are restrained by the suitability of the terrain whereas batteries, such as RFBs, can be readily installed anywhere[42].

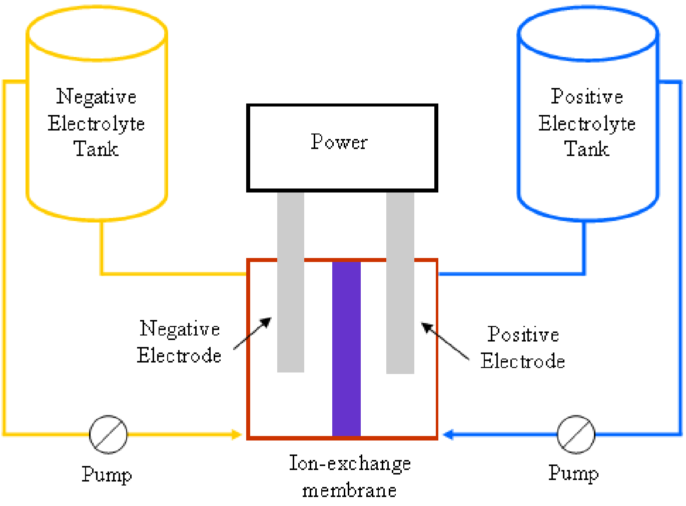

Figure 1.11 Typical structure of a redox flow battery

The RFB typically consists of two external reservoirs which store the electrolyte containing the electroactive species, as shown in Figure 1.11. By controlling the total volume and concentration of the electroactive species, one controls the energy storage density of this storage system[50,44]. The stacks, which consist of two electrodes separated by a membrane with the electrolyte flowing either side, control the power density of the battery. As with all energy storage applications, high power and voltages capacities are often required to meet the electrical demand. RFBs achieve this through stacking unit cells together in an electrical series to increase the voltage and then these stacks can be electrically connected in parallel to obtain high power levels. Figure 1.12 shows the typical set up of “bipolar” electrodes in order to improve the systems feasibility by reducing the weight and volume of the system whilst maximising the voltage and current output[44].

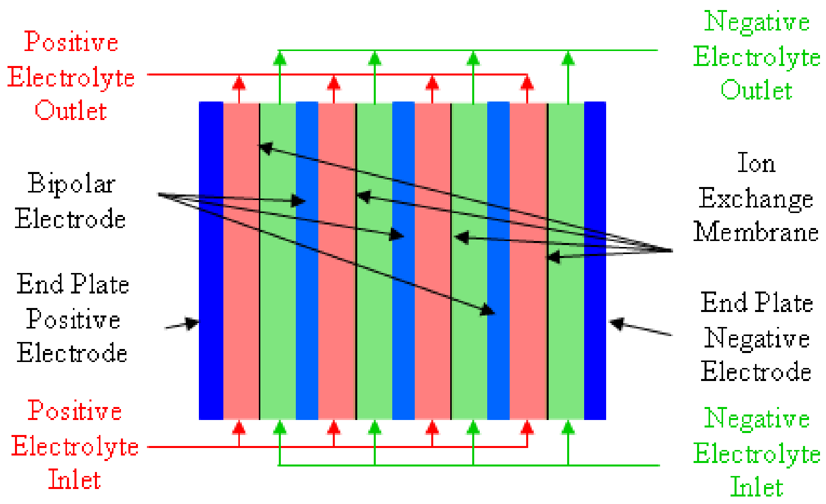

Figure 1.12 Bipolar plates of stacked redox cells

This decoupling of energy capacity and power output is highly desirable as this allows for more efficient designs to meet the various applications of this energy storage system.

Due to the flexibility of RFB systems, the number of research publications and commercial development and deployment of various RFBs have increased over the last decade[18,25,26]. However, from the vast range of RFBs available they are categorised in this report within three types: aqueous, non – aqueous, and hybrid.

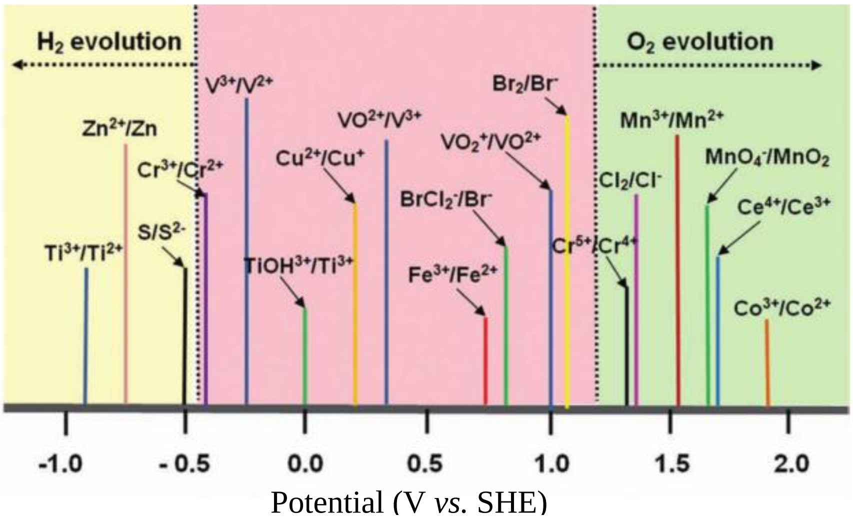

Figure 1.13 Standard potentials of redox couples with hydrogen evolution being taken from a carbon electrode (taken from W. Wang *et. al.*)[26]

Figure 1.13 shows a selection of redox couples that RFBs can use. However, aqueous flow batteries are constrained to the limits where water electrolysis may occur with hydrogen evolution occurring below −0.44 V and oxygen evolution above 1.23 V against a standard hydrogen electrode (SHE).

1.3.1 Aqueous redox flow batteries

Aqueous RFBs are among the most developed with numerous flow battery systems being demonstrated[53,42,52]. As the name suggests, these are systems with a water based electrolyte. Although they have a high-power density, these batteries have low energy densities and high material costs. Despite a number of developments, such as that of the mixed acid electrolyte in the vanadium redox flow battery to yield higher densities[54], these systems are still struggling to compete with alternative technologies. This led to the development of a variety of RFB types.

The all-vanadium RFB is the most iconic and commercially available of all the RFBs. Discovered by M. Skyllas- Kazacos *et. al.* in 1988, the vanadium RFB has seen a lot of development at the fundamental and industrial level[55]. This original system was set as a superior alternative to the iron-chromium RFB which was used by NASA[56]. One of its advantages is its resilience to cross membrane contamination. Since the same element is used on both sides of the cell, should electroactive species cross over, the electrolytes can simply be regenerated through remixing and electrolysis without harm to any of the materials or requirement for the system to undergo complicated separation treatment. However, due to the poor solubility of the vanadium species, vanadyl sulphate was used in concentrated sulphuric acid. This is typically referred to as a Generation I – VRFB[57]. This VRFB gives the following reactions during discharge[58]:

Anode:

$$V^{2+} \rightarrow V^{3+} + e^- \quad E^0 = -0.26\, V\ vs.SHE \qquad \text{Eq. 1.14}$$

Cathode:

$$VO_2^+ + 2H^+ + e^- \rightarrow VO^{2+} + H_2O \quad E^0 = 1.00V\ vs.SHE \qquad \text{Eq. 1.15}$$

Overall:

$$V^{2+} + VO_2^{+} + 2H^{+} \rightarrow V^{3+} + VO^{2+} + H_2O \qquad E^0 = 1.26\ V\ vs.SHE \qquad \text{Eq. 1.16}$$

This gives an overall open circuit voltage of 1.26 V *vs* SHE under standard conditions. The energy density is limited by the concentration at which the vanadium ions can stay within solution. The current operating level is 2 M $VOSO_4$ in 2.0 M sulphuric acid. Above this concentration the VO_2^{+} (V^{5+}) ions can precipitate out as V_2O_5, especially when temperatures are above 40°C whereas the V^{2+}/V^{3+} exists as solid vanadium oxide at temperatures below 10°C[27]. This limits most practical examples of these batteries to operate at a temperature range between 10-40°C with a concentration less than 2 M. Such concentrations gives an open circuit of 1.6 V when fully charged[42]. Despite this however, the VRFB has become the most commercially successful RFB due to its advantages over other systems. This is due to the systems' ability to undergo charge-discharge cycles numerous times leading to the system having long life cycles resulting in better levelized cost of electricity (a measure of economic value over the potential lifetime of the technology), despite the vanadium having a high cost. On top of this, the system also has a 70-90% energy efficiency due to fast kinetics and can be over-charged or undergo deep discharge with no lasting damage to the system. However, when the cell is overcharged, possible side reactions leading to hydrogen evolution can occur at the cathode:

$$2H^{+} + 2e^{-} \rightarrow H_2 \qquad \text{Eq. 1.17}$$

This gas evolution is kept to a minimum by lowering the potential this reaction occurs at through using carbon as an electrode. As the gas evolution can affect the flow of the electrolyte, create imbalance in the electrolyte, increase the cell resistance, and alter the pH of the solution (affecting the proton-exchange membrane).

The main drawbacks of the Generation I model (cost of vanadium, low power density and temperature limits) was tackled in the Generation II model. This system replaced the V^{4+}/V^{5+} of the half-cell with the polyhalide couple Br^{-}/ $ClBr_2^{-}$ [59].

$$V^{2+} + 0.5\,Br_2 \rightarrow V^{3+} + Br^{-} \qquad E^0 = 1.35\ V\ vs.SHE \qquad \text{Eq. 1.18}$$

Using a mixed acid electrolyte of HBr and HCl to ensure available bromide ions on the positive side, saw the battery's energy density almost double (roughly 50 Wh kg^{-1}) while achieving an energy efficiency of 80%[57]. In addition to this, the total volume required on the positive half-cell could be halved to match the negative half-cell, reducing the total volume of electrolyte in the system by a quarter whilst still maintaining an increased the energy density. In addition, the concentration of vanadium could be increased to 3 M due to the precipitation of V^{4+}/V^{5+} no longer being a factor in this system, furthering the energy density even more. However, work was still required in the need of more stable electrode materials, cheaper exchange membranes, and solving the toxic vapour issue from the bromine. The latter was tackled by employing two common complexing agents, *N*-methyl-*N*-ethylpyrrolidinium bromide (MEP) and *N*-methyl-*N*-ethylmorpholinium bromide (EMMB), which could complex with the generated bromine and form an immiscible phase reducing the vapour that was formed. However, the additional cost of the complexing agent, alongside the existing cost of the membrane material and the vanadium electrolyte, led it to be considered inferior to the all vanadium RFBs advantages.

This led to the Generation III VRFB breakthrough which used the same reactions as the Generation I model. By employing a mixed sulphuric and hydrochloric acid electrolyte, the energy capacity increased by more than 70% over the original Generation I model and surpassed the Generation II model. The increased energy capacity stems from the acidic mixture being able to stabilise the electrolyte. Studies have indicated that the VO^{2+} species concentration is determined by the solubility of $VOSO_4$ and the V^{3+} by the solubility of both $V_2(SO_4)_3$ and VOCl. The V^{2+} is stable in both the mixed acid electrolyte and sulphuric acid electrolyte. In addition, the mixed electrolyte also improves the effective temperature range in which the battery can operate, over −5°C to 50°C. This comes from the formation of $VO_2Cl\ (H_2O)_2$ at elevated temperatures which maintains its solubility as opposed to forming the insoluble V_2O_5. This removes the need for expensive temperature controls and cooling systems. This version gives an energy efficiency of 87%, matching that of the previous systems. These have been implemented into the market by various providers such as

RedT Energy (UK), Prudent Energy (China), UniEnergy Technologies (USA), and Sumitomo (Japan).

Alternative aqueous systems with different redox chemistries have been employed to varying degrees of success, aiming at reducing the cost of the RFB while improving the potential energy and power capacities. One such system is that of the polysulfide/halide series. The polysulfide bromine battery (PBB) offers a promising energy storage solution with low material costs[60,61].

Anode:

$$V^{2+} \rightarrow V^{3+} + e^- \quad E^0 = -0.26\, V\, vs. SHE \qquad \text{Eq. 1.19}$$

Cathode:

$$VO_2^+ + 2H^+ + e^- \rightarrow VO^{2+} + H_2O \quad E^0 = 1.00 V\, vs. SHE \qquad \text{Eq. 1.20}$$

Overall:

$$V^{2+} + VO_2^+ + 2H^+ \rightarrow V^{3+} + VO^{2+} + H_2O \quad E^0 = 1.26\ V\, vs. SHE \qquad \text{Eq. 1.21}$$

However, despite these low material costs, this system was found to still require significant developments in order to become economically viable[62]. Through modelling the 12 MW/ 120 MWh plant developed by Regenesys in Little Bradford Power Station, it was found that even with optimal conditions the power plant would operate at a financial loss[63]. It was recommended that for this to become a profitable venture, that the electrode kinetics would need to be improved upon or the capital cost of the battery itself would need to be reduced significantly.

Substantial work has gone into improving the electrode materials employed within the PBB. A cobalt coated carbon felt electrode was developed through electroless plating[64]. This electrode was shown to be more electrochemically reactive than the carbon felt on its own. This was used as the negative electrode and produced energy efficiencies greater than 80%. In addition, a nickel felt alongside a carbon felt were also investigated[65]. The nickel and carbon felts were used as the negative and positive electrodes respectively. This set up was found to have stable cycles and increased the energy efficiency to almost 80%. These electrode developments drastically increase the electrocatalytic activity of the PBB system.

Overall:

$$2NaBr + (n-1)Na_2S_n \rightarrow Br_2 + nNa_2S_{n-1}\ n = 2 \sim 4$$

$$E^0 = 1.54 \sim 1.61\ V\ vs. SHE \qquad \text{Eq. 1.22}$$

However, one aspect the modelling did not take into consideration was the self-discharge caused by the Br_3^- diffusing across the membrane. This is the major contributing reason for the PBB to have an operating at an energy efficiency of ~60%. In other energy storage technologies, such as $ZnBr_2$, the use of quaternary complexes are used to sequestrate the bromine to form an immiscible phase that eliminates this diffusion across the membrane which leads to self-discharge[66,67]. In addition, this also improves the bromine's availability to the electrode surface and can counteract its low solubility[68].

Aside from the PBB, other halides have been used for the polysulfide/halide RFB. Polysulfide iodide RFB (PSIB) also boasts cheap materials but offers a significantly greater energy density in comparison to the PBB[69]. Additionally, iodine itself has a very low solubility, meaning that the much more soluble triiodide species is relied upon in this system which means a third of all the available iodine cannot be utilised in this energy storage application. This I^-/I_3^- limits the upper voltage to prevent the irreversible reaction which precipitates to iodine which reduces the energy capacity[70]. However, work has been carried out on the zinc iodine system which uses bromide as the complexing ion opposed to iodide allowing the solution to achieve a much greater energy capacity: though the ability to independently scale up power and energy is still lost in these hybrid systems[71]. The disadvantage is that the material is highly corrosive and would present a limitation in the life cycle of the electrode[72]. Though this redox couple remains relatively unexplored for a redox flow battery with most of the chemistries on the iodide couple being aimed at the application for dye sensitised solar cells[72,73]. These strategies alongside other methods could be used to enhance the PBB, PSIB and other polysulfide based RFBs to strive towards an energy storage system which can efficiently store renewable energy whilst remaining commercially viable.

1.3.2 Non-Aqueous RFB

Non-aqueous RFBs were developed to yield a large energy density although they suffer from a drastically reduced power density in comparison to aqueous RFBs[74,75,76]. In addition, non-aqueous flow batteries are not constrained to the same potential limits as aqueous batteries where water electrolysis may occur: resulting in higher energy densities[26]. Some of these RFBs have been demonstrated to have operating voltages > 2 V. However, the poor solubility of their electroactive species reduces the current densities these can operate at. In addition, they also suffer from much poorer voltage and energy efficiencies compared to their aqueous counterparts with significant degradation over multiple cycles. Due to their wide variety of choices in redox couples, the types of non-aqueous batteries can be described as either metal-coordinated or organic.

Metal-coordinated RFBs

The first set of these chemistries, metal coordinated, comprises of a metal centre dictating the redox reaction while being supported by organic ligands. This enables chemical design to attempt to achieve high potentials and solubility. There are various metal-based couples that have been developed, using the supporting electrolyte acetylacetonate (acac) ligand species: such as the $V(acac)_3$,[77] $Mn(acac)_3$,[76] $Cr(acac)_3$,[78] and $Ru(acac)_{3.}$[79] The metal complexes formed with acac are soluble in the many organic solvents used as non-aqueous media, such as acetonitrile, and often achieves the highest solubility for the electroactive species. This is not the exclusive choice of ligand with bipyridine (bpy) and acetylacetone (acacen) also being other ligand options[80, 75].

The freedom of design is not restricted solely to the supporting ligand for the metal centre but also to the organic solvent that is used. For the $V(acac)_3$ system, an ionic liquids consisting of tetrabutylammonium hexafluorophosphate ($TEAPF_6$) and 1-ethyl-3-methyl imidazolium hexafluorophosphate ($EMIPF_6$) have been used, in acetonitrile (organic solvent used)[80]. The interest for this was that $V(acac)_3$ had an operating potential of 2.2 V compared to the VRFB at 1.26 V. However, the non-aqueous version still suffered from extremely low energy efficiency due to the low conductivity of the electrolyte and side reactions that occur which lead to degradation on cycling. These ionic liquids increase the conductivity and provide a stable electrolyte to support the electroactive species. Despite these improvements, the coulombic efficiencies were still low with $TEAPF_6$ and $EMIPF_6$ having an efficiency of 56% and 46%, respectively. However, the development of metal-based ionic liquids offers a material that are ionically conducting, allowing it to serve as both an electrolyte supporting material as well as a potentially electroactive species. One of these materials was tested in an all-copper, non-aqueous RFB[81]. The copper species $[Cu\ (MeCN)_4][Tf_2N]$ in acetonitrile, structure shown in Figure 1.14, was shown to provide good ionic conductivity and solubility (1.68 M in acetonitrile). Clear evidence of the improvement obtained was that the coulombic efficiency achieved was 87%. However, the voltage losses were still high, resulting in an energy efficiency of 44% and operation could only be sustained at very low current densities (5 mA cm^{-2}).

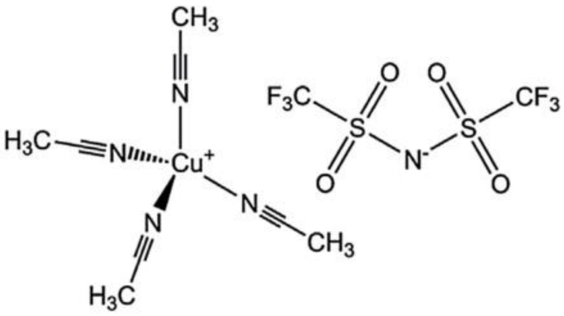

Figure 1.14 Structure of $[Cu\ (MeCN)_4][Tf_2N]$ (taken from Yun Le *et. al.*)[81]

Organic RFBs

Organic RFBs allow for structural diversity in the electroactive material, giving the ability to design these materials to potentially control the solubility and impact on the environment these substances may have[26]. As these are synthesised, this allows the productions of successful redox couples to be in an abundance. One such system is the 4-Oxo 2,2,6,6-tetramethyl-1-piperidinyloxy (TEMPO) and (1S)-(+)-Camphorquinone in a supporting electrolyte of $TEABF_4$/propylene carbonate. These achieved an open circuit potential of 2.12 V at a 50% state of charge[74]. However, these were quasi-reversible (as some of the materials had been irreversibly structurally changed) despite achieving an energy density of 71%. As in the metal coordinated systems, this is due to the low ionic conductivity of the organic solvents used as an electrolyte.

However, organic RFBs are not limited to non-aqueous environments. Aqueous organic RFBs boast a much lower cost than traditional RFBs but are severely limited by the stability and solubility of these materials[47,82]. Quinones have formed the basis of a considerable number of redox materials used in this system. One such system was the 4,5-dibenzoquione-1,3-benzenedisulfonate (tiron) with KCl solution[83]. With this RFB, they managed to achieve an energy efficiency of 82%. However, it was found that the chemistries were pH dependent, with a pH <4 required for the tiron to act as the positive active species but resulted in a quasi-reversible system with some of the capacity becoming irreversible due to a change in the chemical structure.

1.3.3 Hybrid RFB

Finally, hybrid RFBs have been shown to yield high energy and power densities with lower costs but lose the ability to scale up power and energy independent of each other as when charged, material deposits onto the electrode as opposed to remaining in the electrolyte[84,85].

Zinc is an attractive material for use in the flow battery due to its natural abundance and low cost[86]. Additionally, zinc also has a large negative potential which allows for the system to have a high power density when coupled with another electropositive redox couple[87]. During the charge-discharge cycle of the redox flow battery the zinc has an electrodeposition of[44]:

$$\mathrm{Zn^{2+}} + 2\mathrm{e^-} \leftrightarrow \mathrm{Zn} \qquad \mathrm{E^0} = -0.76\ \mathrm{V}\ vs.\mathrm{SHE} \qquad \text{Eq. 1.23}$$

There are a variety of redox species that can couple with zinc, the three that are discussed here are $ZnCl_2$, ZnCe, and $ZnBr_2$.

Zinc Chloride RFB

The zinc chloride battery was developed for the Energy Development Association in America for potential use in energy storage applications during the 1970's[44]. This system is based on the electrochemical reactions of zinc and chlorine from $ZnCl_2$ aqueous solutions, with the chlorine and water reacting chemically at the same time[88]:

$$2\mathrm{Cl^-} \leftrightarrow 2\mathrm{e^-} + \mathrm{Cl_2} \qquad \mathrm{E^0} = +1.36\ \mathrm{V}\ vs.\mathrm{SHE} \qquad \text{Eq. 1.24}$$

This system is highly reversible with a theoretical cell voltage of 2.12 V. Since the $ZnCl_2$ cell does not use complexing agents the theoretical value is equal to the open circuit voltage. This provides a theoretical energy density of 465 Wh kg^{-1} although in practice, 60 to 80 Wh kg^{-1} is normally obtained, dependent on system design[89]. The zinc deposits on the negative electrode and at the positive electrode, the evolution of Cl_2 gas occurs and this is removed to another vessel where it is mixed with water to form chlorine hydrate. During the discharge, the required chlorine is regenerated by heating the chlorine hydrate in the $ZnCl_2$ electrolyte. This is then flowed through to the cathode where it is consumed electrochemically.

There is another storage method for the chlorine gas formed which involves compression until liquefaction occurs and is maintained at roughly 6 atm. However this is less desirable than the previous method due to the cost of this process[89].

The zinc chloride RFB has undergone numerous improvements since 1995. However, despite such developments, the technology was deemed to be too problematic for practical use since it still exhibited a lot of performance as well as economic issues. Additionally, the evolution of chlorine gas posed a severe environmental and health hazard. This caused a cessation of interest in the zinc chlorine battery from being further developed[90,89]. However, in 2012, an American company, Primus Power, developed a 25 MW/ 75 MWh system for an energy farm in California despite this[91,92].

Zinc Cerium RFB

Zinc cerium RFB was introduced by Plurion in the 2000s. This system offered a significantly high current density for discharge: claiming 400-500 mA cm^{-2} [44]. The system used methanesulfonic acid (MSA) as the supporting electrolyte since it was less corrosive than alternative acids and could support cerium at higher concentrations (>1 mol dm^{-3})[93]. In addition to this, it also inhibited the growth of zinc dendrite – discussed later in this section[94]. This RFB also offered a significantly large circuit potential with the cerium half-cell reaction in MSA being:

$$Ce^{3+} \rightarrow 2Ce^{4+} + e^{-} \qquad E^0 = +1.64\,V\ \ vs.\text{SHE} \qquad \text{Eq. 1.25}$$

This gave a cell voltage of 2.4 V. However, the strong oxidising environment for the positive electrode meant that carbon could not be used as the electrode would undergo irreversible oxidation. Therefore, to achieve the best efficiencies, the positive electrode used was a platinised titanium mesh and operated at 60°C which achieved an energy efficiency of 60%[94].

More recently, a membraneless zinc cerium RFB was developed which used a lower acid concentration: enabling a carbon felt to be used[87]. In addition, it also had a 75% energy efficiency. However, the lower acid concentration also resulted in a reduction of the system's energy density, as the optimum cerium concentration dropped to 0.2 mol dm^{-3}. The long-term stability of the felts in this environment is still to be investigated.

Zinc Bromide RFB

The Br_2/Br^- redox couple has been used as the positive electrode reaction in zinc-bromide, polysulphide bromide, and vanadium-bromide batteries as it offers a large positive potential resulting in a high cell voltage for the battery system. At the positive electrode, the standard electrode potential of the Br_2/Br^- redox couple is 1.09 V *vs.* SHE:

$$Br_2 + 2e^- \rightarrow 2Br^- \qquad E^0 = +1.09\,V \;\; vs.\,\mathrm{SHE} \qquad \text{Eq. 1.26}$$

When coupled with zinc gives an overall reaction of:

$$\mathrm{Zn} + Br_2 \leftrightarrow \mathrm{Zn}^{2+} + 2Br^- \;\; E^0 = +1.85\,V \;\; vs.\,\mathrm{SHE} \qquad \text{Eq. 1.27}$$

The chemistry of bromine is very similar to that of the chlorine system with one distinct difference: where chloride converts into chlorine gas, bromide converts into bromine liquid. However, bromine liquid is still very volatile (vapour pressure of 202 mmHg at 298 K) and will result in Br_2 vapour being formed to some extent, meaning that some of the overall battery efficiency will be lost due to this gas escaping into any available head space in the reservoirs[95]. Additionally, bromine is extremely toxic by inhalation (LC50 750 ppm 1 h (mouse))[96]. Despite these issues, the zinc bromine RFB is the second most commercially developed flow battery after the VRFB. However, this system still has numerous issues, such as the growth of dendritic zinc and crossover of bromine, which can be improved to allow this system to become more economically viable.

The first major issue with the zinc-bromine battery is that there is a high rate of self-discharge. This is due to the solubility of the bromine within the electrolyte and being transported through the porous separator where it would react rapidly with the plated zinc on the negative electrode. This would result in what is referred to as self-discharge which drastically reduces the coulombic efficiency of the battery. In addition, as mentioned earlier, the vapour formed in any headspace within the external reservoir also results in a coulombic efficiency loss.

To counteract these limitations, a series of additives are employed to complex with the electrogenerated bromine and hold it within the positive electrolyte. These additives are typically quaternary ammonium compounds that capture the Br_2 and complex this to higher polybromide forms (*e.g.* Br_3^-, Br_5^-or Br_7^-)[97]. Normally, the Q^+ Br_x^- yields an immiscible liquid phase which requires these battery systems to have additional pumping procedures to the positive electrode during discharge. There has been a great deal of interest to synthesis compounds that would reduce the self-discharge of the zinc bromine battery. Many studies have been carried out, dating back to the 1940's when R. Bloch *et. al.* studied the composition that tetramethylammonium bromide would have when mixed with bromine and the physical properties of the new phase that was formed[98]. However, this was before these complexing agents were considered for applications within energy storage. One of the first papers to relate it to batteries was from F. Rallo *et. al.*, where he proposed this method as a way to reduce the solubility of the bromine in the aqueous phase by using low molecular weight tetraalkylammonium halides and perchlorates to form the barely soluble polyhalides[99].

The formation of these liquid-phase polybromides were investigated by D.J. Eustace, where he uses unsymmetrical substituted cyclic quaternary ammonium bromides (QBr)[100]. Three were specifically looked at: *N*-ethyl-*N*-methylmorpholinium bromide (EMMB), *N*-chloromethyl-*N*-methylpyrrolidinium bromide (CMPB) and *N*-methoxymethyl-*N*-methylpiperidinium bromide (MOPB) with structures as shown in Figure 1.15 below.

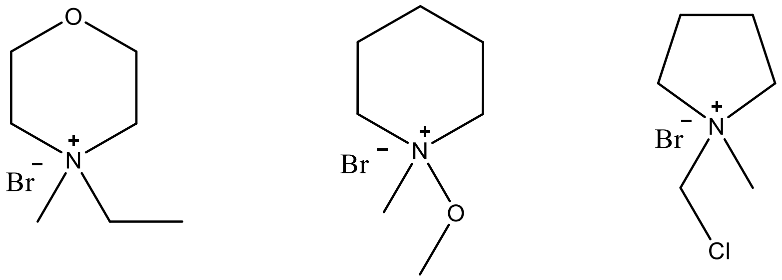

EMMB MOPB CMPB

Figure 1.15 Selection of quaternary complexing agents used by D. J. Eustace

All these compounds were found to create a bromine-fused salt, which was modelled as a micelle-like process, where the dominant phase separation process is controlled by the polyhalide ion activity. From the complexing agents used MOPB was found to be unstable whereas EMMB has been successful in several zinc-bromine systems.

K. J. Cathro *et. al.* noted that, from the studies above, there was a need to increase the number of additives which could complex the electrogenerated bromine at temperatures lower than 25°C[101]. At the time of this paper it was simply reported that at low temperatures and low bromine concentrations, the QBr would lead to the formation of a solid phase which would cause restriction in the electrolyte flow resulting in the battery failing. To assess this situation, many aliphatic and cyclic materials were examined and compared to the EMMB in use at that time. From their work they found that no single compound was shown to be perfectly acceptable in that they all produced a solid phase under certain conditions. However, one of the cyclic compounds (*N*-methyl-*N*-ethylpyrrolidinium bromide (MEP)) and two of the aliphatic compounds (dimethylethylpropylammonium bromide (2-MEP) and diethylmethylpropylammonium bromide (2-EMP)) were shown to be usable as long as the electrolyte did not fall under 10°C. Additionally, they confirmed that the mixing of QBr compounds would lower the freezing point to 0°C by reducing the number of bromides complexed in the polybromide phases produced. More in-depth research for the mixture of MEP/ EMMB termed as a modified electrolyte (MOD) was carried out[102]. However, solidification of the bromine phase still occurred at temperatures <10°C. The problem was resolved by adding 2-EMP and tetrabutylammonium bromide (TBABr) which gave the MOD the properties required to enable it to be used between 5-50°C. This electrolyte composition was found to result in higher concentrations of bromine in the complexed polybromide phase than in the aqueous one, lower ohmic resistances and smaller values for the bromine diffusion coefficients in relation to their original mixture.

In contrast to the previous studies which mostly looked at asymmetric complexing agents, K. Cedzynska examined symmetrical complexing agents: tetraethylammonium bromide (TEABr) and tetrabutylammonium bromide[103]. They observed that the electrochemical process here was diffusion controlled and that the diffusion coefficient was influenced by the kinematic viscosity which altered with the composition and concentrations of the electrolytes.

The use of EMMB, MEP and TBABr complexing agents with the bromine led to the formation of a new oily, immiscible phase with respect to the content of bromine. They found the EMMB and MEP satisfactorily removed the bromine vapours and furthermore had no effect on the kinetics of the bromine reaction. However, their presence was detrimental to the membrane used as an organic layer was formed reduced the voltage efficiency. However, *N*-methyl-*N*-ethylpyrrolidinium bromide (MEP) have continued to be the complexing agent of choice in commercial zinc bromine batteries[66,104,105].

There exists, nevertheless, a considerable interest in developing novel additive compounds that could lead to improvements in the cycling efficiencies, kinetics, cost of materials or physical nature of complexed polybromide phase achieved[106,68,107]. Very few papers focus on the immiscible phase itself other than giving an analysis of its impact on the electrokinetics[108,109]. However, the mass transport issues created by having the secondary phase have been recognised by Yang *et al*[110]. In that study, surfactants were employed to break up the immiscible phase to improve its dispersion within the aqueous electrolyte. Using a small quantity of a polysorbate (polysorbate 20), they managed to increase the dispersion of the polybromide complex phase within the aqueous phase, leading to an increase in the coulombic efficiency.

The second major issue, which affects all zinc systems, is the formation of dendrites. These dendrites are finger like projections which protrude from the negative electrode surface when the battery is being charged and zinc is being deposited, as shown in Figure 1.16.

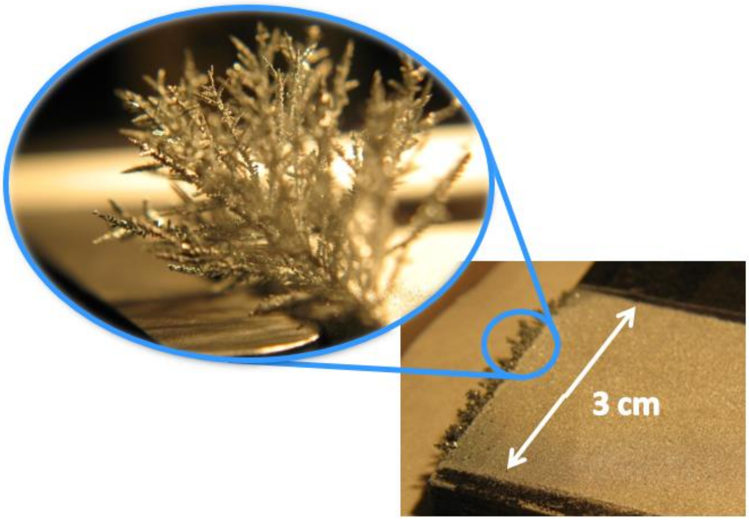

Figure 1.16 Zinc dendrite growth

These dendrites can potentially reduce the coulombic efficiency (if they break off) or drastically reduce the RFBs lifespan (should they pierce the membrane and cause a short circuit). A high rate of zinc electrodeposition and dissolution is usually desirable for cost and performance related parameters, such as high power and lower pumping costs. Therefore, the morphology of such depositions are key to improve the current zinc systems and make them more efficient and cost effective[111]. For instance, the zinc-cerium RFB controlled the zinc depositions indirectly using methanesulfonic acid, which was originally used to increase the solubility of the cerium but was also found to inhibit zinc dendritic growth. However, zinc bromide and zinc chloride are operated in aqueous solutions with no acids and as such do not have this advantage.

Additives, such as polyethylene glycol (PEG, MW = 200) [111], are commonly used to inhibit the growth of these dendrites, PEG has a good stability and is resistant to chemical degradation during the charge/discharge cycles of the zinc battery. These authors reported that the suppression of zinc dendrite growth could be achieved with 1,000 and 10,000 ppm of PEG-200[103]. At these concentrations, the depositions were more compact and at 10,000 ppm, the dendrites were eliminated. However, accompanying kinetic studies revealed that the PEG-200 lowered the current density substantially by forming a passivating film on the electrode surface, leading to a complete inhibition of the battery charging process. To use this material therefore, a delicate balance was required to minimise the internal resistance from the passivating film but also reducing the dendritic growth of the zinc. In more recent work, S. J. Banik used another polymer, polyethylimine (PEI), to inhibit the zinc dendritic growth in an alkaline zinc battery[112]. However, this polymer exhibited the same characteristics as PEG in that the more concentrated the additive, the more it inhibited the surface of the electrode to further electroplating. Therefore, the same balance as with PEG would be needed for this material and the amount required was stated to be no more than 50 ppm.

Ethanol has been employed in a zinc iodine RFB to successfully inhibit the growth of these dendrites[83]. The result led to a finer grain of deposits to be produced. This effect is believed to be the outcome of the ethanol coordination with the zinc ions allowing for the plating overpotential to be enhanced resulting in a lower plating exchange current density. Although this work focused primarily on the zinc iodine RFB, the outcome is of relevance interest to the other aqueous zinc-based hybrid RFBs.

2. Aim

This project focuses on the development of the zinc bromine hybrid redox flow battery. The aim was to understand the underlying chemistries of this energy storage system and to improve them to make them either last longer, operate more efficiently or make them more economically viable. To assess the potential impact of aspects within this work, it was also necessary to understand the benefit this system would have on the wider community, its current challenges toward implementation, and the general trend of opinion within the scientific community.

In addition, as one of the project funders, Lotte Chemical, had issued a research and development zinc bromine RFB at a 25 kW/ 50 kWh scale. This system was to be tested to understand its current ability in terms of efficiency.

Objectives

From the introduction and opportunities available to this project, the objectives stated were:

- to analyse and develop additives used within the $ZnBr_2$ RFB with the aim of improving the electrolyte chemistry
- to develop electrode materials to improve the electrokinetics in the system and scale these up to a lab scale flow cell
- to characterise the coulombic, voltage and energy efficiencies of the 25 kW/ 50 kWh $ZnBr_2$ RFB and identify areas of potential improvement for the development of the follow-up prototype
- (due to successful funding from the PECRE – PEER Exchange Grant) to characterise the areas of efficiency loss in a 200 kW/ 400 kWh vanadium RFB and determine the functionality of this energy system for multiple applications in Martigny, Switzerland

3. Experimental

3.1 Electrode Set-up

Three types of carbon electrode material were used throughout this study. These were

1. carbon composites: graphite flakes bound with phenolic resin (BPP4), fluor polymer (BMA 5), or polypropylene (PPG86) supplied by SGL Carbon, Germany, or polyvinyl ester (PVE) supplied by Entegris Inc, USA;

2. carbon felts: Sigracell GFD-3 (3 mm, PAN-based carbon fibres), Sigracell GFD-4.6 (4.6 mm, PAN-based carbon fibres) and Sigracell GFA-3 (3 mm, Rayon-based carbon fibres) were purchased from SGL Carbon and Mersen Battery Grade (4.6 mm, PAN-based carbon fibres) provided by Mersen Ltd, Scotland.

3. an activated layer comprised of activated carbon (Tog-LF), conductive carbon (Super_P) and binders (GM5070E) as supplied by Lotte Chemical.

3.1.1 Carbon Composites

The carbon polymer composites were used as received and cut into discs with a 7 mm diameter. This gave a geometric electrode surface area of 0.38 cm^2. The discs were then loaded onto a recessed copper rod in a Teflon holder and fixed with silver conducting paint (from RS Components, Scotland). The Teflon resin cap was then pushed level with the carbon electrode and the remaining area between the cap and electrode was sealed off using an epoxy resin, araldite (from RS Components). This is shown in Figure 3.1. The gap between the Teflon holder and cap was then sealed using Teflon tape to prevent any solution getting into contact with the central copper rod. These electrodes were then polished using emery paper grade 1200 (Screwfix, Scotland) and rinsed with isopropanol and dried in an N_2 stream.

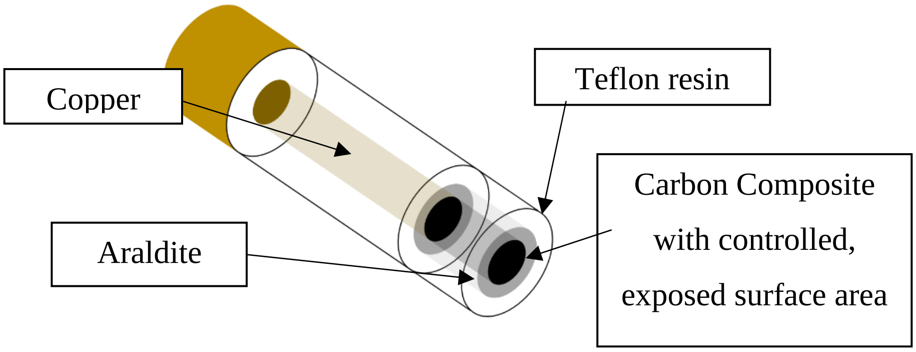

Figure 3.1 Round disc electrode holder and set-up

3.1.2 Felt

The carbon felts were subjected to mild thermal oxidation in an oven at 500°C for 24 hours in air to activate and increase their hydrophilicity through by increasing the number of oxygen-based functional groups on the surface leading to an increase of the hydrogen bonding effects, this effect can be seen in Figure 3.2. These were prepared for use in both the H-cell and the flow cell being cut to 2 x 10 cm and 10 x 10 cm, respectively. The weights before and after were recorded and a slight decrease was observed after thermal treatment. The conductivity of these were measured before application to ensure no faulty samples were analysed. This was done using a multimeter and testing the resistivity across the electrode surface with two probes and ensuring this was less than 2 Ω.

Figure 3.2 before (left) and after (right) thermal oxidation showing an increase in hydrophilicity

3.1.3 Activated Carbon

The “activated layer” refers to the coating material that Lotte Chemical use on the positive electrode of their $ZnBr_2$ RFB system. As such, many specifics on the materials used or the reasoning behind the composition used remained confidential to Lotte Chemical. However, the materials and a simple experimental was provided to determine the effectiveness of their novel electrode material compared to other electrode materials. The activated layer was used on the carbon composites, this was made by mixing 3.5 g of Tog-LF with 0.26 g of Super_P. This mixture was then added to a slurry of 0.28 g of the GM5070E binder in 2.5 g of toluene. Once evenly mixed, more toluene (5.8 g) was added and the mixture was left to stir at room temperature for 3 – 4 hours. This was then evenly cast onto the electrode surface and dried in an oven at 60°C. Since the activated layer was to be roughly 5-6 mg/cm^2 (as was recommended by Lotte Chemical), 9 mg of the mixture was evenly spread onto the positive electrode's surface to allow for the mass of toluene that would evaporate from the mixture in the oven.

3.2 Electrochemical Set-up

Three electrochemical set-ups were used for multiple investigations:

1. 3 – electrode cell was used for most of the electrochemical characterisations of the various electrolyte solutions and electrodes tested throughout this study.

2. H-cell allowed for initial testing through galvanic cycling and acted as an intermediary step between the scale up from the 3 – electrode cell set-up to the flow cell set-up.

3. The flow cell allowed for flow battery conditions to be simulated for further characterisation of the studied chemistries.

3.2.1 3 – Electrode Cell

The first set up for the carbon polymer composites used a small 3 – electrode glass cell. In this cell, the Pt mesh counter electrode (CE) was separated from the working electrode (WE) compartment by a porous membrane (Grade 1, glassfrit). Contact with the saturated (KCl) calomel reference electrode (SCE) was *via* a Luggin capillary, which was positioned as close as possible to the working electrode's surface (displayed in Figure 3.3).

In some instances, it was necessary to use a Ag/ AgCl reference electrode. This was made by heating sodium hypochlorite solution with an immersed silver wire: creating a AgCl surface. This was then placed into a small glass tube sealed off with a molecular sieve with 1% w/w agar enriched with AgCl injected into the tube. With the tube containing the wire and agar solution filled, the open end, where the excess wire protrudes, was sealed using araldite. The quality of the reference electrode was frequently monitored against a SCE to ensure the OCP difference remains at 47 mV, a recognised difference for these electrochemical reference electrodes.

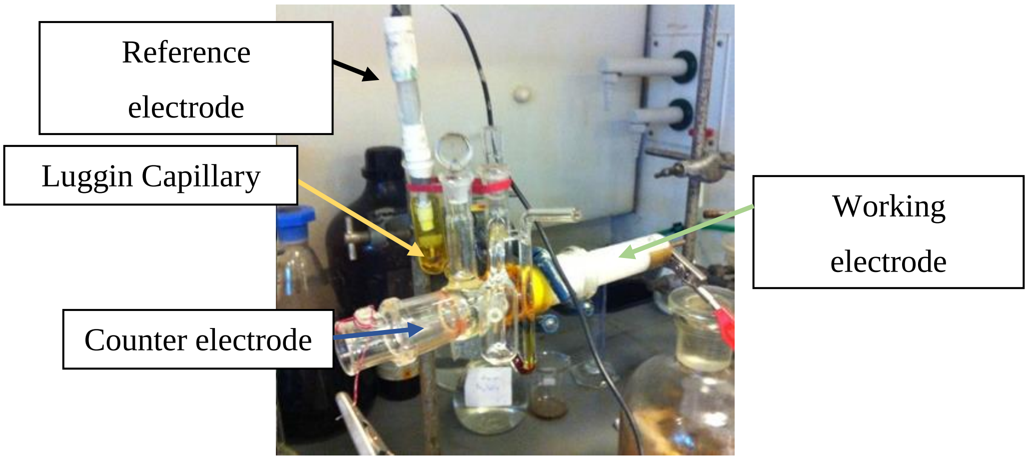

Figure 3.3 The 3-electrode cell containing the carbon coated WE, Pt mesh CE and a SCE in 50 mM $ZnBr_2$, 17 mM MEP and 0.5 M KCl

3.2.2 H-Cell

The second set up for testing the felts used an H-cell with strong magnetically-controlled stirring of the solution to mimic the agitation of the solution in the flow cell. The two compartments were separated by either a Nafion-117 membrane or a polyethylene/ silica porous separator: depending the study being conducted. Equal measures (150 mL) of the electrolyte solution, comprising of 2.25 M $ZnBr_2$, 0.5 M $ZnCl_2$, 5 mL of Br_2 per litre of electrolyte, and 0.8 M MEP, was placed on either side of the H-cell, with the felt being submerged to a measured depth of (7 cm) on one side and a carbon polymer composite electrode on the other side. The surface area of the negative electrode was controlled to 1 cm^2 by wrapping the carbon plate with Teflon tape until the desired surface area was exposed (as shown in Figure 3.4).

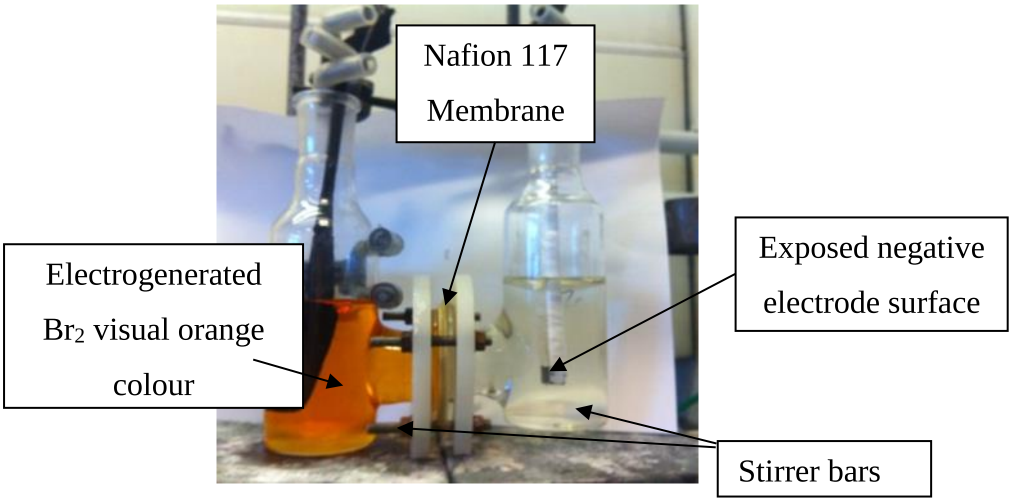

Figure 3.4 H-cell separated by the Nafion 117 membrane with the positive felt electrode and negative carbon composite polymer. 150 mL of 2.25 M $ZnBr_2$, 0.5 M $ZnCl_2$ and 0.8 M MEP in each compartment

3.2.3 Flow Cell

The electrode for the flow cell was attached to a stainless steel or brass metal backing plate. This backing plate was cleaned in hydrochloric acid to remove the oxide layer before the carbon composite (cut to be 10 × 10 cm) was connected to the backing plate using silver conducting paint. Once set, the resistance was tested to ensure it was less than 5 Ω and was placed into the high-density polyethylene mould. This was bolted into place with the edges of the carbon composite electrode being sealed with araldite. Depending the test, a carbon felt may be added to the carbon composite using carbon cement and allowing to cure for 12 h at 60°C. Before constructing the flow cell, the resistance was tested one last time, using a multimeter with two probes, to ensure it was still less than 2 Ω. The plate containing the sealed electrode was placed onto a metal backing frame, the desired flow inlet was noted, and the flow field plate was placed facing toward the electrode with the appropriate flow directions. A black rubber seal was placed on top with the chosen separator being placed over the electrode window. This was then sandwiched together with another rubber seal and a mirror opposite flow field plate facing the second mould containing the second electrode. The bolts thread at the back of the electrode plate acts as the conductive pathway for the potentiostat to be connected. The overall set-up can be seen in

Figure 3.5. The final metal plate was then placed on top of the second mould with the entire flow cell being bolted together with a specified order of the bolts being tightened (order indicated on the metal plate).

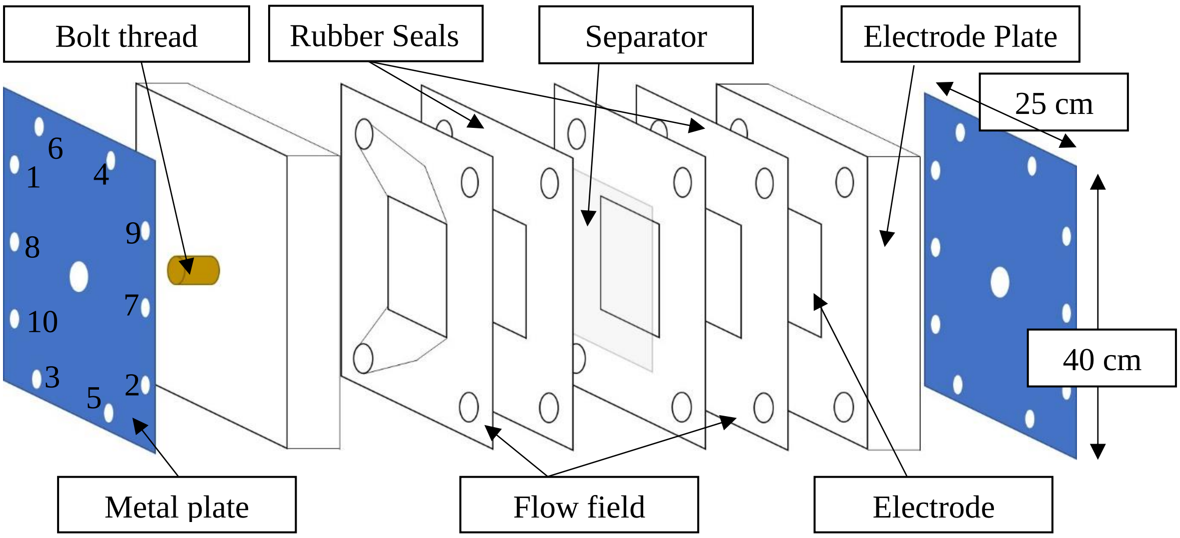

Figure 3.5 Components and order of assembly for the flow cell

Depending the experiment, different types of tubing was secured to the inlets and outlets. Masterflex Tygon was used for the experiments where bromine was not present. Whereas Masterflex Viton was used in the presence of bromine due to its chemical resistivity. The tubing was then set into the peristaltic pump and tested for leaks using a flow of deionised water for an extended period. Figure 3.6 shows the flow cell assembled.

Figure 3.6 Flow cell assembled

3.3 Additive Synthesis

The first set of novel complex additives were synthesised based on two rationales:

1 – they were to have the same cyclic structure as other successful complex additives already identified (pyridine, morpholine and pyrrolidine)[113,66,106];

2 –the longer aliphatic leg of the quaternary ammonium compound was to incorporate a carboxylic acid functional group: known for improving a compound's solubility[114,115].

These conditions led to the synthesis of compounds **QBr1**, **QBr2** and **QBr3**. Compound **QBr1** was synthesised by refluxing 1 molar equiv of pyridine with 1 molar equiv of 2 – bromoacetic acid in 40 mL of ethyl acetate for 4 h. The remaining solvent was removed in a desiccator leaving the precipitated product. Compounds **QBr2** and **QBr3** were synthesised by reacting 1 molar equiv of 4 – methylmorpholine and 1 – methylpyrrolidine, respectively, with 1 molar equiv of 3 – chloropropanoic acid for 4 h. The precipitated compounds were purified by washing the salts with diethyl ether on vacuum filtration and dried in a vacuum oven at low temperature.

The second series of novel complex additives were synthesised based on connecting two cyclic ammonium centres together with an aliphatic leg to create a space between two ammonium ions to trap and enable larger polybromide species.

Compounds **MO1**, **MO2** and **MO3** were produced for this, by refluxing 1 molar equiv of 1,2 – dibromoethane, 1,3 – dibromopropane and 1,4 – dibromobutane, respectively, with 2 molar equiv of 4 –methylmorpholine in 50 mL of 2 – propanol for 24 h. The solvent from these compounds was removed through rotary evaporation. The precipitated salts were then collected and purified by washing with diethyl ether on vacuum filtration and dried in a vacuum oven at low temperature.

The third set of novel complex additives were synthesised on a similar rational as this first set of additives where the longer aliphatic leg of the quaternary ammonium compound was to incorporate a hydrophilic functional group: in this instance a sulphonate group commonly used in medicinal molecular structures for solubility in the human body. This was achieved from refluxing 1 molar equiv. of pyridine, 4 – methylmorpholine and 1 – methylpyrrolidine, separately, with 1 molar equiv of sodium 2-bromoethanesulfonate in deionised water for 12 h to form **PSO**, **MOSO**, and **MPSO**, respectively. Again, the solvent was removed through rotary evaporation, purified by washing with diethyl ether on vacuum filtration and dried in a vacuum oven at low temperature.

All the synthesised quaternary ammonium additives were characterised using ^{1}H and ^{13}C NMR. The ^{1}H and ^{13}C NMR (600 MHz) were recorded in deuterated DMSO. All structures are shown in Figure 3.7.

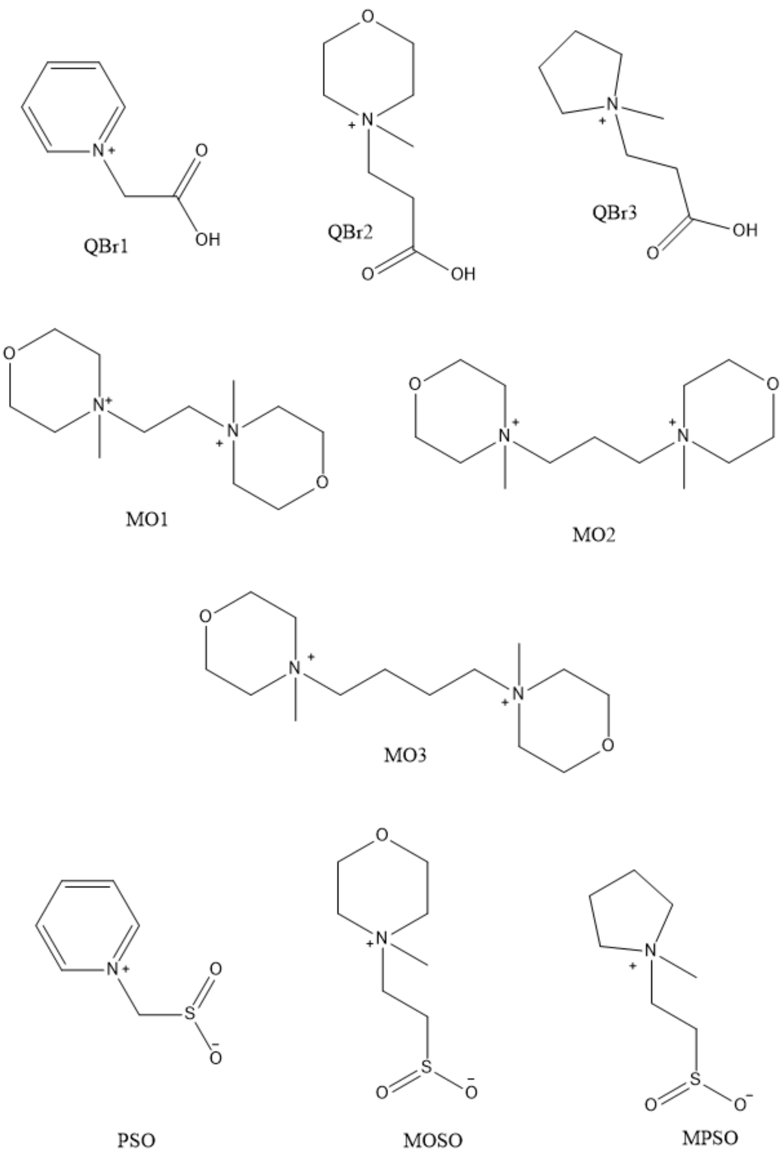

Figure 3.7 Structures of all synthesised compounds

3.4 Electrolyte Production

The $ZnBr_2$ electrolyte composition was provided as excess electrolyte from the 25 kW/ 50 kWh RFB set-up in PNDC, Cumbernauld. However, as part of work with Mersen and to test the felt characteristics for multiple cycle duration it became necessary to produce a vanadium electrolyte. To produce 1 litre of 1.5 M vanadium (V^{4+}) in 2 M sulphuric acid, using a method learnt in the École Polytechnique Fédérale de Lausanne, 210 mL of stock sulphuric acid was diluted with 290 mL of deionised in a three-necked round bottom flask to make 500 mL of 4 M sulphuric acid. The solution was then heated to ~80-90 °C and 136.4 g of V_2O_5 was slowly added to the flask whilst stirring vigorously. Care was taken to prevent the resulting suspension from becoming too viscous by allowing adequate time for the V_2O_5 to disperse. A reflux condenser was attached with a gentle flow of N_2 above the solution in the flask and 64.1 g of oxalic acid was slowly added to carry out the reduction of the V^{5+} to V^{4+} to 95% completion. The slow rate of addition was to take into consideration the induction time of the material in the solution, as once the reaction takes place it produces CO_2 which can cause the solution to form a froth and expand out with the flask. The final 5% of the reduction was completed by adding 2.35 mL dilute hydrazine (hydrazine monohydrate diluted by a half with deionised water) into the solution slowly, where the solution again effervesces. This effect can be reduced by diluting the hydrazine but also prevents the formation of insoluble hydrazine sulphate. On completion, the electrolyte became a blue colour of pure V^{4+}. It was then allowed to cool under the flow of N_2 for a further 1-2 hours. Once cooled, the total volume was made up to 1 litre with deionised water giving the desired concentrations of 1.5 M vanadium and 2 M sulphuric acid.

A sample of the prepared vanadium solution was diluted by a factor of 20 with 2.0 M H_2SO_4 and its UV-Vis spectrum was measured using a Shimadzu UV-1800 UV Spectrophotometer. Once the concentration was confirmed from the spectrum obtained, the electrolyte was placed into one of the flow cell's reservoir with the other reservoir containing a 2 M sulphuric solution. Electrochemical reduction of the solution was then carried out to produce $V^{3.5+}$ which is a solution comprising of a one-to-one ratio of V^{3+} to V^{4+}. The conversion was tracked using the UV-visible spectrophotometer as well as the charge passed during the electrolysis. This produced a solution that could be used in both half-cell reactions. The solution was then charged to an 80% state of charge (SOC), this representing a percentage value of the batteries total charge, using 1.5 electrons in the following equation:

$$n \times F \times c \times V \times SOC = C \qquad \text{Eq. 3.1}$$

Where n is the number of electrons, F is the Faraday constant, c is the concentration, V is the volume (in litres) and C is the number of coulombs. From this, at a constant current, a time duration can be calculated for the charge cycle. Once discharged to a voltage limit of 0.5 V, the battery had the appropriate vanadium oxidation states on each side of the RFB for further cycles. The half-cell reactions for these species show 1 electron, though the initial charge calculates using 1.5 electrons to compensate for the multiple oxidation states it must pass through (*i.e.* V^{4+} to V^{2+} in the analyte and V^{3+} to V^{5+} in the catholyte).

3.5 Electrochemical techniques

Electrochemical characterisation was carried out using either a Solartron S1 1286 or 1287 Electrochemical Interface. Initially, cyclic voltammograms were ran at various scan rates. Cyclic voltammogram was used to examine the Br^- oxidation and subsequent Br_2 reduction and determine the parameters for use in the subsequent electrochemical impedance spectrometry (EIS) and potentiodynamic measurements (shown in Figure 3.8).

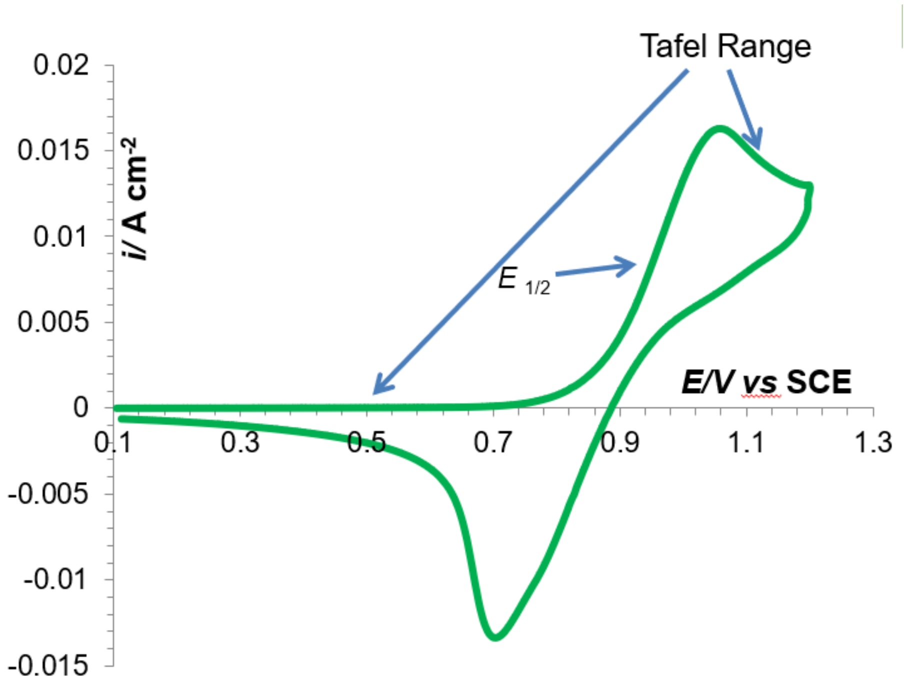

Figure 3.8 CV of the Br⁻ oxidation and subsequent Br_2 reduction for a 50 mM $ZnBr_2$ 16.67 mM MEP solution with the key parameters identified for subsequent measurements

Using the Solartron 1250 or 1255B Frequency Response Analyser with 1286 or 1287 electrochemical interface, the EIS was recorded for each electrode at set potentials over the frequency range of 65,535 Hz to 0.1 Hz. The potentiodynamic measurements (Tafel extrapolation) were carried out between a potential range as determined from the cyclic voltammogram for each electrode and solution at a scan rate of 0.1667 mV s^{-1}.

Using the H-cell, the performance of each of the felts was analysed through galvanic cycling. These cycles provided information on the CE (Eq.1) and VE (Eq. 2) given that the constant current supplied for both charge and discharge was equal:

$$CE\ (\%) = \frac{Time\ of\ discharge\ (s)}{Time\ of\ charge\ (s)} \times 100\% \qquad \text{Eq. 3.2}$$

$$VE\ (\%) = \frac{Potential\ reached\ for\ discharge\ (V)}{Potential\ reached\ for\ charge\ (V)} \times 100\% \qquad \text{Eq. 3.3}$$

The galvanic cycles were measured using charge and discharge rates of 5, 10, 20, 30 and 40 mA cm^{-2} for periods of 1800 s. Voltage limits were imposed to prevent damage to the cell components during charge (1.9) and discharge (0.25 V). Subsequently, the surface area of the carbon polymer composite negative electrode was increased from 1 cm^2 to 10 cm^2 and was charged at 100 mA for 54 hours to charge the solution (hence battery) to a theoretical value of 30% SOC. This would also result in the MEP forming a "new" phase with the generated bromine in the positive electrolyte solution. Galvanic cycles were again carried out on each of the felts and at the different current densities noted above. The sequence was repeated for a 60% SOC zinc bromide electrolyte solution.

The flow cell tested a variety of electrode materials through two electrochemical methods: volumetric mass transport co-efficient and performance efficiencies. The volumetric mass transport co-efficient ($k_L A_{me}$) used a large volume of potassium ferricyanide solution supported by potassium chloride as a supporting electrolyte. The stack was constructed with a Ag/AgCl reference electrode being used in the positive electrode compartment. This reference electrode was made using the same method discussed earlier with the exception that enamelled silver wire was used to allow an effective seal to be made in the flow cell when constructed. In addition, the Nafion 117 membrane was used for this set-up. The potassium ferricyanide solution would then be circulated through the stack, monitoring the OCP with a redox electrode in the positive reservoir to determine the concentration of the electrolyte at given points. A linear single voltammogram was ran at 3 mV s^{-1} to allow for the mass transport plateau to be identified. A given potential was used and both linear single voltammogram and chronoamperometry was used to determine the $k_L A_{me}$ for each electrode at various flow rates, controlled with the peristaltic pumps.

The performance efficiencies were measured in a similar manner to the efficiencies determined through the H-cell. The reference electrode was not used for this experiment as the cell potential was measured and used to control the running of these experiments. Additionally, the porous polyethylene/ silica separator was used in this instance. Each reservoir tank holds 500 mL of 2.25 M $ZnBr_2$, 0.5 M $ZnCl_2$, 5 mL of Br_2 per litre of electrolyte, and 0.8 M MEP. This was circulated through the cell with the peristaltic pump set at rotation speed of 600 mL min^{-1}. A constant current was held for forty-eight hours, fourteen minutes, and thirty-three seconds to achieve an 80% SOC. The same current was then applied to discharge the electrolyte solution for an indefinite period until the cell voltage hits the limit of 0.25 V: indicating the solution has discharged.

3.6 Physical Properties

The complexing ability of the $Q^+ Br_x^-$ additive with Br_2 was investigated by examining specific parameters that can measure the effectiveness of the $Q^+ Br_x^-$ compounds used. The samples used to conduct these tests were prepared by equilibrating these with a saturated bromine solution in the 3:1 molar ratio of Br_2: $Q^+ Br_x^-$. The three regions of this mixture (Figure 3.9): *viz*, bromine vapour formed above the electrolyte solution, bromine concentration in the aqueous layer of the solution and in the complex phase achieved in the immiscible layer were analysed.

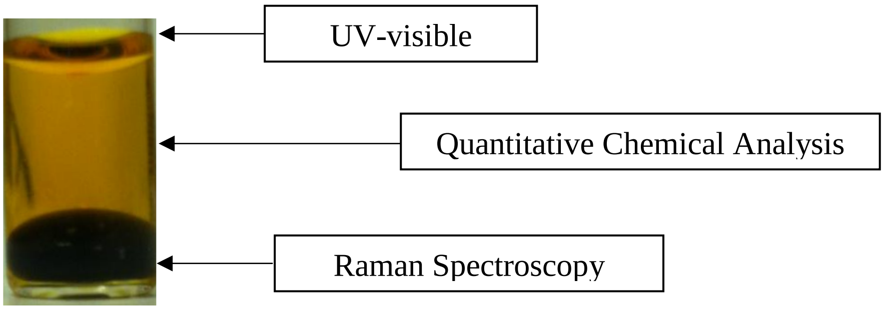

Figure 3.9 Cuvette containing the charged electrolyte sample indicating the regions of analysis

3.6.1 UV-visible

The different components were added to a sealed sample bottle, filling a third of the bottle volume. The bottle was placed in a water bath where the temperature was controlled to ±0.5°C over the range of 20°C to 40°C. The Br_2 concentration in the vapour above the liquid component was measured using the Shimadzu UV-1800 UV Spectrophotometer, considering the absorptivity of the bromine. Once the set temperature was reached the sample bottle was equilibrated for 10 minutes prior to UV-vis measurements. The temperature dependence of the Br_2 vapour pressure above both the aqueous and immiscible phases was measured in this manner and this allowed the enthalpy of vaporizations (ΔH_{vap}) to be determined through the Clausius-Clapeyron equation[116]. The data from these measurements was confirmed by repeating the experiment using an isoteniscope (Figure 3.10)[117]. However, the method involving the UV-visible spectrometer was preferred here as the isoteniscope measures the vapour pressure of both the Br_2 and the water whereas the UV-visible spectrum only examines the Br_2 content.

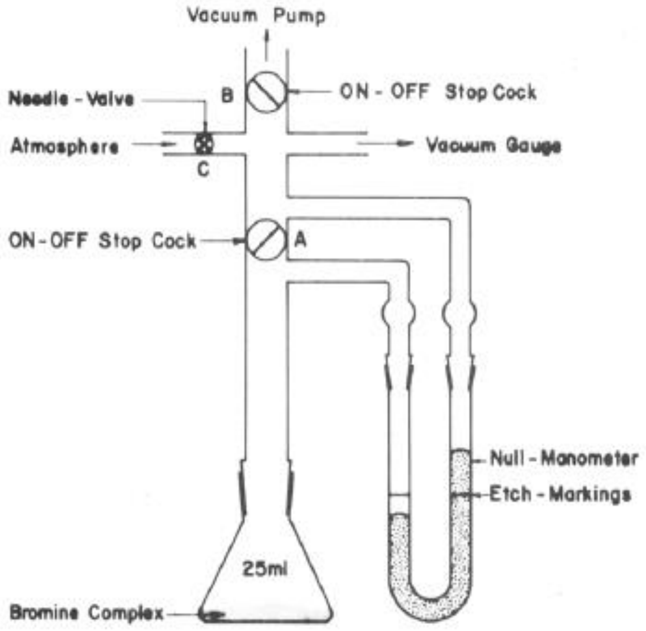

Figure 3.10 Isoteniscope set-up to determine the enthalpy of vaporization of Br_2 for the electrolyte solution compositions [117]

3.6.2 Quantitative chemical analysis

For quantification of the Br_2 content in the aqueous phase, a 0.5 cm^3 aliquot of the solution from this layer was extracted. This aliquot was then added to a round-bottomed flask with 25 cm^3 of 0.5 M potassium iodide (excess). Sodium thiosulphate was employed as the titrant to the iodine generated by the reaction: $Br_2 + 2I^- \rightarrow 2Br^- + I_2$. Two small platinum electrodes, at a fixed distance apart, were placed into the solution and a very small current of (50 nA) was passed through the solution. This formed iodine and iodide in equilibrium at the electrodes keeping the potential steady if I_2 was present. Once the current was set, sodium thiosulphate (0.01 M) at a known flow rate was added into this solution from a burette. Initially, a small voltage difference existed between these two electrodes. However, this all rapidly rises when all the iodine was fully consumed by the reaction with the sodium thiosulphate: $2S_2O_3^{2-} + I_2 \rightarrow S_4O_6^{2-} + 2I^-$. The time for this endpoint was noted and the exact volume of sodium thiosulphate was determined using the flow rate from the burette and so allowing the bromine concentration to be determined.

3.6.3 Raman Spectroscopy

Finally, the polybromide Br_x^- containing the Br_2 captured by the Q^+ Br_x^- additive was analysed through Raman spectroscopy Renishaw RM1000 microscope system with 633 nm HeNe excitation). This was done by extracting a small sample of the immiscible liquid into a 1mm glass cuvette and using a Ventacon macrosampler attached to the objective turret to focus light *via* a NikonMPlan 20×NA 0.4 LWD objective. An integration time of 10 s was used. The presence of both Br_3^- and Br_5^- species could be identified from the Raman spectra[109]. By normalizing the data to the Br_3^- peak, the effectiveness of each of the Q^+ Br_x^- synthesised to capture the Br_2, based on the Br_5^- content, could be compared. The acquisition time and number of acquisitions were controlled by the GRAMS software.

4. Theory

4.1 Cyclic Voltammogram

Cyclic Voltammetry (CV) is an important and widely used analytical technique in electrochemistry. It can be used to study a variety of redox processes to obtain information on the stability of the electrochemical reaction, the presence of intermediates in redox reactions, electron transfer kinetics as well as the reversibility of a reaction. In a CV experiment, the potential of the WE are ramped linearly with time like linear sweep voltammetry.

However, unlike linear sweep voltammetry (which ends at a set potential), when the voltage reaches a set potential, the potential ramp is reversed, usually back to the start potential. This action can be carried out multiple times in a single experiment.

In the interest of explaining, these experiments were carried out with an electroactive species, of 50 mM of $K_3Fe(CN)_6$ and the electrolyte was an aqueous solution of 0.25 M KCl, using a glassy carbon for the WE, platinum for the CE and a calomel electrode for the RE (mercury and mercurous-chloride in contact with a saturated KCl solution).

The scan rates employed were between 20-200 mV in increments of 20 mV. When the current response was plotted against the potential, it showed two peaks (Figure 4.1):

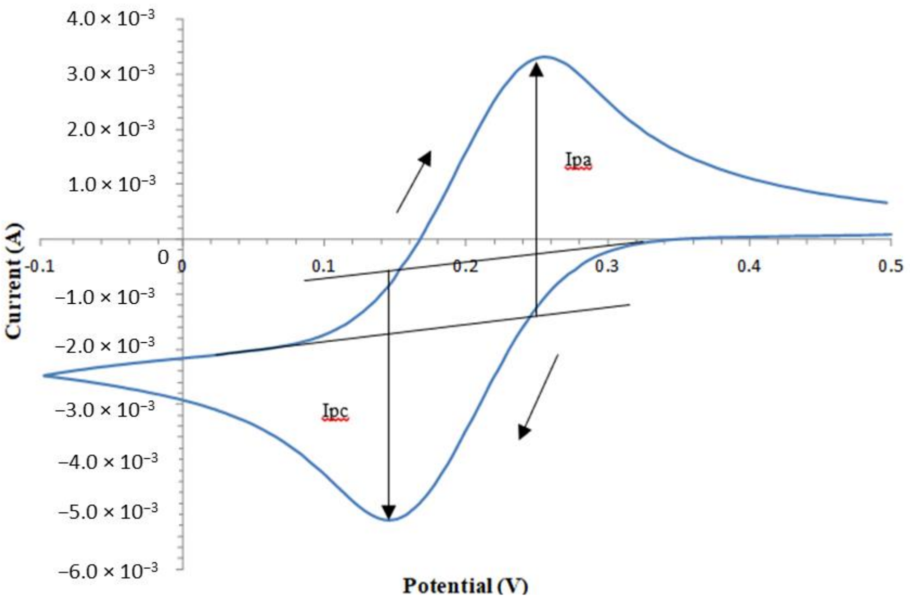

Figure 4.1 Cyclic Voltammogram at 50mM $K_3Fe(CN)_6$ in 0.25 M KCl, WE – Pt, Scan rate – 50 mVs^{-1}

The cathodic peak on the negative scan (at ~ 0.15 V *vs* SCE) is due to the reduction of the ferricyanide to the ferrocyanide and on reversing the scan at 0 V, an oxidation peak due to the reverse reaction is obtained at roughly 0.25 V. A peak is obtained in both instances due to the reaction becoming limited by mass transport between the surface of the electrode and the bulk of the solution.

To determine the diffusion coefficient for this reaction each cathodic peak (*I*) was plotted against the scan rate to the power of a half ($v^{1/2}$), which gave a linear trend in agreement with the Randles-Sevcik equation[118],

$$I_p = (2.69 \times 10^5)n^{3/2}.c_o^{\infty}.D^{1/2}.v^{1/2}.A \qquad \text{Eq. 4.1}$$

Take the gradient of the originally plotted ($Ip/v^{1/2}$) to equal *m*,

$$m = (2.69 \times 10^5)n^{3/2}.c_o^{\infty}.D^{1/2}.A \qquad \text{Eq. 4.2}$$

And with a simple rearrangement the diffusion coefficient (*D*) can be calculated,

$$D = \left(\frac{m}{(2.69\times10^5)n^{3/2}.c_o^{\infty}.A}\right)^2 = 7.29 \times 10^{-6} cm^2 s^{-1} \qquad \text{Eq. 4.3}$$

Where area (A) was 0.38 cm^2, and concentration of the bulk solution (c_0^{∞}) was 50 mM for the potassium ferrocyanide system used. The value obtained for this systems setup diffusion coefficient compares well with literature values[119]. However, this could be further verified by carrying out a potential step analysis and comparing the values obtained.

4.2 Potentiodynamic Scan (Tafel Extrapolation)

To predict the rate of a reaction it is important to work out the fundamental kinetic parameters of the reaction (exchange current density i_o, charge transfer coefficient α and rate constant k_0). These can be obtained from an analytical technique known as Tafel extrapolation.

Thus, starts with the Butler Volmer equation which describes how the electrical current on an electrode depends on the electrode potential:

$$i = i_0 \left\{\exp\left(\frac{\alpha_a nF\eta}{RT}\right) - \exp\left(\frac{-\alpha_c nF\eta}{RT}\right)\right\} \qquad \text{Eq. 4.4}$$

Where η is the activation overpotential (defined in Eq. 4.6), R is the universal gas constant and T is temperature. The exchange current density directly relates to the kinetics through:

$$i_0 = n \cdot F \cdot k^0 \cdot C_O^{\alpha} \cdot C_R^{1-\alpha} \qquad \text{Eq. 4.5}$$

With F is the Faraday constant and C is the concentrations for the oxidant and reductant considering their respective charge transfer coefficients. The Butler Volmer equation has a dependence of the electrode current on the applied overpotential, Figure 4.2. This overpotential is represented by the following equation:

$$\eta = E - E_e \qquad \text{Eq. 4.6}$$

Two limiting factors of this equation (η above 100 mV and η under –100 mV) gives the anodic and cathodic Tafel equations:

η above 100 mV result in the anodic Tafel equation:

$$log(i) = log(i_0) + \left(\frac{\alpha_a nF\eta}{RT}\right) \qquad \text{Eq. 4.7}$$

And η under –100 mV result in the cathodic Tafel equation:

$$log(|-i|) = log(i_0) - \left(\frac{-\alpha_c nF\eta}{RT}\right) \qquad \text{Eq. 4.8}$$

High overpotentials result in the Tafel equation as described above. Low overpotentials on the other hand lead to the linear approximation:

$$i = i_o \cdot \frac{n \cdot F}{R \cdot T} \cdot \eta \qquad \text{Eq. 4.9}$$

To determine the key parameters, the experimental curves are:

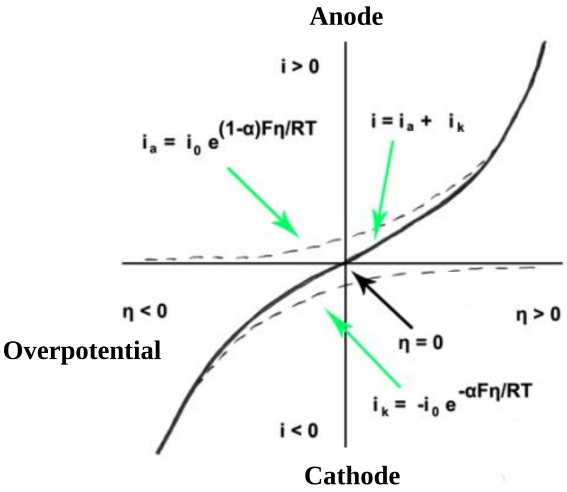

Figure 4.2 Butler-Volmer equation dependence

Plotted as potential against the logarithm of the current, as shown in Figure 4.3.

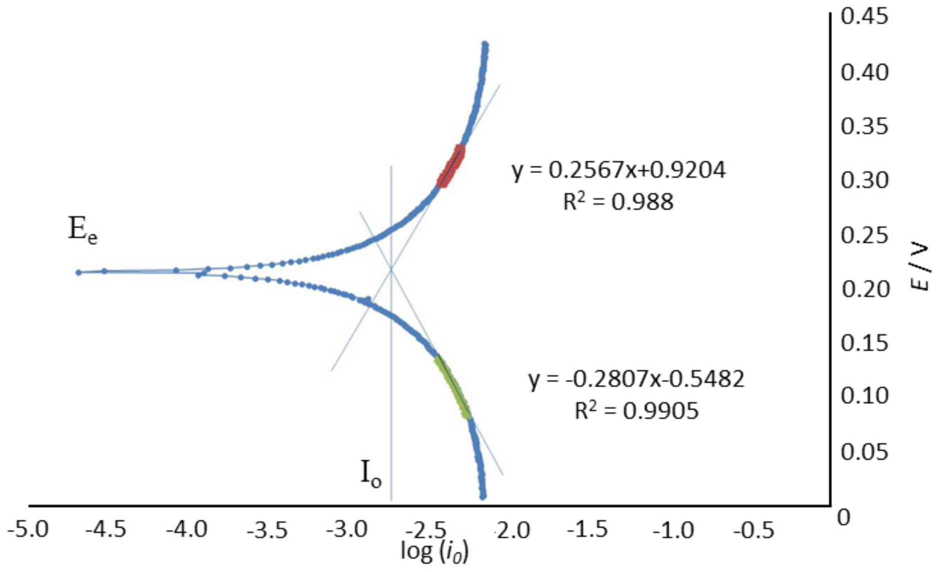

Figure 4.3 Potentiodynamic curves for 50 mM K$_3$Fe(CN)$_6$ and K$_4$Fe(CN)$_6$ in 0.25 M KCl using an Au WE

On this curve the equilibrium potential (E_e) can be clearly identified. Also, the exchange current density can also be determined from the intercepts of the anodic and cathodic Tafel slopes. When the intercept is determined the anti-log is taken to obtain the value for i_o.

Next the charge transfer coefficient is determined through:

$$Slope = \frac{2.3RT}{F\propto_a n} \cong \frac{0.059}{\propto_a} \qquad \text{Eq. 4.10}$$

Rearranging this and using the gradient obtained from the anodic Tafel slope, α_a can be determined. The same can be done to determine α_c and known that:

$$\alpha_C + \alpha_A = 1 \qquad \text{Eq. 4.11}$$

Finally, k_o can be determined using the following equation:

$$i_0 = nFk_0 C_C^{\alpha} C_A^{1-\alpha} \qquad \text{Eq. 4.12}$$

Several experiments were run to determine the different kinetics obtained between using a gold and glassy carbon electrode and varying the concentrations of the electroactive species present, *viz.* $K_3Fe(CN)_6$ and $K_4Fe(CN)_6$. Both ferri and ferrocyanide are used to allow both the anodic and cathodic slopes to be determined. As this experiment runs at a slow potential scan rate (0.1667 mV s^{-1}), if only one were to be used the return reaction would not provide precise data as the material produced over the first slope would not be sufficient and have dissipated to the bulk of the solution away from the electrode's surface.

First a 3-electrode rotating disc electrode (RDE) system was set up using a solution of 50 mM $K_3Fe(CN)_6$ and 50 mM $K_4Fe(CN)_6$ with a supporting electrolyte of 0.25 M of KCl.

Setting up the rotating disc electrode to 10 Hz to increase the mass transport and so enhance the Tafel regions, the differences in the kinetic parameters at their different concentrations were measured.

For both electrodes the kinetic parameters recorded were:

Working Electrode	**Anodic Charge Transfer Coefficient (α)**	**Electron Charge Density i_o (A cm^{-2})**	**Rate Constant k_o (cm s^{-1})**
Glassy Carbon	0.23	3.70×10^{-3}	7.66×10^{-4}
Gold	0.23	4.87×10^{-3}	1.01×10^{-3}

Table 4.1 50 mM $K_4Fe(CN)_6$ and 50mM $K_3Fe(CN)_6$ on GC and Au WE

As can be seen from Table 4.1, gold shows a much higher rate constant and exchange current density than glassy carbon under the same conditions.

Two further solutions were examined, *viz.*, 50 mM $K_4Fe(CN)_6$: 10mM $K_3Fe(CN)_6$ and 10 mM $K_4Fe(CN)_6$:50mM $K_3Fe(CN)_6$. Again, the potentiodynamic curves were ran with both glassy carbon and gold electrodes with the rotation rate being set at 10 Hz.

As can be seen from Figure 4.4, the diffusion plateau for the anodic and cathodic reaction are now different due to the difference in the electroactive species compounds. A similar trend was seen with the 10 mM $K_4Fe(CN)_6$:50mM $K_3Fe(CN)_6$ solution with the exception that it was the cathodic diffusion plateau that was higher as shown in Figure 4.4.

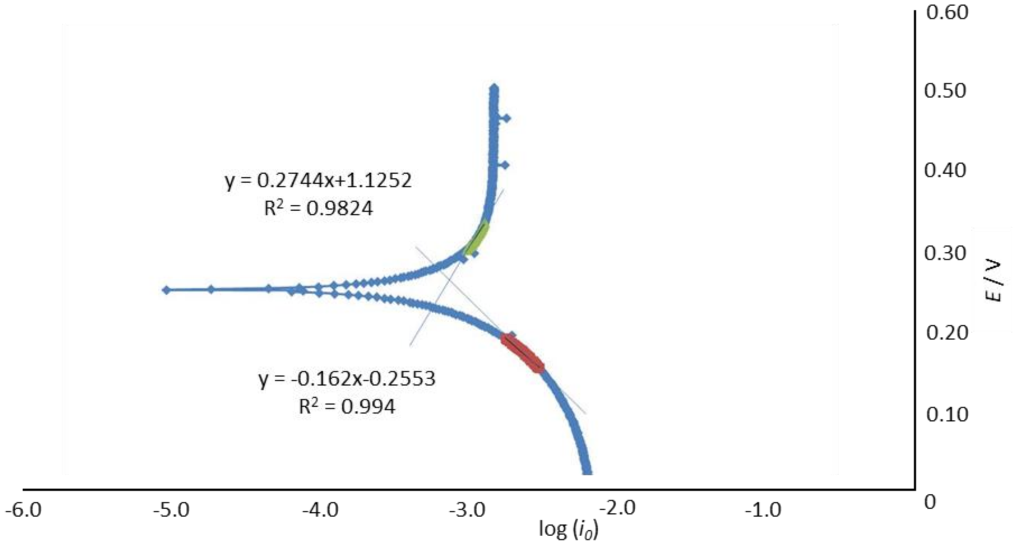

Figure 4.4 Potentiodynamic curves for 10 mV $K_4Fe(CN)_6$:50mV $K_3Fe(CN)_6$ on Au WE

The results for there experiments can be seen in Table 4.2:

Working Electrode	**$K_4Fe(CN)_6$ (mM)**	**$K_3Fe(CN)_6$ (mM)**	**i_o (A cm^{-2})**	**k_o (cm s^{-1})**
Glassy Carbon	50	50	3.70×10^{-3}	7.66×10^{-4}
Gold	50	50	4.87×10^{-3}	1.01×10^{-3}
Glassy Carbon	50	10	1.25×10^{-3}	5.98×10^{-4}
Gold	50	10	1.67×10^{-3}	9.30×10^{-4}
Glassy Carbon	10	50	1.76×10^{-3}	5.05×10^{-4}
Gold	10	50	1.80×10^{-3}	5.29×10^{-4}

Table 4.2 10/50 mM $K_4Fe(CN)_6$:50/10mM $K_3Fe(CN)_6$ on Au/GC WE

From Table 4.2, gold typically shows a larger exchange current density and rate constant than carbon due to it being a better electrocatalytic material. It can also be seen from this experiment that reducing the concentration of the reductant saw an increase in the charge transfer coefficient for both electrodes. For the last two sets of results the diffusion plateau occurred relatively fast which can be improved by controlling the rotation rate of the RDE to ensure that the system remains controlled by solution flow for a sufficient period of time.

4.3 Electrochemical Impedance Spectroscopy (EIS)

Impedance is the measure of the opposition that a circuit presents to a current when a voltage is applied. A small amplitude sinusoidal voltage can be represented as follows:

$$E = \Delta E \cdot sin(2 \cdot \pi \cdot f \cdot t) \qquad \text{Eq. 4.13}$$

Where f is the frequency of the perturbation and ΔE is the maximum amplitude of the applied sinusoidal voltage ΔE is usually less than 10 mV to use the linear approximation to the Butler-Volmer relationship:

$$i = i_o \cdot \frac{n \cdot F}{R \cdot T} \cdot \eta \qquad \text{Eq. 4.14}$$

The current response will also be sinusoidal with the same frequency. However, the amplitude and phase of the current will be different:

$$I = \Delta I \cdot sin(2 \cdot \pi \cdot f \cdot t + \phi) \qquad \text{Eq. 4.15}$$

ΔI is the maximum amplitude of the current responses and ϕ is the phase angle between the current output and the potential perturbation.

The shift in phase and magnitude of the current is caused by the electrode solution interface that behaves in the same way to an electrical circuit which has resistances and capacitances.

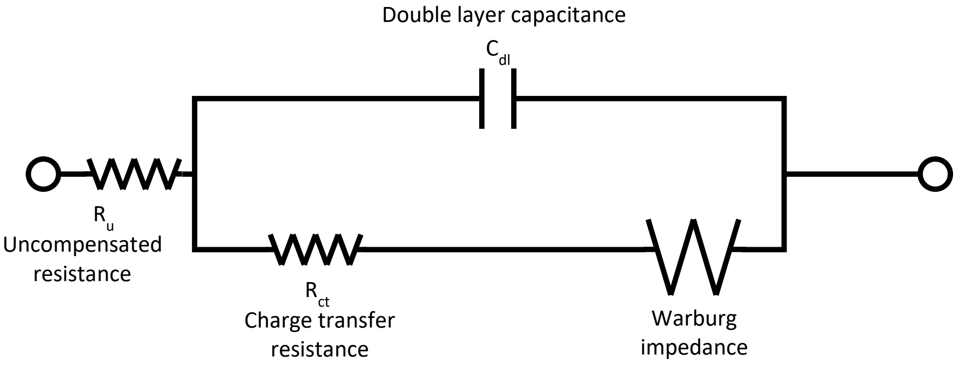

Figure 4.5 Electrical Circuit

This electrical circuit simulates the behaviour of the electrode reaction. Normally a simple circuit is set up initially and then components are added until the experimental frequency dependence of the impedance is equal to that of the circuit. The final step is to analyse the values of the circuit components in terms of physical parameters *i.e.* diffusion coefficient, electron transfer kinetic constants, film thickness *etc.*

The impedance of the electrode reaction is represented as $\tilde{z}$ which is complex, containing both real and imaginary components, defined as:

$$\tilde{E} = \tilde{I} \cdot \tilde{z} \qquad \text{Eq. 4.16}$$

The impedance experiment is investigated as a function of the frequency of the potential perturbation, *f*. The complex impedance is usually represented in the form of a Nyquist plot, Figure 4.6.

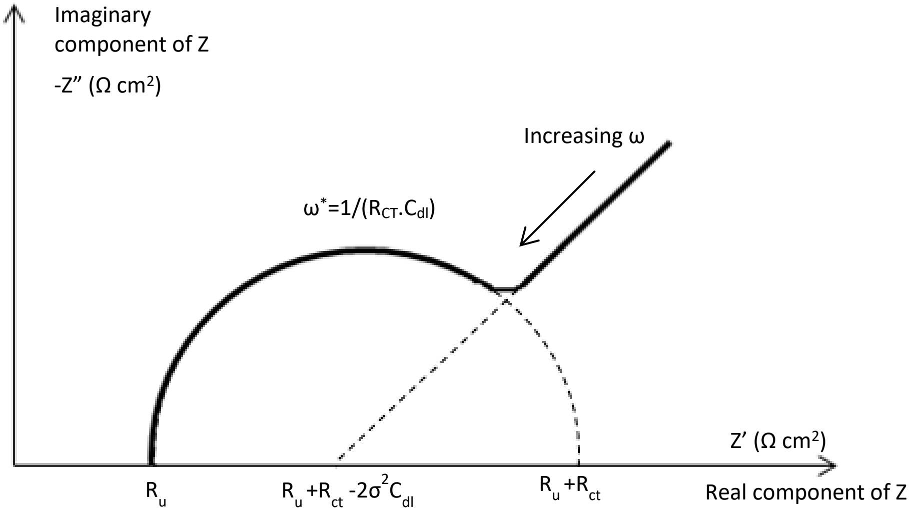

Figure 4.6 Nyquist plot

Where ω is the angular frequency (ω = 2πf. The Nyquist plot is where the imaginary components are plotted against the real components of the impedance as a function of frequency. The real component is the in-phase component that vary with *sin (2πft)* while the imaginary components consist of the quadrature component that varies with *sin (2πft + π/2)*. The determination of the real and imaginary components for impedance is through phase sensitive detection and Fourier transform analysis. Nyquist plots are commonly interpreted with an associated circuit, Figure 4.5.

Figure 4.5 shows the associated circuit for an inert electrode in a solution containing both oxidant and reductant. The electron transfer reaction is shown by the series combination of a resistance (the charge transfer resistance, R_{ct}) and by the Warburg impedance which has a frequency dependent component and exhibits the effects of diffusion (the Warburg impedance). The circuit recognises that the interface will have a double layer capacitance, C_{dl}, and that there will be an uncounted for resistance between the tip of the Luggin capillary and the electrode surface (R_u). This circuit leads to the Nyquist plot, Figure 4.6, which shows how the components are also identified. The charge transfer difference is taken from the semi-circle at higher frequencies and can be used to estimate the exchange current density by:

$$R_{ct} = \frac{R \cdot T}{n \cdot F \cdot i_o} \qquad \text{Eq. 4.17}$$

The gradient of the linear section at low frequency should be at an angle of *(45°)* to the x-axis. To obtain a complete plot that has both the kinetically controlled (semi-circular) and diffusion controlled (linear gradient) regions the measurements are made over a wide range of frequencies, such as 0.01 – 10^4 Hz.

EIS can be used for the determination of the double layer capacitance from:

$$\omega^* = \frac{1}{R_{CT}C_{dl}} \rightarrow 2\pi f^* = \frac{1}{R_{CT}C_{dl}} \rightarrow C_{dl} = \frac{1}{2\pi f^* R_{CT}} \qquad \text{Eq. 4.18}$$

4.4 Double Potential Step Technique

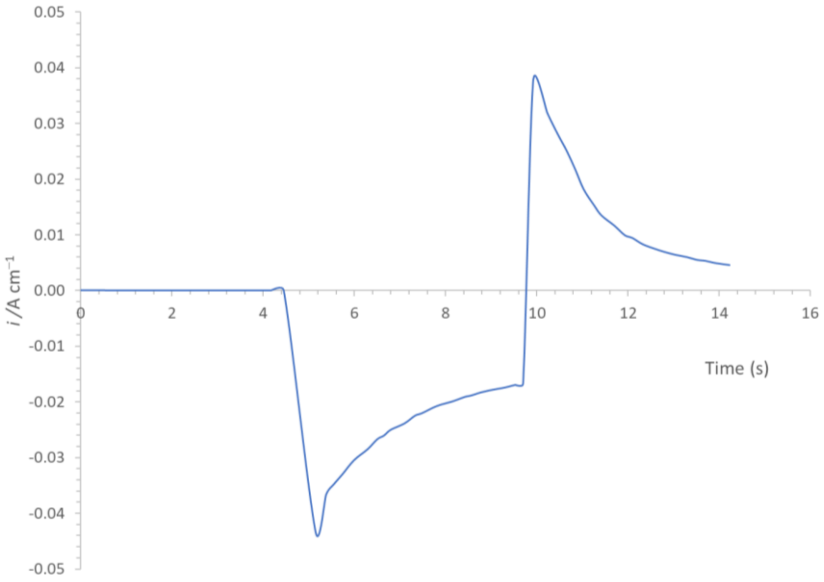

Figure 4.7 Current response because of a step in the Double Potential for 50 mM Ferricyanide solution on a Pt WE

The chronocoulometric experiment is where the total charge, Q, which passes during the time after a potential step is measured as a function of time. Figure 4.7 shows the current responses from two potential steps, both into regions controlled by diffusion of the electroactive species. The first step produces the $Fe(CN)_6^{4-}$ species under diffusion control and in the second step to a potential positive enough that these species are oxidised back to the starting material $Fe(CN)_6^{3-}$, again under diffusion control

This total charge after each step is obtained by integrating the current, i, during the potential step. For diffusion-controlled systems the charge measured can be derived by integrating the Cottrell equation to form the Anson equation:

$$Q_d = \frac{2nFAD_O^{1/2}C_O^{*}t^{1/2}}{\pi^{1/2}} \quad \text{Eq. 4.19}$$

The normalised charge, with respect to potential step duration τ is shown in Figure 4.8 for the ferri-ferrocyanide system. The potential step programs in chronocoulometry are the same as the ones used in chronoamperometry. However, the advantage for the former is that it is recording charge rather than the current which means Q is increasing during potential step rather than falling (I falls as $t^{-½}$) Q reaches a maximum at the end of the step at time τ, as can be observed as can be observed in Figure 4.8.

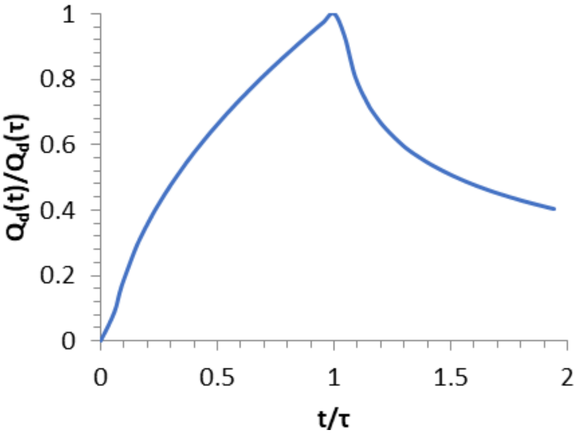

Figure 4.8 Normalised charge for DPS for $Fe(CN)^{3-/4-}$ process

This makes chronocoulometry generally preferable over chronoamperometry for the measurement of the electrode area (A) and the diffusion coefficient (D). This enhanced signal also improves the measurement of the kinetics of the chemical reactions following the first electron transfer. From the double potential step shown previously, the reduced product of the redox couple is still in the area near the electrode surface which, on application of the reverse potential step, can be oxidised again to its previous state. Like chronoamperometry, the signal in the reverse step is much less than the forward step. This charge for an electrochemically reversible species on the reverse step is represented by:

$$Q_r = \frac{2nFAD_O^{1/2}C_O^*}{\pi^{1/2}}\left[\tau^{1/2} + (t-\tau)^{1/2} - t^{1/2}\right] \qquad \text{Eq. 4.20}$$

The values for charge measured at a time equal to 2τ after each step, shown as Q_r and Q_f shown in Figure 4.9, for the system would result in a charge ratio:

$$\frac{Q_r(2\tau)}{Q_f(\tau)} = 0.414 \qquad \text{Eq. 4.21}$$

Any reactions coupled to the electron transfer will result in varying different value for this ratio. For instance, if the product of the reduction reaction from the forward step undergoes a chemical change into an electrochemically inactive species, the charge for the reverse potential step, Q_{r2}, will be smaller and this charge ratio will increase.

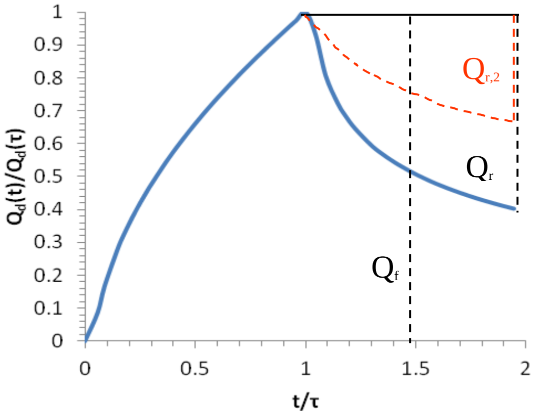

Figure 4.9 The impact of a chemical reaction following the forward step to produce an electrochemically inactive species. Q_f is the full charge in the solution, Q_r is the reverse step charge returned and $Q_{r,2}$ the result of the first step creating an electrochemically inactive species

Figure 4.9 shows the normalised plot for the DPS on the Fe $(CN)^{3-/4-}$ reaction and as expected, the charge ratio, as seen with the earlier equation to give the 0.414 value. On the other hand, a chemical change to the product of the first step giving an electrochemically inactive species gives the curve shown as $Q_{r,2}$. This difference allows for the electrochemical determination of inhibitive products or films being formed on the electrode surface.

As in chronoamperometry, the change in the applied potential of the working electrode will cause the ions in the electrical double layer to rearrange and this leads to the additional contribution to the signal from the electrical double layer capacitive current. The current is integrated over time in chronocoulometry meaning that the charge which is due to capacitive current is included in the total charge at the end step. Double layer charging is rapid which means that the double layer charge, Q_c, and the charge due to the diffusion-controlled Faradaic process, Q_d, are easily distinguishable. Thus, if the total charge for the forward step, Q_r, equivalent to $(Q_d + Q_c)$, and is plotted as a function of $t^{1/2}$, the following is obtained:

$$y = ((2.n.F.A.C_0.D_0^{1/2})/\pi^{1/2})x + Q_c \qquad \text{Eq. 4.22}$$

This is because the double layer charging is practically instant after the potential steps whereas the charging that comes from a diffusion-controlled process depends on the transport of the electroactive active species to the electrode surface to react.

In cases where the electroactive species can be adsorbed at the electrode surface, the species there can obviously under reaction without the need for diffusion from the bulk. This surface concentration of electroactive species is represented as Γ_0. On the application of the forward potential step the electroactive species that is adsorbed to the surface is electrolysed instantly. The charge result, Q_{ads}, from this reaction is given by:

$$Q_{ads} = nFA\Gamma_0 \qquad \text{Eq. 4.23}$$

The total charge of the forward step can now be represented as:

$$Q_t = Q_d + Q_{ads} + Q_c = \frac{2nFAC_0D_0^{1/2}t^{1/2}}{\pi^{1/2}} + nFA\Gamma_0 + Q_c \qquad \text{Eq. 4.24}$$

When adsorbed materials are included the Anson plot is simple the sum of Q_{ads} and Q_c.

Anson plots can be used for both the forward and reversal potential steps. The forward step is plotted as Q_f against $t^{1/2}$ and the reverse step plotted as Q_r against $[\tau^{1/2} + (t-\tau)^{1/2} - t^{1/2}]$. In this instance the oxidant is adsorbed but the product of the electrode reaction is not and the difference of the two intercepts of the two plots gives Q_{ads}. Figure 4.10 shows the Anson plot for the forward potential step for a non-adsorbed analyte (left) and the DPS with an already adsorbed species (right).

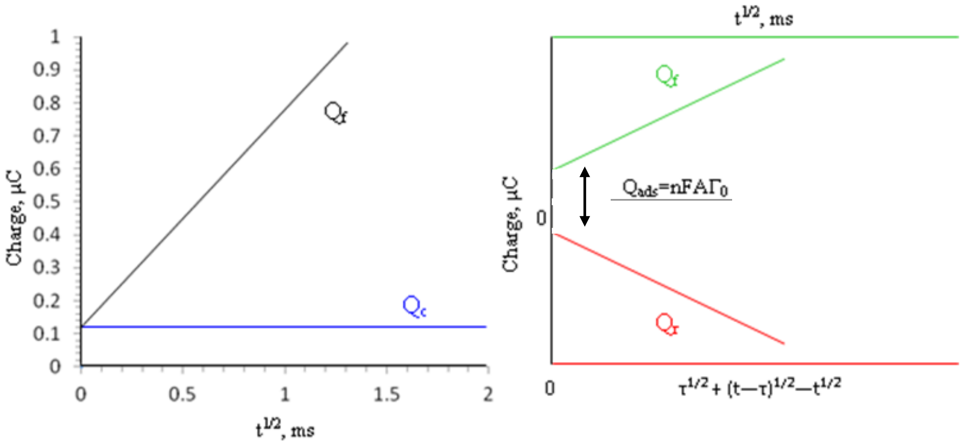

Figure 4.10 Anson plot for forward step (left) and DPS for a pre-adsorbed species (right)

5. Additives

5.1 Introduction

Currently, *N*-methyl-*N*-ethylpyrrolidinium bromide (MEP) is the choice complexing agent for industrial batteries. However, interest lies in developing a complexing agent that will bind with the electrogenerated bromine but remain in the aqueous phase of the solution. This would improve the charged materials ability to disperse throughout the solution and reduce the complexity of the pumping requirements currently used. Several novel additives have been synthesized and characterized by focusing on both their impact on the Br_2/Br^-electrochemical kinetics and on their physical properties.

5.2 Aliphatic Ammonium Complex Additives

5.2.1 Cyclic Voltammetry Analysis

To differentiate any impact the additives may have on the electrolyte solution, it was important to run a control where no additive was present. Figure 5.1 shows the CVs obtained on a variety of electrodes in a 50 mM $ZnBr_2$, 0.5 M KCl solution. The platinum electrode shows one oxidation and one reduction diffusion-controlled peaks. The oxidation peak (occurring at $E = 0.9$ V) corresponds to the bromide ions forming liquid bromine. The lower voltage limit employed here (compared to other electrodes) prevented oxygen gas evolution from occurring. On the reverse scan, the reduction peak ($E = 0.8$ V) was the bromine reverting to bromide ions. The other carbon composite electrodes, BMA 5, BAC 2 and PPG 86 also exhibited the two diffusion-controlled peaks. The major difference between these and the Pt CV was the increase of the separation between the reduction and oxidation peaks (ΔE_p increasing from 10 mV to 30 mV). As previously noted, ΔE_p is indicative of a system's reversibility and can be affected by many factors. In this instance, it indicates that the platinum is a better electrocatalyst in comparison to the carbon composites as the peak separation is smaller than that of the carbon complex materials. Despite platinum being a superior electrode for the Br^-/Br_2 reaction, the carbon composites were used for the remainder of the study in the large-scale studies as platinum is too expensive for use in industrial scale batteries. The data collected on the carbon composites in any event would carry more impact to the technologies development since these materials are already employed in flow battery systems.

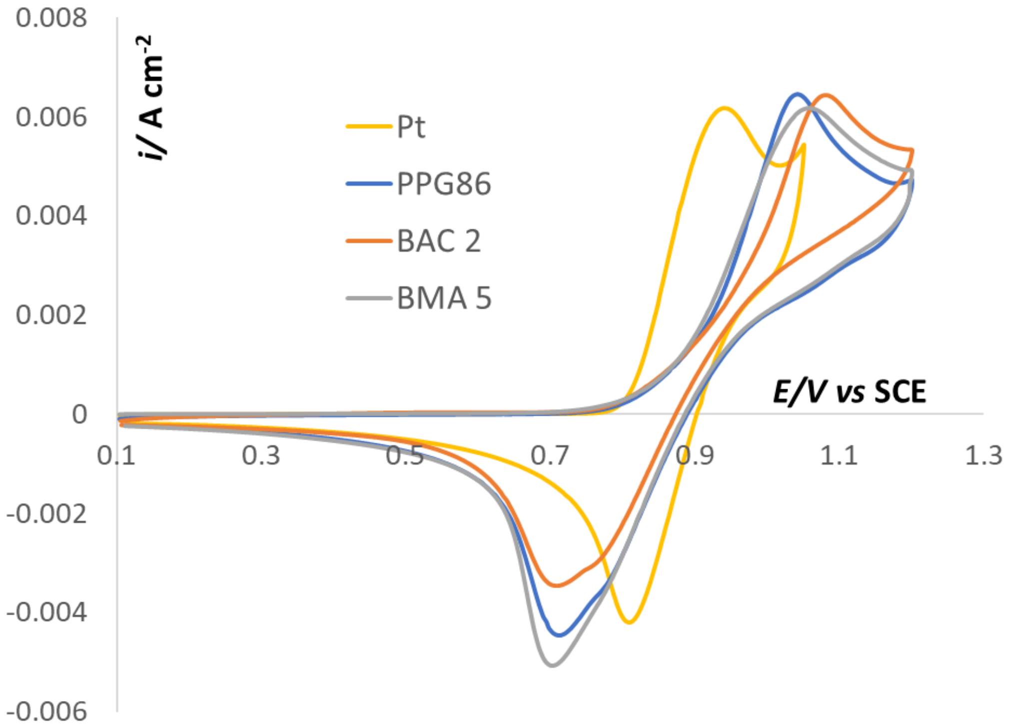

Figure 5.1 CV of 50 mM $ZnBr_2$, 0.5 M KCl with a Pt, PPG86, BAC 2, or BMA 5 WE and a SCE RE, Pt CE. Scan rate 20 mV s^{-1} with electrode area 0.38 cm^2

The first series of additives tested were nitrogen centres with four aliphatic ligands: *viz.* tetrapropylammonium bromide (TPA) and tetrabutylammonium bromide (TBA). The potential limits in the study were increased, to consider any loss in the electrochemical reversibility to the overall system through the additions of these species. It was observed that a second oxidation (and reduction) peak appeared after the initial expected one (at $E \approx 1.15$ V), as shown in Figure 5.2 for all electrodes employed here.

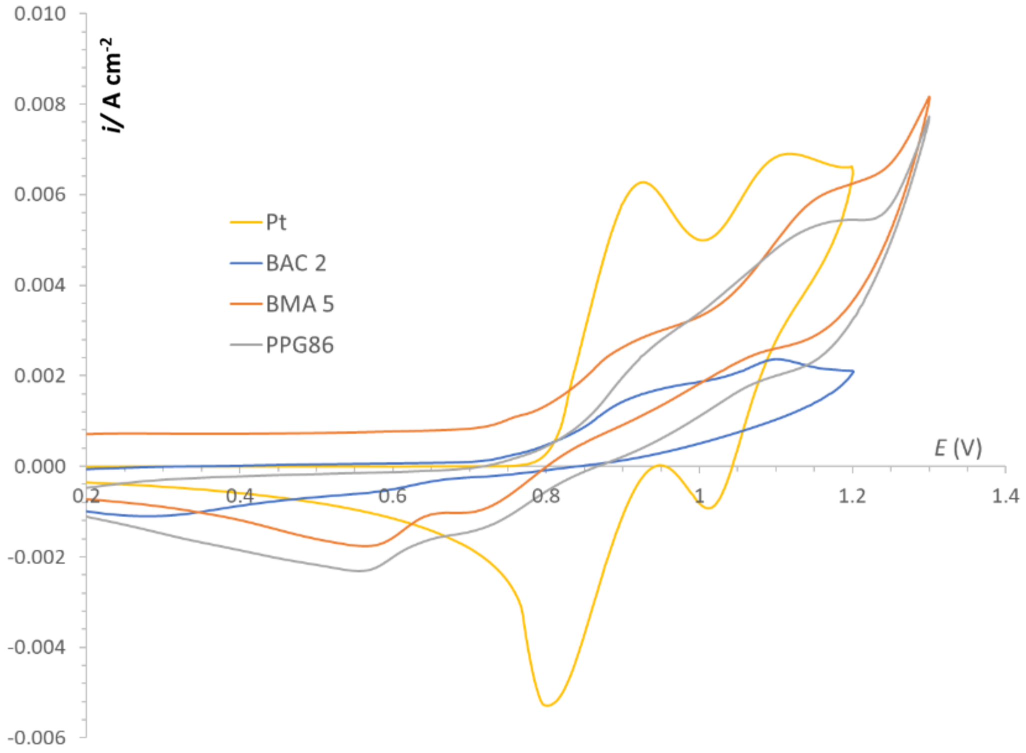

Figure 5.2 CV of 50 mM $ZnBr_2$, 0.5 M KCl, 50 mM TPA with a Pt, PPG86, BAC 2, or BMA 5 WE and SCE RE, Pt CE. Scan rate 20 mV s^{-1}

The possibility of chlorine evolution giving rise to the second peak was eliminated after being run on the platinum electrode, as the peak response was like the first peak, meaning that the process was limited to the concentration of the bromide species. Instead, it was hypothesised that the complex species Br_2Cl^- was formed in the presence of these additives. This was confirmed by running the tests with KNO_3^- in place of KCl. Figure 5.3 shows the CV for the same system but with 0.5 M KNO_3^- with no additive present. As can be observed, there was only one oxidation peak occurring as a result with the secondary increase being attributed to oxygen gas evolution.

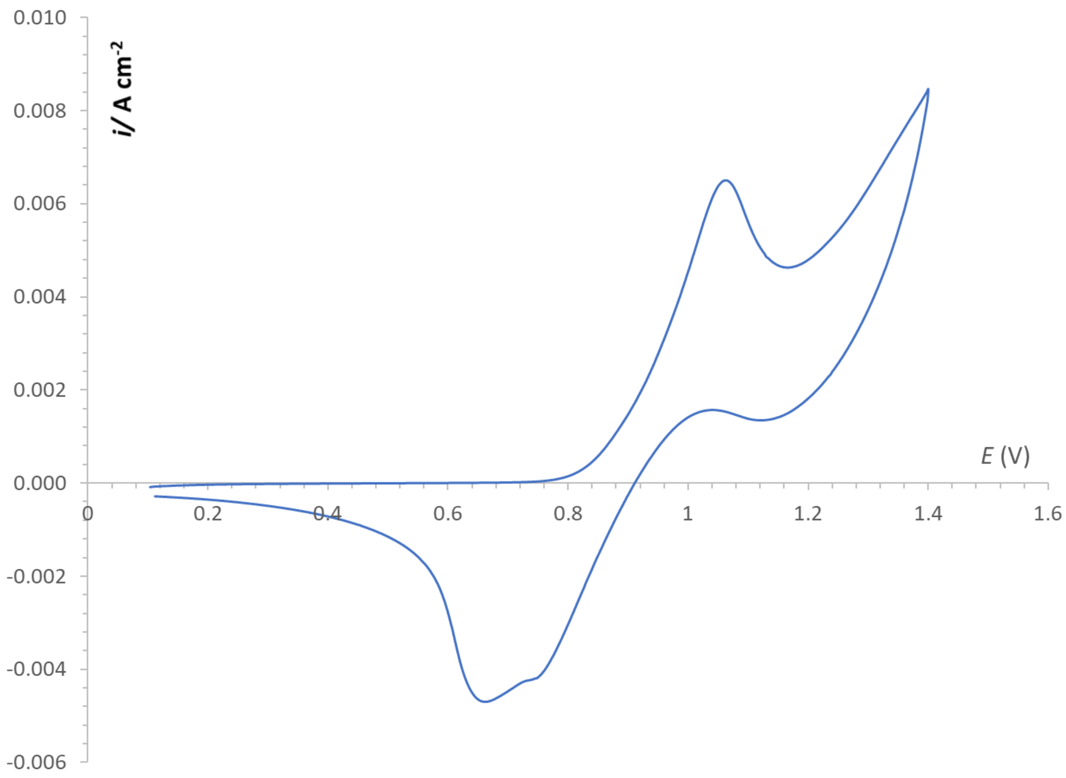

Figure 5.3 CV of 50 mM ZnBr2, 0.5 M KNO_3^- using a PPG86, SCE RE, Pt CE. Scan rate 20 mV s^{-1}

When 50 mM TPA was added to the solution, the CV showed a smaller current peak (nearly 50% smaller) for the second process (Figure 5.4). The shape of the oxidation peak also suggested a reaction causing passivation on the electrode surface in the presence of the TPA. Indeed, from visual inspection of the electrode during the scan, it appeared that a film formed over the entire electrode surface during the oxidation process, but the film then disappeared as the reverse scan occurred. It was assumed that the film was a polybromide phase, from complexation with the additive TPA, collected on the electrode surface. This effect also shows a reduced reversibility with the peak separation increasing by 55 mV. This additive, TPA, shows to be inhibitive through this CV and was investigated further with the KCl supporting electrolyte: as this electrolyte composition gave a larger current response and would better demonstrate these inhibitive effects.

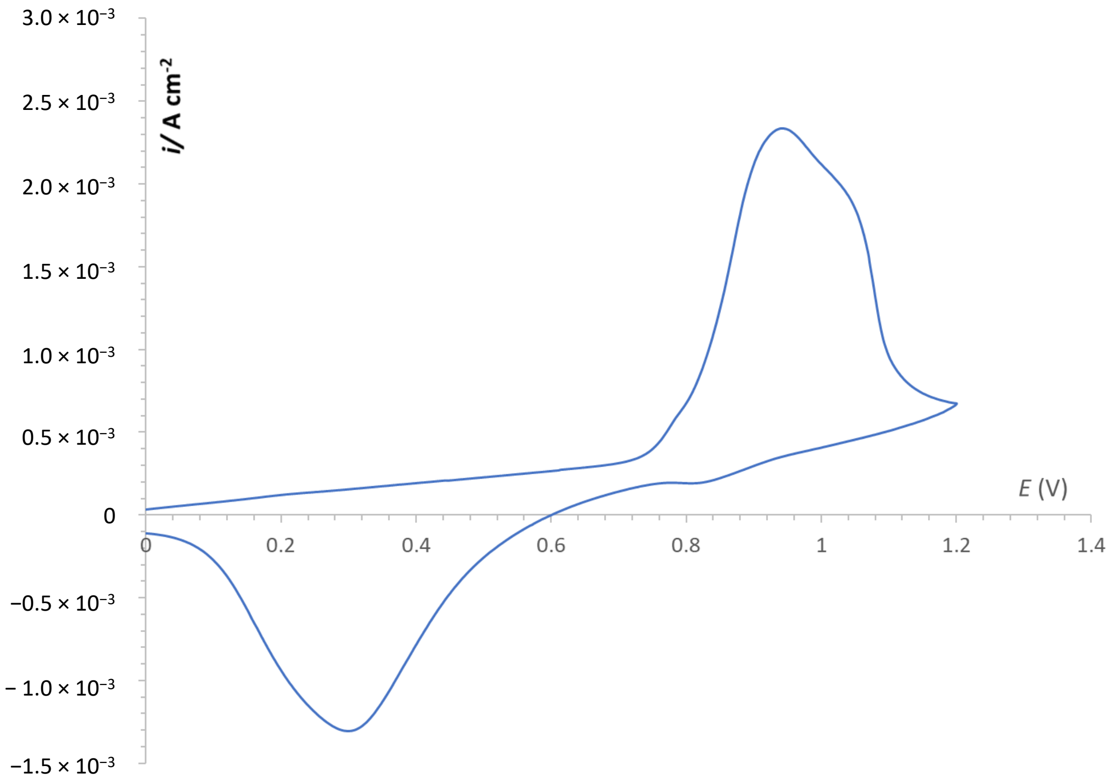

Figure 5.4 CV of 50 mM $ZnBr_2$, 0.5 M KNO_3^-, 50 mM TPA using a PPG86, SCE RE, Pt CE. Scan rate 20 mV s^{-1}

To explore of this process, the supporting electrolyte was changed back to KCl and the platinum electrode used once more in the presence of the TPA additive. As expected, the first cycle occurred as it had before but on the 2nd voltage scan, a sharp current peak occurred, indication a surface-controlled reaction at E = 0.75 V. This could be attributed to the oxidation of the Br^- ions tied up in the surface film since that was at a very similar potential for Br^- oxidation on a clean Pt surface as seen in Figure 5.2. Beyond this event, the current then rose slowly with potential to the potential limit of 1.3 V but then kept rising on the reverse scan to give a peak current at 1.12 V, as shown in Figure 5.5. The nature and formation of the current peak in this manner would suggest that this was s the Br^-/ Br_2 reaction occurring although severely inhibited by the presence of a surface coating. The time lag for the formation of the peak indicates that the transport of the Br^- reacting species through the coating is quite slow. On the reverse scan, two oxidation events were found, one at 0.95 V and the larger second event at 0.75 V. The former was the removal of the inhibitive film caused by the TPA-bromine complex, whereas the reduction peak at 0.7 V, was simply the expected peak for the reduction of the ‘free’ bromine species to bromide ions.

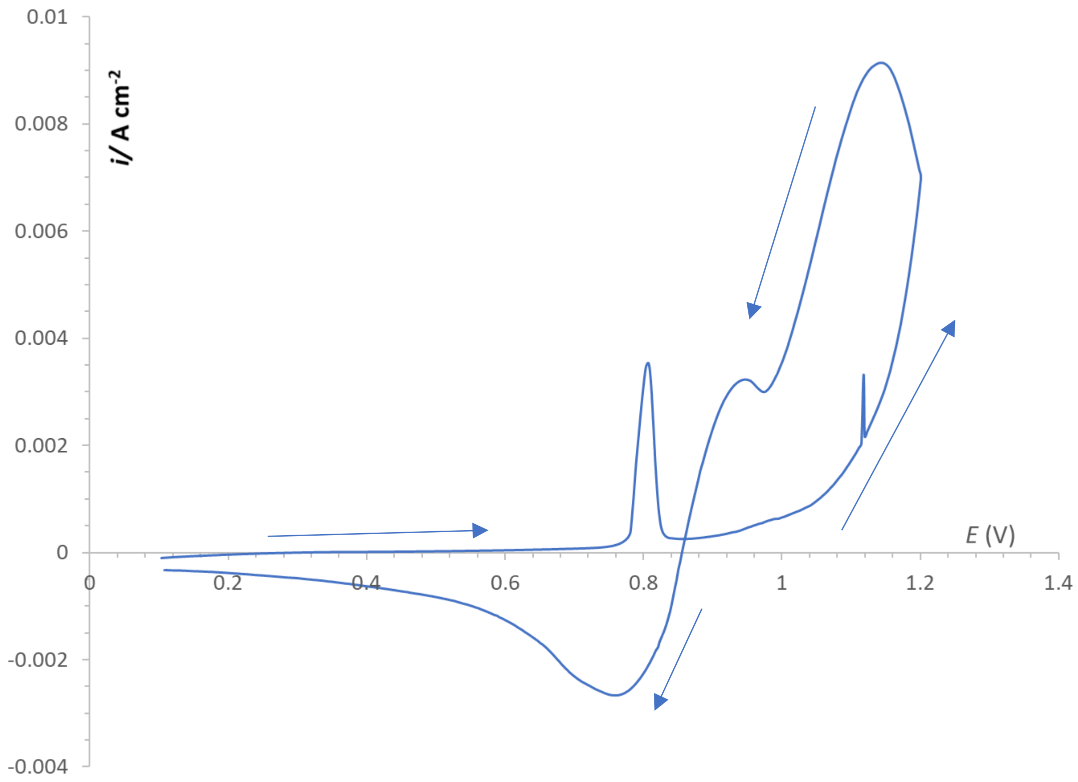

Figure 5.5 2nd subsequent CV of 50 mM $ZnBr_2$, 0.5 M KCl, 50 mM TPA with a Pt WE, SCE RE, Pt CE. Scan rate 20 mV s^{-1}

This behaviour was also observed for the TBA additive, as shown in Figure 5.6 A. With 50 mM TBA in the solution, the first cycle appears as expected, with an onset potential for bromide oxidation at 0.72 V leading to a current peak at 0.9 V. A second broader peak is found beyond this and as before, the events observed here are linked to the formation of bromine which is then complexed with the TBA to give a surface film which hinders further oxidation. The reverse scan leads to an immediate fall in the current and the bromine reduction reaction can only be observed once the TBA^+-Br_2Cl^- surface complex is removed from the surface at 0.95 V and then allowing ‘free’ bromine reduction to occur, giving a peak current at 0.75 V. The subsequent cycles revealed slightly lower oxidation peak for the bromide oxidation as this was very likely happening on a film-covered electrode surface. However, it was noted that at the concentration of 50 mM, the inhibition effect was not as drastic with TBA as it was with TPA. However, when the concentration of the TBA was increased to 100 mM (Figure 5.6 B), although the onset for Br^- oxidation was similar at 0.72 V, the shape of the oxidation curve suggests that the formation of the surface film occurred much faster here than at 50 mM. Again, this surface film had to be removed before ‘free’ bromine reduction could occur. Nevertheless, the electrode surface remained severely inhibited as very little reaction was observed during the second scan. These data indicate that the concentration of the additives here have a big impact on the formation of the inhibitive film, especially when used in excess such as at 100 mM concentration compared to 50 mM Br$_2$ formation.

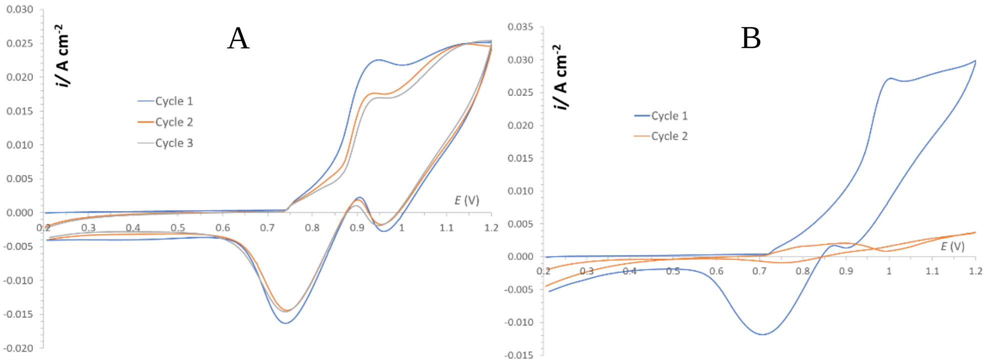

Figure 5.6 1st, 2nd and 3rd CV of 50 mM ZnBr$_2$, 0.5 M KCl, 50 mM TBA (A) and, 1st and 2nd CV of 50 mM ZnBr$_2$, 0.5 M KCl, 100 mM TBA (B) with a Pt WE, SCE RE, Pt CE. Scan rate 20 mV s^{-1}

Additionally, that the effect appears to build over each successive cycle at 50 mM. This can be seen from the data of Figure 5.7 where 3 cycles were run back-to-back. This shows that the current response decreased with each subsequent run on the PPG 86 carbon composite electrode at a 50 mM concentration. Furthermore, the delayed formation of the oxidation current peak became more distinct with subsequent cycles, showing an increase in the inhibitive effect of the surface film containing the complexing agent. Compared to Figure 5.7, this data set shows less pronounced oxidation peaks on the carbon composite electrode than the platinum electrode.

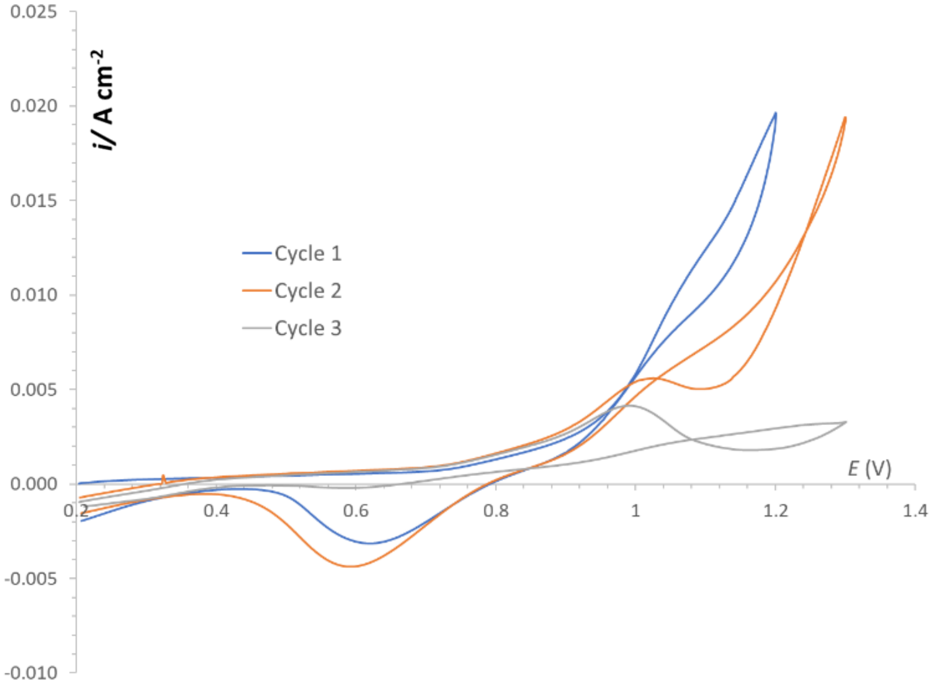

Figure 5.7 1st, 2nd and 3rd CV of 50 mM $ZnBr_2$, 0.5 M KCl, 50 mM TBA with a PPG 86 WE, SCE RE, Pt CE. Scan rate 20 mV s^{-1}

5.2.2 Double Potential Step Analysis

The double potential step (DPS) experiment was used to focus on the oxidation of bromide ions to bromine (forward step) and the subsequent reduction of the bromine formed on the reverse step. This would show the impact of the surface coating formed with the TPA and TBA on the electrode reaction. The data for such an experiment carried out without the additives being present is shown in Figure 5.8, with the potentials selected based on the regions of diffusion control in the CV. By a simple integration of the area under the curve, the charge consumed during Br_2 formation could be compared to that resulting from the reverse reaction, that of Br_2 reduction back to bromide ions.

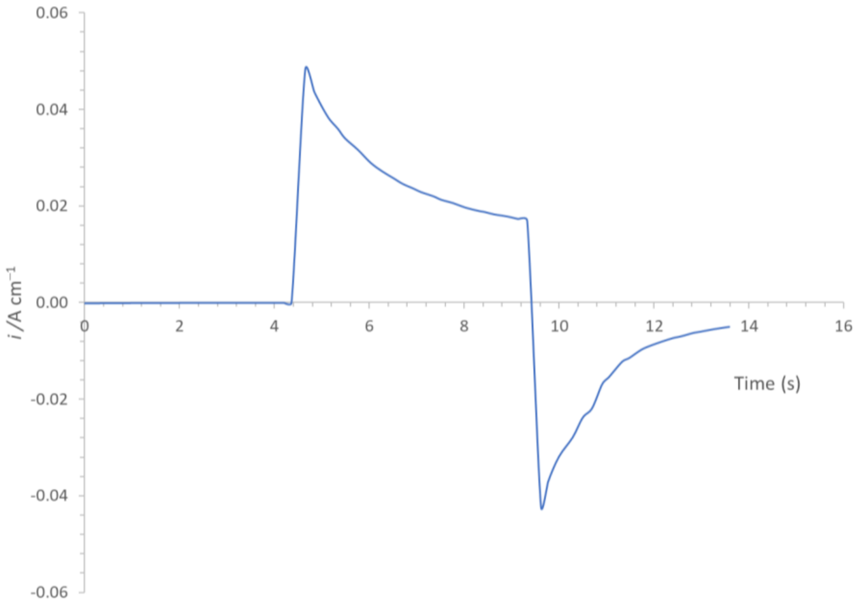

Figure 5.8 Double Potential Scan for 50 mM zinc bromine 0.5 M KCl solution a Pt WE, SCE RE, Pt CE

This experiment was aimed at determining whether the Br^-/Br_2 reaction was becoming electrochemically inhibited by being complexed and at what concentration ratio of the TBA: bromine has the most effect.

DPS was run with and without TPA in the 50 mM zinc bromide and 0.5 M potassium chloride solution. The TPA concentrations used were 2 mM, 5 mM, 10 mM, 20 mM, 50 mM, 100 mM and 200 mM.

It was evident on analysing the individual oxidation and reduction charges at these various concentrations that concentrations above 50 mM of TPA caused a dramatic decrease in charge for both oxidation and reduction processes (Table 5.1). Figure 5.9 shows the individual oxidation and subsequent reduction charges plotted against time for each concentration. The figure shows that at concentrations between 2 – 20 mM of TPA, there is little variation in the absolute charge/discharge profiles, with the baseline being the control data set where there is no additive present. However, at 50 mM and beyond, there is a significant decrease in the absolute charge obtained. The data indicate that at TPA ≥50 mM, the surface film was formed during oxidation which inhibited the overall reaction which also impacted on the reduction reaction as well. Since this effect impacted on both parts of the cycle (as can be seen from Table 5.1), the charge ratio between reduction to oxidation did not deviate far from unity. This inhibitive effect increased significantly with concentration beyond 50 mM TPA. Interestingly, at concentrations between 2 – 10 mM TPA, an increase in the amount of charge obtained during the forward step, compared to the solution with no additive, was found which is in line with the increased Br^- concentration through dissolving the TPA^+Br^- salt. It appears though that even at 20 mM concentration, the inhibitive effect starts off since despite the higher Br^- concentration, the oxidative charge here is much lower than at 10 mM TPA. Indicating that a concentration of 10 mM TPA appears to be the optimal concentration for bringing the electroactive species to the electrode surface.

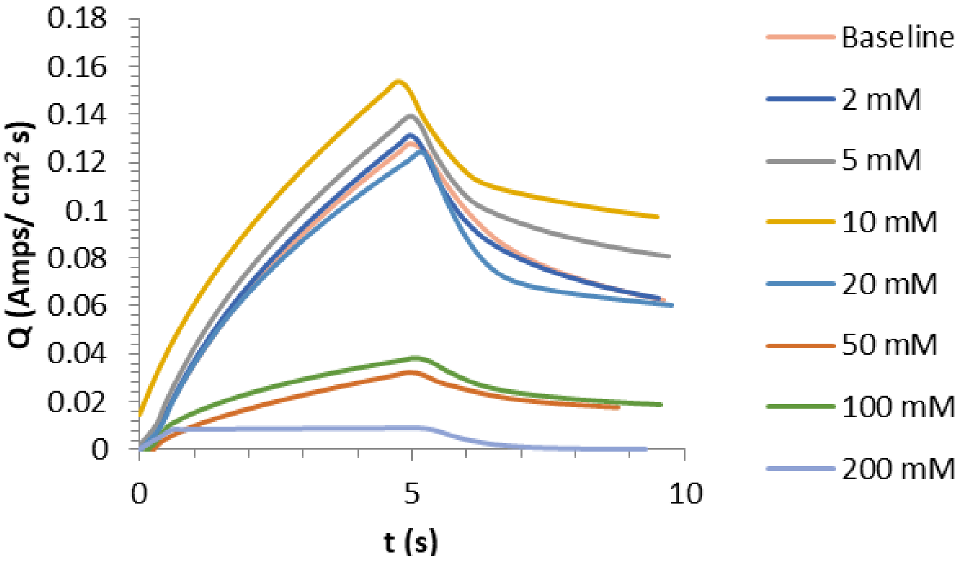

Figure 5.9 Charge vs. time for 50 mM zinc bromine 0.5 M KCl solution, TPA concentrations 0 - 200 mM using a Pt WE, SCE RE, Pt CE

Conc. of TPA (mM)	Forward Step (C/cm^2)	Reversal Step (C/cm^2)
0	0.128	0.126
2	0.138	0.133
5	0.138	0.117
10	0.152	0.127
20	0.125	0.117
50	0.036	0.032
100	0.024	0.024
200	0.009	0.009

Table 5.1 Forward and reversal steps for TPA concentrations 0-200 mM

The DPS measurements were also carried out with the TBA additive at concentrations of 2 mM, 5 mM, 10 mM, 20 mM, 50 mM, 100 mM and 200 mM in the solution of 50 mM zinc bromide and 0.5 M potassium chloride as the electrolyte. The data obtained from the measurements are shown in Table 5.2. Unlike the TPA additive, the inhibitive effect with the TBA becomes apparent even at the 2 mM concentration and becomes more so with increasing concentration (Figure 5.10). Indeed at 100 mM TBA, only *ca*. 10% of the oxidation charge compared to no additive was obtained here, compared to ~20% for the TPA additive.

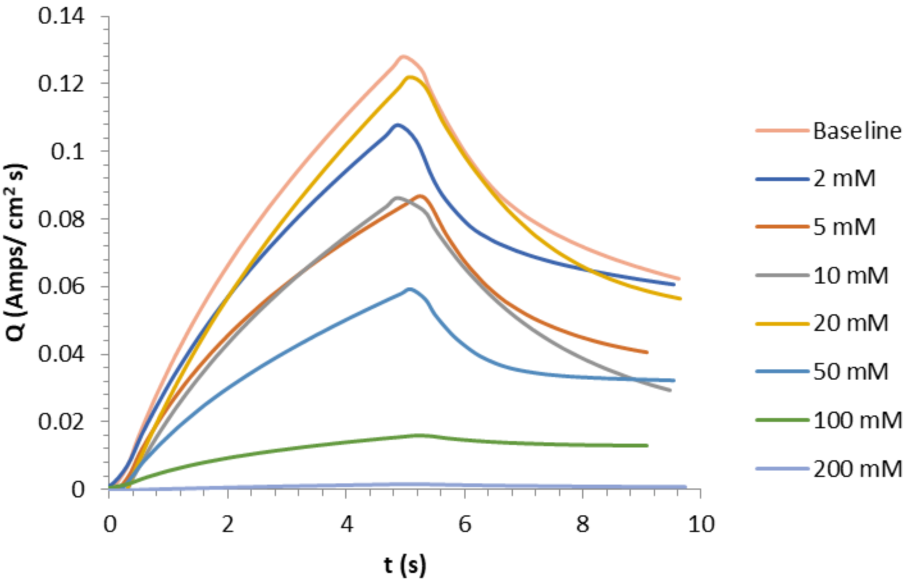

Figure 5.10 Charge vs. time for 50 mM zinc bromine 0.5 M KCl solution with TBA concentrations 0 - 200 mM using a Pt WE, SCE RE, Pt CE

Conc. of TBA (mM)	Forward Step (C/cm^2)	Reversal Step (C/cm^2)
0	0.128	0.126
2	0.107	0.100
5	0.089	0.083
10	0.092	0.104
20	0.129	0.130
50	0.062	0.056
100	0.015	0.008
200	0.002	0.002

Table 5.2 Charge for Forward and reversal steps for TBA concentrations 0-200 mM

These data indicate that TBA formed a more inhibitive layer than the TPA. For both additives though, all concentrations showed a high percentage return of the charge consumed during reduction compared to that generated on oxidation, indicating that even at the highest additive concentrations, the bromine species tied up in the complex on the electrode surface or in the solution next to the electrode is accessible for conversion back to bromide ions.

Thus, the behaviour of the TBA complexing agent is very similar to the TPA in that it does not seem to alter the oxidised products into electrochemically inactive materials.

On examination of the electrode surface following evidence of electrochemical inhibition from DPS, a yellow coating could be observed, as shown in Figure 5.11. The exact composition of the film was not investigated and assumed to be a polybromide phase complexed by the additive.

Figure 5.11 Yellow coating on Pt electrode surface from TPA

To investigate the physical impact of this surface film, a fresh polished electrode was used for the DPS experiment. The charge against time was plotted for the polished electrode. The experiment was then repeated using the same unpolished electrode and the data obtained is presented in Figure 5.12.

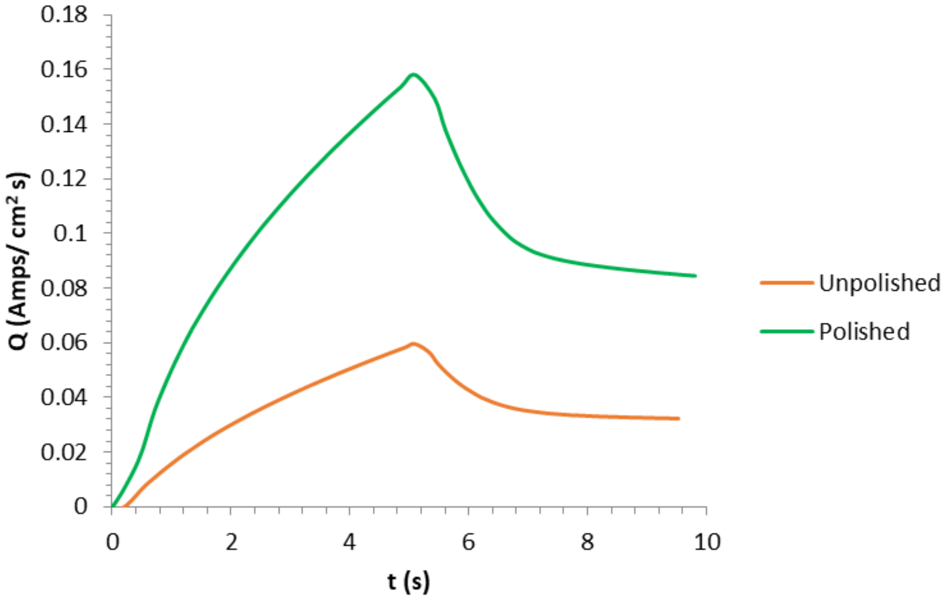

Figure 5.12 Double Potential Scan for 50 mM zinc bromine 0.5 M KCl solution with 50 mM TBA on a unpolished/polished electrode Pt WE, SCE RE, Pt CE

Clearly the physical barrier of the coating was inhibiting the reaction process by preventing direct access of the electroactive reactants to the surface of the electrode. It could well be that, with a flow of the electrolyte past the electrode surface (as would happen in a redox flow battery), these surface species could be removed and so prevented from building up on the electrode surface.

To understand the impact of a flowing solution on the coating, a rotating disk electrode (RDE) was used. A comparison was done on the RDE data obtained at the critical 50 mM concentration of the TBA complexing agent (above which severe inhibition occurs) and at a lower concentration of 10 mM. Cyclic voltammograms were first obtained at these concentrations on a freshly polished Pt electrode, as shown in Figure 5.13. A rotation rate of 20 Hz was employed for the RDE, corresponding to a Reynold’s number of $Re = 350$.

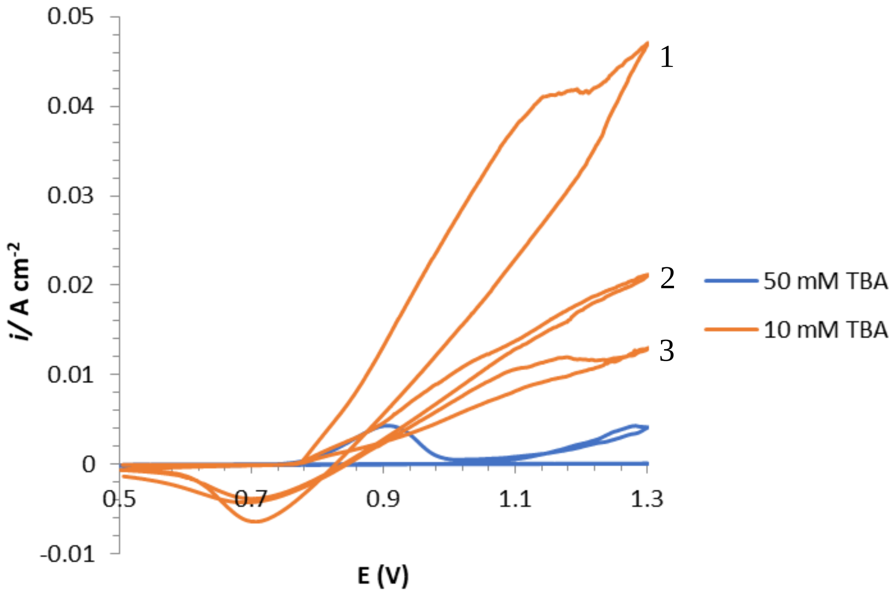

Figure 5.13 CVs of RDE 10 & 50 mM TBA (Scan rate = 10 mV s^{-1}) using 50 mM zinc bromine 0.5 M KCl solution a Pt WE SCE RE, Pt CE. Electrode rotation rate = 20 Hz.

From the data in Figure 5.13, the 50 mM TBA produced a small peak on the first cycle at *E* = 0.9 V with clear evidence of a surface passivation beyond that. No reverse reduction peak was observed. The latter would be expected for a RDE experiment since the electroactive species generated during the oxidation process would have been removed from the vicinity of the electrode surface. However, one would have expected the presence of the complexed bromine in the passivating surface film to have been reduced on the reverse scan. That this was not observed is puzzling. There was a negligible current response for the two subsequent scans. This shows that the TBA at this concentration was completely passivating the electrode surface.

For the 10 mM TBA solution, there was a reduction in the electrochemical oxidation activity with each successive cycle, but the effect was less significant for the reduction process. There was clearly a slow build-up of the surface film even at this low concentration which reduced the redox activity. This effect was not observed in the cyclic voltammograms carried out under stationary conditions (*i.e.* no rotation) and showed the impact of increased mass transport delivering more electroactive components to the electrode surface. For the reduction process however, the complexed bromine present in the surface film underwent reduction which explains why beyond the first cycle, the peak height (and charge under the peak) remained essentially similar.

The effect of solution flow was also investigated using DPS measurements and the impact of whether the electrode had been polished can be seen in Figure 5.14.

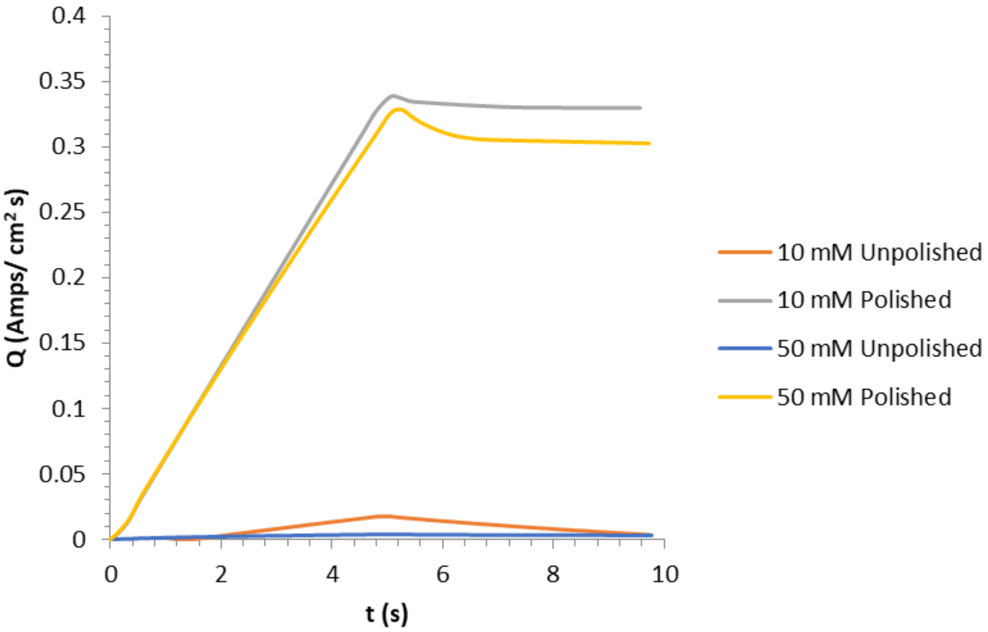

Figure 5.14 DPS of 10 & 50 mM TBA using 50 mM zinc bromine 0.5 M KCl solution a Pt WE polished/unpolished RDE (at 20 Hz), SCE RE, Pt CE

The runs which had the polished electrodes showed much higher charges again with the concentration only showing a slight effect on this. This is consistent with previous data and further backs up the argument that the formation of the film on the electrodes surface causes drastic reduction in the systems efficiency. Furthermore, the data here indicates that for the polished electrodes at both 10 mM and 50 mM TBA concentration, there was no significant reduction of the electrogenerated bromine on the reverse scan, as expected from RDE experiments and observed from the CV data. However, it can be clearly stated that the coating has a strong influence on the electrochemical response as the unpolished surface for both 10 and 50 mM TBA caused strong inhibition to occur.

The data from these additives experiments demonstrate the need of a complexing species that does not affect the electrochemical activity and to ensure that the species does not inhibit this process, which is fundamental to the performance of the zinc-bromine redox flow battery.

5.3 N-Methyl-N-Ethylpyrrolidinium (MEP)

The most commonly used additive for commercial scale zinc-bromine RFBs is *N*-methyl-*N*-ethylpyrrolidinium bromide (MEP). These additives complex with the electrogenerated bromine to form a higher polybromide species (Br_3^-, Br_5^- or Br_7^-) which produces an immiscible, viscous phase as shown in Figure 5.15. This immiscible phase increases the size of the electroactive species which helps prevent the bromine crossover from the positive compartment to the negative compartment of the flow battery, thus averting the self-discharge of the battery.

Figure 5.15 Bromine liquid with MEP added at a 3 Br_2: 1 MEP ratio

The initial tests investigated the impact that MEP had on the electrokinetics in the 50 mM $ZnBr_2$ in 0.5 M KNO_3 electrolyte solution. CV was used to determine the effects that these complexes had on the reversibility of the reaction and also to identify the voltage range to be used for subsequent electrochemical analysis[120]. Figure 5.16 shows the CV in the absence of MEP and with MEP at 25 mM, 100 mM, and 130 mM concentrations. The large increase in peak heights for the MEP compared to the electrolyte with no additives is simply due to the indirect increase of bromide ions introduced to the electrolyte through the additives where the counter ion is bromide. It can be observed that the Br_2 reduction peak in the presence of MEP is higher but also occurs at a more negative potential. The shape of the reduction peak also suggests the presence of a surface-controlled reaction with a rapid loss of active species beyond the current peak. This behaviour is similar to that seen in metal stripping peaks where the reaction is a surface controlled process[121,122]. It also shows that the system was not inhibitive as there was no loss of peak height from subsequent cycles (not shown).

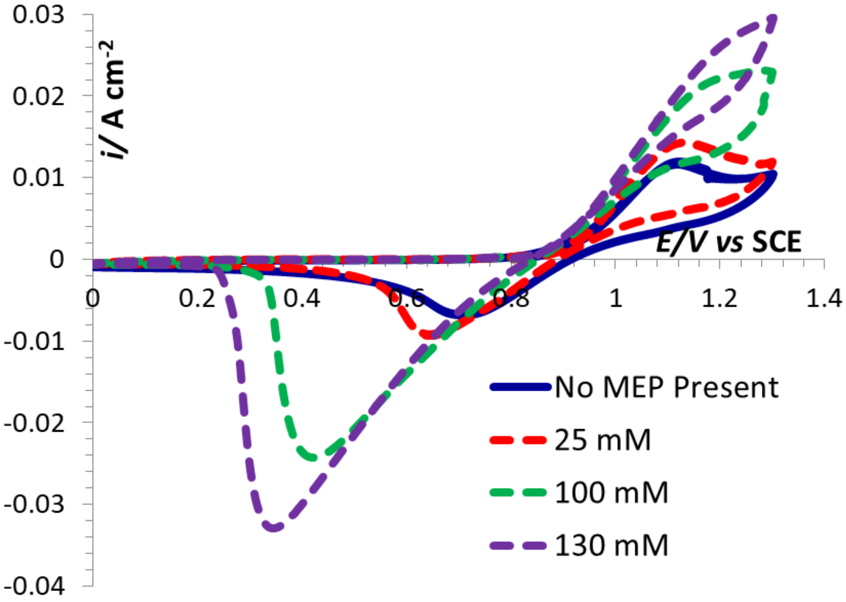

Figure 5.16 CV of 50 mM $ZnBr_2$, 0.5 M KNO_3^- with varying concentrations of MEP with a PPG86 WE, SCE RE, Pt CE. Scan rate 20 mV s^{-1}

To examine in more detail, the electrokinetics of the reaction, EIS was carried out. Figure 5.17 shows a clear difference in the impedance spectra of the solutions with and without MEP, measured at the half-wave potential, $E_{½}$. Clearly, in the presence of MEP, the size of the 'semi-circle' was significantly smaller. This indicated that the resistance associated to the charge transfer was reduced when MEP was present. The fitting of the EIS data was carried out by using the equivalent circuit (inset to Figure 5.17) comprising of a resistance (R_S) in series with a parallel R_{CT} – C_{CPE} – W circuit, corresponding to the uncompensated solution resistance R_S between the RE and WE, the charge transfer resistance R_{CT}, a constant phase element CPE and a Warburg diffusional impedance, W. This data also revealed that the double layer capacitance (obtained from the CPE and R_{CT} values) was almost 5 times larger for MEP than that observed in the solutions with no additives, as shown later in Table 5.3 (Page 87). This is attributed to the presence of the oily immiscible phase on the electrode surface partially displacing the aqueous layer associated with the normal double layer.

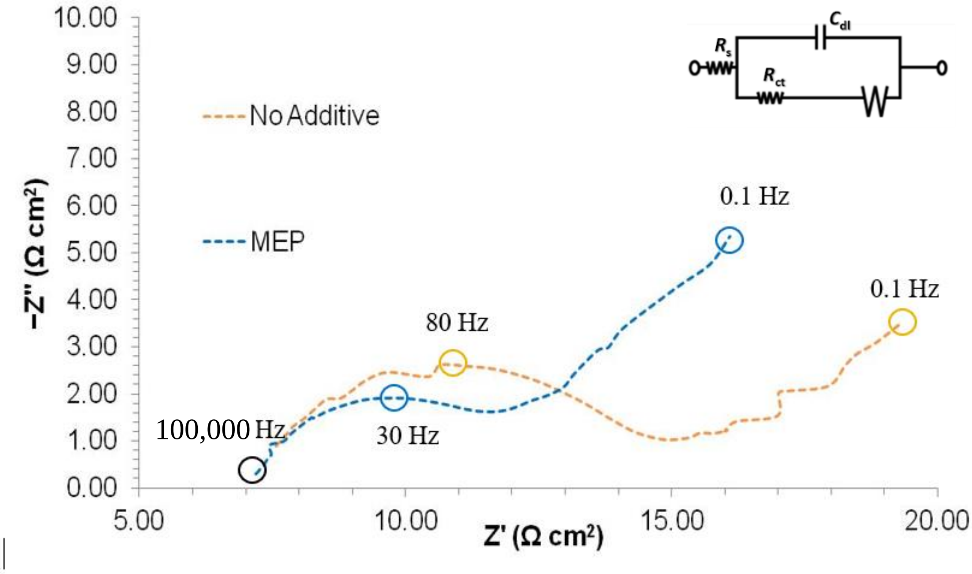

Figure 5.17 50 mM $ZnBr_2$, 0.5 M KCl with no additive and 16.67 mM MEP. EIS scan from 100,000 Hz to 0.1 Hz

Potentiodynamic polarisation (Tafel extrapolation) was also used to get an understanding of the electrokinetics. The data obtained is shown in Figure 5.18. The relatively small shift in the equilibrium potential in the presence of the MEP reflects the fact that the reaction is taking place on effectively a modified electrode surface. The anodic Tafel slope B_a for the bromide oxidation reaction with no additives is close to the ideal value (~60 mV) for a 2-electron transfer with an assumed anodic charge transfer coefficient α_A of 0.5. With the MEP present, this increased slightly to 72 mV but produced an exchange current density, i_o, three times greater (shown in Table 5.3) than the value obtained without the MEP additive. This is in good agreement with the trend observed from the EIS measurements.

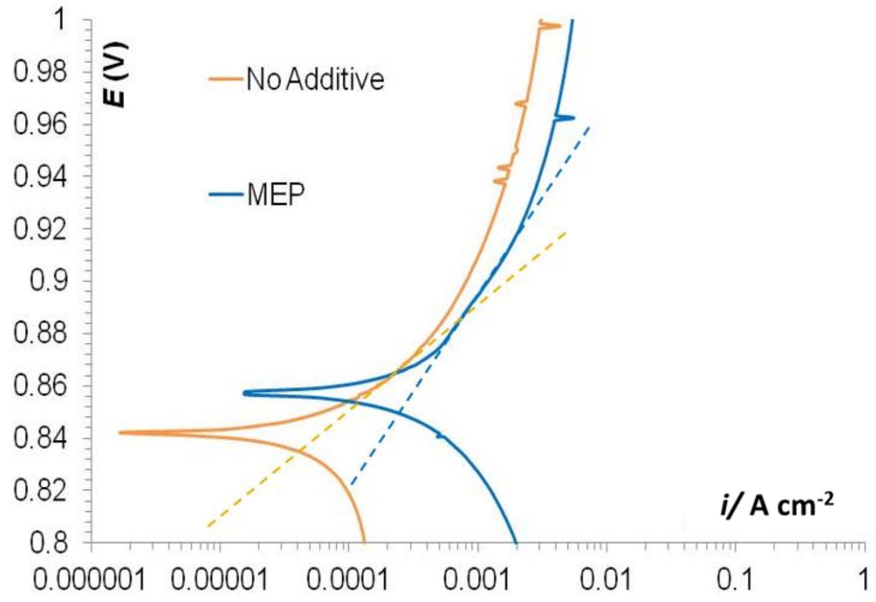

Figure 5.18 50 mM $ZnBr_2$, 0.5 M KCl with no additive and 16.67 mM MEP. Tafel slopes measured with a scan rate 0.1667 mV s^{-1} both using PPG86 WE, SCE RE, Pt CE

The relatively low concentrations required for the refined electrochemical characterisation did not however permit the physical interactions between the $Q^+ Br_x^-$ compounds and the bromine to be determined. To examine this in greater detail, a ratio of 3 moles of bromine liquid to 1 mole of complex (in aqueous solution) was used when carrying out these studies. Immediately, the solution with MEP produced the dense, deep red immiscible phase which had the viscosity of that comparable to oil but left no significant bromine vapour above the aqueous phase. It is worth noting that the aqueous solution without MEP, had the intense orange colour in the solution associated with the Br_2 with vapour above the solution. To verify that the bromine was found in a soluble complex within the aqueous phase (as well as in the small volume of immiscible phase), the vapour, aqueous and immiscible phases were analysed for their bromine content and for their enthalpy of vaporisation which would give a measure of the strength of the bromine interaction formed with the additives.

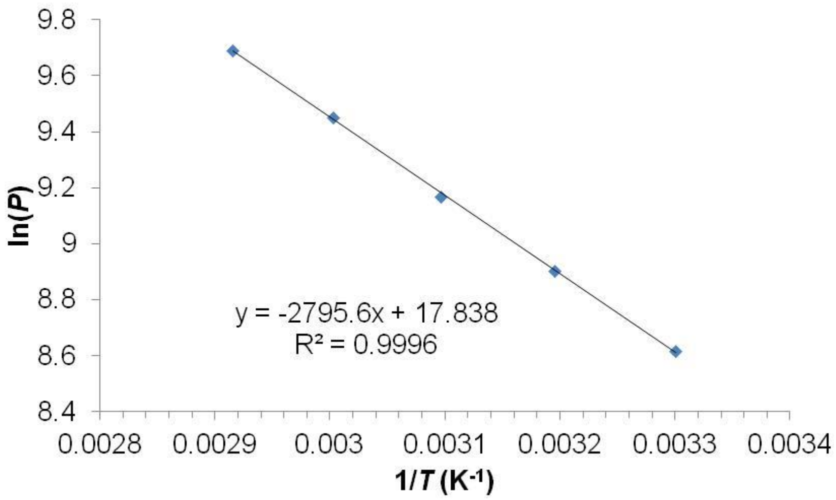

Figure 5.19 Plot of ln Br_2 (vapour pressure) against 1/T

The enthalpy of vaporisation of Br_2 was determined from the Clausius-Clapeyron equation for the vapour formed above the aqueous phase. An example of the plot obtained is shown in Figure 5.19. The enthalpy for the aqueous solution without MEP was found to be $\Delta H = 15.9$ kJ mol^{-1}. However, the enthalpy for the aqueous solution with MEP was $\Delta H = 21.6$ kJ mol^{-1} indicating that more energy was required to produce the Br_2 vapour from the aqueous phase which also contained MEP.

The amount of bromine in the aqueous phase was quantified through iodometric titrations, as discussed in chapter 4. The data from the iodometric titrations also indicated that the remaining Br_2 concentration in the aqueous phase with MEP present was 0.063 ± 0.002 mol dm^{-3} whereas the solution with no MEP contained 0.131 ± 0.002 mol dm^{-3} of bromine. The remainder of the bromine content for the MEP/aqueous mixture was then contained within the immiscible, polybromide phase. Since the immiscible phase could not be determined through the titration (as the time of bromine release is slower and the titrant used would be imprecise), Raman spectroscopy was used to determine the nature and relative amounts of the polybromide species present in that phase. Figure 5.20 shows the Raman spectra acquired from samples with the concentration ratio of 1:1 and 5:1 of Br_2: MEP. Two peaks can clearly be identified at *ca.* 160 cm^{-1} and *ca.* 250 cm^{-1} which correspond to the polybromide species Br_3^- and Br_5^- respectively[109]. As expected, as the bromine content increases, the preferred polybromide species changes from Br_3^- to Br_5^-.

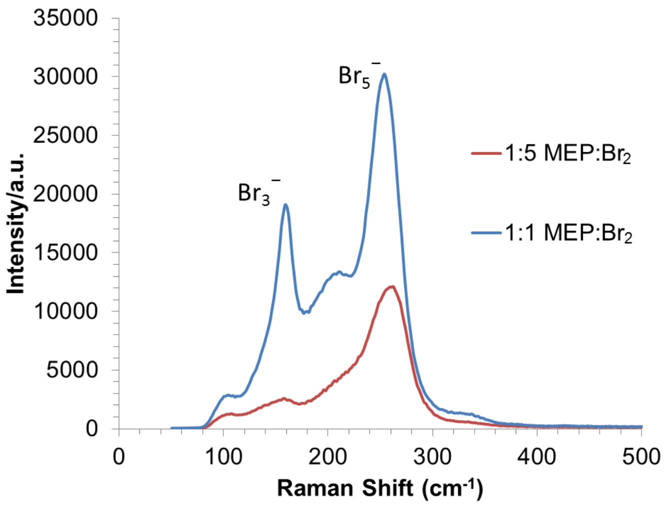

Figure 5.20 Raman spectra of the immiscible phase formed on mixing MEP with Br_2 solution in 1:1 and 1:5 molar ratios

Having established the baseline for comparing the other additives with MEP using the various techniques discussed above, the same sequence of techniques were then used with the novel additives developed during this study. The design of the new additives followed two pathways:

1. Dicationic structures, where there is a bridging ligand between the nitrogen centres of two cyclic structures, creating a natural cage to support the complexation of the bromide species to higher polybromide states and
2. the presence of hydrophilic functional groups which are used on one of the aliphatic ligands attached to common nitrogen-based complexing agents to improve their solubility and so prevent the formation of an immiscible phase.

5.4 Dicationic Structures

The following set of additives were synthesised using the assumption that they were to have the same cyclic structure as other successful complex additives (morpholine) currently used in the zinc-bromine battery system. However, two of these nitrogen centres related to a bridging ligand, with a varying chain length, to create a dicationic structure with a natural cavity to complex polybromides. The structures of these can be found in Figure 5.21. Compounds with pyridine or pyrrolidine as the core of the structure were attempted. However, these either produced an immiscible oil or the target molecule was not achieved during the synthesis.

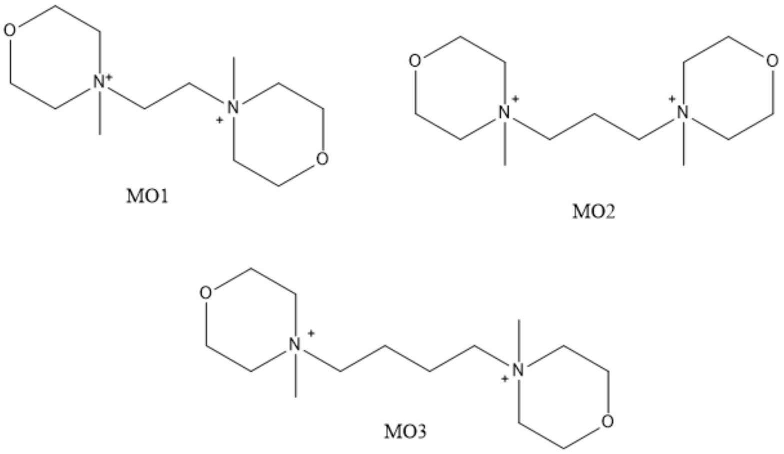

Figure 5.21 Structures of the novel additives using a bridging ligand to form a dicationic structure

Figure 5.22 shows that from the CV, these complex additives gave similar behaviour as to the previous additives of TPA and TBA, albeit with a slightly reduced electrochemical reversibility and peak current response. A surface film was evident on the electrode as well. In addition, the reduction peaks appear to be surface controlled, as with the MEP, indicating the stripping of the film from the electrode surface.

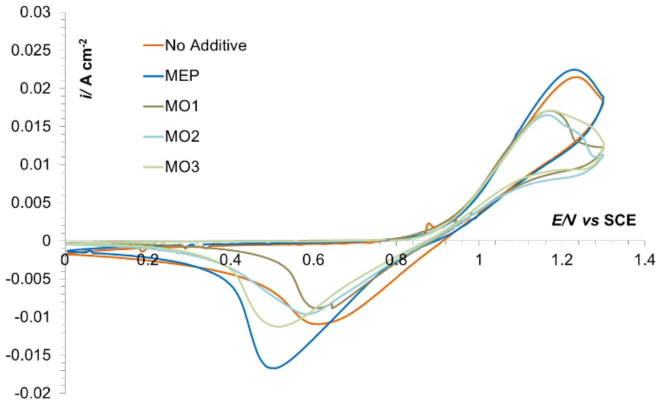

Figure 5.22 CV comparing the electrolyte solution of 50 mM ZnBr2, 0.5 M KNO3 with 16.67 mM of either MEP, MO1, MO2 or MO3. Scan rate of 50 mV s^{-1}. PPG 86 WE, SCE RE, Pt CE

As before, potentiodynamic polarisation and EIS measurements were carried out for the MO1, MO2 and MO3 compounds. The data obtained from the analyses are presented in Table 5.3 which shows that these additives had overall similar responses as to the MEP, but with much poorer exchange current densities. The Tafel slope was slightly larger for the MO1, MO2 and MO3 additives compared to MEP and this could reflect a small change in the energy requirements required for the rate determining step for the bromine formation in the presence of these new additives. The charge transfer resistance for all the new additives appears to have improved when compared to the solution with no additive. The capacitance for MEP is significantly higher than for any of the solution mixtures present and may be key to MEPs success, by creating an electroactive film with high reactant concentration on the electrode surface resulting in the highest i_0.

	Tafel Extrapolation			EIS	
Compound	B_a (mV)	i_0 (mA cm^{-2})	E_0 (mV)	R_{CT} (Ω cm^2)	C_{dl} (µF cm^{-2})
No Additive	62.3	0.108	0.84	7.6	295
MEP	71.6	0.304	0.86	5.4	1069
MO1	85.3	0.086	0.85	6.2	286
MO2	88.1	0.100	0.86	5.4	188
MO3	86.5	0.065	0.86	7.0	166

Table 5.3 Electrochemical analysis of electrolyte solutions with no additive, MEP and MO1-3

However, when this series of compounds were introduced to the saturated Br_2 solution they each formed an insoluble precipitate with various visual characteristics, such as yellow flakes dispersed throughout the solution or as a solid red precipitate at the bottom of the solution. Since these molecules were dicationic, the concentration ratios were lowered to 1:6 and 1:12 of Br_2: $Q^+Br_x^-$ but the results obtained were the same insoluble precipitates. As these molecules did not even form the immiscible phase, they were not considered further as suitable candidates for alternative complex agents for the zinc-bromine battery system.

5.5 Carboxylic Acid Functional Groups

The second line of development for new additives examined whether the solubility of the immiscible phase could be improved by introducing hydrophilic functional groups to the long aliphatic chain. This was pursued with the first series of compounds having the carboxylic acid functional group added. Three molecules were synthesised in this vein: 1-(carboxymethyl) pyridine-1-ium (QBr1), 1-(2-carboxymethyl)-1-methylmorpholin-1-ium (QBr2), and 1-(2-carboxymethyl)-1-methylpyrrolidin-1-ium (QBr3). These structures are shown in Figure 5.23.

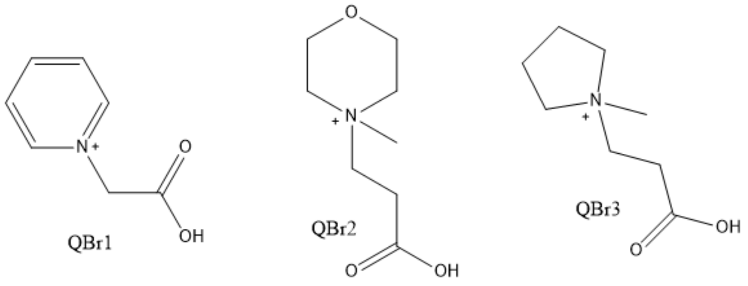

Figure 5.23 Structures of the novel additives using carboxylic acid functional groups

Figure 5.24 shows the cyclic voltammetry in the absence and presence of 16.67 mM MEP and QBr1, QBr2 and QBr3. As noted previously, the slight increase in peak heights for the Q$^+$ Br$_x^-$ compared to the electrolyte with no additives was simply due to the indirect increase of bromide ions introduced to the electrolyte through the additives where the counter ion is bromide. It can be observed that the Br$_2$ reduction peak in the presence of MEP is higher but also occurs at a more negative potential. The latter could simply arise because of a surface film in the case of MEP attenuating the applied potential. The shape of the reduction peak also suggests the presence of a surface-controlled reaction with a rapid loss of active species beyond the current peak.

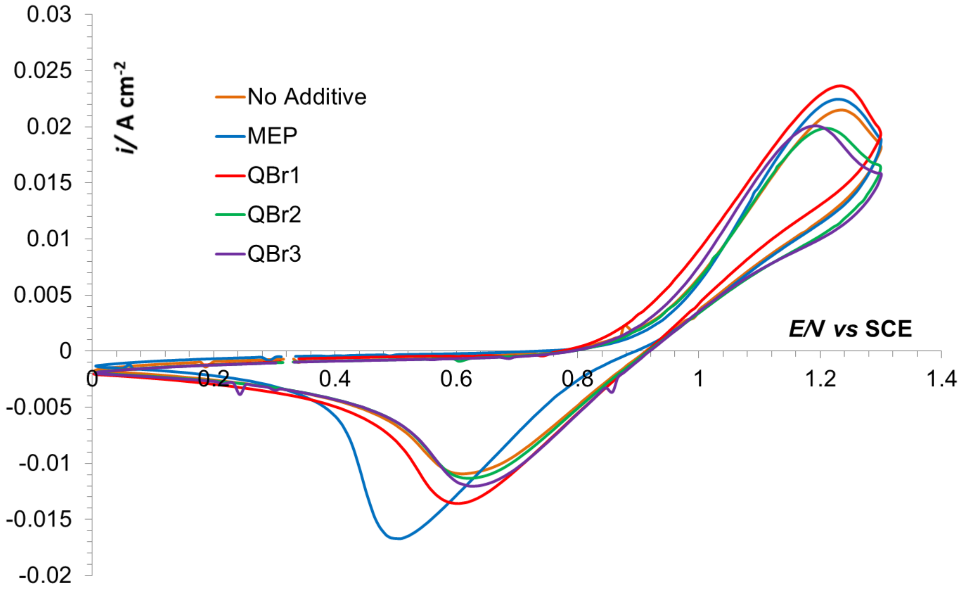

Figure 5.24 CV comparing the electrolyte solution of 50 mM ZnBr2, 0.5 M KNO3 with 16.67 mM of either no additive, MEP, QBr1, QBr2 or QBr3. Scan rate of 50 mV s^{-1}. PPG 86 WE, SCE RE, Pt CE

It was interesting to note that the additives QBr1, QBr2 and QBr3 produced very similar cyclic voltammograms in terms of the size and position of both the oxidation and reduction peaks. However, visual inspection of the glassy carbon electrode after the voltammograms with these additives indicated that a surface coating was evident, despite their reductive peaks maintaining a diffusion-controlled profile. This would indicate then that the Br_2-containing complexes formed with the QBr1, QBr2 and QBr3 additives are indeed mostly found in the aqueous solution and diffuse to the electrode surface to be reduced. The surface film observed on the surface of the electrode then acts as a chemically modified electrode and does not impact on the electrode kinetics of the Br^- / Br_2 and so, the complexes perform their designed function of capturing the electrogenerated bromine.

	Tafel Extrapolation			EIS	
Compound	B_a (mV)	i_0 (mA cm^{-2})	E_0 (mV)	R_{CT} (Ω cm^2)	C_{dl} (μF cm^{-2})
No QBr	62.3	0.108	0.84	7.6	295
MEP	71.6	0.304	0.115	5.4	1069
QBr1	54.3	0.115	0.84	6.3	401
QBr2	50.1	0.092	0.84	8.3	296
QBr3	50.2	0.101	0.84	8.5	321

Table 5.4 Electrochemical data from analysis of electrolyte solutions (50 mM $ZnBr_2$, 0.5 M KNO_3, 16.67 mM of $Q^+Br_x^-$) with no additive, MEP and Compounds QBr1, QBr2 and QBr3.

The trend in the R_{CT} values in Table 5.4 is consistent with the above discussions. The ready availability of the Br_x^- species in the case of MEP would mean that the electron transfer step could occur more readily (lower R_{CT}). In the case of the QBr1, QBr2 and QBr3 additives, since the complexes formed are much more soluble, the surface concentration of available Br_x^- would be lower which would impact then on the R_{CT} values. Indeed, for QBr2 and QBr3 complexes, the R_{CT} values are larger than for the aqueous solution with no additive, suggesting that there is a slight inhibition of the electron transfer step with these compounds. The results from the potentiodynamic measurements (Tafel extrapolation) shown in Table 5.4 indicates that MEP has over double the exchange current density value compared to the other additives or with no additive. It is worth noting that a similar trend in the electrokinetics was obtained. As noted above, the anodic Tafel slope B_a for the bromide oxidation reaction with no additives is close to the ideal value (~60 mV) for a 2-electron transfer with an anodic charge transfer coefficient α_A of 0.5. With the MEP present, this increases slightly to

72 mV but decreases to <55 mV in the presence of the QBr1, QBr2 and QBr3 compounds. This would suggest small changes in the value of α_A, reflecting the impact that complexation has on the product of the oxidation reaction.

	Δ*H* of Vaporisation		Aqueous Br_2 concentration (mol dm^{-3})
Compound	Oil Phase (kJ mol^{-1})	Aqueous Phase (kJ mol^{-1})	
No QBr	N/A	15.9	0.131
MEP	37.8	21.6	0.061
QBr1	27.8	19.1	0.065
QBr2	33.2	23.2	0.065
QBr3	N/A	29.7	0.062

Table 5.5 Data showing enthalpy of vaporisation for Br_2 from the various phases formed with MEP and complexed compounds and the concentration of Br_2 remaining in the aqueous phase of the solution.

With the QBr1, QBr2 and QBr3 mixtures however, it was observed that the volume of immiscible liquid formed was significantly reduced, in accordance with the original expectations of the work. Again here, Br_2 vapour above the aqueous phase was insignificant. To verify that the bromine was tied into a soluble complex within these aqueous phases (as well as in the small volume of immiscible phase), these phases were analysed for their bromine content and for their enthalpy of vaporisation so that they could be directly compared to MEP. Table 5.5 summarises the enthalpies of vaporisation and the Br_2 content remaining in the aqueous phase for each of the Q^+ Br_x^- compounds after equilibration with aqueous bromine solution. The enthalpy of vaporisation for Br_2 from the immiscible phase was determined as 37.8 kJ mol^{-1}. For the QBr1, QBr2 and QBr3 compounds, the enthalpy of bromine vaporisation from the solution mixture containing QBr1 was slightly lower than that of MEP but for QBr2 and QBr3, the values were higher and significantly so for the latter. As the data from the iodometric titrations also indicated that the remaining Br_2 concentration in the aqueous phase were very similar (0.063 ± 0.002 mol dm^{-3}) for all the additives, the increased enthalpy of vaporisation measured for QBr2 and QBr3, with respect to that for MEP, is very encouraging.

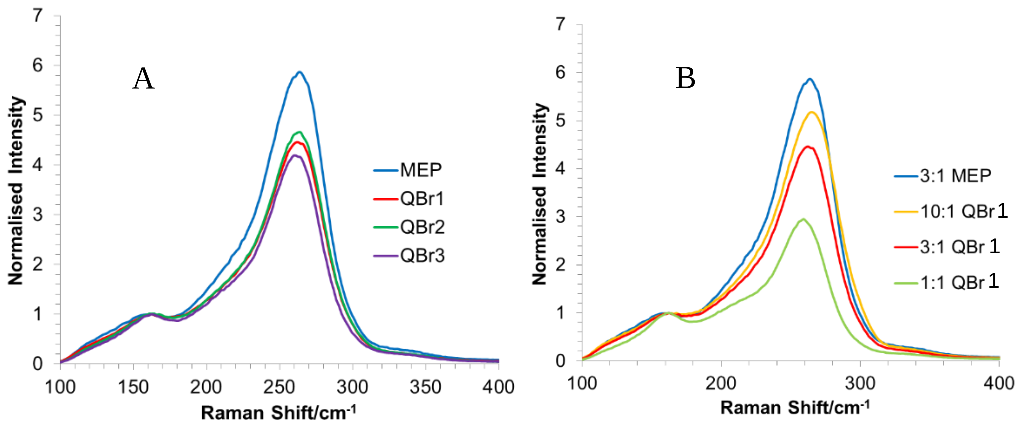

Figure 5.25 Raman spectra normalised to the Br_3^- signals, (A) comparing the Br_5^- signal from the immiscible phases formed with MEP, QBr1, QBr2 and QBr3 in the 3:1 Br_2: $Q^+ Br_x^-$ ratio and (B) comparing the impact of different concentration ratios for QBr1 with that of 3:1 MEP.

To compare the effectiveness of the novel QBr1, QBr2 and QBr3 additives with MEP, the Br_3^- peak was normalised to allow the proportion of the higher polybromide state of Br_5^- to be highlighted. Figure 5.25 (a) shows that for the same concentration ratios MEP still proves to be superior in forming the Br_5^- state. In fact, Figure 5.25 (b) shows that despite varying the concentration of the complex additive from a 1:1 ratio to a 10:1 ratio, MEP still enables the formation of the Br_5^- complex to a greater degree.

5.6 Sulphonate Functional Group and Phosphonium Centre

Like the previous group of additives, this series of additives sought to increase the solubility of the compound by replacing the carboxylic acid functional group with the more soluble sulphonate functional group. In addition, a phosphonium based additive was also used to investigate similar structures with different centres, as seen in Figure 5.26. The phosphonium, having a positively charged centre, is also very soluble (40 g/ L).

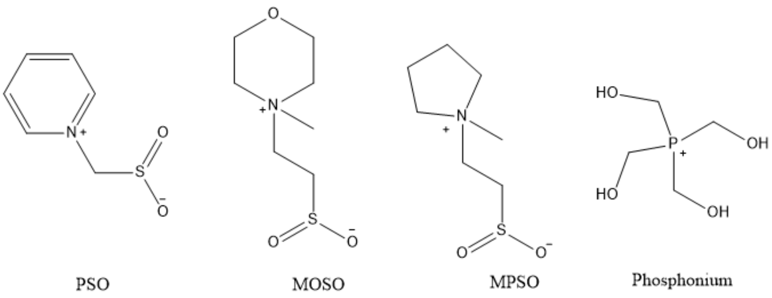

Figure 5.26 Structures of additives with sulphonate functional groups and of the phosphonium additive

Much like QBr1, QBr2 and QBr3, these additives produced very similar cyclic voltammograms in terms of the shape and position of both the oxidation and reduction peaks (Figure 5.27). However, it can be noted that the oxidation and reduction peaks are slightly lower than MEP. Unlike the previous additives, the reduction peak shape shows a gradual build up to the peak with a rapid decline afterward, typically associated to being a surface-controlled reaction: as a diffusion controlled peak would show a symmetry in that the gradual gradient change would occur on both sides of the peaks. This would indicate that the Br_2-containing complexes formed are found at the electrode surface, much like the behaviour of MEP. However, visual observations during the CV showed no film formation for any of the new additives.

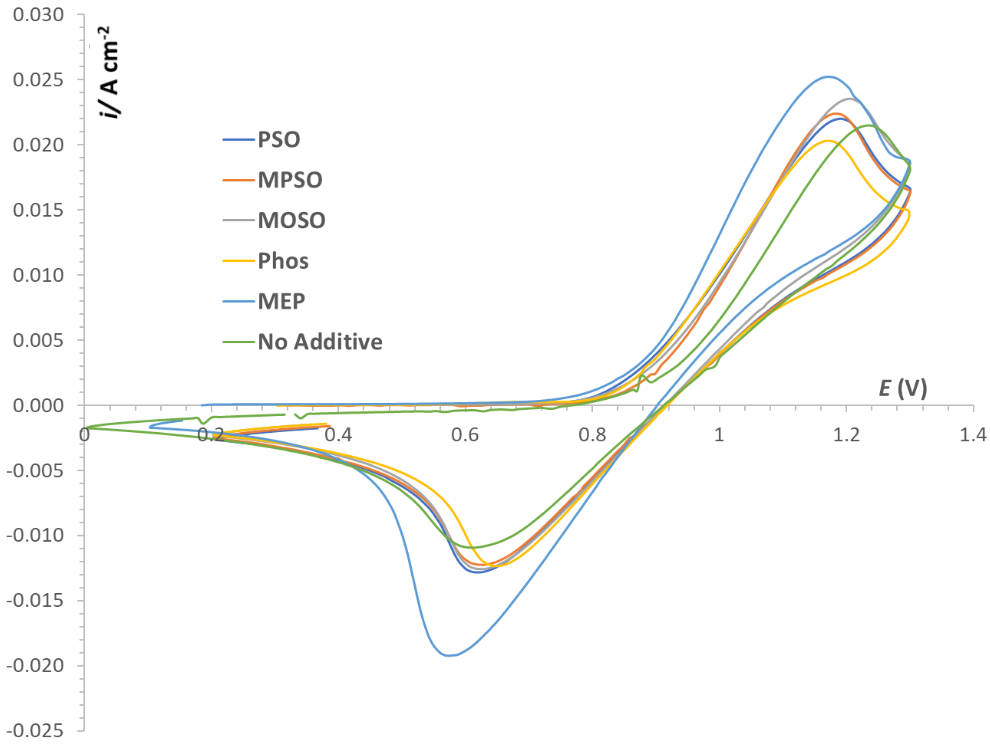

Figure 5.27 CV comparing the electrolyte solution of 50 mM ZnBr2, 0.5 M KNO3 with 16.67 mM of either MEP, MO1, MO2 or MO3. Scan rate of 50 mV s^{-1}. PPG 86 WE, SCE RE, Pt CE

The trend in the R_{CT} values in Table 5.6 shows an overall drop in the charge transfer resistance. However, the lower capacitance values could indicate that the surface film is formed, though unlike MEP is resistive as opposed to improving the overall electrochemical kinetics. The Tafel data mostly correlates with the EIS data except for PSO: where the current density is slightly higher than that of the electrolyte system with no additive. The phosphonium based additive shows the worse kinetics of the additives tested in this table. This may be that the materials do not complex as well as the nitrogen centred complexes or that the phosphonium centre being large than the nitrogen centre makes it harder for the electroactive species to reach the electrode surface.

	Tafel Extrapolation			EIS	
Compound	B_a (mV)	i_0 (mA cm^{-2})	E_0 (mV)	R_{CT} (Ω cm^2)	C_{dl} (μF cm^{-2})
No QBr	62.3	0.108	0.84	7.6	295
MEP	71.6	0.304	0.115	5.4	1069
PSO	64.5	0.117	0.84	11.1	259
MPSO	60.5	0.086	0.84	10.8	234
MOSO	63.7	0.092	0.83	9.1	270
Phosphonium	49.6	0.049	0.83	13.6	181

Table 5.6 Electrochemical data from analysis of electrolyte solutions (50 mM $ZnBr_2$, 0.5 M KNO_3, 16.67 mM of $Q^+Br_x^-$) with no additive, MEP and Compounds PSO, MPSO, MOSO and Phosphonium

Despite the poor electrokinetic performances of these additives, they successfully produce no immiscible phases when introduced to the concentrated bromine solution. Table 5.7 shows the enthalpy of vaporisation and the concentration of the Br_2 in the aqueous solution. It is worth noting, that the values for No QBr and MEP differ to the previous results. As bromine liquid is an extremely volatile and dense liquid, the exact masses are difficult to achieve with significant error being present in the measuring of the liquid and the lost vapour when being made into a solution. To counter this, the solutions for No QBr and MEP are measured at the same time as the additives in the given study. The aqueous bromine solution is taken from a stock solution to ensure a uniform concentration across all measured samples. The behaviour of MEP and No QBr match the previous behaviour, with the enthalpy being greater for the MEP while the aqueous Br_2 concentration was roughly half of the concentration found in the No QBr sample. The immiscible phase recreated a similar enthalpy to the previous values showing a consistency in the materials characteristics.

Compound	ΔH of Vaporisation Oil Phase (kJ mol^{-1})	ΔH of Vaporisation Aqueous Phase (kJ mol^{-1})	Aqueous Br_2 concentration (mol dm^{-3})
No QBr	N/A	25.5	0.022
MEP	38.2	35.1	0.013
PSO	N/A	27.9	0.076
MPSO	N/A	21.8	0.045
MOSO	N/A	44.7	0.026
Phosphonium	N/A	23.6	0.059

Table 5.7 Data showing enthalpy of vaporisation for Br_2 from the various phases formed with MEP and complexed compounds and the concentration of Br_2 remaining in the aqueous phase of the solution

However, the additives yielded a varied response in terms of the acquired enthalpy of vaporisations. PSO and MOSO produced higher enthalpies, with the latter additive being higher than MEP also. Whereas, MPSO and Phosphonium based additive achieved an enthalpy slightly less than the solution with no additive. This varied response will be indicative to how effectively the additives complexes the bromine.

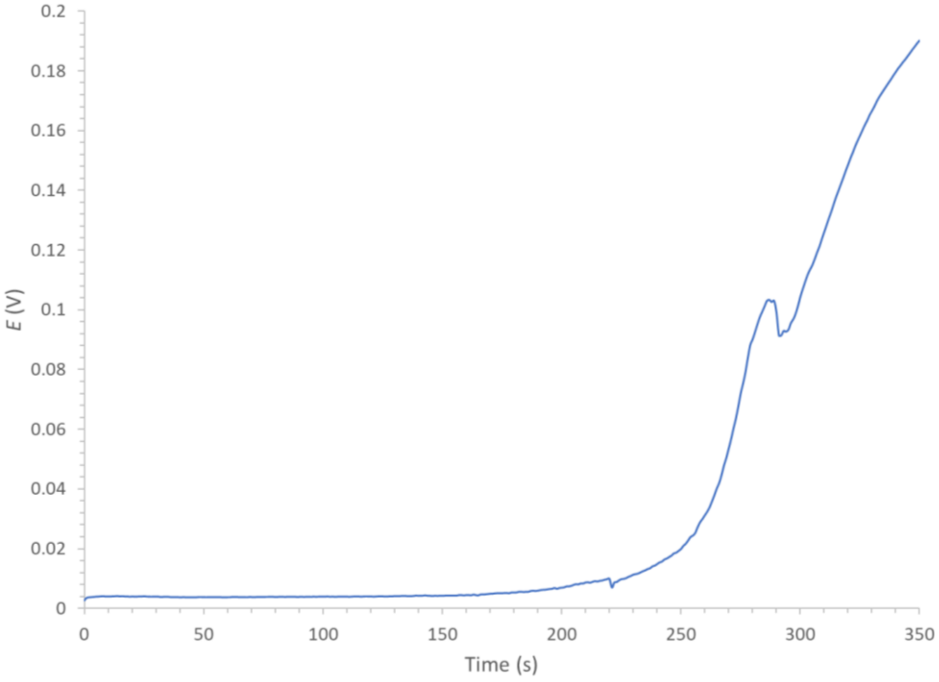

Figure 5.28 Electroanalytical titration of aqueous bromine phase using QBr2 as an additive

From the qualitative chemical analysis, the additives show concentrations greater than the concentration of the solution with no additive present (Figure 5.28). As the concentration of the solution could not have increased. It could potentially be that the additive that remains in the aqueous phase complexes the bromine and results in a time lag from the slower reaction kinetics. This is supported from the nature of an electroanalytical curve where the current increasing indicates the iodine from the reaction has been reduced to iodide for the QBr2 additive. However, after the first peak formed the potential continued to rise indicating a different mechanism was occurring. This mechanism could be the time-lag from any QBr2 that remains in the aqueous phase complexing a small portion of the remaining Br_2 concentration. This run was not one of the titrations ran used to determine the data, as the flow rate at the end was accidentally increased, though proves useful in the creation of the hypothesis of the potential interactions taking place between the additives and Br_2.

5.7 Conclusions

Initial studies found that the aliphatic produced a surface film, and the electrode became passivated causing the current to drop significantly. The CV showed, for the platinum, a typical response to film formation whereas the carbon polymer composites and glassy carbon showed the current dropping consistently after each run. Higher concentrations of the complexing agent saw the cell current reducing to negligible values. A new series of QBr compounds, with the objective to reduce the immiscible liquid phase were successfully synthesised. This was evident from both visual inspections and the effect that QBr had on the physical properties. MEP still proves to be the better additive in terms of electrochemical kinetics.

The dicationic structures however were unsuccessful as these resulted in a solid precipitate when complexing high concentrations of bromine. These additives making use of the carboxylic acid functional groups provided a partial success by reducing the volume of immiscible phase achieved. This led to the development of other additives making use of the sulphonate functional groups and an additive with a phosphonium centre as opposed to an ammonium centre. The initial results showed no immiscible phase was formed but gave good indications that complexation still occurred. These additives yielded poorer electrokinetics and very varied ability in reducing the vapour formed when compared to a bromine solution with no additive.

Despite poorer electrokinetics, these additives exhibited promising physical characteristics. A hypothesis was drawn that these additives were causing a time-lag where the incidental complexation taking place within the aqueous phase was reducing the release of the bromine during the titration, thus, taking longer to convert the iodine to iodide resulting in a false value with the titration method in use. This would require further work to be verified.

6. Electrodes

6.1 Introduction

Electrode materials are one of the key parts of an RFB that can be altered or designed to improve the performance of the battery. In the $ZnBr_2$ RFB, carbon composites are most commonly utilised for their good electrokinetics for the reactions concerned and for their lower cost. These carbon electrodes can come in a variety of structures (*e.g.* felts, plates) and utilise different polymer binders for the carbon in forming the composites or applied as coatings.

This chapter investigates these various electrode materials and their applicability to the $ZnBr_2$ RFB. Initial tests are conducted in an H-cell, to demonstrate whether this technique could establish the most promising electrode materials for further development as well as allowing for comparison between the various carbon composites, activated carbon layers, and carbon composite plate electrodes. The H-cell studies were also used to track the bromine formation as a degree of the state of charge. The latter part of this chapter then employs these electrodes in a flow cell and examines their performance in this RFB environment.

6.2 H-Cell

Using the H-cell set-up described in page 39, two carbon composite electrode types (BMA 5 as the positive electrode and BPP4 as the negative electrode) were used in the cell with the surface area being controlled with PTFE tape exposing a known surface area. The optimal surface areas for the electrodes were found to be 1 cm^2 for the negative electrode and 4 cm^2 for the positive electrode as preliminary studies had revealed that using a 1:1 ratio in electrode areas did not produce enough bromine. However, the preliminary measurements showed that the coulombic efficiency decreased significantly as the current density used in the galvanic cycles carried out in the H-cell increased. This limited the current set-up to using a maximum current density of 10-20 mA cm^{-2}. Various combinations of the carbon composites (BMA 5 and BPP4, PPG86 and PVE) were used to examine if this performance was limited to the nature of the carbon composite itself. As Table 6.1 indicates, very low coulombic efficiencies were obtained beyond a current density of 5 mA cm^{-2} for the different combinations tried, indicating that this was therefore not due to the composite electrodes employed. The low coulombic efficiencies achieved was due to the dispersion, into the volume of electrolyte, of the complex phase containing the bromine formed during charging. At the relatively low SoCs used here (5-10%), there was insufficient material in the electrolyte and near the positive electrode for the discharge reaction to be sustained and the voltage limit set for the discharge was very quickly reached. The voltage efficiency decreased with increasing current density, as expected, due to higher overpotential and ohmic losses.

Carbon Composites	**BMA 5 (+) - BPP4 (−)**		**PPG86 (+) – PVE (−)**	
Current density (mA cm^{-2})	**Coulombic Efficiency**	**Voltage Efficiency**	**Coulombic Efficiency**	**Voltage Efficiency**
5	76%	22%	84%	39%
10	5%	13%	6%	22%
20	0%	0%	2%	16%

Table 6.1 various carbon composite combinations in the H-cell show that current density region is limited to 20 mA cm^{-2} due to higher current densities exceeding the lower voltage limit immediately upon discharge

In contrast to the planar carbon composite plates, carbon felt offers a greater surface area per cubic volume. However, potential issues with the carbon felts were that it would affect the flow of electrolyte through the positive compartment in a flow cell and could experience, as a result, shorter life cycles due to the electrolyte flow creating "channels" (which are passages created from flow erosion or path of least resistance for the electrolyte) within the felt matrix. The carbon felt therefore replaced the positive electrode in the H-cell with the PPG86 composite remaining as the negative electrode. Three felts (GFA 3, GFD 3 and GFD 4.6) were tested in the H-cell and using galvanic cycles and the coulombic and voltage efficiencies obtained are given in Table 6.2. It is evident that high coulombic efficiencies were obtained over the current density range (5 mA cm^{-2} to 40 mA cm^{-2}) employed. The key difference here in the use of the felt is the larger surface area available for bromine generation. Although for a given current density (based on the negative electrode area) the amount of bromine generation will be the same as that at a planar carbon composite surface, the bromine generated in the felt (forming the complex oily phase) was retained within it rather than being dispersed in the volume of the electrolyte. There was therefore a high local concentration of the bromine species within the felt which accounts for the high coulombic efficiencies found for all the felts examined.

Figure 6.1 compares the galvanic cycles obtained with the felts and with the carbon composite plates and shows that the voltage plateau during discharge is for longer compared to the smooth carbon composites. This is a direct effect of the limiting factor in the discharge changing from the bromine concentration to the plated zinc as before, once the limiting reactant was depleted (in the case of the felt, the amount of deposited zinc) the cell voltage dropped rapidly. In the case of where the positive electrode was a carbon composite plate, the limiting reactant there was the electrogenerated bromine.

Carbon Felt	**GFD 4.6**			**GFD 3**			**GFA 3**		
Current density (mA cm^{-2})	**CE**	**VE**	**EE**	**CE**	**VE**	**EE**	**CE**	**VE**	**EE**
5	85%	81%	69%	84%	84%	71%	68%	82%	56%
10	92%	65%	60%	88%	71%	62%	75%	69%	52%
20	92%	52%	48%	84%	35%	29%	92%	37%	34%
30	89%	31%	28%	89%	32%	28%	89%	25%	22%
40	88%	21%	18%	84%	20%	17%	83%	15%	12%
50	95%	4%	4%	88%	9%	8%	90%	5%	5%

Table 6.2 Coulombic and voltage efficiencies of the three felts across the measured current density range. Data were collected using 2.25 M $ZnBr_2$, 0.5 M $ZnCl_2$ and 0.8 M MEP with a 1 cm^3 exposed PPG86 CE

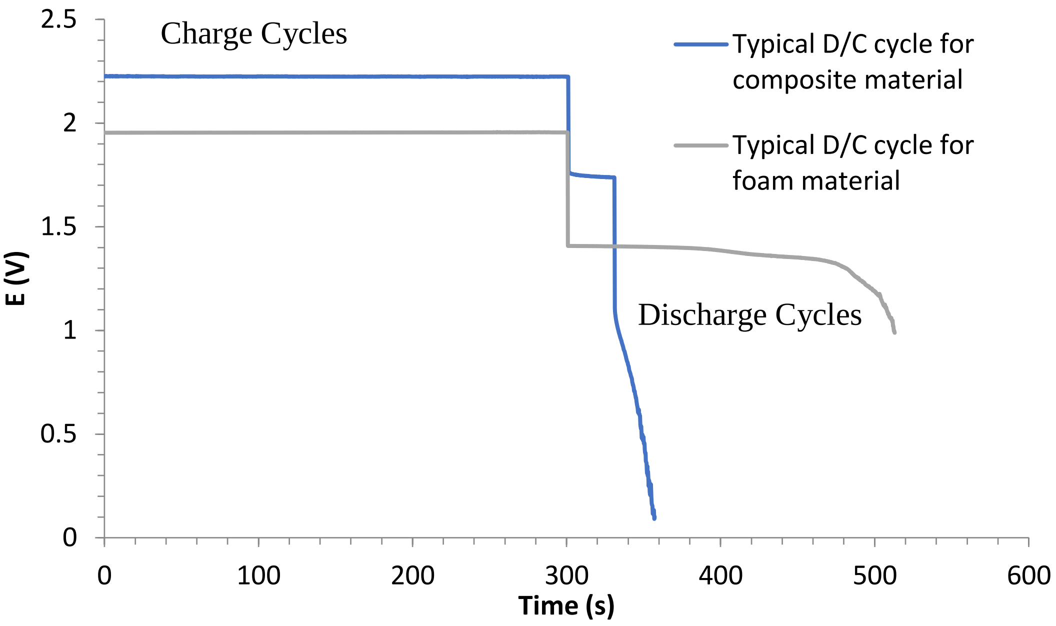

Figure 6.1 Comparison of one galvanic cycle from smooth carbon composite electrode (blue) and the carbon felt electrode (grey). The charge cycle in this instance lasts 300 s, at 10 mA cm^{-2}.

A consequence of the increased electrochemical surface area of the felts, as detailed in Table 6.3, is that the local current density would be much lower than that stated for the nominal charge/discharge current density and so the reaction could be sustained for much longer by the felts since the depletion of the reaction species would occur at a much lower rate.

Felt	GFD 4.6[123]	GFD 3[123]	GFA 3[124]
Surface area (m^2 g^{-1})	0.40 - 0.45	0.40 - 0.45	0.60 – 1.00
Mass of felt (g)	2.30	0.79	0.92
Surface area in electrolyte (cm^2)	650	220	390

Table 6.3 SGL Carbon product specifications on felt and the resultant surface area submerged in the electrolyte solution

Further evidence of the felt retaining the electrogenerated bromine was obtained through carrying out iodometric titration to determine the amount of bromine in the aqueous phase. As Figure 6.2 shows, the SOC (measured iodometrically) increased in a linear manner in the cell with the amount of charge consumed during the charging stage. Initially, there was good correspondence between the measured and theoretical Br_2 generation (based on charge consumed) up to 2.5% SOC. If any Br_2 lost as vapour was negligible (as there was clear vapour-free area above solution), then any difference in the concentration determined through iodometry would be due to the Br_2 complexing to form the polybromide phases using the selected standard additive, MEP (due to its use in current commercial zinc bromine RFBs).

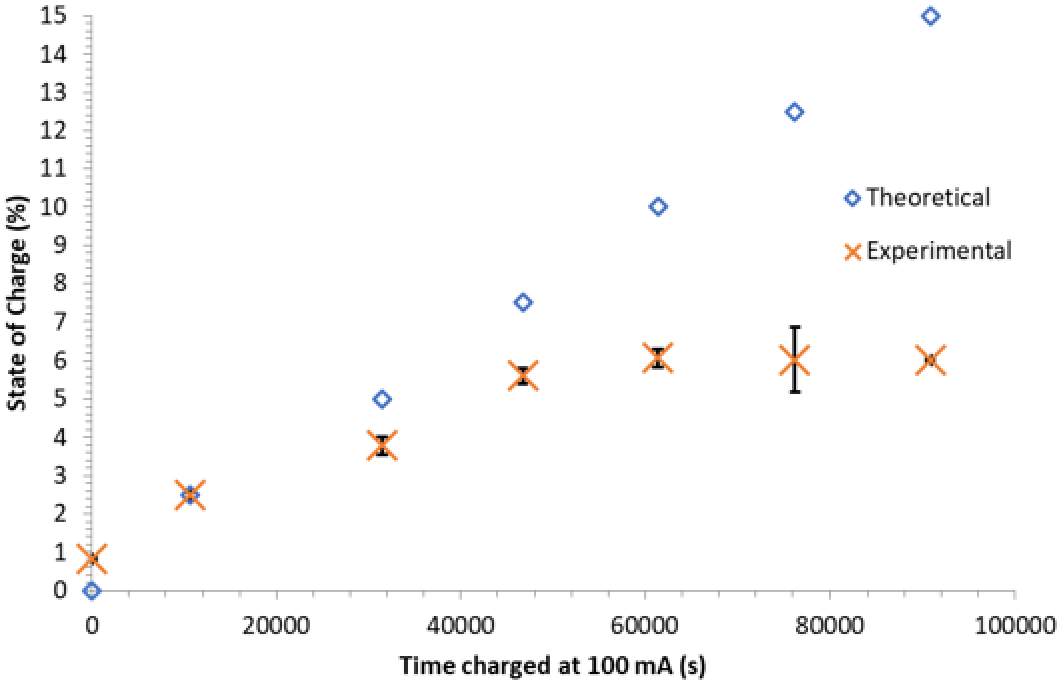

Figure 6.2 Comparison of Br_2 generation assuming 100% current efficiency and iodometrically measured values for Br_2 (aq) at different SOCs. Error bars represent maximum and minimum titrations from each point that the average was taken.

However, between SOC of 2.5% – 5%, the experimental value diverted from the theoretical value. Visual observations of the H-cell at that point showed no complex bromine with MEP. However, after gentle pressure was applied to the felt, the oily phase came out and it was evident that the complex phase was contained within it. The oily phase only appeared in the volume of the positive electrolyte after a substantial amount of the complex QBr_x phase had formed, causing the excess to fall out of the felt to the aqueous solution. As Figure 6.2 indicates, beyond the 5% SOC, the concentration of bromine in the aqueous phase plateaus at *ca.* 0.14 M which is the equivalent of 6% SOC. Thus, the bulk of the Br_2 beyond this SOC was to be found in the QBr_x complex phase.

Further studies using galvanic cycles to determine the voltage efficiency the H-cell used a SOC of 30% and 60%. At this SOC, the complex agent has formed an oily phase which was visible in the bulk positive electrolyte.

Felt	**GFD 4.6/ BMA 5**		**GFD 4.6/ BPP4**		**GFD 4.6/ PPG86**		**GFD 4.6/ PVE**	
Current density (mA cm^{-2})	**Voltage Efficiency**							
	SOC 30%	**SOC 60%**	**SOC 30%**	**SOC 60%**	**SOC 30%**	**SOC 60%**	**SOC 30%**	**SOC 60%**
5	72%	78%	81%	83%	74%	78%	80%	80%
10	52%	56%	69%	70%	55%	59%	56%	67%
20	32%	33%	44%	44%	32%	38%	31%	44%
30	13%	19%	23%	28%	16%	22%	13%	22%
40	3%	7%	8%	15%	N/A	11%	N/A	15%

Table 6.4 Voltage efficiency of the felt material GFD 4.6 coupled with different carbon composites at 30% and 60% SOC, CE = 100% for all experiments with a charge period 1800s

To examine if the SOC affected the VE of the battery, the electrolyte solution was charged to 30% and 60% SOCs. Galvanic cycling was carried out using various current densities for 30-minute charge/ discharge periods. Clearly here, the coulombic efficiency would be 100% for these for these cycles. To evaluate the CE, a deep discharge (where the battery is set to discharge to a SOC of 0%) would need to be measured which was not within the scope of the experiment at this stage. The data obtained are shown in Table 6.4. The VE was always higher for galvanic cycles carried out at 60% SoC which would suggest better discharge kinetics (lower overpotential) here than at 30% SoC. This is due to the increased Br_2 availability at the electrode, as the complexed polybromide species formed with MEP becomes more dense (or reaching a higher polybromide phase) with Br_3^- complexing further to form Br_5^- or Br_7^- as the SOC increases. However, on comparing the VE data in Table 6.2 with that of Table 6.4, it can be noted that the voltage efficiency had decreased in the presence of the QBr_x complex phase. This could be simply because the presence of the oily phase would have displaced, within the felt matrix, much of the aqueous phase with higher electrolyte conductivity resulting in an increased overall resistance of the felt. Although felts are not currently used in $ZnBr_2$ flow batteries, these felts offer an advantage in flow cells by sustaining stable efficiencies at higher current densities and providing better energy efficiencies at lower *j* over several galvanic cycles as seen in Figure 6.3.

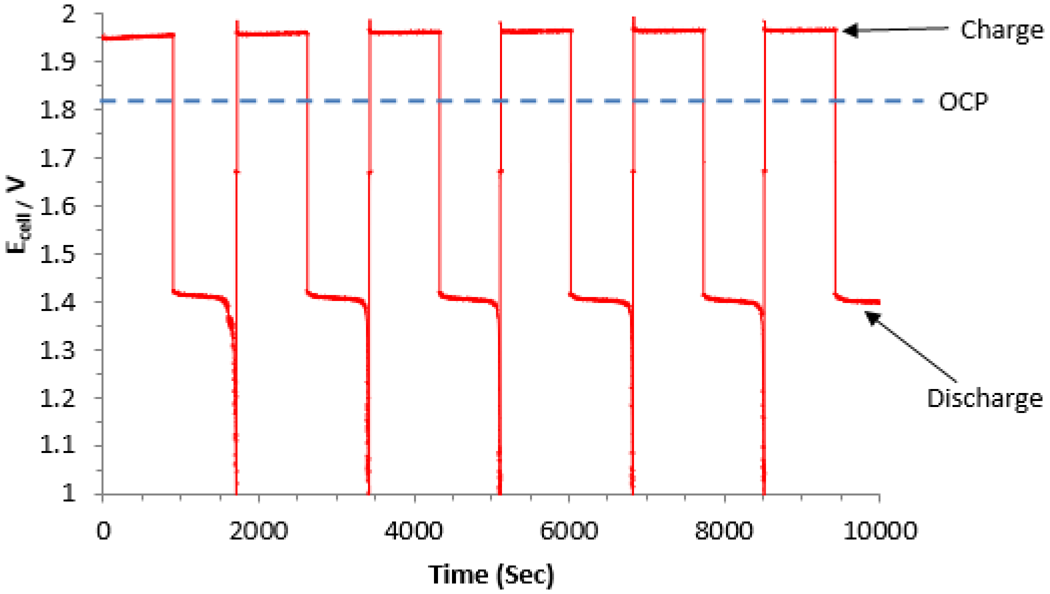

Figure 6.3 Galvanic cycles of 2.25 M $ZnBr_2$, 0.5 M $ZnCl_2$, 0.8 M MEP solution with a felt carbon anodic electrode (GFD 3) and a carbon composite cathodic electrode (PVE). This solution was at a 30 % state of charge and the charge/ discharge cycles lasted 1800 seconds each at 10 mA cm^{-2}

An alternative to the use of the carbon felt and carbon composite electrodes was also tried in the H-cell studies. Here a carbon paste was applied on top of the smooth carbon composite (PVE) to produce a surface coating (the exact materials used in the making of this carbon-based coating were not shared as they were Lotte Chemicals intellectual property). Electrochemical characterisation techniques were used to compare the performance of these coatings with those of the carbon composite. Initially, a cyclic voltammogram was measured on each to show the regions of oxidation and reduction reactions, as shown in Figure 6.4.

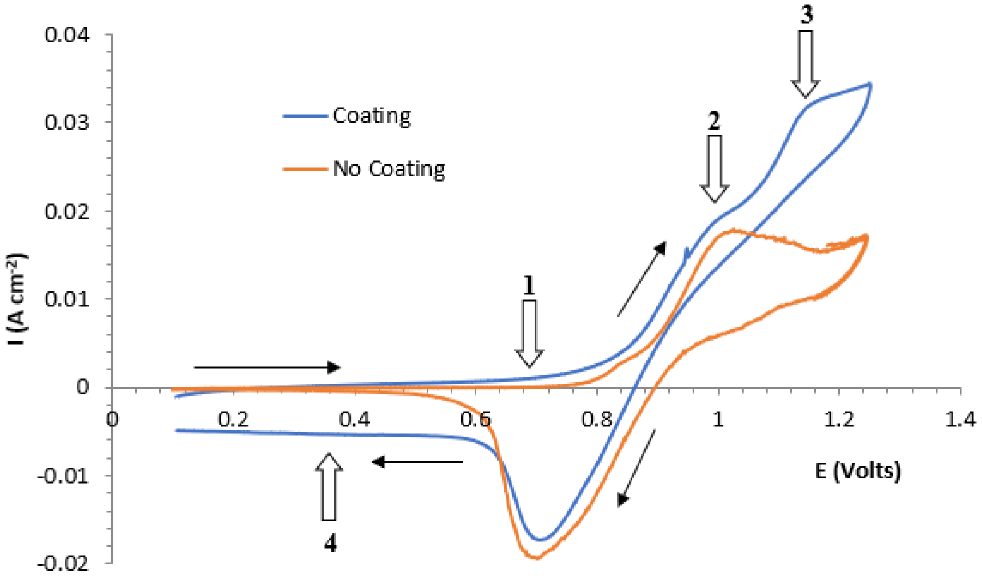

Figure 6.4 Cyclic voltammogram of both smooth carbon composite electrode (orange) and the carbon coating electrode (blue) in a 3-cell electrode with a Pt mesh CE and a SCE RE. An electrolyte solution of 50 mM $ZnBr_2$, 0.5 M KCl and 16.67 mM MEP was used.

From the CV, several features were observed. At marker point 1, the CV of the coated electrode shows a small current whereas the composite shows none, *i.e.* there was a lower onset for the coated electrode for the bromine formation. It could also be though that the larger surface area for the coated electrode allowed more non-Faradaic double layer charging to occur. The 2nd point shows a current peak in the coating CV at the same point of the main peak for the CV with no coating. This would correspond to the bromine formation on the coated surface. The characteristic at point three shows a further oxidation peak occurring at a more positive potential. It was originally suspected that this was due to the supporting electrolyte (KCl) forming Br_2Cl^- complexes, but this was ruled out when the CV was reproduced with KNO_3 in place of KCl. It is not clear what this process is due to but seeing that only one clear reduction peak was obtained on the reverse scan, it must be also linked to the bromine formation reaction. It could be that the presence of the coating could have accelerated the formation of the polybromide species with MEP, as the Br^- within the reaction layer at this approached the electrode surface. This Br^- would then undergo oxidation at a higher potential. Finally, upon reaching point 4, it is noted that the current did not return to the baseline which suggests an underlying process was occurring on the coated surface.

The EIS was measured for on both electrode surfaces at their respective $E_{1/2}$ values.

Figure 6.5 shows the impedance plots for the different electrode surfaces. Both electrodes show compressed semi-circles normally indicative of a porous or roughened surface. It is evident from this graph that the coated electrode gave the much smaller, depressed semi-circle. This indicates that the R_{CT} values for the coated was much lower that the non-coated electrode and thus gave more rapid kinetics. This was confirmed by fitting the EIS data obtained to the equivalent circuit previously described and the results are shown in Table 6.5.

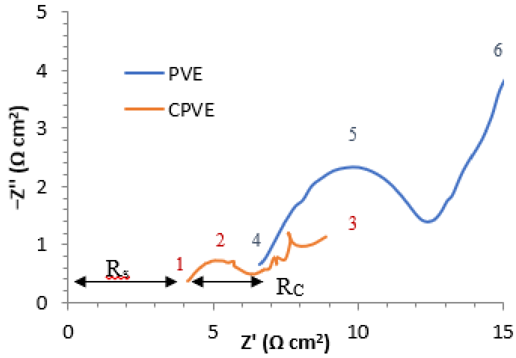

Point	1	2	3	4	5	6
Frequency (Hz)	7940	251	1	655	16.5	1

Figure 6.5 EIS of both smooth carbon composite electrode, PVE (blue) and the carbon coating electrode, CPVE (red) in a 3-electrode cell with a Pt mesh CE and a SCE RE. An electrolyte solution of 50 mM $ZnBr_2$, 0.5 M $ZnCl_2$ and 16.67 mM MEP was used. Frequency range was 65535 – 0.1 Hz

From the data in Table 6.5 the solution resistance (R_S) between the working electrode and the reference electrode showed some variation. Since the electrolyte used is the same for both electrodes the difference in R_S is not significant and may simply be a small change in distance between the Luggin capillary and the working electrode. However, the charge transfer resistance (R_{CT}) shows the resistance to the electron transfer process at the electrode interface and this clearly much lower for the coated electrodes indicating that the coating does have an impact on the electrokinetics. The value for R_{CT} is also directly linked to the exchange current density (j_o) through use of the linearised form of Butler-Volmer equation: $j_o = \frac{\mathrm{RT}}{\mathrm{nFR_{CT}}}$ where R is the universal gas constant, T is temperature (K), n is the number of electrons involved in the electrode reaction and F is the Faraday constant. The values obtained are also shown in Table 6.5.

	Electrode	R_S (Ω cm^2)	R_{CT} (Ω cm^2)	i_o (mA cm^{-2})
Non-coated	**BMA 5**	4.9	8.6	1.493
	PPG86	5.6	6.5	1.975
	PVE	6.3	7.1	1.808
Coated	**BMA 5**	4.7	3.2	4.012
	PPG86	3.2	3.5	3.668
	PVE	3.6	3.4	3.776

Table 6.5 Electrochemical characteristics from the impedance plot in an electrolyte solution of 50 mM $ZnBr_2$, 0.5 M $ZnCl_2$ and 16.67 mM MEP was used

This was supported by analysing the data obtained from the potentiodynamic measurements, shown in Figure 6.6. This shows that the E_o value did not vary greatly meaning the electrode surface remained similar in each experiment.

Table 6.6 shows the parameters obtained from these measurements. The observed i_o for the coated electrodes are higher in all instances. The data for the coated PPG86 appears to be an outlier result in that it was the only coated electrode in which i_o did not exceed 1 mA cm^{-2}. Nevertheless, the trends from the EIS data is consistent with those from the Tafel data in that the coated electrodes display faster rates for kinetics than that of their non-coated counterparts. The i_o values calculated from the Tafel and EIS do not quite coincide though and this could be because of the potential chosen, at the halfwave potential ($E_{1/2}$) in a linear sweep voltammetry, to do the EIS measurements.

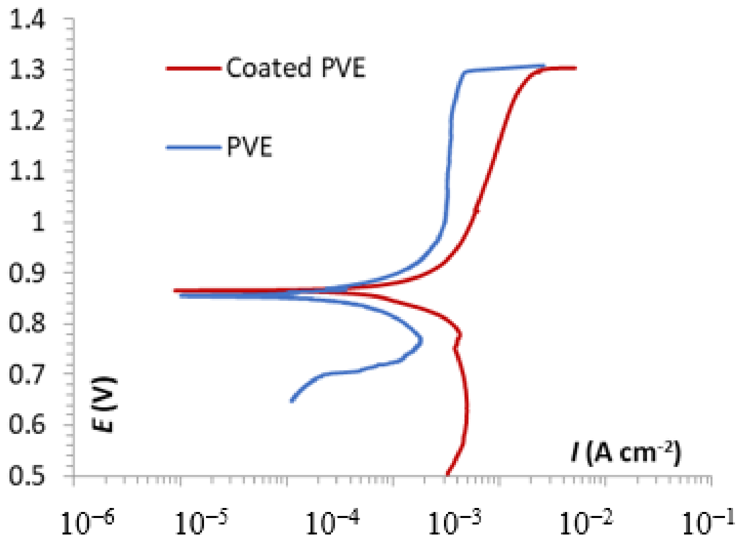

Figure 6.6 Potentiodynamic of both smooth carbon composite electrode (blue) and the carbon coating electrode (red) in a 3-electrode cell with a Pt mesh CE and a SCE RE. An electrolyte solution of 50 mM $ZnBr_2$, 0.5 M $ZnCl_2$ and 16.67 mM MEP was used. Scan rate 0.1667 mV s^{-1}

	Electrode	B_a (V)	i_o (mA cm^{-2})	E_o (V)
Non-coated	**BMA 5**	69.4	0. 868	0.852
	PPG86	101.27	0.388	0.868
	PVE	107.31	0.433	0.855
Coated	**BMA 5**	95.778	1.023	0.849
	PPG86	108.02	0.411	0.858
	PVE	119.85	1.105	0.866

Table 6.6 Electrochemical characteristics from the Tafel slopes

6.3 Flow cell

6.3.1 Volumetric Mass Transport Coefficient ($k_L A_{me}$)

The first measurement taken in the flow stack was for the determination of the volumetric mass transport coefficient, $k_L A_{me}$. This gives an indication of the electrochemical surface area accessed by the flowing solution. Rearranging Eq. 6.1, allows for the product of the mass transport coefficient and effective surface area to be obtained from the measurement of the limiting current (I). This was then normalised with the electrode volume to yield the $k_L A_{me}$ value, shown in Eq. 6.2.

$$I = n \cdot F \cdot k_L \cdot A \cdot c \qquad \text{Eq. 6.1}$$

$$\frac{k_L A}{V} = \frac{I}{nFcV} = k_L A_{me} \qquad \text{Eq. 6.2}$$

Where F is Faraday constant, A is the 2 dimensional area of the electrode, c is the concentration of the catholyte and k_L is the To achieve this, the mass transport limited plateau currents at different controlled flow rates were measured. This region is shown in Figure 6.7, varies with flow rate allowing a relationship between current response and flow rate to be used to determine the k_LA_{me}. Due to instrumental limitation, appropriate concentrations of the $Fe(CN)_6^{3-}$ were used to avoid the signal from electrochemical reaction taking place saturating the potentiostat.

Cathode:

$$[Fe(CN)_6]^{3-} + e^- \rightarrow [Fe(CN)_6]^{4-} \qquad \text{Eq. 6.3}$$

Anode:

$$2H_2O \rightarrow O_2 + 4H^+ + 4e^- \qquad \text{Eq. 6.4}$$

The voltage scan was run at 5 mV s^{-1} to identify the desired potential in the mass transport plateau. This potential was then used to run chronoamperometry experiments with the solution passing through the cell either in a single-pass mode (with constant inlet concentration) or in batch recirculation mode, where a redox electrode was used in the reservoir to monitor the change in the solution concentration.

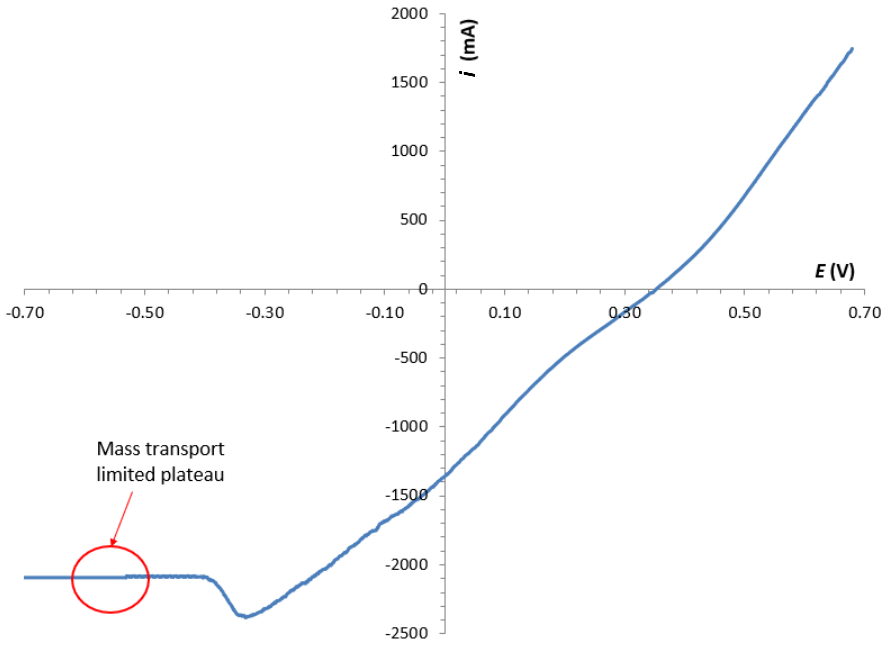

Figure 6.7 A linear single voltammogram of 0.01 M potassium ferricyanide 0.5 M KNO_3^- (catholyte) and 0.5 M KNO_3^- electrolyte (anode). After the current peak show the mass transport plateau

The plateau currents were plotted for each electrode, as shown in Figure 6.8, as a function of flow rate. The peak formed was due to the scan rate being too high. However, it could not be set lower, since the flow was solely fresh electrolyte (*i.e.* would not be passed through the cell again), this would have resulted in the total electrolyte volume to have passed before the experiment's completion. The carbon composite (CC), BMA 5, showed the lowest magnitude of $k_L A_{me}$ and the smallest change in gradient with flow. This is due to the laminar solution flow over the electrode surface in the cathodic compartment where the reaction was occurring. The felts on the other hand showed an improved response, with varying gradients due to the solution becoming more turbulent, as it passed through the felts. It is worth noting that the GFA 3 and GFD 3 felts from SGL Carbon represent rayon- and PAN-based carbon fibre felts, respectively. The 3 represent the 3 mm thickness of the felts. GFD 4.6 then represents a thicker electrode which occupied the entire volumetric area available in the half-cell and so, there was little chance of flow by-pass. This would result in a greater flow response than from the thinner felts. Significantly, the gradient of both the GFD 3 and GFD 4.6 felts are very similar, suggesting that the effect observed here was due to the thinning of the static electrolyte layer between the felt electrode surface and the flowing solution. The Mersen felt (same geometric size as GFD 4.6) had a stronger response with the flow. The enhanced $k_L A_{me}$ could be a direct effect from the higher surface area within the felt, whereas the greater gradient achieved was indicative of the enhanced mass transport interactions due to the flow.

This experiment was repeated for each electrode multiple times. The results obtained for the SGL felts and the carbon composite were very repeatable and thus are not represented in the figure. However, the results for the Mersen felt showed some variation, as indicated by the error bars. This was mainly due to the rate of species consumption within the felts and the consequence of using lower concentrations in these experiments. The $k_L A_{me}$ values obtained here are comparable to those found in the literature. One study in particular examined a variety of Pt/ Ti mesh electrode structures in the flow cell[125]. The felt and micromesh structures tested in that work gave values between 1.5×10^{-2} s^{-1} to 5.0×10^{-2} s^{-1}, with lower values found for planar carbon structures. similar to the trends found in this study. The one key difference was that the gradient response with the flow rate was higher, though this would be dependent on the cell design used in the study.

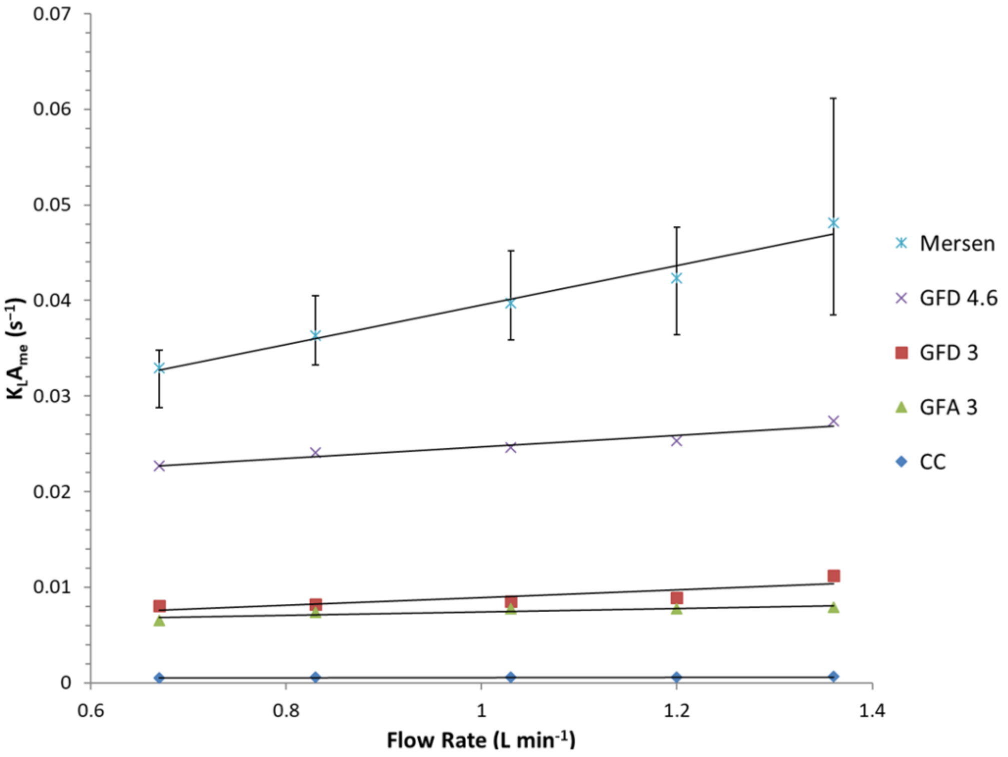

Figure 6.8 k_LA_{me} for each electrode at various flow rates

6.3.2 Charge/ Discharge Cycles

The felt electrode materials were then used in a 1 A charge and discharge cycle, set to achieve a SoC of 80% before discharge to the lowest SOC it could reach before hitting the lower potential limit. During the charge cycle, the solutions in the reservoir are static, to collect the immiscible phase at the bottom. This shows a drop-in volume over time (from 500 mL to ~350 mL), caused by the immiscible phase being denser than the aqueous phase. However, the tubing is lowered in the oil phase and stirring occurs to distribute the immiscible phase during the discharge cycles. The electrolyte used for this was 2.25 $ZnBr_2$, 0.5 $ZnCl_2$, 0.8 M MEP and 5 mL of Br_2 per litre. The data obtained from these studies are shown in Figure 9. The carbon composite used for both electrodes (BMA 5) gave a reading of a constant voltage during charge of *ca.* 2.3 V. During the discharge however, there was a gradual fall in the voltage as the reactants (particularly, the bromine phase) was consumed until the sharp fall indicating that there were not enough reactants to maintain the set current. More coulombs could potentially be extracted from the electrolyte if discharged at lower currents. However, for comparison, the coulombic efficiency data determined in Table 6.7 was when the lower cell voltage limit (0.5 V) was reached for the 1 A discharge. From here, the only electrode to change was the positive electrode for the Br^-/ Br_2 couple. As the usage of felts on the negative electrode would cause blockages due to the plating of zinc.

The activated carbon coating, used by Lotte Chemical in their 25 kW/ 50 kWh RFB system, proved to be the most effective from the tests conducted achieving 86% CE and 65% VE. Flat charge and discharge voltage profiles were obtained for the activated carbon surface. The carbon composite surface gave a sloping voltage discharge and at lower voltage than the activated carbon. In terms of overall cell performance though, the carbon composite and activated carbon electrodes, with nominally flat surfaces, performed much better than the felts which had the supposed advantage of a superior surface area. The GFD 3 felt initially showed good voltage stability during charge, matching both activated carbon and the carbon composite, until near the end of the cycle where there was a sudden increase in the voltage. It could well be that here, the GFD 3 felt could have become saturated with oily bromine complex which would have caused a large increase in resistance. Such a phenomenon would also be likely to be accompanied by the electrolyte by-passing the felt altogether. The GFA 3 felt has the larger surface area and so a lower void volume within the felt. It has been noted previously that the immiscible oily phase begins to form at SoC as low as 5% SoC. If the charged immiscible material was trapped within the surface, this could coat the electrode surface creating an additional barrier for fresh reactant in the aqueous phase to reach an active site as well as increased electrical resistance. This would lead to a much higher charge voltage as the felt became saturated with the oily phase very rapidly. The GFD 3 felt on the other hand, having a more open structure, would result in the immiscible phase being more easily removed from the felt allowing the reactant in the aqueous phase to reach the electrode.

The initial dip in voltage observed during discharge with the GFA 3 felt may be from the high and readily available concentration of the complexed bromine held within the felt becoming consumed.

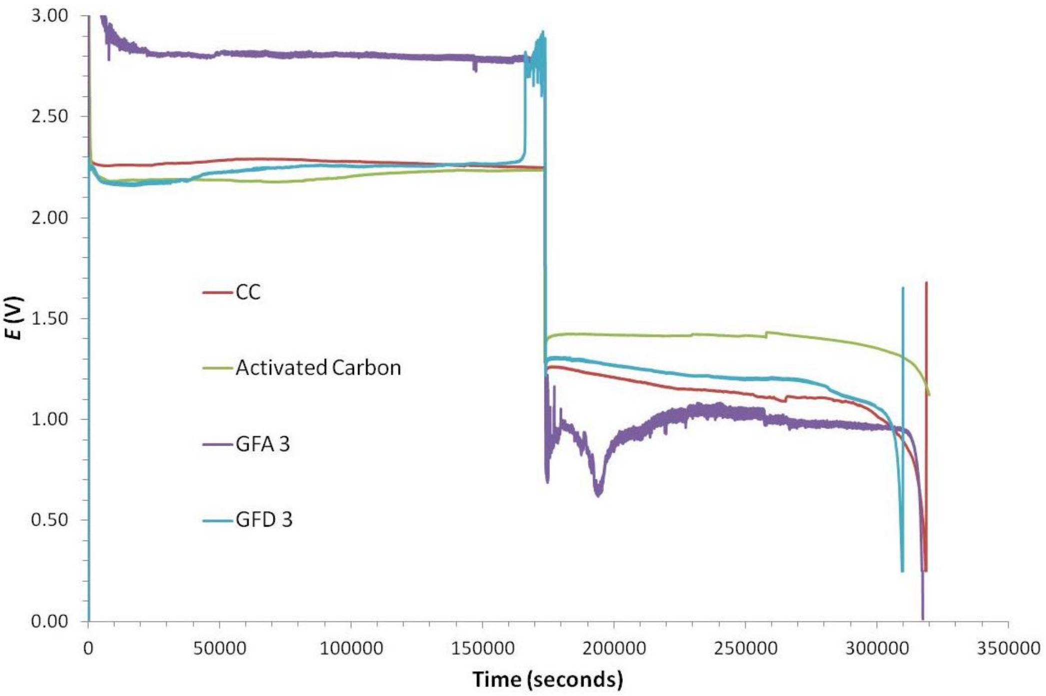

Figure 6.9 Charge/ discharge cycle for various electrodes

The data in Figure 6.10 compares the use of two thicker felts to the carbon composite electrode and brings to the fore some of the issues in attaching the felts to the carbon composite backing plates. All the runs carried out with the felt material in this study resulted in the felts being pulled off the backing plate. The reason for this was that here, the felt occupied the entire cell flow area of the half-cell. With the formation of the immiscible phase within the felts during charging could have resulted in a large enough back pressure to force the felt away from the backing plate. Clearly then, the carbon cement used to bind the felts to the backing plates was inadequate to the task. Very noisy charge voltage profile was obtained, with the voltage ranging from 2.6 V to 3.7 V. The noisy data could then be the impact of the immiscible phase forming and being intermittently removed from the felt because of increased flow pressure on any partial blockages caused by this viscous phase. However, it was during the discharge that the impact of the felt not being properly attached to the backing plate was most keenly observed. The discharge data from Attempt 1 indicated that the expected higher value for the discharge voltage could be obtained but was dependent on the level of attachment to the backing plate. The repeat of this experiment (Attempt 2) gave the same noisy charge voltage (with a higher value than in Attempt 1) but during discharge, the low voltage attained suggests that there was poor electrical contact between the felt and the backing plate. As the GFD 3 felt used here had previously achieved a CE of 82%, the lower CE (65% and 64%) from Attempts 1 and 2 respectively, was from the loss of electrical contact when the felt was dislodged. The Mersen felt (thickness, 4.6 mm) used in this part of the study gave the same trend as for the GFD 3 but here, an even lower CE (60%) was obtained but because of the issues outlined above, this electrode material's capabilities was not truly assessed in this run. An important note from this part of the study was that the immiscible phase could create an additional barrier to the fluid flow which could not only limit the access to electroactive material but also created a back pressure which could cause the felt to be dislodged from the backing plate.

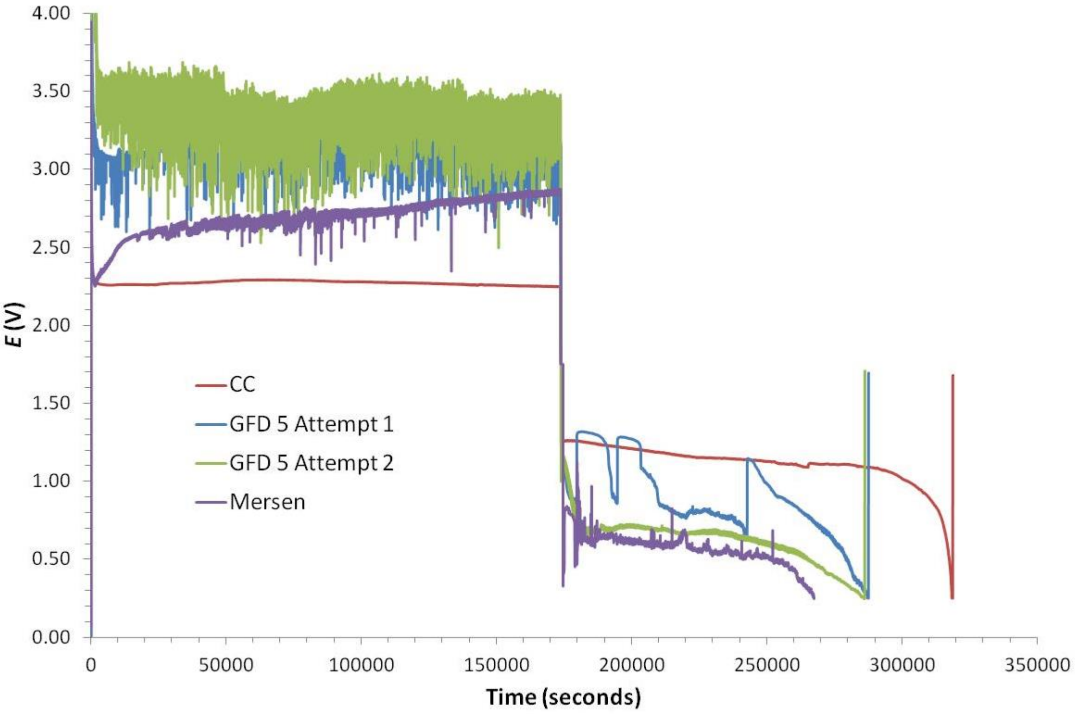

Figure 6.10 Charge/ discharge cycle for 4.6 mm felts compared to carbon composite electrode

	CC	Activated Carbon	GFD 3	GFA 3	GFD 4.6	Mersen
CE (%)	81	86	82	78	65/64	53
VE (%)	50	65	54	40	46/24	21

Table 6.7 Coulombic and voltage efficiencies of electrode materials tested

Despite the lack of quantifiable data from these thicker felts, the Mersen felt was carried forward for runs using multiple charge-discharge cycles in a system where both charged and discharges species in the positive and negative electrolytes remained in the solution.

Cycles were ran in a 1.5 M $V^{3.5+}$, 1.5 M H_2SO_4 electrolyte solution. For the specific volume and concentration of the vanadium electrolyte employed here, to achieve an 80% SOC from a $V^{3.5+}$ electrolyte, 1 A of constant current was applied for 16 hours, 4 minutes and 51 seconds. The initial part of Figure 6.11 shows the charging of the electrolyte to the 80% SOC, with the voltage starting to rapidly rise towards the end of the experiment. This rise indicated the evolution of hydrogen gas, a common side reaction at the negative electrode of the VRFB which can be controlled by either using voltage limits, decreasing the current applied after a certain SOC, or reducing the set SOC value. In this system, the formation of hydrogen will reduce the coulombic efficiency and reduce the acid concentration, leading to reduced solubility of the V^{5+}species. During discharge, the voltage falls concomitantly with SOC until the battery is discharged when a rapid fall in voltage occurs. With voltage limits to ensure it did not go above at 1.9 V during charge or below 0.25 V during discharge

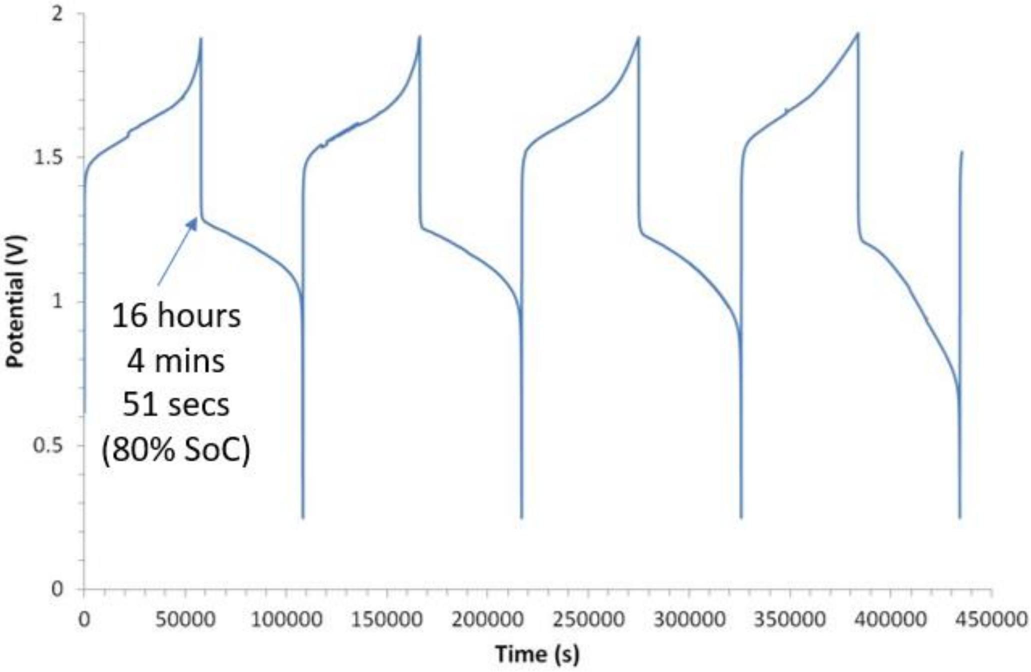

Figure 6.11 Charge and discharge cycles with the Mersen felt

Table 6.8 shows the efficiencies achieved from the cycles shown in Figure 6.11. The coulombic efficiency achieved was consistently high. However, the voltage efficiency decayed with each subsequent cycle causing it to reduce the overall energy efficiency. The control data set used was from the GFD 4.6 electrode (which had been used throughout the calibration of the cell and initial runs in previous chare-discharge studies) which yielded coulombic and voltage efficiencies significantly lower than for the Mersen felt. As the charge and discharge of were operated at the same current, the VE was calculated from the median value from each plateau, whereas CE was simply a ratio of coulombs in *vs.* coulombs out.

	Cycle 1	**Cycle 2**	**Cycle 3**	**Cycle 4**	**Control**
CE (%)	87	87	87	86	46
VE (%)	75	72	69	61	42
EE (%)	65	62	60	53	19

Table 6.8 Efficiencies from the first set of cycles

Following these cycles, the cell was taken apart for visual inspection. No issues were found as to the cause of the fall in the voltage efficiency in cycle 4 (*i.e.* condition of the electrode, leakages/ blockage in the flow, nitrogen supply to the V^{2+} /V^{3+} reservoir remained uninterrupted). A new Mersen felt was put in place, and a second series of cycles were measured under the same conditions. A further 6 cycles were run, as shown in Figure 6.12. These cycles produced smooth, consistent charge and discharge profiles. The only exception was in the 6th cycle. This cycle was where the electrolyte from the negative reservoir (50 mL) was transferred to the positive reservoir to function as electrolyte balancing which occurs due to water transfer from positive to negative electrolyte across the membrane. This is a known effect in all VRFBs employing cation exchange membranes. Therefore, the coulombic loss was expected from this change in electrolyte composition. Table 6.9 shows that the coulombic efficiency has improved from the reconstruction of the cell.

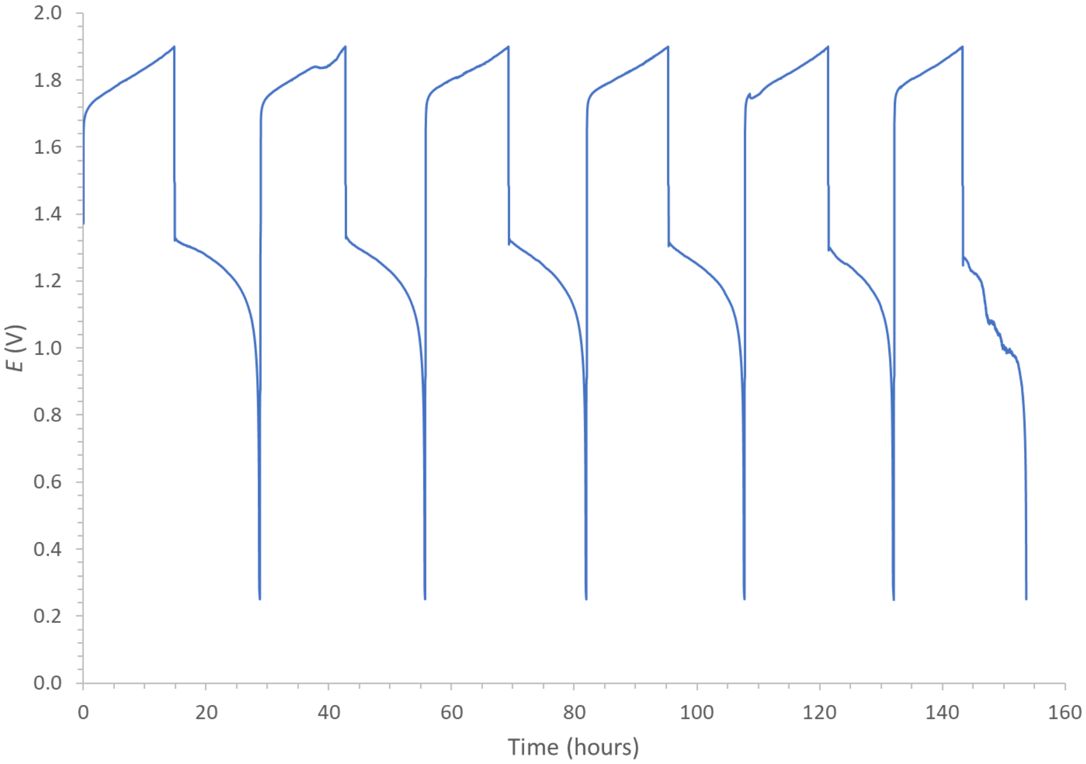

Figure 6.12 Second series of charge/ discharge cycles for the vanadium flow cell operating at 1 A charge and discharge cycling from an of SOC 0% to 80%

	Cycle 1	Cycle 2	Cycle 3	Cycle 4	Cycle 5	Cycle 6
CE (%)	91	90	92	90	75	91
VE (%)	69	68	67	67	67	60
EE (%)	62	61	61	60	50	55

Table 6.9 Efficiencies from the second set of cycles

A final series of cycles were conducted using 2 A to charge-discharge to a SOC of 50%, taking roughly 4.5 hours. Again, as can be seen from Figure 6.13, these cycles produced smooth, consistent charge and discharge profiles. A noticeable difference from Figure 6.13 is the expected higher charge voltage lower discharge voltage. However, the coulombic and voltage efficiencies achieved, as shown in Table 6.10 were stable at 95% ± 1% and 37% ± 1%, respectively. It is significant to note here that this was the first time this flow cell set-up had been able to achieve 2 A for charging and discharging.

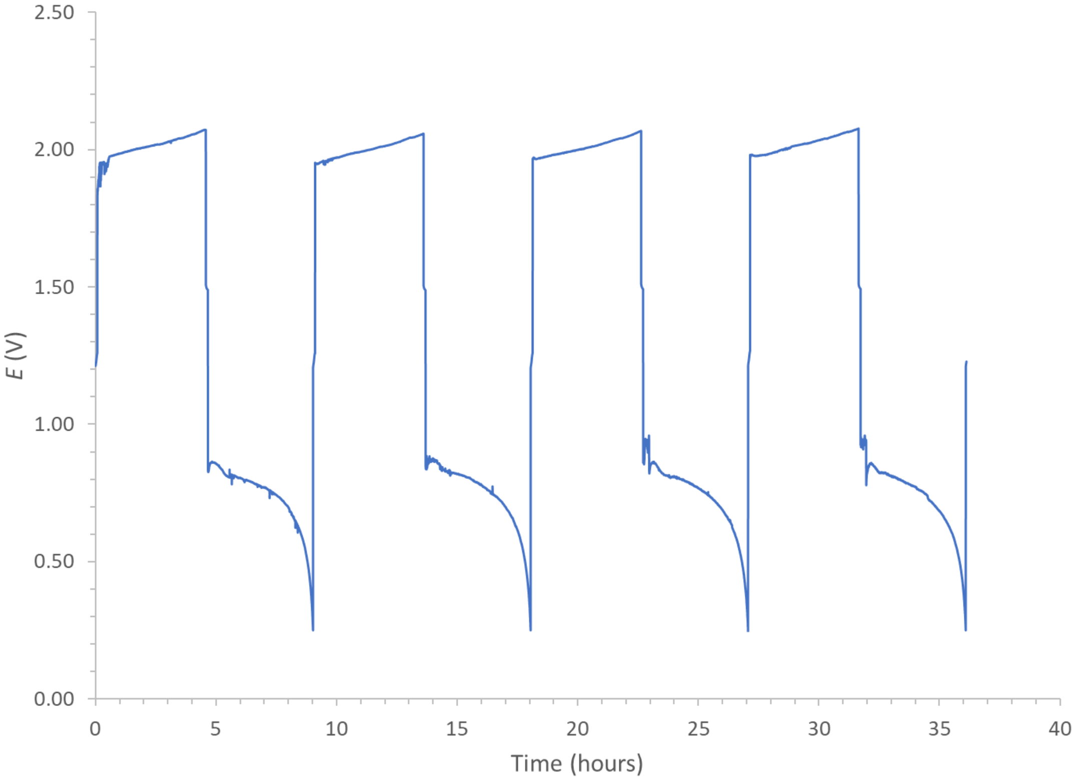

Figure 6.13 Third series of charge/ discharge cycles for the vanadium flow cell. operating at 2 A charge and discharge cycling from an of SOC 0% to 50%

	Cycle 1	Cycle 2	Cycle 3	Cycle 4
CE (%)	95	94	96	94
VE (%)	38	37	37	36
EE (%)	36	35	35	34

Table 6.10 Efficiencies from the third set of cycles

6.4 Vanadium Electrolyte Production

Normally, V^{4+} would be produced from either dissolving the appropriate amount of vanadium (IV) oxide in sulphuric acid or reducing vanadium pentoxide with hydrazine. Both techniques involve costly components with the latter using a very volatile reducing agent. To optimise this process, oxalic acid was introduced (being both cheaper and safer to handle) to reduce 95% of vanadium pentoxide under the following reaction:

$$V_2O_5 + C_2H_2O_4 + 2\,H_2SO_4 \rightarrow 2\,VOSO_4 + 2\,CO_2 + 3\,H_2O \qquad \text{Eq. 6.5}$$

The remaining 5% was reduced with hydrazine, which was diluted to allow for safer handling and reduce the likelihood of insoluble hydrazine sulphate being formed in the presence of the sulphuric acid. This reaction is:

$$V_2O_5 + \tfrac{1}{2}\,N_2H_4 + 2\,H_2SO_4 \rightarrow 2\,VOSO_4 + \tfrac{1}{2}\,N_2 + 3\,H_2O \qquad \text{Eq. 6.6}$$

As can be seen from both reactions, the production of water occurs. This is compensated by running the reaction at a lower overall volume with the amount of acid required evaluated considering the consumption of both the acidic protons and the resulting dilution. Throughout this reaction, clear colour changes in the electrolyte production were visible: from the V^{5+} orange suspension to the V^{4+} blue solution, as shown in Figure 6.14.

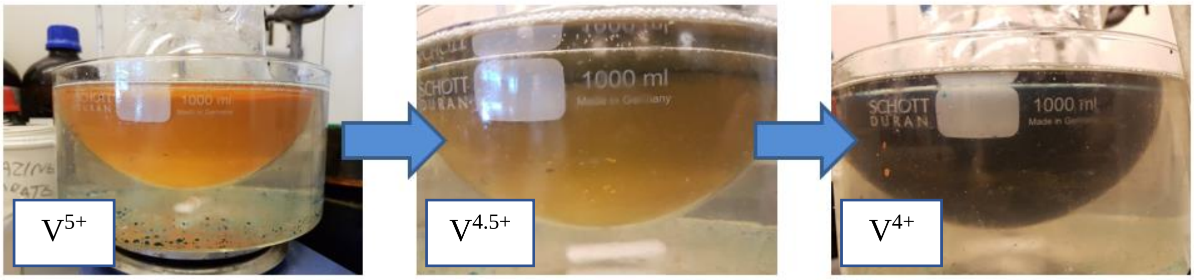

Figure 6.14 vanadium electrolyte reducing from an oxidation state of 5+ to 4+

The concentration of the electrolyte was verified using UV-visible measurements by modelling the spectra on Mathcad using Beer-Lambert law and calibrated data to determine the experimentally obtained concentration from the absorbance value at λ = 760 nm, shown in Figure 6.15.

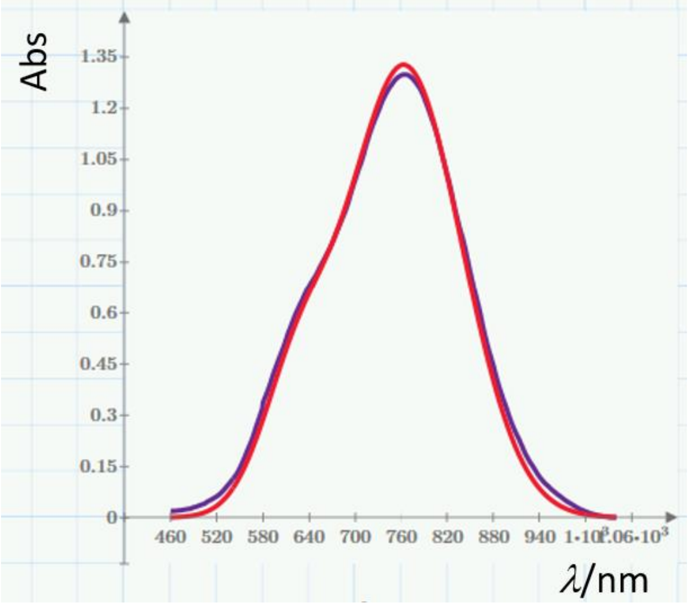

Figure 6.15 Experimental data with fitted model to determine the obtained concentration as shown in Mathcad. Experimental data (red) and theoretical data (blue)

The final stage of the electrolyte production was to convert the electrolyte into a 1:1 ratio of V^{3+} and V^{4+}. During the electrolysis, the concentration was tracked using the UV-visible spectrophotometer. As V^{3+} was produced, a peak in the UV-visible spectrum would appear at λ 400 nm with the V^{4+} peak at 760 nm decreasing. This spectrum could be simulated, using calibrated data for V^{3+} and V^{4+} to determine the concentration of both species. As the conversion progressed, this change was monitored until the V^{3+} and V^{4+} concentrations were equal, as shown in Figure 6.16. Converting to this ratio allows for the electrolyte to be placed into both reservoirs and charge to obtain their respective oxidation states required for the RFB.

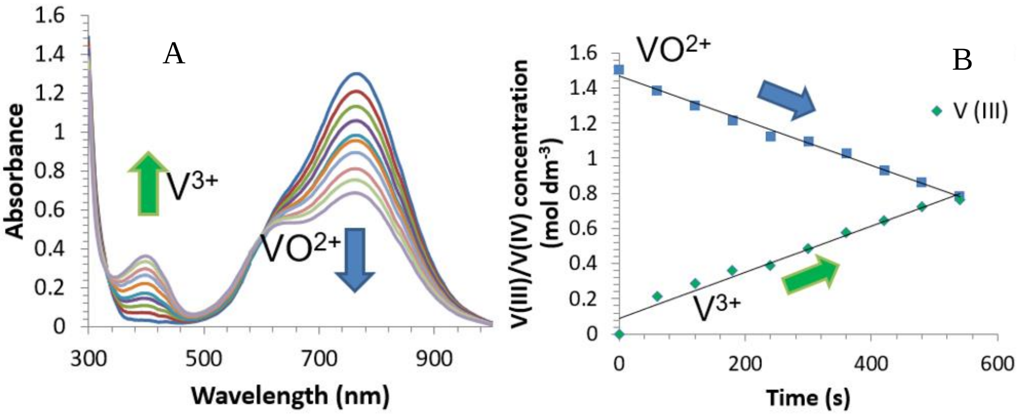

Figure 6.16 UV- visible spectra showing the increase of V^{3+} and decrease of V^{4+} during conversion (A). Concentrations from the spectra showing a linear relationship and trending towards the $V^{3.5+}$ (B).

6.5 Conclusions

Currently, carbon-composites are commonly used as electrode materials in the $ZnBr_2$ hybrid redox flow battery. The material of this electrode could potentially be improved using felts (which provides a superior surface area) and carbon coating (potentially providing better kinetics). Comparing both felts and carbon coating to use of carbon-composites alone has allowed their effectiveness to be determined.

Using the H-cell, carbon felts showed promise as a potential positive electrode material. Through galvanic cycling the felt was shown to provide better coulombic and voltage efficiencies than the carbon composites. When the SOC of the H-cell was increased the felt showed that it could retain a substantial volume of the complex bromine phase within its structure which may lead to a faster discharge response. The carbon coating produced a more active surface in comparison to the carbon-composite obtained faster electrode kinetics.

From the flow cell, the volumetric mass transport co-efficient (k_LA_{me}) was successfully measured in the flow cell using the 0.1 M $K_3Fe(CN)_6^{3-}$ probe species. This showed that the Mersen felt yielded the higher values than any of the alternative felts or carbon composite tested. Using the 2.25 M $ZnBr_2$, 0.5 M $ZnCl_2$, 0.8 M MEP solution for the charge/ discharge cycles in the flow cell showed that the carbon felts could eventually become blocked with the immiscible phase and this resulted in an additional barrier for reactants to reach the electrode surface. From these experiments, the electrode using the activated carbon coating proved to have the better VE and CE of all electrodes tested. This immiscible phase also caused the thicker felts to be pulled from the electrode plates. This highlights the advantage that could be achieved with the additive, discussed earlier, that can achieve complexation without forming a secondary phase. The Mersen felt was then used in a 1.5 M $V^{3.5+}$, 1.5 M H_2SO_4 flow cell to test the electrodes performance over a series of cycles. The first series of cycles at 1 A set achieved high coulombic efficiencies of >85%. The second series of cycles produced higher coulombic efficiencies (90%-92%) with exception of a cycle where electrolyte rebalancing took place. The voltage efficiency for the first 5 cycles maintained a relatively constant value (62 - 60%). The third series of cycles at 2 A again achieved higher coulombic efficiencies (94% - 96%).

7. Power Networks Demonstration Centre (PNDC)

7.1 Introduction

The PhD sponsor, Lotte Chemical, have three stages of product development for their zinc bromine redox flow battery: 25 kW/ 50 kWh, 250 kW/ 500 kWh, and 750 kW/ 1 MWh. The first system, 25 kW/ 50 kWh, was installed at the University of Strathclyde’s Power Network Demonstration Centre (PNDC) with the aim to evaluate the overall battery’s performance, robustness to grid like instabilities, and identify potential points of improvement for subsequent stages.

Figure 7.1 25 kW/ 50 kWh zinc bromine redox flow battery set-up

The $ZnBr_2$ RFB, shown in Figure 7.1, consisted of eight stacks which were paired in series and the four pairs being connected in a parallel circuit with DC/DC converters. Each paired series provided a nominal 6.25 kW power output with a voltage range of 100 – 240 VDC. These stacks consisted of bipolar electrodes with the negative electrode being an unnamed carbon composite and the positive electrode having an activated carbon layer on its surface, as investigated earlier in the electrode material chapter of this thesis. These electrodes are separated using a porous separator. The reservoir consisted of three tanks capable of comfortable storing the 500-litre electrolyte capacity. In addition to the expected catholyte and anolyte tanks, there is a tank for the second phase generated during charging in the positive electrolyte (catholyte) consisting of an immiscible phase. These tanks are controlled through an automated 4-way valve. The electrolyte composition was 2.25 M $ZnBr_2$, 0.5 M $ZnCl_2$, 5 mL Br_2 per litre of electrolyte with 0.8 M MEP as the complexing additive.

Throughout the tests and performance assessment process, the engineers at PNDC had tested this RFB using PNDC's independent grid, examining the AC in/AC out energy conversion efficiencies to a set SoC (~30%). However, Lotte Chemical also desired a more comprehensive understanding of the electrochemical performance of the system at higher SoCs. The initial studies had raised concerns that faulty stacks were causing the lower voltage limit during discharge to be tripped resulting in the RFB to stop discharging early, resulting in a false representation to the RFB's capability. After the poorest performing stacks were replaced the results were improved by a nominal amount.

The following work looked at the individual stack performance during both charge and discharge at various power levels. This was to determine the source of the efficiency losses and to suggest recommendations for system improvements.

7.2 Experimental

Due to the level of investment and associated risks this system presents, a series of procedures were developed and adhered to. Before the RFB was switched on, physical checks were made on the gas detection system – no alarms should be present, and the LCD display should read 0.00 (alarm 1 set at 0.5 ppm; alarm 2 set at 0.8 ppm). Once this was completed, the 63A socket was energised and allowed to stabilise with a series of tests being conducted to the RFBs connectivity and emergency shutdown capabilities. Following successful checks, the charge procedure would be set-up, started by opening the ball valves in the module enclosure and ensuring the temperature of the electrolyte was above 8°C. A USB is connected to the human machine interface (HMI) panel to collect the data from the measured cycles. The program of work was set-up through the HMI interface's system control (Figure 7.2), where the series of controls were set to auto and pump flow rates were set according to the function of the cycle (*i.e.* charge, discharge, and stripping) as shown in Table 7.1.

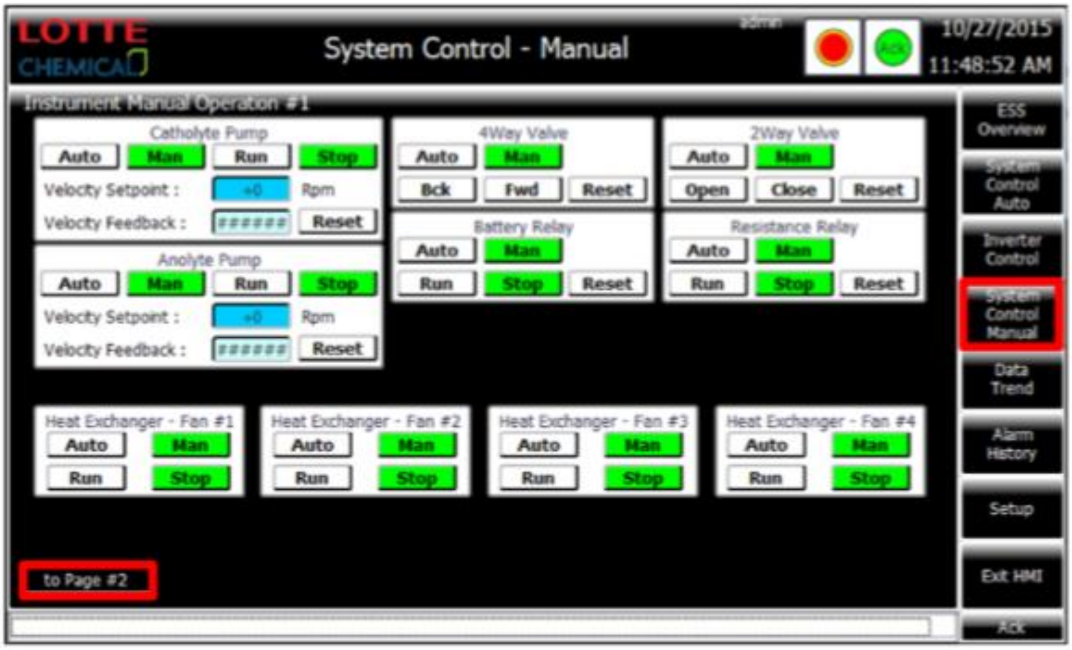

10/27/2015 11:48:52 AM

Velocity Setpoint : +0 Rpm
Velocity Feedback : ######

Velocity Setpoint : +0 Rpm
Velocity Feedback : ######

Figure 7.2 HMI Panel System Control panel

Mode	Catholyte Pump (RPM)	Anolyte Pump (RPM)
Wake-Up	2300	2000
Charge	2300	2000
Discharge	2400	2000
Strip	2300	2000
Shutdown	2500	2000

Table 7.1 Pump flow rates for various stages of operation

Following this, a schedule of work could be set-up allowing for wake-up, rest, and shut-down periods to be placed amongst the charge and discharge cycles, as shown in Figure 7.3. These cycles can be controlled by either constant current, constant voltage, or constant power. For the work conducted in this chapter, all cycles were controlled using constant power, allowing for the discharge power limit to be set when the voltage drops below a set value (100 V). The schedules of work operated are detailed in the Appendix although the nominal charge and discharge of this battery was 17 kW and 12 kW, respectively, which were used as guides during the setting up of the schedule.

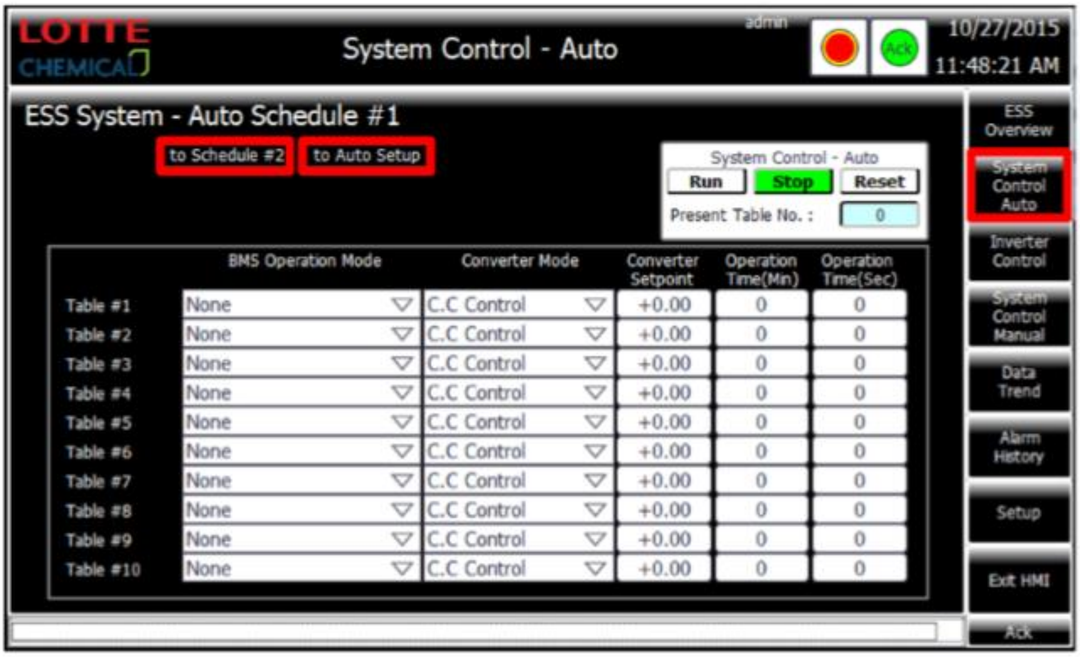

Present Table No. : 0

	BMS Operation Mode	Converter Mode	Converter Setpoint	Operation Time(Min)	Operation Time(Sec)
Table #1	None	C.C Control	+0.00	0	0
Table #2	None	C.C Control	+0.00	0	0
Table #3	None	C.C Control	+0.00	0	0
Table #4	None	C.C Control	+0.00	0	0
Table #5	None	C.C Control	+0.00	0	0
Table #6	None	C.C Control	+0.00	0	0
Table #7	None	C.C Control	+0.00	0	0
Table #8	None	C.C Control	+0.00	0	0
Table #9	None	C.C Control	+0.00	0	0
Table #10	None	C.C Control	+0.00	0	0

Figure 7.3 HMI screen for the schedule of work to be carried out

Once the schedule of work was running, the status and progress of the RFB could be monitored through the energy storage system overview in the HMI interface (Figure 7.4). From this, the status of the DC/AC inverter, DC/ DC convertors, temperatures, pump operations, and states of charge could be monitored. However, the main analysis was through the monitoring and recording of the individual stack data which could be accessed through this panel to open the smaller pop-up panel displayed at the top-right corner of Figure 7.4. An additional pop-up could be accessed showing the current and power being applied to or taken from each stack.

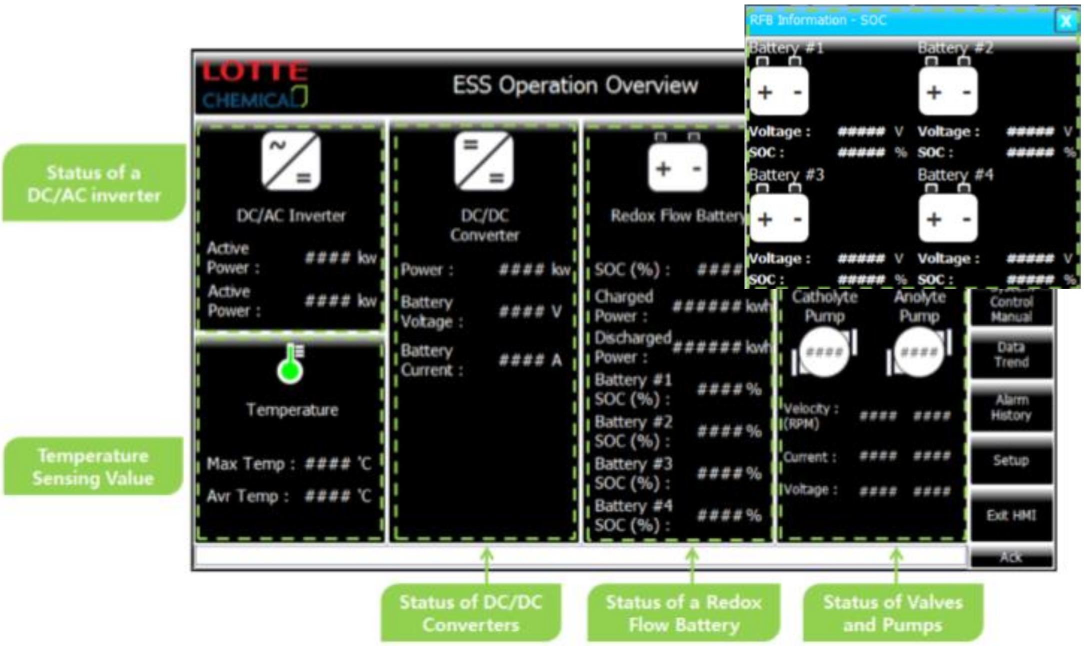

Status of a DC/AC inverter

Temperature Sensing Value

Status of DC/DC Converters

Status of a Redox Flow Battery

Status of Valves and Pumps

Figure 7.4 HMI Interface showing the overview of the energy system during its schedule of work with a pop-up window showing the individuals stack's voltages and SOCs

Once these schedules were complete, the battery was shut down by ensuring all pumps, heat exchangers, relays, valves, and convertors were switched off from the HMI panel before turning of the module’s power source at the 63 A switch.

However, after every fifth successive charge/ discharge cycle it became necessary to run a stripping cycle to remove any zinc depositions remaining on the electrode surface after the discharge cycle. This involved operating the battery in a similar way to the charge/ discharge cycles with a very small current being passed. Once the individual stack voltages fell below 100 V, the battery relay was replaced with the resistance relay and left until all stack readings reach under 1 V. The SOC% for each stack was then reset to 0% for the next charge cycle.

7.3 Charge-Discharge Cycles

Run 1

This schedule of work was to charge the battery at 17 kW until a theoretical SOC of 50% was achieved. When it was attempted to start charging at 17 kW, the upper voltage limit alarm was tripped, as can be seen on Figure 7.5 by the outlier before the main charge cycle. It was concluded that approaching any rate of charge or discharge would be done *via* staggered steps which would involve 1-minute charging at each 8 kW and 12 kW building up to 17 kW and 1-minute discharges of −4 and −8 kW building up to −12 kW. This work up sequence was applied from this point onwards.

The power was reduced in this instance to 12 kW for 120 minutes which achieved 23.86 kWh of stored power. This discharge cycle was intended to be two cycles of 120 minutes each at −8 kW and −4 kW. However, the lower limit alarm for stack 2 tripped before the discharge cycle at −8 kW was completed. The discharged power was −15.65 kWh resulting in a DC/DC efficiency of 65.6%. The AC/DC efficiency was 54.59% with a recorded charged energy of 26.35 kWh and that for discharge of −14.38 kWh.

The figures for this data represent the voltage (V), power (P) and current (I) achieved across all 4 stacks (1,2,3,4). The onset plateau before the charge started was the time difference between setting up the recorded and starting the flow battery.

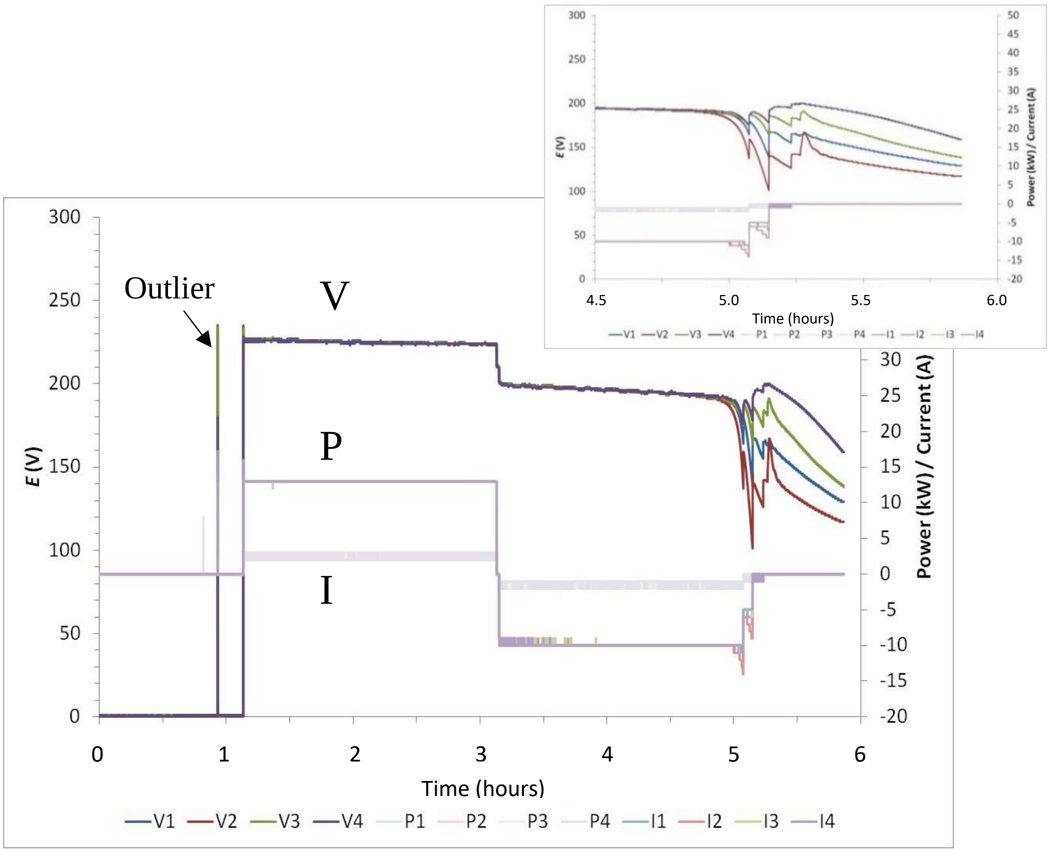

Figure 7.5 Charge 12 kW/ Discharge –8 kW

Run 2

The schedule of work was to test the recommended parameters, as stipulated by Lotte Chemical and determine both the DC/DC and AC/DC efficiencies. As such, the battery was charged at 17 kW for 210 minutes providing a total current of 73.2 A and a voltage of 232 V across the battery's stacks which resulted in a total of 59.62 kWh input energy. The battery was then discharged at −12 kW for 200 minutes where the lower voltage alarm was triggered by stack 2. The discharge cycle achieved an output of −40.37 kWh which gave a DC/DC efficiency of 67.71%. The AC/DC efficiency achieved for this system was 57.67% with 65.2 kWh charge and a −37.6 kWh discharge.

The profile of Figure 7.6 shows similar features to the previous schedule of work, in that the voltage during charge remains constant throughout the cycle with minor changes. Whereas, the voltage for discharge shows a steady decrease until a voltage of ~180 V, after which the voltage decrease becomes quite rapid until the lower limit is reached by at least one stack.

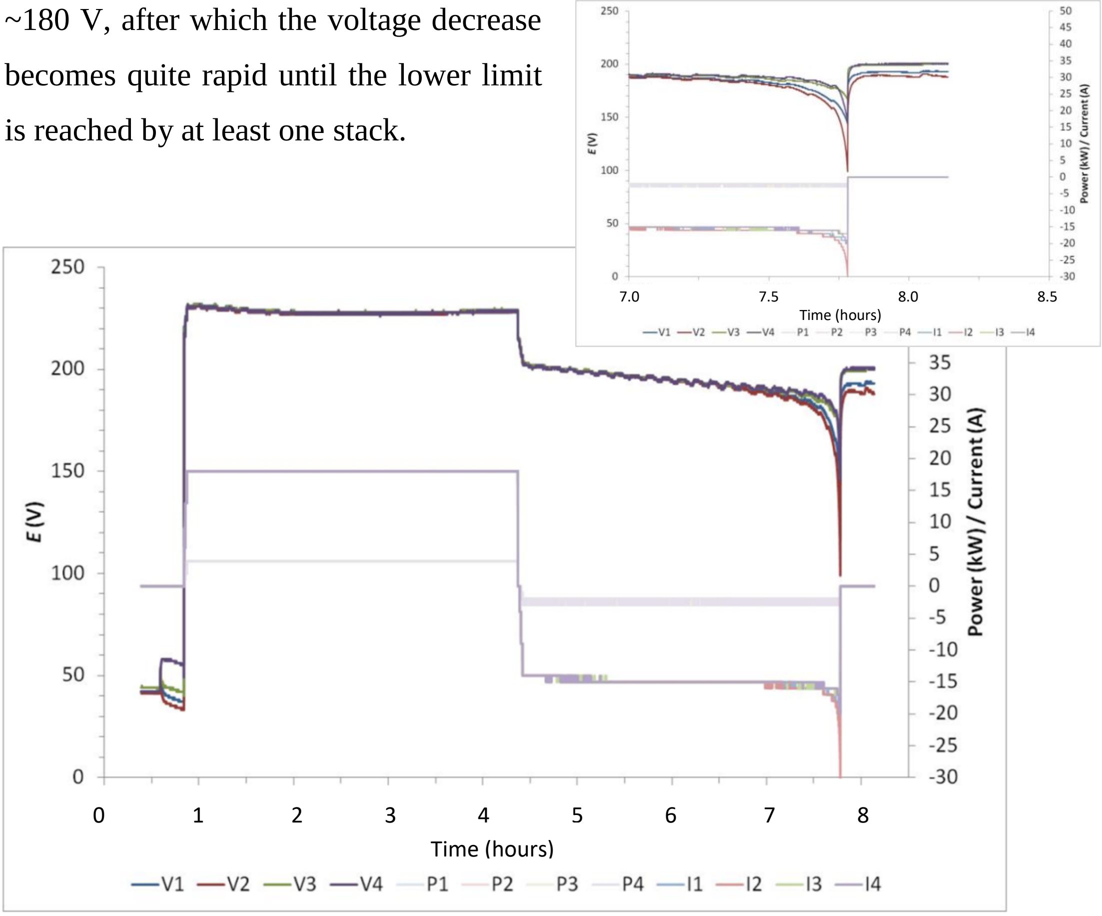

Figure 7.6 17 kW charge/ −12 kW Discharge with an amplified region where the lower voltage limit was tripped

Run 3

The aim of this schedule of work was to attempt to increase the efficiency of the system by manipulating the power input/output with the hypothesis that this would better suit the loss of electroactive material in the electrolytes as the battery became more charged (and the converse during discharge). The battery was charged at 17 kW for 88 minutes and 12 seconds where the achieved SOC was 34%. The charging power was then decreased to 12 kW for 75 minutes achieving a SOC of 54.5%. A further decrease to 6 kW, lasting 96 minutes achieving a final SOC of 67.9% resulting in 49.66 kWh of input energy. The discharge cycle was staggered in a similar manner with output power being set at −12 kW for 105 minutes (returning −21.14 kWh of energy), −8 kW for 60 minutes (returning −7.94 kWh) and −4 kW for 55 minutes (returning −3.1 kWh). This returned a total output of −32.18 kWh which gave a DC/DC efficiency of 64.8%. For AC/DC the efficiency obtained was 54.16% with a charge of 54.85 kWh and a discharge of −29.71 kWh.

Figure 7.7 displays the staggered method and shows that this has an immediate effect on the voltage at both charge and discharge. However, the overall efficiency in discharged energy remains the same with stack 2 being the first to trip the lower voltage limit alarm.

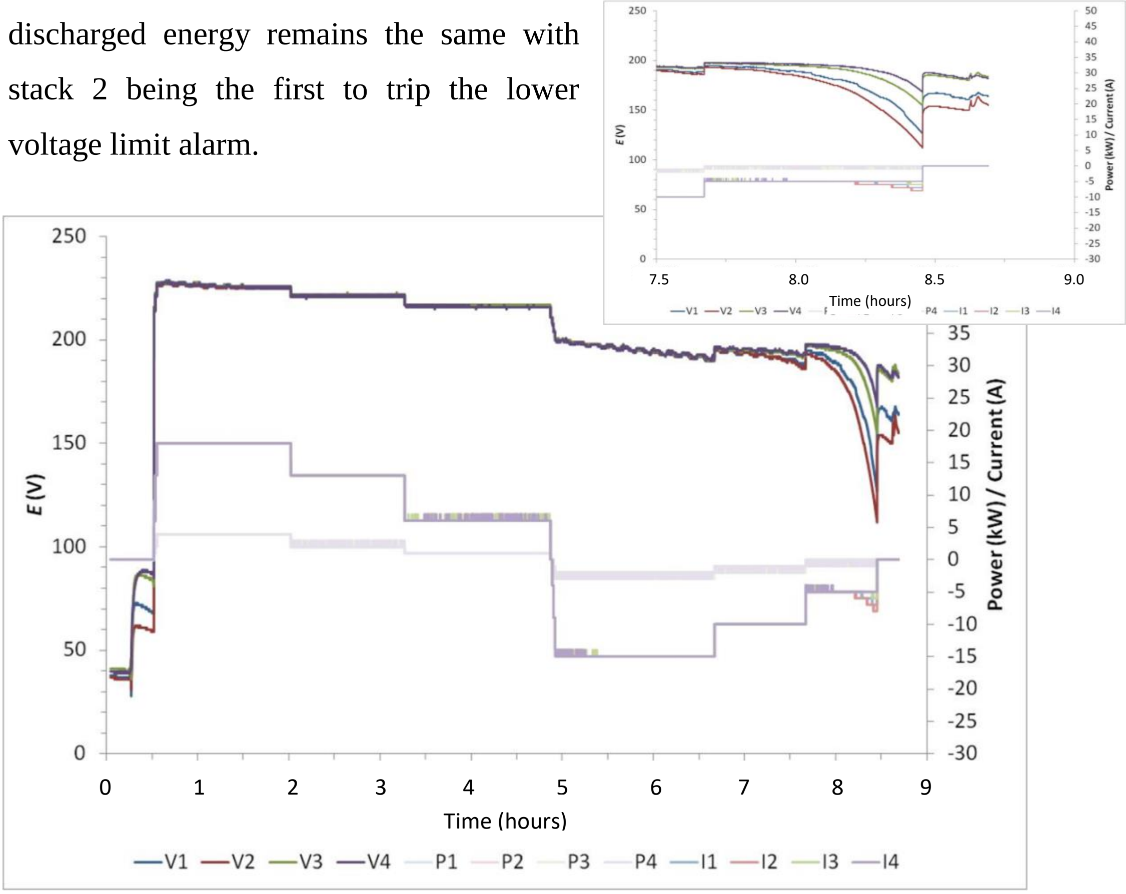

Figure 7.7 Staggered charge/ discharge cycle

Run 4

This schedule of work was to test the recommended charge duration at the specified parameters established in Run 1. Additionally, a modification was made to the procedure for the strip cycle. The stripping cycle was to achieve <1 V as opposed to the original <5 V specification (shown in Appendix). A charge of 17 kW for 240 minutes achieved a charged energy of 68.08 kWh with the follow up discharge cycle at −12 kW for 240 minutes achieving an output energy of −41.83 kWh. This gave a DC/DC efficiency of 62% and an AC/DC efficiency of 56% with the recorded charge and discharge energies being 68.06 and −41.83 kWh respectively.

Figure 7.8 shows that, once again, the lower voltage alarm was tripped. However, in this instance it was stack 4 that tripped the alarm rather than stack 2 which has been the case in the last two instances.

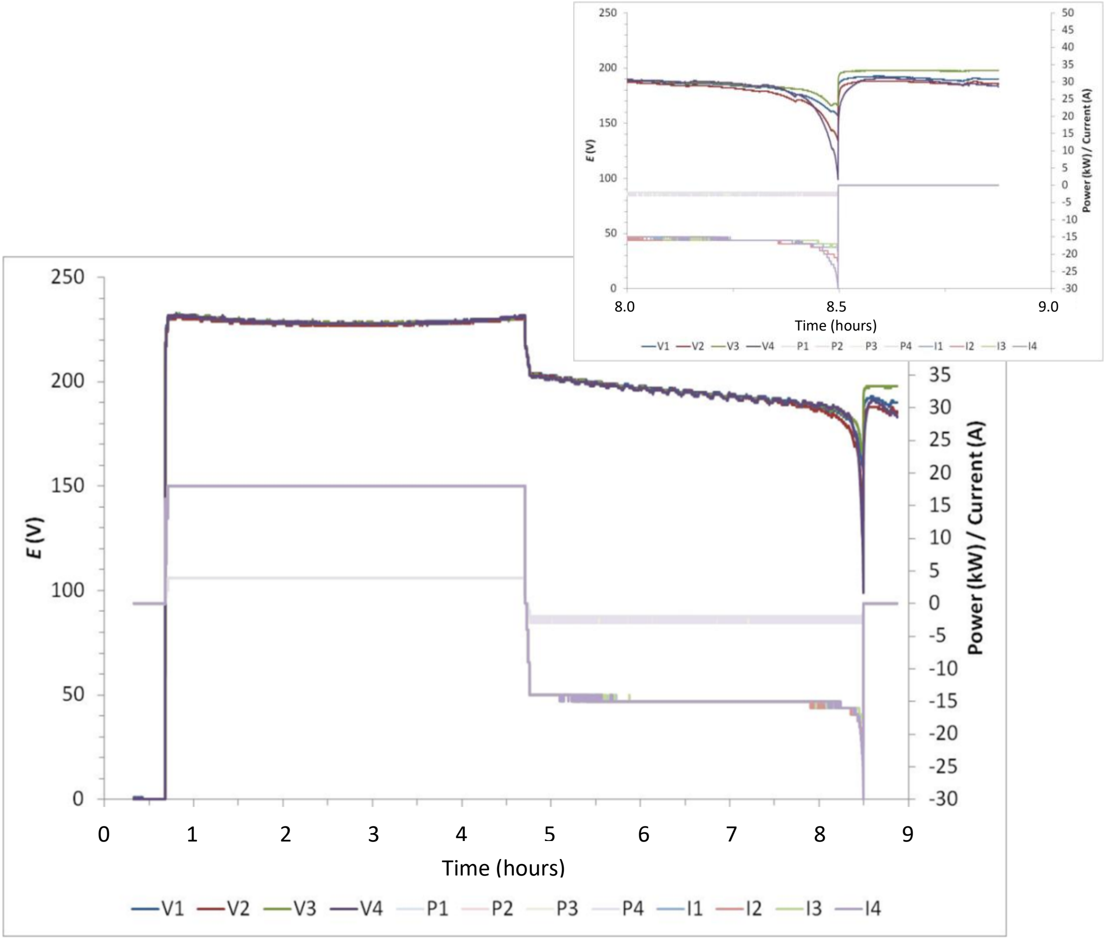

Figure 7.8 Charge 17 kW/ Discharge −12 kW for 240 minutes each cycle

Run 5

The objective for this schedule of work was to attempt to increase the efficiency of the battery by decreasing the power output from −12 kW to −8 kW. The charge cycle was kept at the specified power of 17 kW for a shorter period (180 minutes) achieving an energy input of 51.11 kWh. This was to compensate for the extended time required during the discharge cycle due to the power output being lower to be able to complete the charge/discharge cycle within a reasonable working day. The discharge rate of −12 kW was set up for 360 minutes. However, the lower voltage alarm was tripped before this time was achieved resulting in an output of −33.69 kWh. This resulted in the DC/DC efficiency being 65.91% and the AC/DC efficiency 55.46% with recorded charge and discharge being 56.0 kWh and −31.06 kWh respectively.

Figure 7.9 shows that stack 2 tripped the low voltage limit alarm. Despite the stacks maintaining similar voltages for most of the cycle these variances become more apparent at the end of the cycle. However, despite stack 2 consistently tripping the alarm, it is not believed that solving this stack’s inefficiency that the overall efficiency would increase by any appreciable margin. This is drawn from the fact that all the stacks exhibit similar characteristics in that they are starting to sharply decrease and would trip the alarm in a similar time frame.

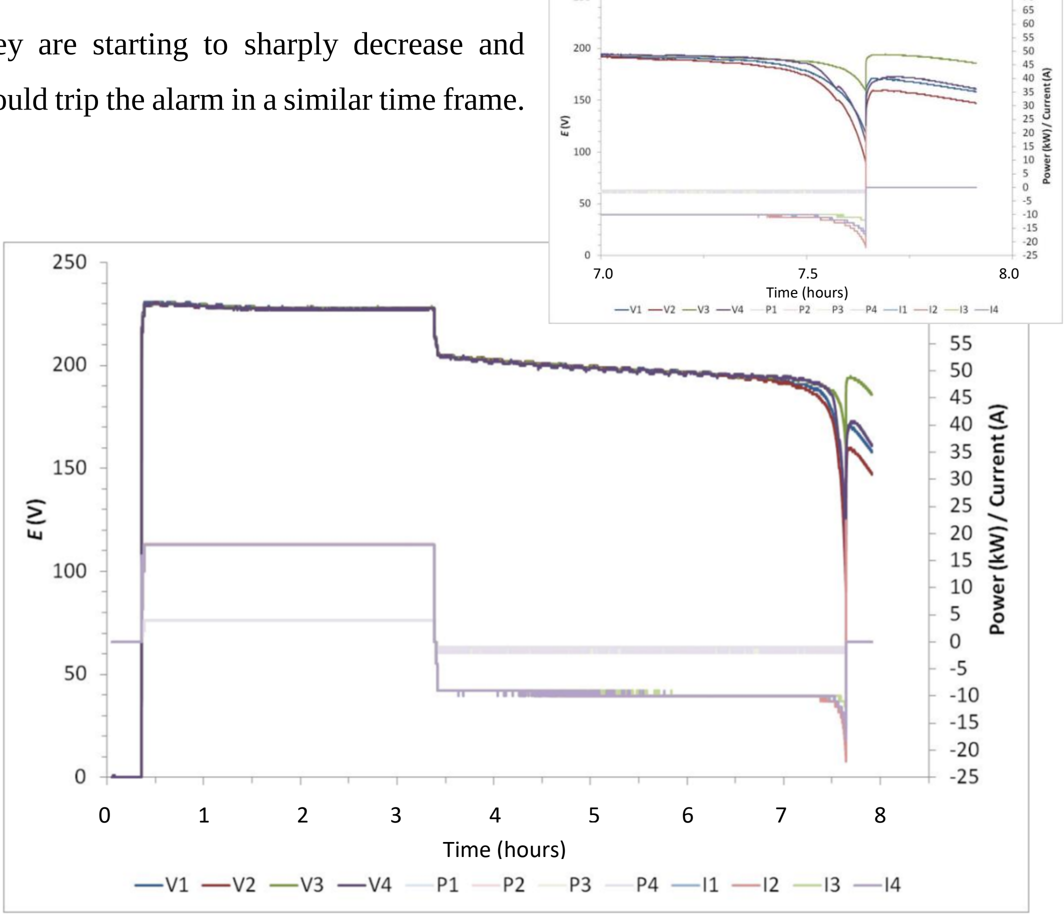

Figure 7.9 Charge 17 kW/ Discharge −8 kW

Run 6

Like the objective for Run 5, this schedule of work was aimed at observing the effect that lowering the power output to 4 kW would have on the overall efficiency. The charge cycle achieved 51.12 kWh from 240 minutes at 17 kW (for 180 minutes), which is consistent with previous runs. The discharge at −4 kW for 420 minutes achieved an output power of −27.84 kWh resulting in a DC/DC efficiency of 55% and an AC/DC efficiency of 43.4% (with recorded charge and discharge being 56.1 kWh and −24.36 kWh respectively).

However, it can be seen from Figure 7.10 that the lower voltage alarm had not been tripped. Rather the time limit imposed in the schedule of work had been successfully reached leading to the battery to go to its shut down stage. It is uncertain if this would have achieved an efficiency of DC/DC 66%. However, it is certain that if allowed to continue until the lower alarm was tripped that the efficiency would have been significantly higher.

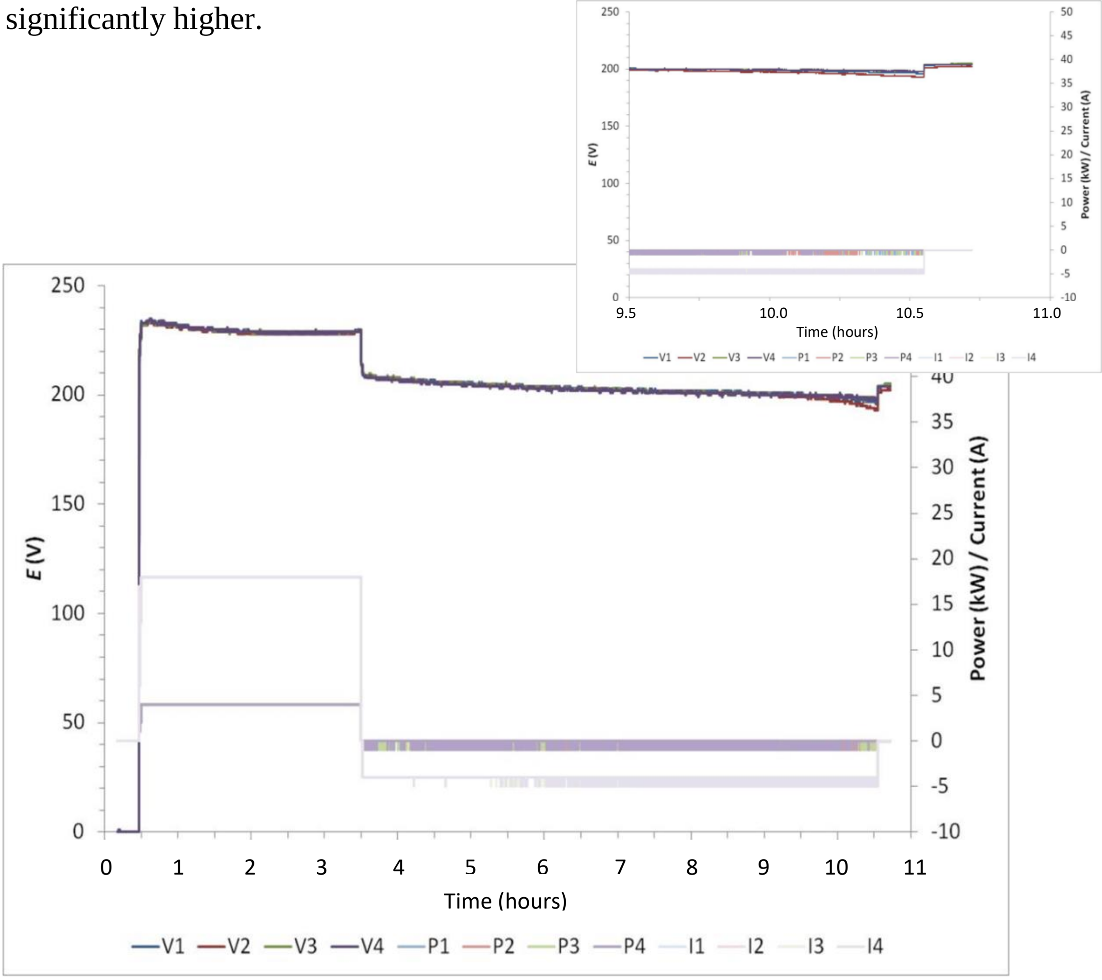

Figure 7.10 Charge 17 kW/ Discharge −4 kW

Run 7

This schedule of work was to evaluate whether shorter periods of time with a higher power output could achieve greater efficiencies. The battery was charged at 17 kW for 60 minutes achieving 17.23 kWh (the over-shot of the stored power is due to the incremental charged steps before reaching 17 kW *i.e.* 6 and 12 kW for one minute each). Discharging at the higher power output of −14 kW led to a discharge of −8.10 kWh with stack 4 causing the lower voltage limit to trip. The battery was then discharged at a lower power output of −8 kW and only achieved a further −0.68 kWh. This resulted in a DC/DC efficiency of 50.96% and an AC/DC efficiency of 38.69% (with recorded charge and discharge being 56.1 kWh and −24.36 kWh respectively).

Figure 7.11 shows both discharge cycles after a single charge cycle. At the end of the data series the drop-in voltage is due to a strip cycle being underway at the end of the day. It can be noted that both discharge cycles had their lower voltage limits tripped by a drop-in voltage from stack 4 despite other stacks remaining relatively high.

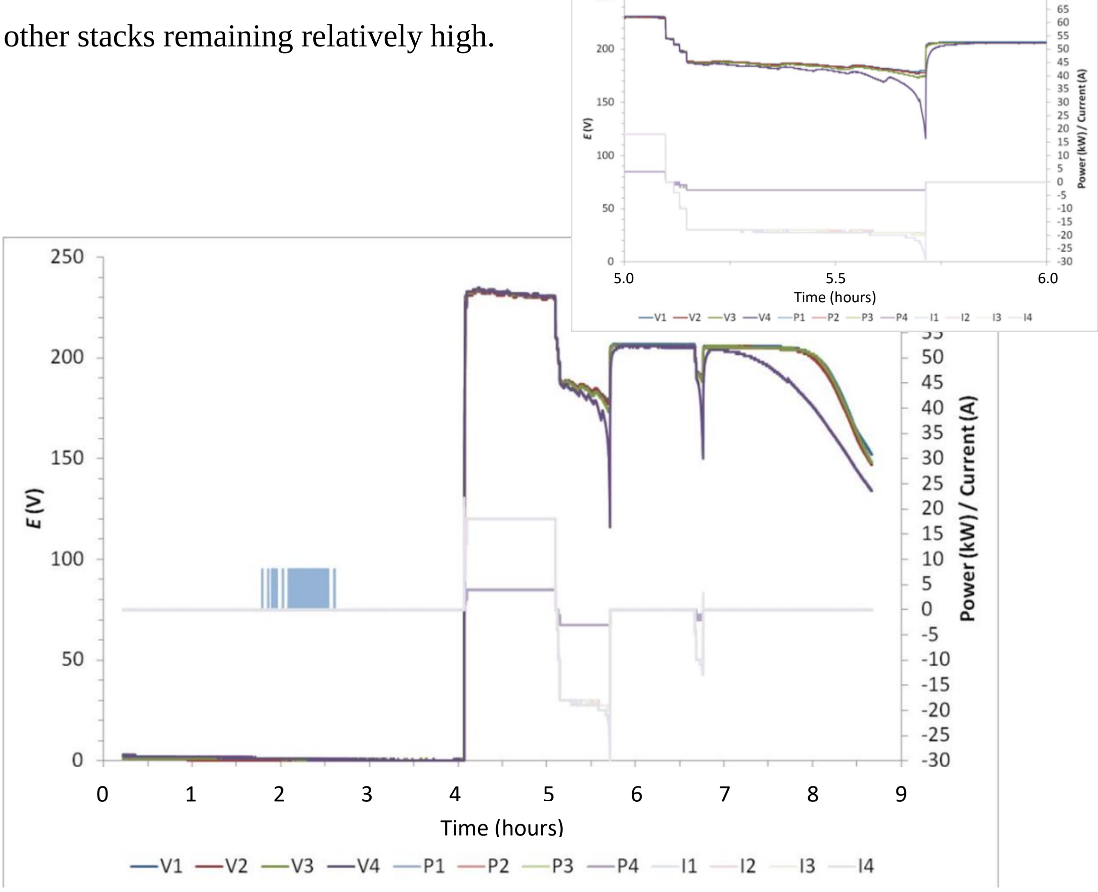

Figure 7.11 Charge 17 kW/ Discharge −14 & −8 kW (60-minute cycles)

Run 8

The schedule of work here was to see if the efficiency is scalable with increased charging time. In this instance the charge and discharge remained at 17 kW and −12 kW, respectively, though both times were reduced from 240 minutes to 180 minutes. After the cycles were completed the charged energy input was 51.12 kWh and the discharged output was −34.35 kWh, resulting in a DC/DC efficiency of 67.19%. The AC/DC efficiency was recorded to have 56.12 kWh of charged input and −32.12 kWh of discharged output giving an efficiency of 57.23%

Figure 7.12 shows that stack 4 tripped the alarm again with the other three stacks looking relatively high in comparison. The subsequent decrease in the voltage of the stacks after the alarm was tripped was down to a strip cycle being started in the attempt to reduce the OCP to less than 100 V.

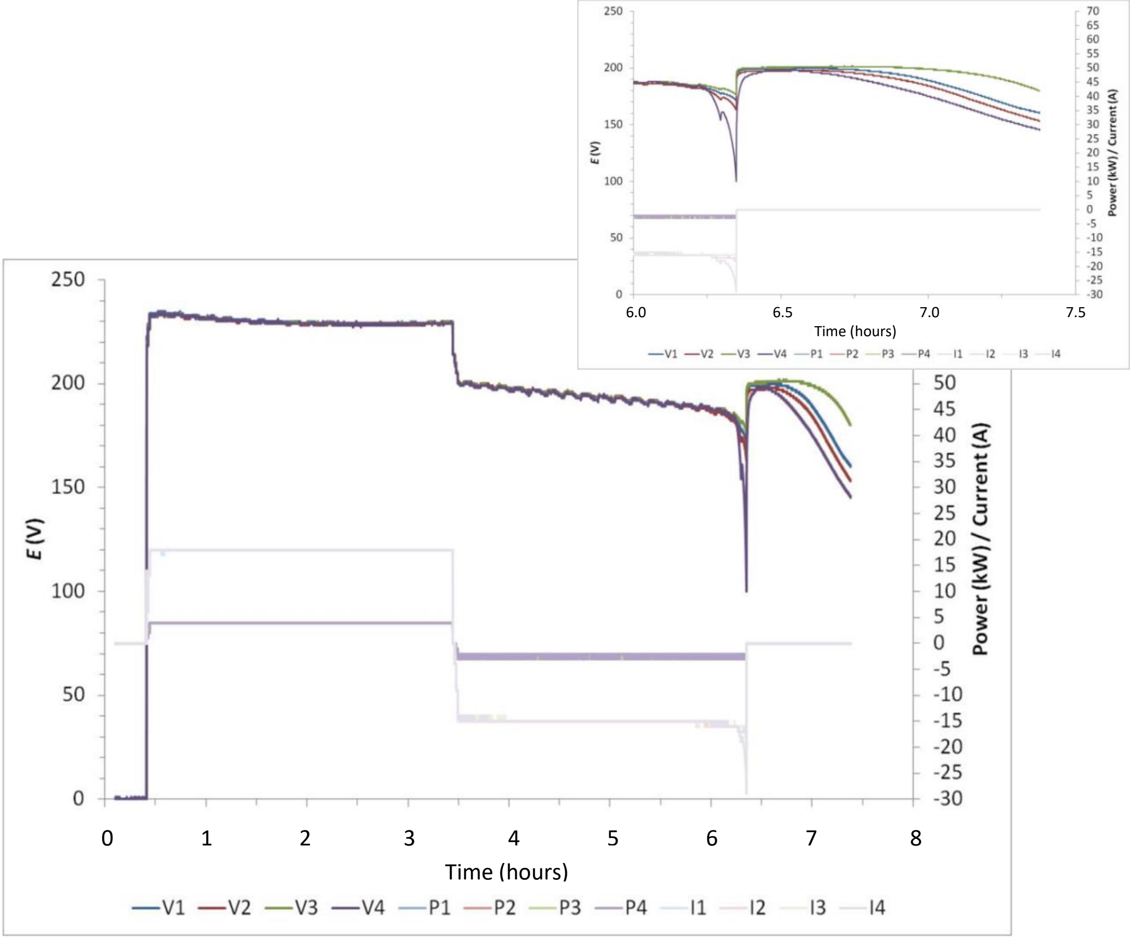

Figure 7.12 Charge 17 kW/ Discharge −12 kW (180-minute cycles)

Run 9

This schedule of work was to look at the scalability of reduced time from Run 8 with lower charge and discharge inputs. Charging at 12 kW for 180 minutes achieved 35.93 kWh of stored energy while the discharge cycle was ran at −8 kW for 180 minutes again and achieved an overall discharge of −23.77 kWh. Therefore, the overall DC/DC efficiency was 66.15% with the AC/DC recording 55.5% (with recorded charge and discharge being 39.53 kWh and −23.77 kWh respectively).

Figure 7.13 shows an outlier in the current data series (I2) at the end of the discharge cycle. This was assumed to be noise in the system. It can also be noted that both stacks 2 and 4 had decreased enough to trip the lower voltage limit alarm.

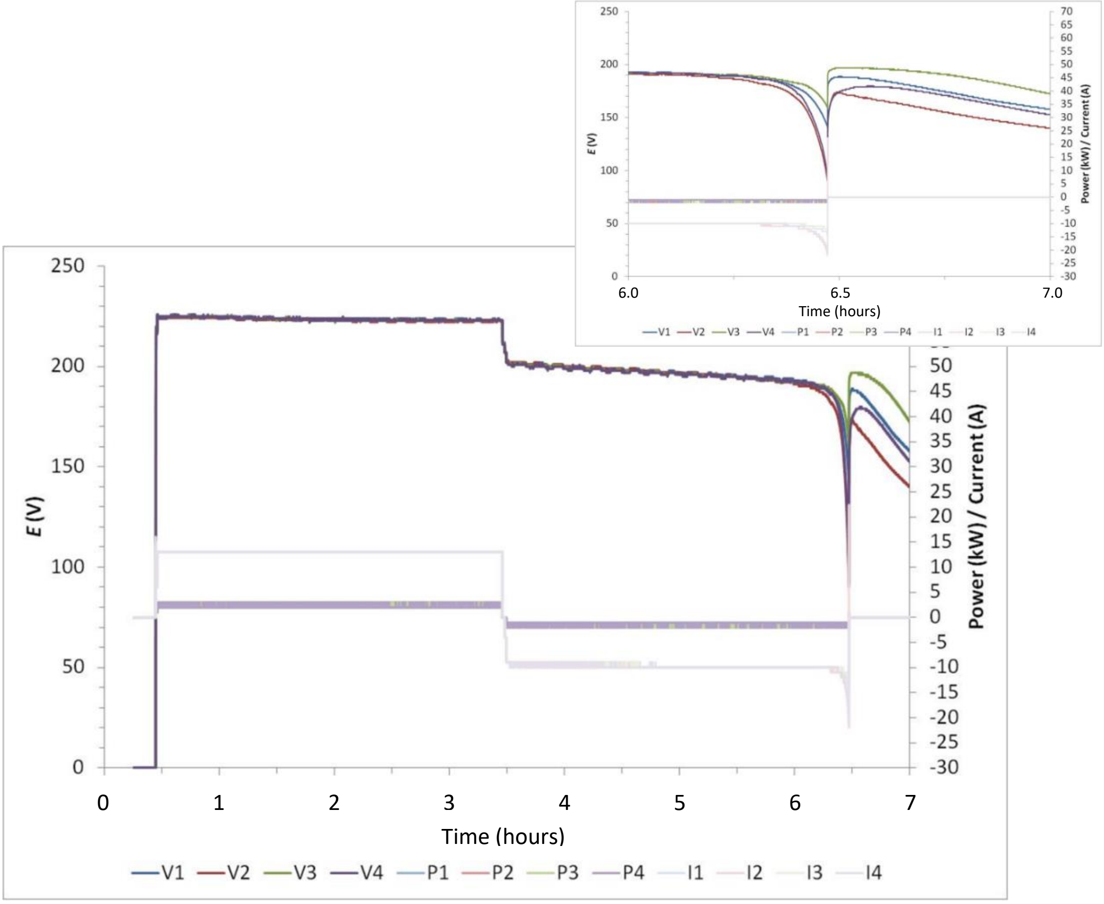

Figure 7.13 Charge 12 kW/ Discharge −8 kW (180-minute cycles)

Run 10

This schedule of work was to take further on the concept from the schedule of work of Run 9 by decreasing the charge and discharge rate values. Charging at 8 kW for 180 minutes achieved 23.84 kWh of stored energy while the discharge cycle was ran at −4 kW for 240 minutes and achieved an overall discharge of −14.63 kWh. Therefore, the overall DC/DC efficiency was 61.37% with the AC/DC recording 48.03% (with recorded charge and discharge being 26.67 kWh and −12.81 kWh respectively).

Figure 7.14 shows another outlier in the current data series (I4) at the end of the discharge cycle. It can also be noted that stack 2 had tripped the lower voltage limit alarm. This sequence yielded lower efficiencies than previously seen with the largest drop from DC/DC to AC/DC of 13% being recorded. The drop in DC/DC to AC/DC efficiency is again due to lower convertor efficiency when operating at low power. The poorer DC/DC efficiency could be explained by the battery not achieving a high enough SOC to support the power output on discharge, like that of the results from the work carried out on Run 7.

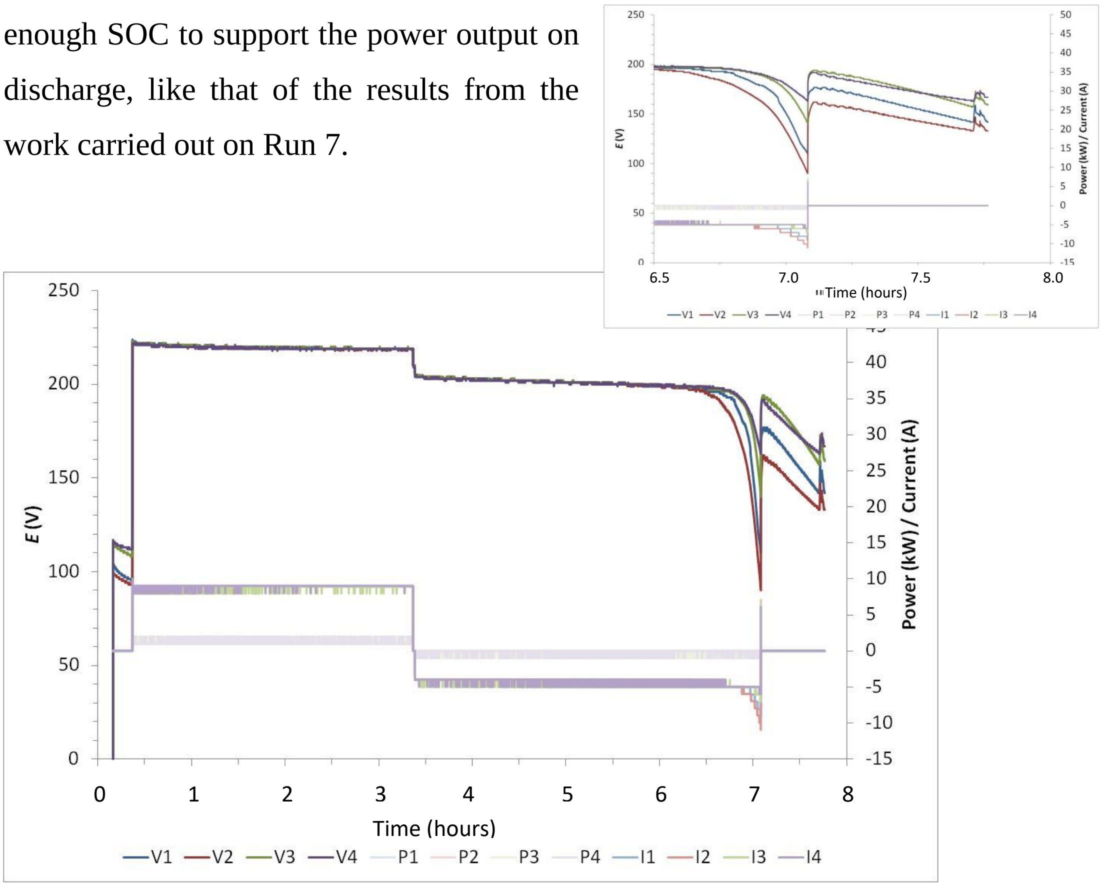

Figure 7.14 Charge 8 kW/ Discharge −4 kW

7.4 Conclusions

Several parameters have been tested on the 25 kW/ 50 kWh zinc bromide hybrid redox flow battery. As can be seen from Table 7.2, most of the sequences ran achieved an average DC/DC efficiency of ~66%. Only in two instances, runs 6 and 7, did this not occur. All schedules of work employed in these tests can be found at the end in the appendix.

	Charge Cycle			Discharge Cycle			Efficiency	
Run	Power (kW)	Time (min)	Charge (kWh)	Power (kW)	Time (min)	Discharge (kWh)	DC/DC [%]	AC/DC [%]
1	12	120	23.86	−8	120	15.65	66	55
2	17	200	59.62	−12	220	40.37	68	58
3	17/ 12/ 6	90/ 75/ 100	49.66	−12/ −8/ −4	105/ 60/ 50	32.18	65	54
4	17	240	68.08	−12	240	44.86	66	56
5	17	180	51.11	−8	255	33.69	66	55
6	17	180	51.12	−4	420	28.28	55	43
7	17	60	17.23	−14	60	8.78	51	39
8	17	180	51.12	−12	180	34.35	67	57
9	12	180	35.93	−8	190	23.77	66	56
10	8	180	23.84	−4	240	14.63	61	48

Table 7.2 Summary of Charge/ Discharge data

The schedule of work for Run 6 involved a discharge at a very low power which resulted in a long time required to discharge. However, unlike the other sequences employed in the tests, the lower voltage limit alarm, signifying discharged status on at least one stack had been reached, had not been tripped. The discharge therefore was not complete for this test and was limited by the discharge duration set up in the sequence. Certainly, it can be seen from the characteristics of the different stack voltages during discharge, in Figure 7.10, that the power output could have been maintained for longer as these were still well above 180 V with the voltage limit set at 100 V. The data for Run 7 involved a short charge duration of only 60 minutes and a high discharge rate which could not be sustained because of the low state of charge of the battery.

Despite these two outliers in the results, the efficiencies obtained were consistent regardless of value of power employed during charge and discharge. There were a few points worth of note: the lower the discharge rate, the larger the discrepancy between

DC/DC and AC/DC efficiencies and this is associated with a lower convertor efficiency at these low powers. It is noticeable that the first stack to reach the voltage limit during discharge is either stack 2 or 4. As this was a research and development rig, the flaws of these stacks could have been from a flaw in their manufacture.

Reviewing the stripping data (Appendix), when the electrolyte flow is left on without any power being applied to the stacks, the stack voltages slowly decrease. This implies a loss of stored energy which decreases the efficiency of the overall battery system. This loss in voltage could be the result of two factors. The first factor is that the pressure generated from the flow of electrolyte is forcing some of the electrogenerated bromine through the porous separator causing self-discharge with the plated zinc. The second factor could be that the flow is dislodging some of the plated zinc causing a drop-in efficiency. The latter case could potentially be solved by allowing for a slower build-up in the flow rate from the pumps. However, it is more likely that the electrogenerated bromine is being pushed through the separator as the voltage drop is gradual over the period the electrolyte flow is left on.

Upon review of the profiles in the charge-discharge cycles, the value given for the state of charge (SOC) stored material is simply derived from the current passed through the battery's stacks. However, this does not consider any side reactions *e.g.* evolution of gases. If this were the case, the efficiency being at ~66% could be explained that reactions are occurring during the higher states of charge that are not reversible and would, therefore, not be recoverable. This can be mitigated by having staggered charges and discharges to ensure the power input/ output can be maintained at the relevant concentration levels. Capping the maximum level of charge would also prevent this risk from occurring. For instance, during charge, 17 kW could be used until a state of charge (SOC %) of 50% was achieved where the power could be decreased to 12 kW and then 8 kW when the appropriate SOC% is achieved. Additionally, the battery could "capped" at an SOC% of 80% to ensure that throughout the entire charge cycle the side reactions are minimised by providing a power input that the concentration of electroactive material at the electrode surface could maintain. During discharge, a similar sequence could be employed for the same reasons with a "lower SOC% cap" of 20%. This staggered sequence was tried, as can be seen from the data for Run 3, although the efficiency obtained was just slightly lower than under normal charge/discharge conditions. Again here, convertor losses at the lower power ratings could account for the lower efficiency values.

The end of this project saw this RFB being installed into a small, remote Scottish community, Findhorn. This was made possible due to the collaborative efforts of the University of Strathclyde, PNDC, Lotte Chemical, and the Findhorn community with supporting funding to facilitate this project from Local Energy Scotland.

7.5 Recommendations

Following the completion of this work, a report was submitted to Lotte Chemical with two summary recommendations: one aimed at immediate impact and another aimed at long-term development:

Immediate – The method in which Lotte Chemical wanted the batteries to be analyses was from a SOC 0% with the discharge to return to this state. However, as the battery approaches either SOC 0% or 100% the ohmic losses increase rapidly making it near impossible to return all the coulombic charge in a single cycle. The recommendation made was to operate the battery between two intermediate SOC % *e.g.* SOC 20% to 80%. This would result in the coulombic, and subsequently energy, efficiencies to dramatically increase over several cycles. This is common practise among large-scale redox flow batteries.

Long-term – One of the major areas of efficiency loss was through the necessitated down time to run a stripping cycle after every five charge/ discharge cycles. This is conducted to remove any zinc deposits on the electrode surface after a discharge cycle. Therefore, preventing any risk of short circuiting the system or piercing the separator. However, if developments could take place to develop additives that inhibit dendritic growth or novel cell designs to reduce their formation, this would increase the confidence of the battery's operation and allow for the stripping cycle to be required less frequently. This would result in the overall operating time of the battery to increase and be active for a greater percentage of its life cycle.

8. EPFL

8.1 Introduction

Switzerland introduced the "Energy Strategy 2050" strategy after the Fukushima incident in Japan and this was recently accepted, *via* public vote, in 2017. This aims to reduce the nation's energy consumption, increase energy efficiency and promote the use of renewable energy sources[126]. In 2016, Switzerland produced less than 0.2% of their electricity demand from wind energy: producing 600 GWh per year[127]. This new strategy aims to increase that capacity to 4000 GWh per year by 2050. In addition, solar energy is set to produce 20% of electricity in Switzerland by 2020 compared to the 1% attained in 2013[128]. However, it is appreciated that energy supplied from renewable sources is often intermittent and can fluctuate significantly depending on weather and location within Switzerland[129,50]. To counter this and achieve the strategic goals, significant interest lies in developing a feasible energy storage strategy to improve the nation's energy efficiency and security.

One energy storage system, located at the Station d 'épuration (STEP) facility in Martigny, is a 200 kW/ 400 kWh vanadium flow battery, based on the type 1 model using concentrated 2 M sulphuric acid and was provided by Gildemeister and operated by École Polytechnique Fédérale de Lausanne – Laboratory of Physical and Analytical Electrochemistry (EPFL – LEPA). This battery forms the centrepiece of the refuelling station which also hosts an electric vehicle fast charger (50 kW), and two electrolysers which produce hydrogen for the refuelling of the centre's fuel cell vehicles[130,131]. The objectives of this demonstration project is to investigate the connections of the battery to the grid and to better understand energy transfer from the grid to transport applications. Additionally, the site can simulate energy productions from intermittent energy sources to determine the battery's capability to store this excess energy for later use.

The purpose of this chapter is to relate the work that was carried out at the energy centre which was to analyse and characterise this redox flow battery and determine its capacity, efficiencies, the sources of energy losses, self-discharge rate, response time, functionality and commercial viability based on the available applications.

8.2 Experimental

The analysis of the 200 kW/ 400 kWh vanadium RFB operations required large volumes of data to be recorded in each run. This was achieved through two recording systems: Siemens TIA Portal Program and an APPA 503 multimeter Logger. These recorded the data successfully at specified time allotments during the batteries work sequence. The Siemens TIA Portal Program and the operation of the battery could both be accessed using the TeamViewer (12): software which grants remote access to other computer systems.

Siemens TIA Portal Program

The data logger, specific to the battery, was in the Siemens TIA Portal program under PC Station FB200400 > HMI_RT_8 > Historical Data. This opened a window with an editable file named "Name Here", indicated by point A in Figure 8.1. Before continuing, all the time allotments were altered to the desired duration between data points (point C in Figure 8.1). However, the file could only record 500,000 data points from 64 individual parameters for each time allotment, meaning that the total run durations vary in relation to the frequency of the data (Table 8.1).

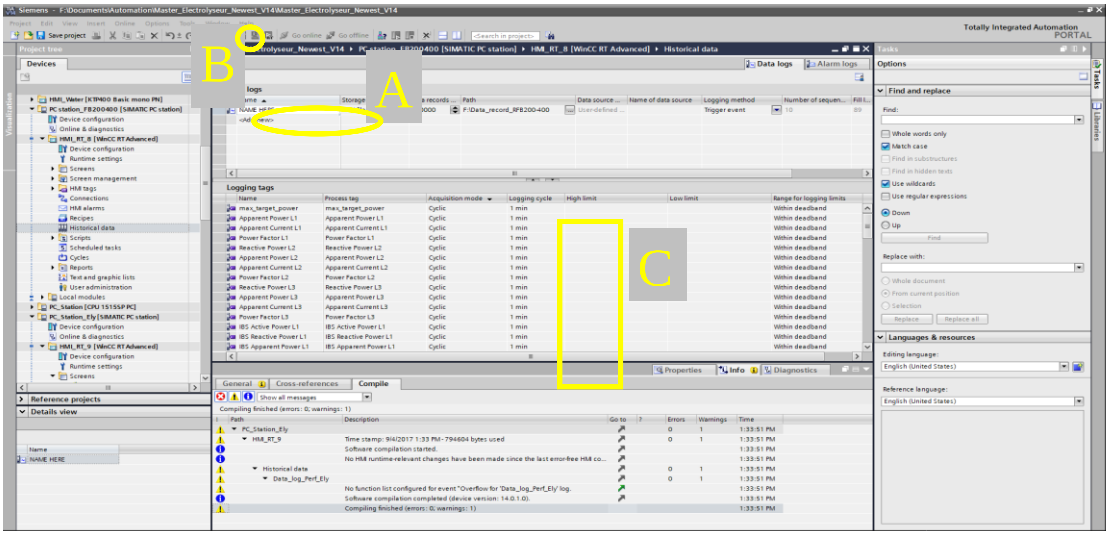

...logs

...ame	Storage	...records ...	Path	Data source ...	Name of data source	Logging method	Number of sequen...	Fill l...
NAME HE...		...0000	F:\Data_record_RFB200-400	User-defined ...		Trigger event	10	89
<Ad... new>								

Logging tags

Name	Process tag	Acquisition mode	Logging cycle	High limit	Low limit	Range for logging limits
max_target_power	max_target_power	Cyclic	1 min			Within deadband
Apparent Power L1	Apparent Power L1	Cyclic	1 min			Within deadband
Apparent Current L1	Apparent Current L1	Cyclic	1 min			Within deadband
Power Factor L1	Power Factor L1	Cyclic	1 min			Within deadband
Reactive Power L2	Reactive Power L2	Cyclic	1 min			Within deadband
Apparent Power L2	Apparent Power L2	Cyclic	1 min			Within deadband
Apparent Current L2	Apparent Current L2	Cyclic	1 min			Within deadband
Power Factor L2	Power Factor L2	Cyclic	1 min			Within deadband
Reactive Power L3	Reactive Power L3	Cyclic	1 min			Within deadband
Apparent Power L3	Apparent Power L3	Cyclic	1 min			Within deadband
Apparent Current L3	Apparent Current L3	Cyclic	1 min			Within deadband
Power Factor L3	Power Factor L3	Cyclic	1 min			Within deadband
IBS Active Power L1	IBS Active Power L1	Cyclic	1 min			Within deadband
IBS Reactive Power L1	IBS Reactive Power L1	Cyclic	1 min			Within deadband
IBS Apparent Power L1	IBS Apparent Power L1	Cyclic	1 min			Within deadband

Compiling finished (errors: 0; warnings: 1)

Path	Description	Go to	?	Errors	Warnings	Time
PC_Station_Ely		↗		0	1	1:33:51 PM
HMI_RT_9	Time stamp: 9/4/2017 1:33 PM - 794604 bytes used	↗		0	1	1:33:51 PM
	Software compilation started.	↗				1:33:51 PM
	No HMI runtime-relevant changes have been made since the last error-free HMI co...	↗				1:33:51 PM
Historical data		↗		0	1	1:33:51 PM
Data_log_Perf_Ely		↗		0	1	1:33:51 PM
	No function list configured for event "Overflow for 'Data_log_Perf_Ely' log.	↗				1:33:51 PM
	Software compilation completed (device version: 14.0.1.0).	↗				1:33:51 PM
	Compiling finished (errors: 0; warnings: 1)					1:33:51 PM

Figure 8.1 RunTime program screen displaying the data log for the flow battery

To create a new file, which would record the live information, the name was changed before going to the Start Centre. Selecting "Transfer" brought up a loading window. Returning to the RunTime program and selecting the button highlighted as B, in Figure 8.1, brought up a new window where the option of "Overwrite All" appeared.

Checking this box and pressing load opened a new window with the HMI for the recorder. Sliding the FB200400 button on initiated the recording of the data. This could be checked by looking at the file's location where the data size of the file would increase depending on the time allotment selected for data recording.

Time allotment (seconds)	Total recording time
10	22 hours 43 mins
20	44 hours 3 mins
30	68 hours 16 mins
60	136 hours 36 mins

Table 8.1 RunTime recording time for various time allotments between data points

Once the cycle was completed, the slider on the recorder was turned off to prevent the data limit being reached: as the recorder would wipe the previous data recorded unless a new file name was set into the program. The CSV file from this data was used in Microsoft Excel to analyse the various data series recorded. A full list of the data tags recorded are shown in Appendix – Table of Recorded Data at the end of this chapter.

APPA 503 multimeter set-up

The multimeter was attached to an individual stack with the purpose of recording the voltage produced from this single stack: stack A11. The set-up involved two exposed wires with 100 Ω resistors soldered to each. The multimeter was connected to these as shown in Figure 8.2.

Figure 8.2 multimeter connected to single stack within the RFB

Before the multimeter was connected to the battery, it was necessary to set up the multimeter to ensure that its program recorded the DC potential during the measurements. This was done by setting the dial to “V” followed by pressing the button with the blue bar and observing that DC was visible on the display (point A in Figure 8.3). The multimeter was capable of recording 20,000 data points before the internal memory became full. This altered the length of recording available on the multimeter depending on the time allotment between each recorded data point. The time allotment was set by selecting the option “Log Rate” (point B in Figure 8.3) and setting the desired time in seconds for the measurement using the up and down function. Once this had been set, the value was confirmed by pressing “Enter” and then returning to the main screen (screen shown in Figure 8.3) by pressing “Cancel”. The voltage range was determined by the degree of precision used. For the flow battery in question, the range of 0 – 400 V_{DC} was used and indicated by there being only one decimal place. This could be altered with the “Range” button (point C in Figure 8.3) but it is worth noting the other ranges and associated errors to these in Table 8.2. Accuracy was ± (% of reading + 20*(number of digits)) at 23°C ± 5°C, where the number of digits is indicative to the last digit recorded *i.e.* if the reading were 41.16 V the error would be ± ((0.03% (41.16) + 20*(0.06))[132].

Potential range (V_{DC})	Digits	Error (%)
0 – 4	0.000	(± 0.03 % + 20d)
0 – 40	0.00	
0 – 400	0.0	
0 – 1000	0	

Table 8.2 Potential ranges on the multimeter

Finally, the multimeter could start logging the data by selecting “Data Log” (point D in Figure 8.3) and pressing “Enter”. The data recording was indicated by a number appearing above the voltage value indicated and should increase with every data point recorded. Once the recording had started, the multimeter was connected to the battery by inserting the cables into the appropriate ports: black cable to the “COM” port and red cable to “V” port.

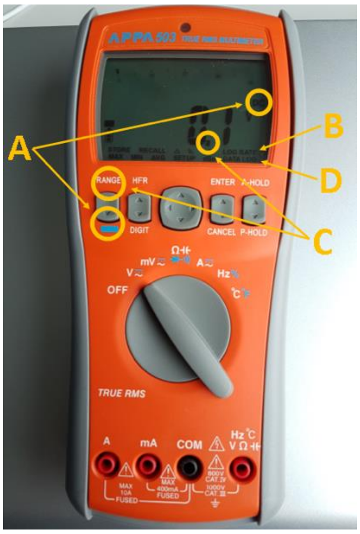

Figure 8.3 Multimeter display and functions. A = Set-up, B = Log rate, C = Range, D = Data log

Once the measurement was completed, the multimeter was disconnected from the battery by removing the two cables from the ports on the multimeter and downloading the data to a computer with the “Data Downloading” software, which allowed the data to be saved as a .txt file. The data collected could contain data from previous work sequences after the end of the run (as the memory is not wiped after the download is complete). This is due to the data collector overwriting the pre-existing data from the starting point until the memory limit is reached. Finally, it was important to note that the battery life on the multimeter is 100 hours and operated from four standard AA batteries.

Battery work sequences

These could only be accessed from the battery’s computer directly or through Team Viewer. This program allowed for work sequences to run and to monitor the battery in real time. From the main screen, to create a work sequence, the “Plan” button (Figure 8.4 (B)) needed to be selected to open a new screen. Each row in this screen signified a work function; the first column represented the task to be carried out with the second column indicating the desired power to be achieved. The command key for the first column was “wait=” followed by a number. This number signified how long (in minutes) the desired power input would operate for. The order of entry was important, as the desired power put into the first row would operate for the time in the second row, as shown in Figure 8.4 (A). The first-time input was the time required for the battery to activate the number the stacks (between 2 and 4) required for the desired power output. The optimal time for this was found to be three minutes. All the work sequences employed can be found in Appendix – Work Sequences with stated aims and results for each.’

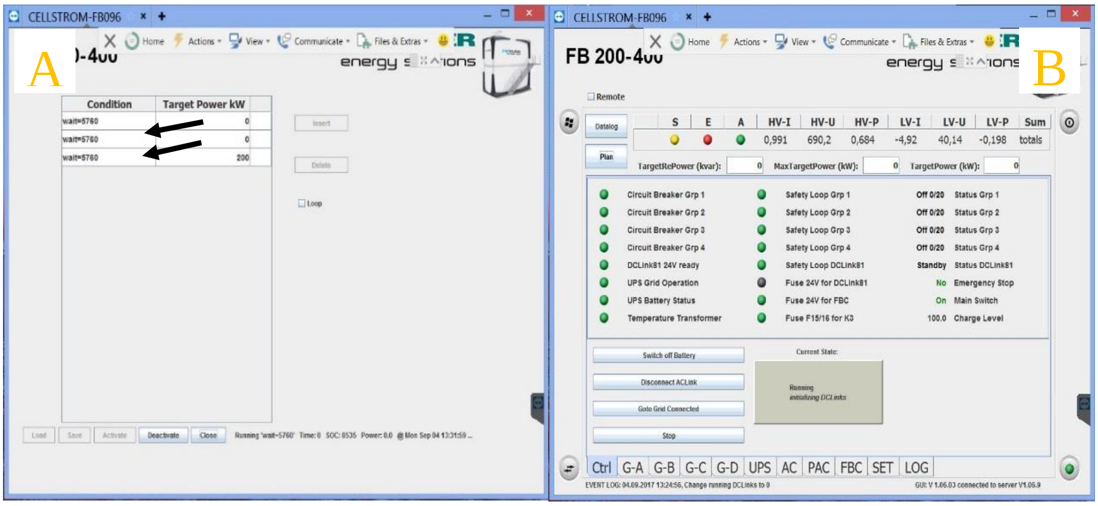

Condition	Target Power kW
wait=5760	0
wait=5760	0
wait=5760	200

Running 'wait=5760' Time: 0 SOC: 8535 Power: 0.0 @ Mon Sep 04 13:31:59 ...

S	E	A	HV-I	HV-U	HV-P	LV-I	LV-U	LV-P	Sum
●	●	●	0,991	690,2	0,684	-4,92	40,14	-0,198	totals

TargetRePower (kvar): 0

MaxTargetPower (kW): 0

TargetPower (kW): 0

●	Circuit Breaker Grp 1	●	Safety Loop Grp 1	Off 0/20	Status Grp 1
●	Circuit Breaker Grp 2	●	Safety Loop Grp 2	Off 0/20	Status Grp 2
●	Circuit Breaker Grp 3	●	Safety Loop Grp 3	Off 0/20	Status Grp 3
●	Circuit Breaker Grp 4	●	Safety Loop Grp 4	Off 0/20	Status Grp 4
●	DCLink81 24V ready	●	Safety Loop DCLink81	Standby	Status DCLink81
●	UPS Grid Operation	●	Fuse 24V for DCLink81	No	Emergency Stop
●	UPS Battery Status	●	Fuse 24V for FBC	On	Main Switch
●	Temperature Transformer	●	Fuse F15/16 for K3	100.0	Charge Level

Current State:

Running
initializing DCLinks

EVENT LOG: 04.09.2017 13:24:56, Change running DCLinks to 0

GUI: V 1.06.03 connected to server V1.06.9

Figure 8.4 (A) An example of a work sequence with the arrows signifying what desired power is associated with the following time command. (B) The main screen shows some basic information and the operation state of the battery

Once the work sequence had been set, the battery could be started or stopped by pressing the “Activate” and “Deactivate” buttons, respectively. Once activated, the data acquisition could be followed on this screen *e.g.* state of charge (SOC), time progressed into step, desired power of the step and the real time of the battery operation. Selecting “Close” returned to the main screen where the “Plan” button became red. During the operation of the battery, various data sets could be seen from the main screen, such as the FBC screen and the live output screen. The points of reference on the main screen were the charge level, the number of stacks in use and any errors that could have occurred. The FBC screen (Figure 8.5 (A)) could display more data such as the open circuit potential (OCV), the temperature is the stack was operating at and the hydrogen level present within the tank. Finally, the live output screen (Figure 8.5 (B)) displayed four dials which represented the charge level, the power being applied to/taken from the battery, the DC BUS voltage and the reactive power.

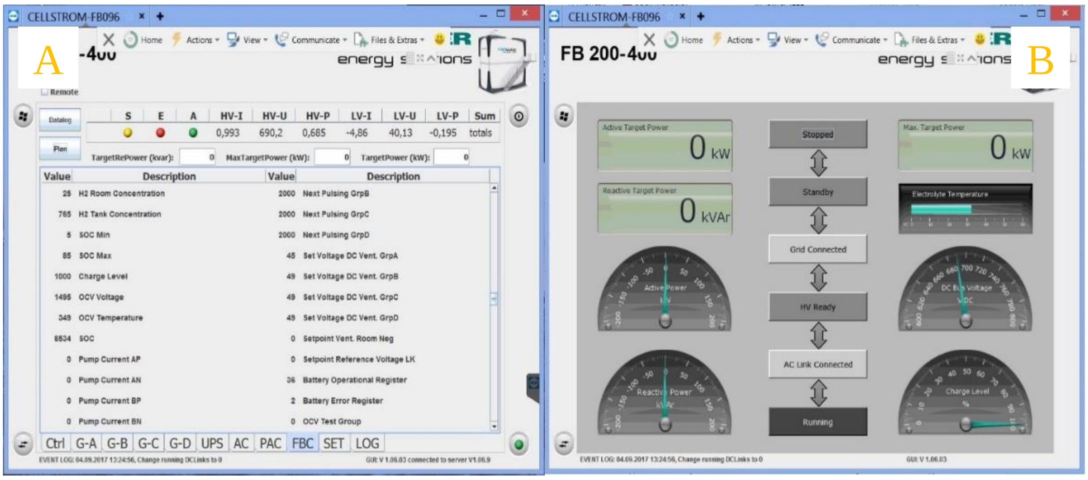

S	E	A	HV-I	HV-U	HV-P	LV-I	LV-U	LV-P	Sum
●	●	●	0,993	690,2	0,685	-4,86	40,13	-0,195	totals

TargetRePower (kvar): 0
MaxTargetPower (kW): 0
TargetPower (kW): 0

Value	Description	Value	Description
25	H2 Room Concentration	2000	Next Pulsing GrpB
765	H2 Tank Concentration	2000	Next Pulsing GrpC
5	SOC Min	2000	Next Pulsing GrpD
85	SOC Max	45	Set Voltage DC Vent. GrpA
1000	Charge Level	49	Set Voltage DC Vent. GrpB
1495	OCV Voltage	49	Set Voltage DC Vent. GrpC
349	OCV Temperature	49	Set Voltage DC Vent. GrpD
8534	SOC	0	Setpoint Vent. Room Neg
0	Pump Current AP	0	Setpoint Reference Voltage LK
0	Pump Current AN	36	Battery Operational Register
0	Pump Current BP	2	Battery Error Register
0	Pump Current BN	0	OCV Test Group

```
EVENT LOG: 04.09.2017 13:24:56, Change running DCLinks to 0
GUI: V 1.06.03 connected to server V1.06.9
```

Active Target Power 0 kW
Reactive Target Power 0 kVAr
Max. Target Power 0 kW

```
EVENT LOG: 04.09.2017 13:24:56, Change running DCLinks to 0
GUI: V 1.06.03
```

Figure 8.5 (A) The “FBC” screen shows more in-depth data such as SOC, OCV, errors and H_2 concentrations. (B) Live action screen shows the real power being applied with the DC Bus voltage and charge level

From these recorded values and operational programs, many cycles were performed at various levels of power to assess this battery. The charge level limits were determined by allowing the battery to charge/ discharge at 200 kW until it reached its charge level limitations (0-100%) which were the equivalent to the SoC being 5-85% limits. This data allowed for the stored energy capacity and the charge/discharge profiles to be understood for the individual runs. The cycles from the battery could charge for a theoretical time that would achieve 100% charge level and immediately discharge. This gave the initial evaluation of the system’s coulombic efficiency and, from the multimeter attached to the individual stack, the voltage efficiency.

The battery was then operated using incremental power levels to understand the power requirements for the centrifugal pumps, the AC/DC and DC/DC convertor efficiencies and the accuracy of the OCV value in assessing the SoC. Finally, the battery was also operated under standby condition with a various numbers of stack groups being kept active. This was measured over a 48-hour period to determine the extent of self-discharge in the system.

8.3 Results

Battery Characteristics

The 200 kW/ 400 kWh vanadium RFB, shown in Figure 8.6 (A), comprised of four groups of stacks and two electrolyte tanks. Each group had twenty stacks individually connected to the main DC line with a DC/DC convertor. The mains voltage was connected to the battery via the AC/DC convertor (three phase AC). A single stack consisted of 27 bipolar cells, an example design of which is shown in Figure 8.6 (B), which has a carbon composite as the bipolar current collector. Attached to these current collectors were GFD 4.6 graphitic felts with a dimension of 28 cm × 19.5 cm × 0.46 cm for each felt electrode. With a stated surface area of 0.4 $m^2\ g^{-1}$. Therefore, with a sample piece of GFD 4.6 of 20 cm^2 weighing 3.3 g, this would mean that the sample piece had a surface area of roughly 1.32 m^2. Scaling this up to the size of a typical electrode would give a surface area of 36.0 m^2 and the entire battery an area 15.6×10^4 m^2. The membrane was unknown, but it was assumed that it is a type of proton exchange membrane.

For the operation of the battery, the positive and negative electrolytes were pumped into each group of stacks from a centrifugal pump. The total electrolyte volume was 26,000 litres and consisted of 1.6 M vanadium species in concentrated sulphuric acid (2 M). The battery also operated many sensors to measure and control the ventilation, hydrogen sensor, temperature, electrolyte level in the tanks, electrolyte leakage, *etc*. These sensors allowed for regulated control of the operational temperatures, balancing of the electrolytes and to detect any potential errors within this system. There were two issues which were known with this RFB system in that two of the stacks (Stack A07 and Stack C19) or their corresponding DC/DC convertors, were faulty.

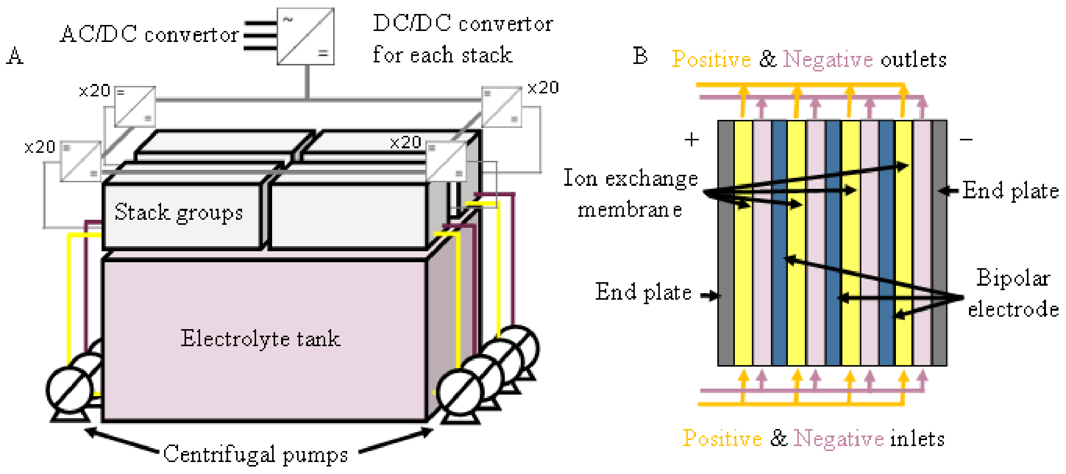

Figure 8.6 (A) Simple representation of the 200 kW/ 400 kWh vanadium RFB. (B) Structure of the bipolar plates used in the stacks of the RFB

This battery was operated between nominal charge levels of 0% to 100% (on the HMI) which was between the states of charge 5% to 85% respectively. The control program within the battery also had in place measures to ensure that any potential risks are minimised, such as limiting the active power output during charge and discharge when the SOC reached the upper and lower limits of the charge level.

Figure 8.7 (A) shows the 200 kW of power being applied over time. However, when the charge level reached 90% SoC, the amount of applied power decreased linearly until it 100% SoC was achieved where the power had decreased to *ca.* 140 kW.

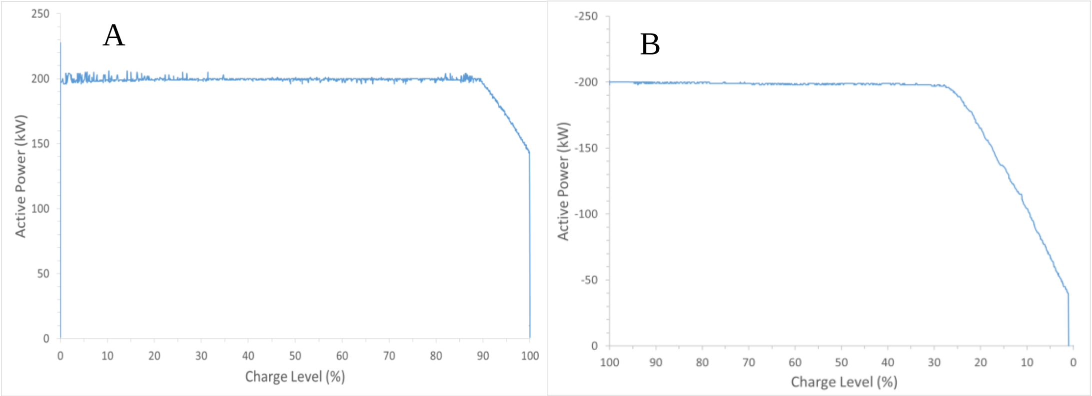

Figure 8.7 Power profiles when charging (A) and discharging (B) to the whole charge level range at nominal power, 200 kW

Figure 8.7 (B) represents the discharge profile, where 200 kW is being drawn from the

As can be seen, the behaviour during discharge was overall very similar to the charge profile. When the charge level had reduced to between 25% to 15% (depending on the applied voltage level), the power decreased along with it and although the initial drop was linear, the remaining 10% of charge had a reduced rate of return. Additionally, once the charge level had reached 0% SoC (40 kW), there were still pulses of power being applied. This was to prevent the charge level dropping below 0% SoC and to ensure that the stacks were sufficiently fed with electrolyte to reduce the response time when charging was restarted. The limiting of the power inputs and outputs, through set voltage limits at these stages was to minimise the risk of secondary reactions (in terms of H_2 evolution or vanadium precipitation from a drop in acidity) and damage to the electrode materials[133]. The issues relating to the rate of self-discharge and the power applied to the pumps (and other regulatory processes) will be analysed in a later section to determine the sources of the energy losses in the system.

System efficiency

Several cycles with various power set-points were conducted to determine the system's energy efficiency. These were operated between 50 – 200 kW in increments of 50 kW to provide information on the battery's power capability over this comprehensive range. In addition, a cycle at 60 kW was also run to simulate its function for the on-site alkali electrolyser. Connected through the STEP facility where both were connected and controlled from a central unit.

Figure 8.8 displays a typical data set achieved from these cycles. It is worth noting here that the charge level for the 200-kW charge was not taken to 100% to avoid the linear reduction in power near the charge level's upper limit. However, the battery was set to fully discharge to understand how much energy can be returned from the discharge cycle.

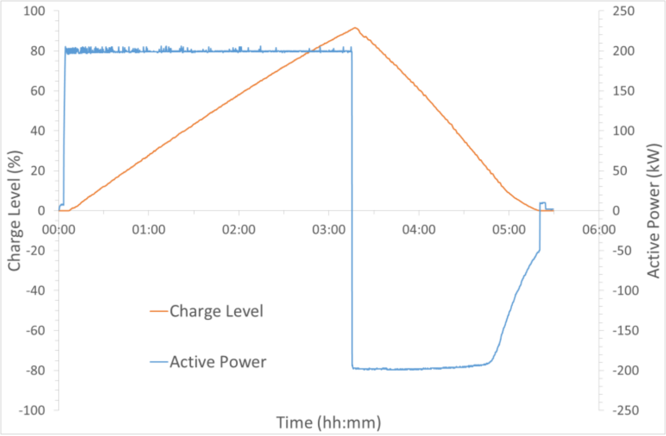

Figure 8.8 Charge and discharge cycle at 200 kW tracking the charge level

The energy efficiency is simply based on a ratio of the total energy returned from what was originally stored in the battery. Table 8.3 gives the full account of energy efficiencies for each cycle carried out. The battery maintained a consistent system energy efficiency at charging/discharging power ≥60 kW of 56%. At 50 kW, the energy efficiency found was 48%. The table also shows that cycling at 100 kW was repeated as the initial energy efficiency obtained was 47%. This lower performance was attributed to the higher electrolyte temperature accumulated from the cycle ran immediately prior to this one.

Cycle Power (kW)	Time Charging (mins)	Charged Energy (kWh)	Charge Level (%)	Time Discharging (mins)	Discharged Energy (kWh)	Energy Efficiency (%)
50	894.0	737.79	91.8%	426.7	352.68	48%
60	744.5	739.33	98.2%	419.0	416.15	56%
100 (a)	438.0	742.96	92.6%	216.3	350.27	47%
100 (b)	443.0	727.13	100.0%	272.0	434.79	59%
150	292.7	729.92	95.8%	172.0	397.44	54%
200	191.8	637.76	91.6%	125.0	364.79	57%

Table 8.3 Energy efficiencies of the various cycles

It can be noted that the maximum charge level achieved does not correlate with the amount of energy stored in the battery, as the 50 kW charge achieved a charge level of 91.8% with 737.8 kWh compared to that at 200 kW which achieved 91.6% with 637.8 kWh. However, these values were determined through the value of the OCV as opposed to simply calculating the theoretical charge level from the power input over time. Figure 8.9 shows this relationship between the charge level and the OCV as it is indicative with that expected if the Nernst equation is applied to the cell reaction. At the lower limit of the charge level it is observed from Figure 8.9 that the OCV starts to decrease rapidly. A similar response would also be observed at the upper limit of state of charge, but this was not observed on this battery as this was controlled by the charge level limit.

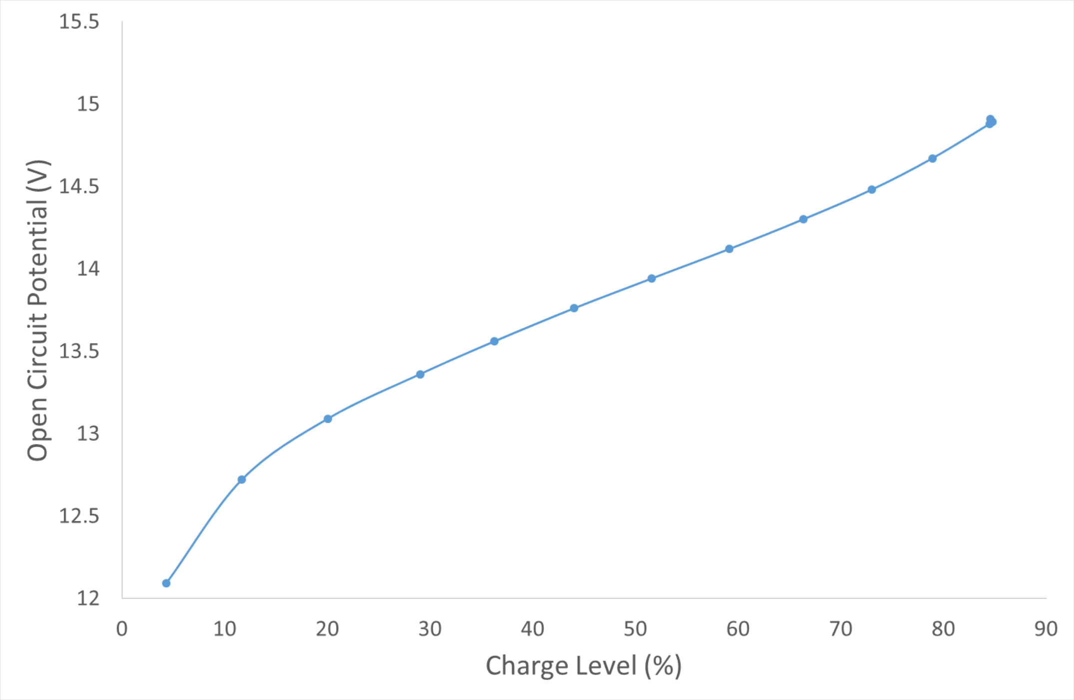

Figure 8.9 Relationship between the open circuit voltage and the battery state of charge

Voltage efficiency

To identify the various contributions to the voltage inefficiency, the measured energy efficiency was decoupled into its separate voltage and coulombic efficiencies. The voltage efficiency is the ratio of the average voltage output during discharge to that during the charge. Table 8.4 shows that the higher the power employed for charge/discharge, the lower the voltage efficiency.

Cycle Power (kW)	Mean Charge Voltage (V)	Mean Voltage Discharge (V)	Voltage Efficiency (%)
50	38.08	34.65	91.0%
60	37.73	34.97	92.7%
100	37.8	33.64	89.0%
150	38.55	32.65	84.7%
200	39.25	31.44	80.1%

Table 8.4 Voltage efficiency values

The change in voltage efficiency shown in Table 8.4 comes from ohmic losses due to internal resistances, from the membrane and electrolyte. Overpotential losses at the anode and cathode, associated with electron transfer processes at the electrode-electrolyte interface will also contribute to the lowering of the voltage efficiency. As the power is increased, the ohmic losses also increase due to the higher current density. This relationship is explained as $P = I^2 R$ and is apparent from Figure 8.10. At the latter stages of the discharge, it can be noted that the voltage started to decrease rapidly, which is from the effect of electrolyte composition, in not having enough reactants to sustain the reaction, though immediately plateaus for the remainder of the “discharge” time when −26.6 V was reached, indicating that the lower charge level limit was reached. However, the upper voltage limit is not achieved due to the restriction on the state of charge imposed by the upper charge level limit.

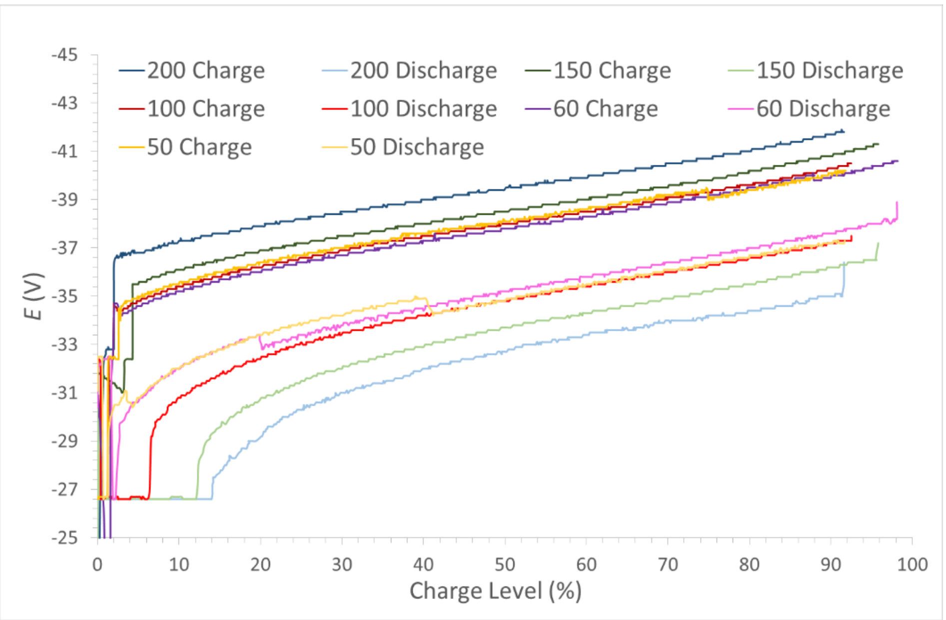

Figure 8.10 Voltage outputs from stack A11 at various constant power cycles

However, the voltage efficiency measured in this system was found to be in the range 80% to 93% which suggests therefore that the coulombic efficiency must be the main contributor to the low energy efficiency values obtained.

Identification of the energy losses

The overall system efficiency represented, in Table 8.3 shows the energy efficiency as measured on the AC electrical line. This efficiency includes all the energy consumed by regulatory systems, such as the centrifugal pumps used to circulate the positive and negative electrolytes through the four stacks; sensors used to monitor temperature, state of charge, hydrogen and leakages, and convertor losses between AC/DC links (at the same point as the regulatory systems) and DC/DC links (connected to each stack in the RFB). Figure 8.11 gives a visual representation of the order.

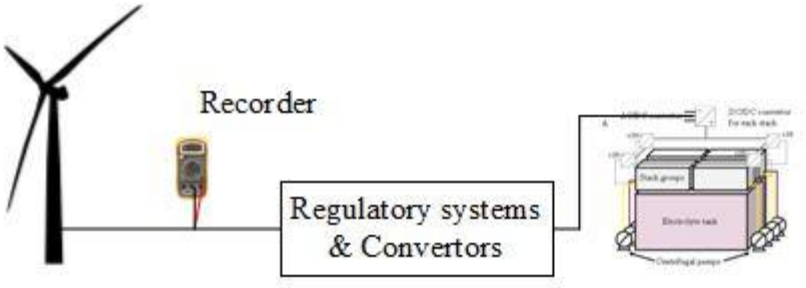

Figure 8.11 Placement of the data recorder of the AC line between the battery and power source

To determine the coulombic efficiencies, the method by which energy is stored and returned in this system must be considered as the following:

$$E_{eff} = \frac{(E_{Rec}+E_{Reg}+E_{Conv})_{discharge}}{(E_{Rec}-E_{Reg}-E_{Conv})_{charge}} \qquad \text{Eq. 4.5.1}$$

Where E_{Rec} is the recorded energy, E_{Reg} is the energy required by the regulatory systems, and E_{Conv} is the energy loss from the convertors at the respective charge and discharge cycles. Using these values, it allowed for the energy efficiency of the battery, to be independently determined. Thus, the coulombic efficiency could be determined from this and the measured voltage efficiency.

The following sections will determine the losses in the energy consumption by the pumps and the energy lost from the AC/DC and DC/DC convertors.

Convertor efficiencies

The AC/DC converter and the DC/DC convertors have inefficiencies associated with them. It was usually observed that the AC/DC convertor had larger losses than the DC/DC convertor. However, the values obtained from this system showed roughly equivalent losses possibly due to the number of DC/DC convertors this system operated. The DC/DC convertor losses could be up to 7% with the discharge typically performing worse than on charge. Table 8.5 shows these efficiencies at the various powers employed at charge/ discharge. The low voltage (LVP) and high voltage (HVP) values were recorded from the Siemens' program which represent the potentials before and after the DC/DC convertors from the entire system, with the ratio of low voltage to high voltage for charge and the high voltage and to the low voltage for discharge.

Power (kW)	HVP (V)	LVP (V)	DC/DC Efficiency
200	182	175	96.2%
-200	213	224	95.1%
150	139	134	96.4%
-150	163	171	95.3%
100	90	86	95.6%
-100	111	116	95.7%
60	49	46	93.9%
-60	69	74	93.2%
50	42	39	92.9%
-50	57	61	93.4%

Table 8.5 DC/DC efficiencies

Since the power to the regulatory systems originates from the AC power, the efficiencies are calculated in the following manner, using the values from Table 8.6.

$$\frac{AC}{DC}eff_{charge} = \frac{HVP}{(PGrid - Selfsupport\ P)} \times 100\% \qquad \text{Eq. 4.5.2}$$

$$\frac{AC}{DC}eff_{discharge} = \frac{(PGrid + Selfsupport\ P)}{HVP} \times 100\% \qquad \text{Eq. 4.5.3}$$

These losses can contribute up to 10% of the losses and typically show that the discharge losses are less than the charge loss. However, the data for 100 kW was an outlier within this trend: performing slightly better in the charge. These inefficiencies contribute to the system efficiencies, shown in Table 8.8, where the amount of energy returned recorded is a lot less than expected due to some of the energy being used in the regulatory systems and losing efficiency from convertors.

Power (kW)	P-Grid (kW)	Regulatory Systems (kW)	HVP (V)	AC/DC Efficiency
200	203.7	8.52	182	93.2%
-200	198.6	8.54	213	97.3%
150	151.8	8.33	139	96.9%
-150	150.5	8.32	163	97.4%
100	99.0	6.45	90	97.2%
-100	98.9	8.22	111	96.5%
60	62.6	8.09	49	90.0%
-60	60.6	6.98	69	97.9%
50	49.5	6.12	42	96.9%
-50	52.0	4.17	57	98.6%

Table 8.6 AC/DC Efficiencies

Pump energy consumption

Since the program used to control the battery did not record the power consumed by each pump throughout the cycle, the values were manually recorded for each stated power at three charge levels: 20%, 50% and 80%. From these values, the energy consumed between the three indicated charge levels were averaged and used as a representation of the pumps’ energy requirement over the given charge/ discharge cycle. The total energy consumed was then calculated from this power using the time of charge/discharge in Table 8.3. The values obtained are given in Table 8.7 with a full breakdown in

Appendix – Centrifugal Pump Power Consumptions. Table 8.7 shows that the amount of power used by the pumps is indicative to the number of stacks that were active to support a given cycle power. For instance, powers between 100 – 200 kW consumed roughly 8 kW, whereas for <100 kW, only 4.5 – 6 kW was required. This correlates to the number of stacks active, since 100 – 200 kW uses four groups, three groups for 60 – 100 kW and two groups for 50 kW. In addition, the lower the power employed for the charge/discharge cycles, the larger the contribution for the energy consumed by the pumps due to their prolonged operation. Furthermore, it can be noted that the energy consumed at any given power is greater during charge than at discharge. This is due to the charging cycle taking longer than the discharge cycle for any given applied power, as the power for the regulatory systems come from the AC mains during the charge cycle, whereas the power for these systems during the discharge cycle came from the energy stored in the battery which depleted the battery more quickly.

Cycle Power (kW)	Power to pumps (kW)	Time (mins)	Total energy consumed by pumps (kWh)
200	8.02	191.83	25.64
-200	7.92	125.00	16.49
150	8.00	292.67	39.01
-150	7.93	172.00	22.74
100	7.99	438.00	58.30
-100	7.94	216.33	28.63
60	5.97	744.50	74.04
-60	5.93	419.00	41.41
50	4.52	894.00	67.40
-50	4.60	426.67	32.71

Table 8.7 Pump power usage and total energy consumption for all powers used for charge and discharge

Electrochemical energy efficiency and coulombic efficiency

With the data for the energy consumption by the regulatory systems and losses from the convertors evaluated, the actual energy stored in the electrolytes could be determined. Using the altered efficiency equation previously described (Eq. 4.5.1), the corrected energy efficiency and voltage efficiency could be used to determine the coulombic efficiency.

During charge, the convertor losses and energy to the pumps could be subtracted from the total energy put into the battery whereas, during discharge, these would be added on to the energy returned to the load. In this way, a more accurate energy efficiency could be calculated. However, this did not consider the additional auxiliary systems power requirements (*e.g.* for the sensors, cooling systems, recording apparatus, *etc.*) and so, the efficiency would still be lower than the given value.

Table 8.8 shows the difference between the system efficiency (incorporating the losses from the pump energy consumptions and convertor losses) compared to the electrochemical energy efficiency. These losses in the system can account for up to 24% of the overall efficiency losses. In addition, the coulombic efficiency could now be determined from the voltage and energy efficiencies which yielded values between 73% - 97%. The 50 kW cycle provided the lowest coulombic efficiency (77%) and operating in the 60 – 200 kW power range gave on average ~90% efficiency. This fell within the range expected/observed for this system and, as evaluated from simple Faraday's law calculations and the monitoring of the open circuit voltage after the various charging/discharge regimes.

	Charge		Discharge				
Cycle Power (kW)	Energy in (kWh)	Energy Stored (kWh)	Energy out (kWh)	Energy Stored (kWh)	System Efficiency	Energy Efficiency	Coulombic Efficiency
50	737.79	596.62	352.68	415.61	48%	70%	77%
60	739.33	550.44	416.15	497.09	56%	90%	97%
100 (a)	742.96	632.08	350.27	408.11	47%	65%	73%
100 (b)	727.13	616.71	434.79	503.90	60%	82%	92%
150	729.92	642.95	397.44	450.66	54%	70%	83%
200	637.76	546.16	364.79	410.97	57%	75%	94%

Table 8.8 System, energy and coulombic efficiency from calculated consumptions

Effect of the electrolyte temperature

The overall system energy efficiencies were then examined as a function of the average temperature of both electrolyte solutions. The cycles that had the superior performances were found to be the runs where the electrolyte solution had low temperatures. Figure 8.12 and the data in Table 8.8 show that for the cycles operating at 150 kW and at 100 kW (a) had the lowest temperatures resulting in higher energy efficiencies. Additionally, this trend is also observed with the cycles that operated with the lowest efficiency also having the highest electrolyte temperature. However, the 60 kW cycle is the outlier to this trend as it produced one of the highest electrochemical efficiencies but had one of the higher electrolyte temperatures of. The step-like distortions during the charge for the lower powers could be an effect of the environmental change of temperature over the course of the run which included evening and night. Temperatures in Martigny, Switzerland, dropped significantly at night in comparison to the daytime temperature.

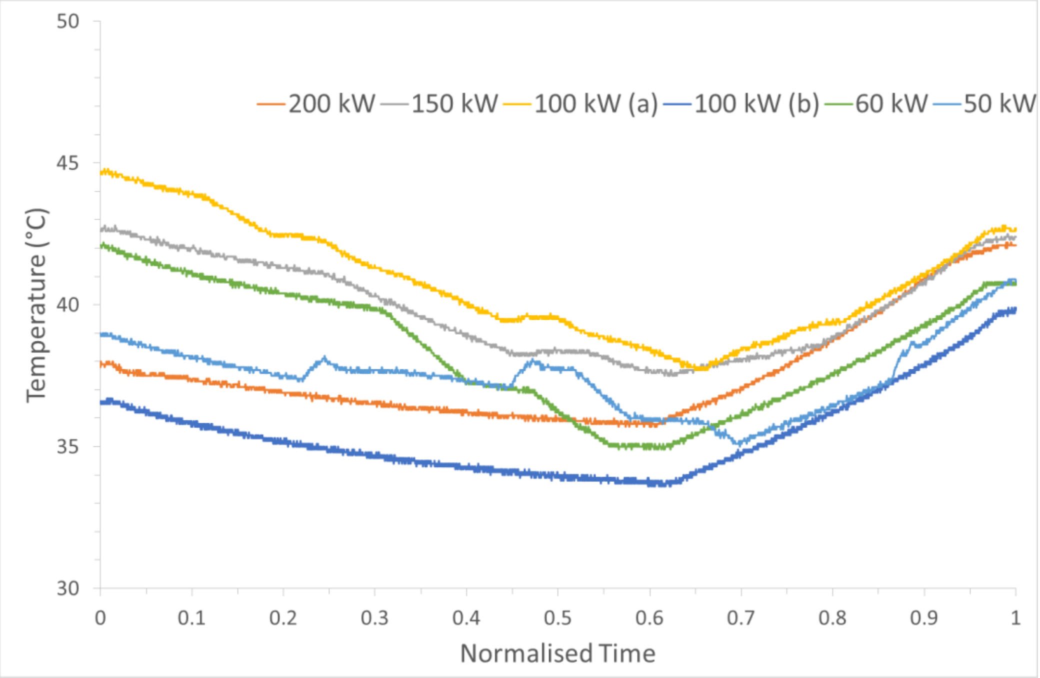

Figure 8.12 Temperature profiles for each cycle under a normalised time for direct comparison

In addition, these drops in temperature could be from the flow returning to the nominal temperature from a higher temperature caused from a previous discharge cycle. Alternatively, it could be an effect from the regulatory system using more coolant as response to a limit within the program being reached.

Charge inefficiencies

It was noted in Figure 8.13 that during charge, the gradient of the charge level decreases as the battery approaches the upper limit. This effect becomes more apparent with lower charging power as can be observed from the graphs in Appendix – Active Power/ Charge Level *vs.* Time. To assess the extent of the energy loss occurring from potential side reactions, the initial linear portion of the charge level at low levels was extended to create the trend the charge should follow if all the energy was used to charge the vanadium electrolyte. The equations for both lines were determined by linear regression and by integration, the respective areas under the curves were found. A limit of y = 100 was placed on the ideal curve and the difference between both curves allowed for energy used in the side reactions to be determined.

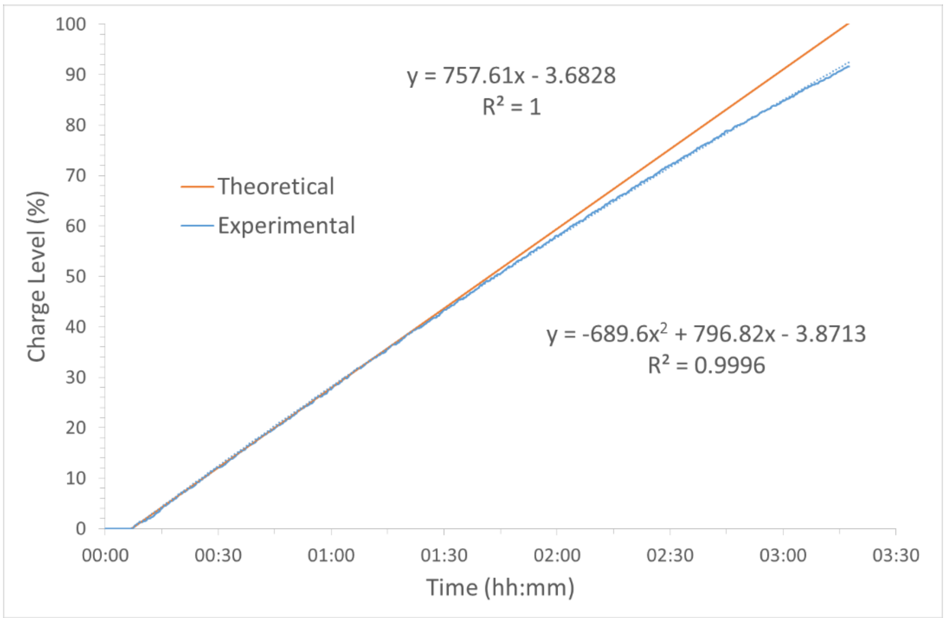

Figure 8.13 Theoretical charge level increase from power input to experimental charge level increase showing the extent of energy loss

The extent of the energy diverted into the side reactions correlates with the performances of the battery. Examining the 100 kW (a) and 50 kW cycle, which lost the most energy to side reactions, these were also the cycles with the highest electrolyte temperatures, as indicated in Table 8.9. This suggests that the temperature increase from 37±1 °C to 43±1°C could have provided a suitable environment to allow the hydrogen evolution reaction to occur at a rate which decreased the performance of the battery from the expected theoretical outcome. The losses from the system could be attributed to this effect and could also be potentially minimised with sufficient control on the electrolyte temperature. The loss of the input energy to these side reactions prolonged the charging of the battery to reach the set charge level limit. This resulted in additional energy being consumed by the regulatory systems which further reduced the system’s efficiency.

Cycle (kW)	Percentage Loss	Energy (kWh)	Start Temperature (°C)
200	3.64%	26.84	37.0
150	5.11%	37.75	42.7
100 (a)	7.84%	58.27	44.8
100 (b)	3.54%	22.59	36.6
60	2.40%	17.48	42.1
50	13.66%	99.70	38.0

Table 8.9 Energy consumption from side reactions occurring within the battery

Error related to the fluctuations of the battery system's power

Another aspect that had to be determined before the coulombic efficiency could be evaluated was the error associated with the measurements. There were two main sources for this error: *viz.* the energy stored by the battery and the power used by the pumps. The error in the energy stored comes from the variance in active power used by the battery at any given time. Since each of the stated powers had a variance of ±3 kW, the size of the error comes from the duration between recorded points, as indicated in Table 8.10. This was determined through the integration of the curves produced from the respective power *vs.* time curves plotted in Appendix – Active Power/ Charge Level *vs.* Time. The error from the power input into the pumps on the other hand could be assumed to be negligible on the basis that any power fluctuations in the pump were balanced through the cycle.

Cycle Power (kW)	Time Duration (s)	Active Power Error (± kWh)
200	10	5.31
-200	10	3.04
150	10	6.08
-150	10	3.31
100	20	12.38
-100	20	5.84
60	30	18.48
-60	30	10.40
50	40	24.59
-50	40	11.76

Table 8.10 Error present in the recorded stored energies

Rate of self-discharge

The final aspect of battery operation examined was the rate of self-discharge. In order to improve the stacks' response time to satisfy the energy demand, these stacks were kept prepared by periodically flowing electrolyte through them. However, in doing so, the battery also loses a small amount of stored chemical energy in the form of vanadium crossover as well as energy consumed by the pumps. The standard operating procedure was that one group of stacks was kept on constant standby and this consisted of a regular pulse (duration = 300 s) of fresh electrolytes through those stacks. However, to quantify the extent of self discharge, two separate experiments were conducted in which had four and then two groups of stacks were kept active. From Figure 8.14, the electrolyte pulses can be clearly seen as the charge level decreases in steps rather than a constant decrease. As expected the more groups of stacks that were active, the faster the rate of self-discharge with the experiment using four groups losing almost 70% of its charge in 24 hours compared to the only 40% from the experiment with two stacks. This was in line with the expectation that the level of discharge in the two stack groups would be would be approximately half that of the four active stack groups. The precise measurement to ascertain when this occurs was not possible as the Siemens controlling program was not set-up to allow the recording of this data and so, this can only be assessed as a contibuting factor to the system's efficiency loss.

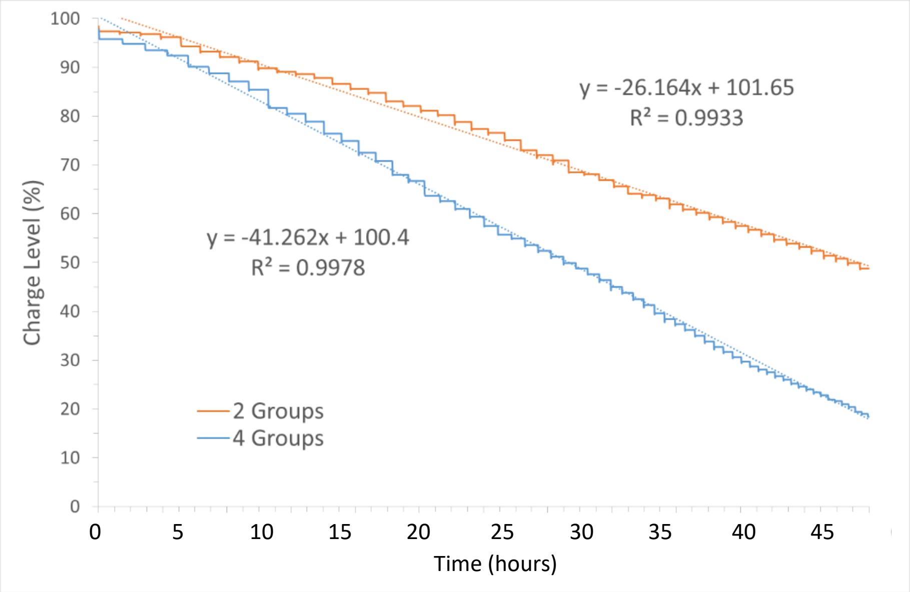

Figure 8.14 Rates of self-discharge with four and two groups of stacks kept active

8.4 Conclusions

The battery has an AC system efficiency between 48% and 60% over the power range of 50 – 200 kW applied for charging and discharging. It was determined that from the regulatory procedures (including the centrifugal pumps, sensors and cooling system) and the AC/DC and DC/DC convertor losses that these combined to contribute up to 24% of the system energy consumption.

From the electrochemical characteristics of the battery, the voltage efficiency and coulombic efficiencies were very high, in the range 80% – 93% and 73 – 97% respectively, to give an energy efficiency range between 65% and 90%. The main source of electrochemical energy loss for this battery originated from the energy consumed during the charge cycle and was related to the temperature of the electrolyte. This could be prevented by monitoring the electrolyte temperature and operating the charge cycle when this was below 40°C.

The coulombic and voltage efficiencies that have been reported here were in good agreement with the values found in literature. The system's main source of energy loss came from the apparent low efficiency of the centrifugal pumps used to circulate the electrolyte and from the energy losses in the AC/DC and DC/DC convertors. However, the pump inefficiencies could also come from the pumps operating out with their recommended specifications: as the differential head stated in the battery could have been much higher than the pumps stated capabilities.

8.5 Operating Recommendations

To maximise the vanadium battery’s performance several recommendations were made:

1. The battery’s electrolyte temperature should be monitored before charging is carried out. I If the temperature was above 40°C the extent of side reactions occurring during charge increased lowering the coulombic efficiency of the battery.
2. The battery’s centrifugal pumps will consume energy from the AC mains. To minimise the effects this energy consumption has on the system efficiency, the charging should be carried out at high power level’s, preferably ≥150 kW. This reduces the pumps operation time, increases the voltage efficiency by not charging at the maximum power and will allow the set charge limit to be reached without the voltage limit controlling the power output.
3. Due to the extent of self-discharge occurring over prolonged periods at standby mode, the battery should be discharged preferably within one day and only one stack remaining active for fast response. If the standby mode is required over extended periods, it is recommended that the battery (and the pumps) be turned off.
4. Due to the current high rate of self-discharge, the battery acting as an electric vehicle refuelling station is not recommended due to this application requiring fast initiation times over a long-time duration. This would mean that the battery would need to have 4 of the stacks with a flow through it which, as shown, would result in a rapid self-discharge over the duration of non-use. As such, people wishing to charge the car have to make appointments ahead of arriving to allow the necessary preparations in the RFB.
5. The battery should be able to power the electrolyser to produce hydrogen or to store energy from renewable sources when the production is in excess and feed it back into the grid during times of peak demand.

9. Conclusions & Future work

Work was successfully completed on identifying new novel additives with the objective to complex the bromine sufficiently while keeping the complex in the aqueous phase. These additives were characterised in terms of their electrochemical behaviour in physical properties when complexed with the electrogenerated bromine and the data were compared to the currently used additive, *N*-methyl-*N*-ethylpyrrolidinium. The dicationic structures were unsuccessful as these resulted in a solid precipitate when complexed with high concentrations of bromine. However, the additives making use of the carboxylic acid functional groups provided some success in reducing the volume of immiscible phase achieved. This led to the development of other additives making use of the sulphonate functional groups and one with a phosphonium centre, as opposed to an ammonium centre. The initial results showed no immiscible phase was formed but gave good indications that complexation with the bromine had still occurred.

Different carbon felt electrode materials and activated carbon electrode coatings were investigated for their potential use as the positive electrode in the Zn-Br_2 battery. Although the felt greatly increased the overall electrochemical surface area, it was found to cause issues, particularly with the electrolyte flow, due to the immiscible phase becoming trapped. This led to an increase in flow pressure which ultimately led to loss of contact of the felt from the backing plate. The activated carbon coating was found to be preferable for use here with both improved electrode kinetics and ease of removal of the immiscible phase. A new carbon felt electrode was tested with the Zn-Br_2 system and in the all-vanadium redox flow battery and good performance was found.

Finally, two large scale batteries were characterised and optimised as part of this work. The $ZnBr_2$ 25 kW/50 kWh RFB was characterised at the Power Network Demonstration Centre, Scotland and the all-vanadium 200 kW/400 kWh RFB was characterised at the École Polytechnique Fédérale de Lausanne – Laboratory of Physical and Analytical Electrochemistry, Switzerland. For the $ZnBr_2$ 25 kW/ 50 kWh, a sequence of operating conditions was introduced to examine the system performance and improve the overall energy efficiency. The study resulted in an increase in the ac energy efficiency from 39% to 58%, with a series of recommendations to be considered to further increase beyond that. The end of this project saw this RFB being installed into a small Scottish community at Findhorn, on the Moray Firth. This was made possible due to the collaborative efforts of the University of Strathclyde, PNDC, Lotte Chemical, and the Findhorn community with supporting funding to facilitate this project from Local Energy Scotland.

The all-vanadium 200 kW/400 kWh RFB was originally thought to have an energy efficiency of 47 – 60%. However, it was discovered that from the regulatory procedures (including the centrifugal pumps, sensors and cooling system) and the AC/DC and DC/DC convertor losses that these combined to contribute up to 24% of the system energy consumption which was not taken into consideration. Once these sources of energy loss were accounted for, it was found that the voltage efficiency and coulombic efficiencies were very high, in the range 80% – 93% and 73 – 97% respectively, to give an energy efficiency range between 65% and 90%. The main source of electrochemical energy loss for this battery originated from the energy consumed during the charge cycle and was related to the temperature of the electrolyte. This could be prevented by monitoring the electrolyte temperature and operating the charge cycle when this was below 40°C.

From the work conducted throughout this study, several follow-up objectives could be made. Significant work could be carried out on the additive chemistries discovered. These additives require further testing and scaling up to the flow cell apparatus to ascertain the benefit these may have. It would be particularly interesting to use the new additives with the carbon felts to see if the voltage efficiency would increase because of the removal of the immiscible phase. Additionally, the effect these additives have on the morphology of the zinc depositions should be investigated. Finally, the diversity of additive structures were not exhausted in this study, new structures could be conceptualised with the aim to improve complexation and electrochemical kinetics.

For the electrode study, it would be valuable to investigate alternative conductive binding methods for the carbon felts to the carbon composite backing plate. This should be aimed to improve the strength of the binding without losing electrical conductivity. For the felts themselves, thermal oxidation treatments could be varied to see what impact this would have. Additionally, the felts should undergo mechanical analysis to understand the effect that the immiscible phase may have on their structural integrity.

10. References

1 U. S. E. I. A. (EIA), *Monthly Energy Review April 2012*, 2012.

2 R. L. Murray, *Nuclear Energy (Sixth Edition) An Introduction to the Concepts, Systems, and Applications of Nuclear Processes*, Butterworth-Heinemann, 6th Editio., 2008.

3 S. F. Ashley, W. J. Nuttall, R. A. Fenner and G. T. Parks, *ICE Proc.*, 2013, **166**, 74–81.

4 V. Mourogov and K. Fukuda, *Prog. Nucl. Energy*, 2002, **40**, 285–299.

5 D. S. C. Purushotham, V. Venugopal and A. Ramanujam, *J. Radioanal. Nucl. Chem.*, 2000, **243**, 199–203.

6 E. C. Pearcy, J. D. Prikryl and W. M. Murphy, *Appl. Geochemistry*, 1994, **9**, 713–732.

7 G. L. P. M. G. Inghram, D. C. Hess, P. R. Fields, *Phys. Rev*, 1951, **83**, 1250–1251.

8 M. Seier and T. Zimmermann, *Int. J. Life Cycle Assess.*, 2014, **19**, 1919–1932.

9 R. Broomby and BBC News, France struggles to cut down on nuclear power, http://www.bbc.co.uk/news/magazine-25674581, (accessed 10 May 2015).

10 Key World 2017 Energy Statistics, https://www.iea.org/publications/freepublications/publication/KeyWorld2017.pdf, (accessed 10 December 2017).

11 M. Grätzel, *Philos. Trans. A. Math. Phys. Eng. Sci.*, 2007, **365**, 993–1005.

12 F. Díaz-González, A. Sumper, O. Gomis-Bellmunt and R. Villafáfila-Robles, *Renew. Sustain. Energy Rev.*, 2012, **16**, 2154–2171.

13 P. S. Georgilakis, *Renew. Sustain. Energy Rev.*, 2008, **12**, 852–863.

14 L. Bird, M. Bolinger, T. Gagliano, R. Wiser, M. Brown and B. Parsons, *Energy Policy*, 2005, **33**, 1397–1407.

15 Renewables 2017, https://www.iea.org/publications/renewables2017/,

(accessed 10 December 2017).

16 C. J. Winter, *Int. J. Hydrog. Energy*, 2009, **34**, 1–52.

17 Smarter networks, http://www.smarternetworks.org/Project.aspx?ProjectID=1630, 2015, (accessed 18 June 2017).

18 H2 Aberdeen, http://aberdeeninvestlivevisit.co.uk/Invest/Aberdeens-Economy/City-Projects/H2-Aberdeen/H2-Aberdeen.aspx, (accessed 10 November 2017).

19 U. S. E. I. A. (EIA), Germany, http://www.eia.gov/countries/country-data.cfm?fips=GM&trk=m, (accessed 7 May 2015).

20 International Energy Agency, 2014 Key World Energy STATISTICS, http://www.iea.org/publications/freepublications/publication/KeyWorld2014.pdf, (accessed 8 May 2015).

21 Federal Ministry for Economic Affairs and Energy, The Energy of the Future, https://www.bmwi.de/Redaktion/EN/Publikationen/vierter-monitoring-bericht-energie-der-zukunft-kurzfassung.pdf?__blob=publicationFile&v=14, (accessed 5 August 2018).

22 Scottish Government, Energy in Scotland 2018, https://www.gov.scot/Resource/0053/00531701.pdf, (accessed 5 August 2018).

23 Climate change impacts, http://www.noaa.gov/resource-collections/climate-change-impacts, (accessed 10 December 2017).

24 Adoption of the Paris Agreement., Adoption of the Paris Agreement. Proposal by the President., http://unfccc.int/resource/docs/2015/cop21/eng/l09r01.pdf, (accessed 2 September 2017).

25 B. Dunn, H. Kamath and J.-M. Tarascon, *Science (80-.).*, 2011, **334**, 928–935.

26 W. Wang, Q. Luo, B. Li, X. Wei, L. Li and Z. Yang, *Adv. Funct. Mater.*, 2013, **23**, 970–986.

27 Z. Yang, J. Zhang, M. C. W. Kintner-Meyer, X. Lu, D. Choi, J. P. Lemmon and

J. Liu, *Chem. Rev.*, 2011, **111**, 3577–3613.

28 K. Bradbury, Energy Storage Technology Review, https://www.researchgate.net/publication/265064873_Energy_Storage_Technology_Review, (accessed 5 March 2018).

29 W. E. Council, World Energy Resources: Hydropower | 2016, https://books.google.com/books?id=WLC7CdLOZosC&pgis=1, (accessed 6 April 2018).

30 J. P. Deane, B. P. Ó Gallachóir and E. J. McKeogh, *Renew. Sustain. Energy Rev.*, 2010, **14**, 1293–1302.

31 Energy Storage Technology Roadmap, https://www.iea.org/publications/freepublications/publication/TechnologyRoadmapEnergystorage.pdf, (accessed 30 March 2016).

32 S. Rehman, L. M. Al-Hadhrami and M. M. Alam, *Renew. Sustain. Energy Rev.*, 2015, **44**, 586–598.

33 E. McLean and D. Kearney, *Energy Procedia*, 2014, **46**, 152–160.

34 HydroWorld.com, FERC receives permit application for seawater-powered Hawaii pumped-storage, http://www.hydroworld.com/articles/2015/01/ferc-receives-permit-application-for-seawater-powered-hawaii-pumped-storage.html, (accessed 11 May 2015).

35 BINE Informationsdienst, Compressed air energy storage power plants, http://www.bine.info/fileadmin/content/Publikationen/Englische_Infos/projekt_0507_engl_internetx.pdf, (accessed 15 April 2015).

36 Modern Power Systems, Adele CAES Pilot: Site Selected but Project Delayed: The RWE/GE Led Consortium That Is Developing an Adiabatic Form of Compressed Air Energy Storage Is to Establish Its Commmercial Scale Test Plant at Stassfurt. the Testing Stage, Originally Slated for 20, http://business.highbeam.com/4364/article-1G1-297718155/adele-caes-pilot-site-selected-but-project-delayed, (accessed 11 June 2015).

37 B. Roberts, *IEEE Power Energy Mag.*, 2009, **7**, 32–41.

38 R. Takahashi, T. Murata and J. Tamura, *2005 Int. Conf. Power Electron. Drives Syst.*, 2005, **2**, 932–937.

39 H. Ibrahim, A. Ilinca and J. Perron, *Renew. Sustain. Energy Rev.*, 2008, **12**, 1221–1250.

40 B. Diouf and R. Pode, *Renew. Energy*, 2015, **76**, 375–380.

41 G. M. Ehrlich, *Handb. Batter.*, 2002, 1–94.

42 M. Skyllas-Kazacos, M. H. Chakrabarti, S. a. Hajimolana, F. S. Mjalli and M. Saleem, *J. Electrochem. Soc.*, 2011, **158**, R55.

43 J. J. C. Kopera, Inside the Nickel Metal Hydride Battery Inside the NiMH Battery, http://www.cobasys.com/pdf/tutorial/inside_nimh_battery_technology.pdf, (accessed 8 June 2015).

44 P. Leung, X. Li, C. Ponce de León, L. Berlouis, C. T. J. Low and F. C. Walsh, *RSC Adv.*, 2012, **2**, 10125.

45 M. Rahman, X. Wang and C. Wen, *J. Electrochem. Soc.*, 2013, **160**, A1759–A1771.

46 V. Amstutz, K. E. Toghill, F. Powlesland, H. Vrubel, C. Comninellis, X. Hu and H. H. Girault, *Energy Environ. Sci.*, 2014, **7**, 2350–2358.

47 B. Huskinson, M. P. Marshak, C. Suh, S. Er, M. R. Gerhardt, C. J. Galvin, X. Chen, A. Aspuru-Guzik, R. G. Gordon and M. J. Aziz, *Nature*, 2014, **505**, 195–8.

48 H. Sezer, M. Aygun, J. H. Mason, E. Baran and I. Celik, *ECS Trans.*, 2015, **69**, 91–100.

49 P. Peng and F. Jiang, *Int. J. Heat Mass Transf.*, 2016, **103**, 1008–1016.

50 H. Zhao, Q. Wu, S. Hu, H. Xu and C. N. Rasmussen, *Appl. Energy*, 2014, **137**, 545–553.

51 T. Shigematsu, *SEI Tech. Rev.*, 2011, **73**, 5–13.

52 A. Z. Weber, M. M. Mench, J. P. Meyers, P. N. Ross, J. T. Gostick and Q. Liu, *J. Appl. Electrochem.*, 2011, **41**, 1137–1164.

53 F. Rahman and M. Skyllas-Kazacos, *J. Power Sources*, 2009, **189**, 1212–1219.

54 S. Roe, C. Menictas and M. Skyllas-Kazacos, *J. Electrochem. Soc.*, 2016, **163**, A5023–A5028.

55 M. Rychcik and M. Skyllas-Kazacos, *J. Power Sources*, 1988, **22**, 59–67.

56 D. Bryans, B. G. McMillan, M. Spicer, A. Wark and L. Berlouis, *J. Electrochem. Soc.*, 2017, **164**, A3342–A3348.

57 M. Skyllas Kazacos and G. Kazacos, *J. Energy*, 2010, 182–189.

58 C. Ding, H. Zhang, X. Li, T. Liu and F. Xing, *J. Phys. Chem. Lett.*, 2013, **4**, 1281–1294.

59 M. Skyllas-Kazacos, *J. Power Sources*, 2003, **124**, 299–302.

60 Z. Huang and G. Du, *Nickel-based batteries for medium- and large-scale energy storage*, Elsevier Ltd., 2015.

61 A. Price, S. Bartlety, S. Male and G. Cooley, *Power Eng. J.*, 1999, **13**, 122.

62 D. P. Scamman, G. W. Reade and E. P. L. Roberts, *J. Power Sources*, 2009, **189**, 1220–1230.

63 D. P. Scamman, G. W. Reade and E. P. L. Roberts, *J. Power Sources*, 2009, **189**, 1231–1239.

64 H. Zhou, H. Zhang, P. Zhao and Y. Baolian, *Electrochemistry*, 2006, **74**, 296–298.

65 P. Zhao, H. Zhang, H. Zhou and B. Yi, *Electrochim. Acta*, 2005, **51**, 1091–1098.

66 G. Poon, A. Parasuraman, T. M. Lim and M. Skyllas-Kazacos, *Electrochim. Acta*, 2013, **107**, 388–396.

67 S. Winardi, G. Poon, M. Ulaganathan, A. Parasuraman, Q. Yan, N. Wai, T. M.

Lim and M. Skyllas-Kazacos, *Chempluschem*, 2015, **80**, 376–381.

68 D. Bryans, L. Berlouis, M. Spicer, B. G. McMillan and A. Wark, *ECS Trans.*, 2017, **77**, 33–36.

69 Z. Li, G. Weng, Q. Zou, G. Cong and Y. C. Lu, *Nano Energy*, 2016, **30**, 283–292.

70 P. H. Svensson and L. Kloo, *Chem. Rev.*, 2003, **103**, 1649–84.

71 G.-M. Weng, Z. Li, G. Cong, Y. Zhou and Y.-C. Lu, *Energy Environ. Sci.*, 2017, **10**, 735–741.

72 M. Wang, N. Chamberland, L. Breau, J.-E. Moser, R. Humphry-Baker, B. Marsan, S. M. Zakeeruddin and M. Grätzel, *Nat. Chem.*, 2010, **2**, 385–389.

73 F.-T. Kong, S.-Y. Dai and K.-J. Wang, *Adv. Optoelectron.*, 2007, **2007**, 1–13.

74 S. K. Park, J. Shim, J. Yang, K. H. Shin, C. S. Jin, B. S. Lee, Y. S. Lee and J. D. Jeon, *Electrochem. commun.*, 2015, **59**, 68–71.

75 D. Zhang, H. Lan and Y. Li, *J. Power Sources*, 2012, **217**, 199–203.

76 A. E. S. Sleightholme, A. A. Shinkle, Q. Liu, Y. Li, C. W. Monroe and L. T. Thompson, *J. Power Sources*, 2011, **196**, 5742–5745.

77 Q. Liu, A. E. S. Sleightholme, A. A. Shinkle, Y. Li and L. T. Thompson, *Electrochem. commun.*, 2009, **11**, 2312–2315.

78 Q. Liu, A. A. Shinkle, Y. Li, C. W. Monroe, L. T. Thompson and A. E. S. Sleightholme, *Electrochem. commun.*, 2010, **12**, 1634–1637.

79 Y. Matsuda, K. Tanaka, M. Okada, Y. Takasu, M. Morita and T. Matsumura-Inoue, *J. Appl. Electrochem.*, 1988, **18**, 909–914.

80 J. H. Kim, K. J. Kim, M. S. Park, N. J. Lee, U. Hwang, H. Kim and Y. J. Kim, *Electrochem. commun.*, 2011, **13**, 997–1000.

81 Y. Li, J. Sniekers, J. Malaquias, X. Li, S. Schaltin, L. Stappers, K. Binnemans, J. Fransaer and I. F. J. Vankelecom, *Electrochim. Acta*, 2017, **236**, 116–121.

82 Y. Ding, Y. Zhao and G. Yu, *Nano Lett.*, 2015, **15**, 4108–4113.

83 B. Li, Z. Nie, M. Vijayakumar, G. Li, J. Liu, V. Sprenkle and W. Wang, *Nat. Commun.*, 2015, **6**, 1–8.

84 L. Zhang, H. Zhang, Q. Lai, X. Li and Y. Cheng, *J. Power Sources*, 2013, **227**, 41–47.

85 Q. Lai, H. Zhang, X. Li, L. Zhang and Y. Cheng, *J. Power Sources*, 2013, **235**, 1–4.

86 H. S. Lim, A. M. Lackner and R. C. Knechtli, *J. Electrochem. Soc.*, 1977, **124**, 1154.

87 P. K. Leung, C. Ponce De León and F. C. Walsh, *Electrochem. commun.*, 2011, **13**, 770–773.

88 J. Jorné, J. T. Kim and D. Kralik, *J. Appl. Electrochem.*, 1979, **9**, 573–579.

89 D. Pavlov, G. Papazov and M. Gerganska, *Battery Energy Storage Systems, the United Nations Educational, Scientific and Cultural Organization, Regional Office for Science and Technology for Europe, Technical Report*, 1991, vol. 7.

90 P. C. Butler, Utility battery storage systems program report for FY93.

91 Sandia Nat, ARRA Energy Storage Demonstrations, http://www.sandia.gov/ess/docs/ARRA_StorDemos_4-22-11.pdf, (accessed 26 June 2015).

92 Primus Power, Wind Firming EnergyFarm Primus Powers EnergyFarm System, http://energy.gov/sites/prod/files/Primus.pdf, (accessed 26 June 2015).

93 P. K. Leung, C. Ponce de Leon, C. T. J. Low, A. A. Shah and F. C. Walsh, *J. Power Sources*, 2011, **196**, 5174–5185.

94 G. Nikiforidis, L. Berlouis, D. Hall and D. Hodgson, *Electrochim. Acta*, 2013, **113**, 412–423.

95 L. Su, A. F. Badel, C. Cao, J. J. Hinricher and F. R. Brushett, *Ind. Eng. Chem. Res.*, 2017, **56**, 9783–9792.

96 R. M. J. Withers and F. P. Lees, *J. Hazard. Mater.*, 1986, **13**, 279–299.

97 J. Noack, N. Roznyatovskaya, T. Herr and P. Fischer, *Angew. Chemie - Int. Ed.*, 2015, **54**, 9776–9809.

98 F. W. R. Bloch, L. Farkas, J. Schnerb, *J. Phys. Chem.*, 1949, **53**, 1117–1125.

99 F. Rallo and P. Silvestroni, *J. Electrochem. Soc.*, 1972, **119**, 1471.

100 D. J. Eustace, *J. Electrochem. Soc.*, 1980, **127**, 528–532.

101 P. M. H. K.J.Cathro, K.Cedzynska, D.C.Constable, *J. Power Sources*, 1986, **18**, 349–370.

102 K. Cedzynska, *Electrochim. Acta*, 1995, **40**, 971–976.

103 K. Cedzynska, *Electrochim. Acta*, 1989, **34**, 1439–1442.

104 K. J. Cathro, K. Cedzynska and D. C. Constable, *J. Power Sources*, 1985, **16**, 53–63.

105 J.-D. Jeon, H. S. Yang, J. Shim, H. S. Kim and J. H. Yang, *Electrochim. Acta*, 2014, **127**, 397–402.

106 M. Schneider, G. P. Rajarathnam, M. E. Easton, A. F. Masters, T. Maschmeyer and A. M. Vassallo, *RSC Adv.*, 2016, **6**, 110548–110556.

107 G. P. Rajarathnam, M. E. Easton, M. Schneider, A. F. Masters, T. Maschmeyer and A. M. Vassallo, *RSC Adv.*, 2016, **6**, 27788–27797.

108 W. Kautek, a Conradi, C. Fabjan and G. Bauer, *Electrochim. Acta*, 2001, **47**, 815–823.

109 G. Bauer, J. Drobits, C. Fabjan, H. Mikosch and P. Schuster, *J. Electroanal. Chem.*, 1997, **427**, 123–128.

110 J. H. Yang, H. S. Yang, H. W. Ra, J. Shim and J.-D. Jeon, *J. Power Sources*, 2015, **275**, 294–297.

111 S. J. Banik and R. Akolkar, *J. Electrochem. Soc.*, 2013, **160**, D519–D523.

112 S. J. Banik and R. Akolkar, *J. Electrochem. Soc.*, 2015, **179**, 475–481.

113 E. Lancry, B. Z. Magnes, I. Ben-David and M. Freiberg, *ECS Trans.*, 2013, **53**, 107–115.

114 D. S. Vicentini, R. V. Salvatierra, A. J. G. Zarbin, L. G. Dutrac and M. M. Sá, *J. Braz. Chem. Soc.*, 2014, **25**, 1939–1947.

115 R. Zhang and J. A. Moore, *Macromol. Symp.*, 2003, **199**, 375–390.

116 S. A. Tittlemier and G. T. Tomy, *Environ. Toxicol. Chem.*, 2001, **20**, 146–148.

117 S. N. Bajpal, *J. Chem. Eng. Data*, 1981, **26**, 2–4.

118 D. Pletcher and F. C. Walsh, *Industrial Electrochemistry*, Springer Netherlands, Dordrecht, 1993.

119 S. J. Konopka and B. McDuffie, *Anal. Chem.*, 1970, **42**, 1741–1746.

120 R. S. Nicholson, *Anal. Chem.*, 1965, **37**, 1351–1355.

121 F. Chen, Q. Sun, W. Gao, J. Liu, C. Yan and Q. Liu, *J. Power Sources*, 2015, **280**, 227–230.

122 P. K. Leung, C. Ponce-De-León, C. T. J. Low and F. C. Walsh, *Electrochim. Acta*, 2011, **56**, 6536–6546.

123 S. Carbon, EC-GFD-46EA Sigracell Graphite Felt, http://fuelcell.com/product/ec-gfd-46ea-sigracell-graphite-felt/, (accessed 19 July 2016).

124 Electrochem Inc, EC-GFA-6EA Sigracell Graphite Felt, http://fuelcell.com/product/ec-gfa-6ea-sigracell-graphite-felt/ (Visited 19-07-2016), (accessed 19 July 2016).

125 L. F. Arenas, C. Ponce de Leon and F. C. Walsh, *Electrochim. Acta*, 2016, **221**, 154–166.

126 Energy Strategy 2050, Energy Strategy 2050, http://www.bfe.admin.ch/energiestrategie2050/06445/index.html?lang=en, (accessed 2 September 2017).

127 Wind Energy Plants, Wind Energy Plants, http://www.uvek-

gis.admin.ch/BFE/storymaps/EE_WEA/index.php?lang=en, (accessed 2 September 2017).

128 Swissinfo.ch, Swiss Solar, https://www.swissinfo.ch/eng/green-energy_a-place-in-the-sun-for-swiss-solar-power/38103970, (accessed 8 September 2017).

129 H. Lund, *Energy*, 2007, **32**, 912–919.

130 EPFL-LEPA, Charging an electric car, https://actu.epfl.ch/news/charging-an-electric-car-as-fast-as-filling-a-tank/, (accessed 3 September 2017).

131 EPFL-LEPA, Future Fuelling Station, https://actu.epfl.ch/news/epfl-inaugurates-the-fueling-station-of-the-future/, (accessed 3 September 2017).

132 APPA Tech, Multimeter manual, http://www.appatech.com/upload/download/file13389726864585.pdf, (accessed 4 September 2017).

133 C. Ding, H. Zhang, X. Li, T. Liu and F. Xing, *J. Phys. Chem. Lett.*, 2013, **4**, 1281–1294.

11. Appendices

Appendix – Publication & Conferences

Publications

- Complexing Additives to Reduce the Immiscible Phase Formed in the Hybrid ZnBr2 Flow Battery, Nov 2, 2017, *Journal of the Electrochemical Society*
- Synthesis and Characterisation of Novel Additives for Use in the Hybrid ZnBr2 Flow Battery, May 19, 2017, *ECS Transactions*

Conferences

- WestCHEM Research Day (invited), 2018, Oral (Award), Glasgow
- Energy Technology Partnership, Annual Conference 2017, Oral & Poster (Award), Edinburgh
- IFBF 2017, Oral & Poster, Manchester
- UK RFB Network Meeting, 2017, Oral & Poster, Manchester
- 231st ECS Meeting, 2017, Oral, New Orleans
- UK Energy Storage Conference 2016, Oral & Poster, Birmingham
- Energy Technology Partnership, Annual Conference 2016, Oral & Poster, Aberdeen
- Early Career Scientist RSC 2016, Oral & Poster, London
- Scotland and North of England, Electrochemistry Symposium 2016, Poster (Award), Glasgow
- Energy Technology Partnership, Annual Conference 2015, Oral & Poster, Glasgow
- ECS Conference on Electrochemical Energy Conversion & Storage with SOFC-XIV, 2015, Poster, Glasgow
- Electrochem 2015, Oral, Durham

Appendix - Stripping Cycle

Strip 1

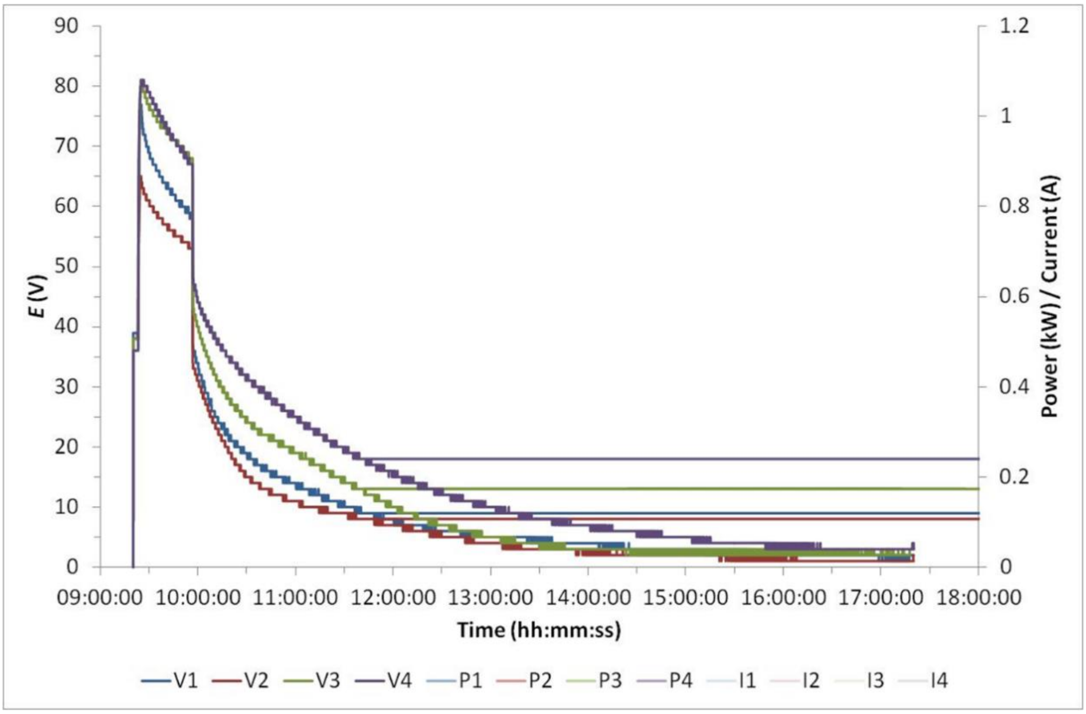

Strip 2

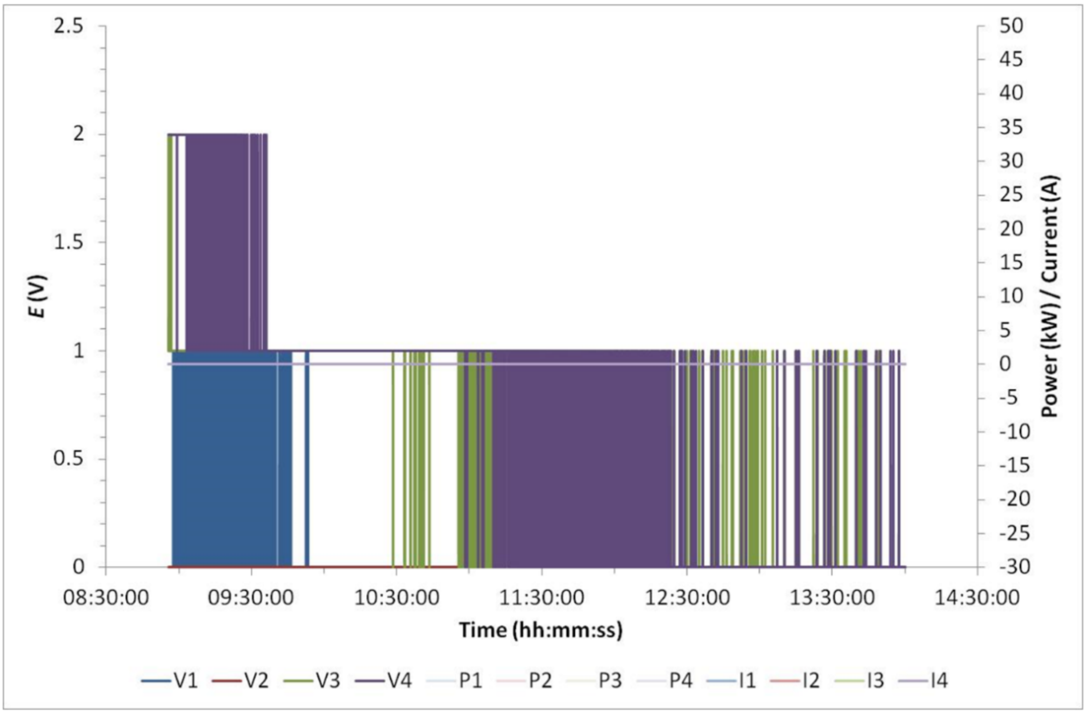

Strip 3

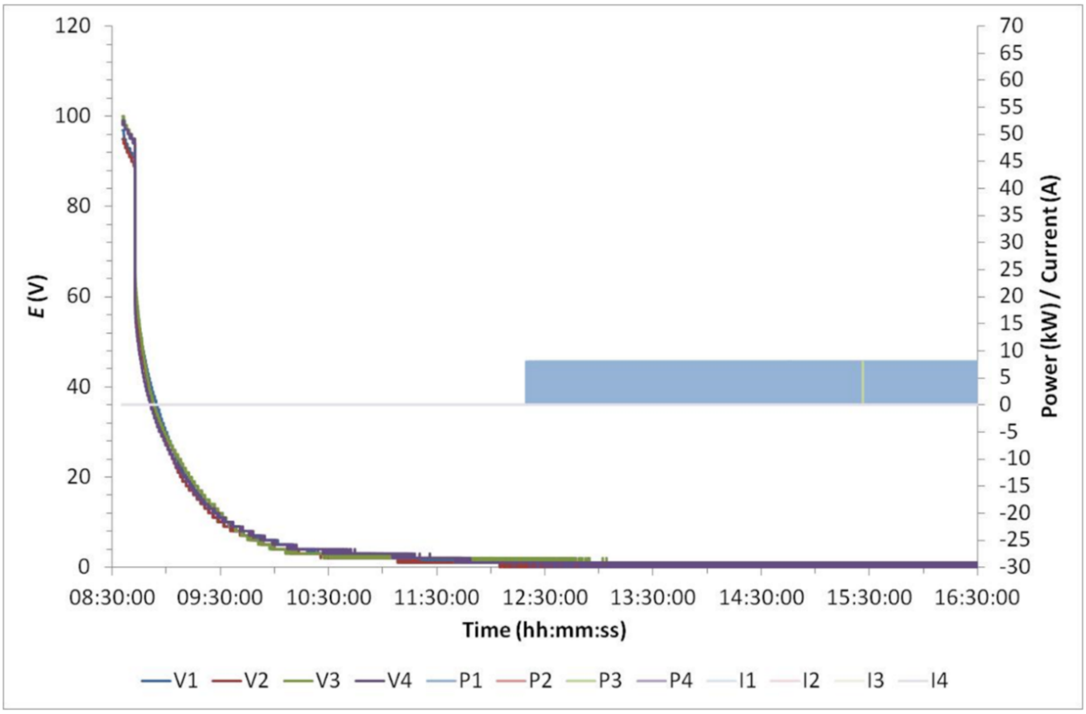

Strip 4

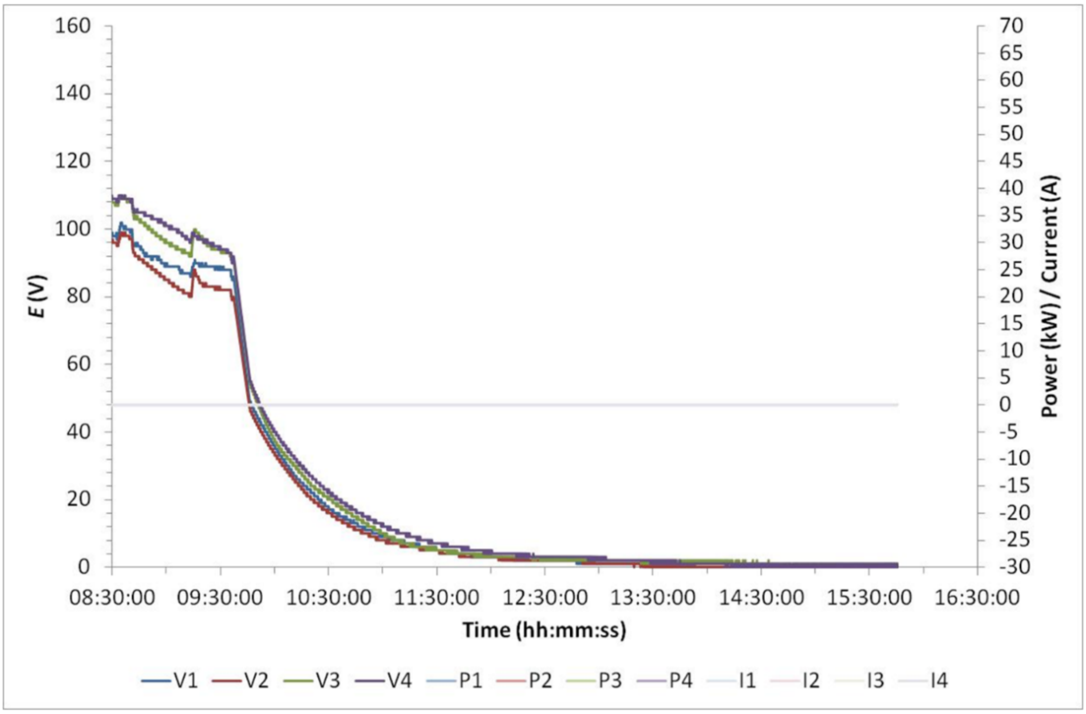

Appendix – Sequence of Work

Run 1

Table	Operation	Mode	Set Point	Min	Sec	Time	Notes
1	Wake-Up	CP	0	20	0	10:05	OK
2	Charge	CP	17	100	0	10:26	Tripped the alarm for over voltage DC Battery #1
1	Wake-Up	CP	0	5	0	10:32	OK
2	Charge	CP	12	120	0	10:37	OK
3	Rest	CP	0	1	0	12:37	SOC % <40% achieved
4	Discharge	CP	−8	120	0	12:38	Tripped the alarm for St #2 <100 V but continues the sequence through tables (Table 4&5)
5	Discharge	CP	−4	120	0	14:38	Charge Power +23.86 kWh: Discharge Power -15.65 kWh
6	Rest	CP	0	1	0	16:38	OK
7	Shutdown	CP	0	1	0	16:39	OK
8	Off	CP	0	1	0	16:40	OK

Run 2

Table	Operation	Mode	Set Point	Min	Sec	Time	Notes
1	Wake-Up	CP	0	15	0	09:35	OK
2	Charge	CP	6	1	0	09:50	OK
3	Charge	CP	12	1	0	09:51	OK
4	Charge	CP	17	200	0	09:52	Stack (230.1 V, 18.4 A, 4.24 kW) Total (231.9 V, 73.2 A)
5	Rest	CP	0	1	0	13:22	12.52 reached 70% SOC, time extended from 200 to 210
6	Discharge	CP	−4	1	0	13:23	Stack (200.3 V, −15 A, −2.98 kW) Total (200.3 V, −59.7 A, −11.95 kW)
7	Discharge	CP	−8	1	0	13:24	OK
8	Discharge	CP	−12	220	0	13:25	Discharge time changed from 220 to 215
9	Rest	CP	0	1	0	17:00	OK
10	Shutdown	CP	0	1	0	17:01	OK
11	Off	CP	0	1	0	17:02	OK

Run 3

Table	Operation	Mode	Set Point	Min	Sec	Time	Note	
1	Wake-Up	CP	0	15	0	09:46	OK	
2	Charge	CP	6	1	0	10:01	OK	215 V 13.5 A
3	Charge	CP	12	1	0	10:02	OK	222 V 13.5 A
4	Charge	CP	17	88	12	10:03	OK	227.5 V 18.6 A
4	Charge	CP	12	75	0	11:31	OK	221.5 V 13.5 A
4	Charge	CP	6	96	0	12:46	OK	217 V 6.9 A
5	Rest	CP	0	1	0	14:22	OK	49.66 kWh Charge
6	Discharge	CP	−4	1	0	14:23	OK	208.5 V −4.8 A
7	Discharge	CP	−8	1	0	14:24	OK	204.5 V −9.8 A
8	Discharge	CP	−12	105	0	14:25	OK	200.9 V −14.9 A
8	Discharge	CP	−8	60	0	16:10	OK	196 V −10 A
8	Discharge	CP	−4	55	0	17:10	OK	198.4 V −5.1 A
9	Rest	CP	0	1	0	18:05		32.18 kWh
10	Shutdown	CP	0	1	0	19:04		
11	Off	CP	0	1	0	19:06		

Run 4

Table	Operation	Mode	Set Point	Min	Sec	Time	Note	
1	Wake-Up	CP	0	15	0	08:55	OK	
2	Charge	CP	6	1	0	09:10	OK	
3	Charge	CP	12	1	0	09:11	OK	Must remember to take stack values for pre-charge steps
4	Charge	CP	17	240	0	09:12	OK	Stacks: 230.5 V: 18.3 A
5	Rest	CP	0	1	0	13:12	OK	SOC 94.6 % Charged Power 68.08 kWh
6	Discharge	CP	−4	1	0	13:13	OK	Stacks: 213 V: −4.6 A
7	Discharge	CP	−8	1	0	13:14	OK	Stacks: 208.4 V: −9.6 A
8	Discharge	CP	−12	240	0	13:15		Stacks: 204.5 V: −14.6 A
9	Rest	CP	0	1	0	17:15		Discharged Power 41.83%: Time
10	Shutdown	CP	0	1	0			
11	Off	CP	0	1	0			

Run 5

Table	Operation	Mode	Set Point	Min	Sec	Time	Note	
1	Wake-Up	CP	0	15	0	08:35	OK	
2	Charge	CP	6	1	0	08:50	OK	
3	Charge	CP	12	1	0	08:51	OK	
4	Charge	CP	17	180	0	08:52	OK	
5	Rest	CP	0	1	0	11:52	OK	51.11 kWh Charge
6	Discharge	CP	−4	1	0	11:53	OK	
7	Discharge	CP	−8	1	0	11:54	OK	
8	Discharge	CP	−8	360	0	11:55	OK	
9	Rest	CP	0	1	0	16:08		33.69 kWh Discharge
10	Shutdown	CP	0	1	0			
11	Off	CP	0	1	0			

Run 6

Table	Operation	Mode	Set Point	Min	Sec	Time	Note	
1	Wake-Up	CP	0	15	0	08:43	OK	
2	Charge	CP	6	1	0	08:58	OK	
3	Charge	CP	12	1	0	08:59	OK	
4	Charge	CP	17	180	0	09:00	OK	233 V 18.2 A
5	Rest	CP	0	1	0	12:00	OK	51.12 kWh Charge: 71.0% SOC
6	Discharge	CP	−4	1	0	12:01	OK	210 V −4.7 A
7	Discharge	CP	−4	1	0	12:02	OK	
8	Discharge	CP	−4	420	0	12:03	OK	202 V −4.7 A
9	Rest	CP	0	1	0	19:03		28.28 kWh
10	Shutdown	CP	0	1	0	19:04		
11	Off	CP	0	1	0	19:06		

Run 7

Table	Operation	Mode	Set Point	Min	Sec	Time	Note	
1	Wake-Up	CP	0	15	0	12:03	OK	
2	Charge	CP	6	1	0	12:04	OK	217 V
3	Charge	CP	12	1	0	12:05	OK	228 V 13.3 A
4	Charge	CP	17	60	0	12:06	OK	230 V 18.3 A
5	Rest	CP	0	1	0	13:06	OK	17.23 kWh
6	Discharge	CP	−4	1	0	13:07	OK	
7	Discharge	CP	−8	1	0	13:08	OK	
8	Discharge	CP	−14	60	0	13:09	OK	187 V 18.5 A
9	Rest	CP	0	1	0	19:03		8.78 kWh
10	Shutdown	CP	0	1	0	19:04		Stack 4 - 140 V
11	Off	CP	0	1	0	19:06		Stack 1 - 159 V

Run 8

Table	Operation	Mode	Set Point	Min	Sec	Time	Note		
1	Wake-Up	CP	0	15	0	08:39	OK		
2	Charge	CP	6	1	0	08:54	OK	219 V 6.8 A	
3	Charge	CP	12	1	0	08:55	OK	227 V 13.1 A	
4	Charge	CP	17	180	0	08:56	OK	233 V 18.2 A	
5	Rest	CP	0	1	0	11:56	OK	Charged	51.12 kWh
6	Discharge	CP	−4	1	0	11:57	OK	210 V −4.7 A	
7	Discharge	CP	−8	1	0	11:58	OK	206 V −9.6 A	
8	Discharge	CP	−12	180	0	11:59	OK	201 V −14.9 A	
9	Rest	CP	0	1	0	14:59	OK	Discharged	34.35 kWh
10	Shutdown	CP	0	1	0	15:00	OK		
11	Off	CP	0	1	0	15:01	OK		

Run 9

Table	Operation	Mode	Set Point	Min	Sec	Time	Notes	
1	Wake-Up	CP	0	15	0	08:41	OK	
2	Charge	CP	6	1	0	08:56	OK	218 V 6.9 V
3	Charge	CP	12	180	0	08:57	OK	225 V 13.2 A // 223.5 V 13.4 A
4	Rest	CP	0	1	0	11:57	OK	Charged 35.93 kWh
5	Discharge	CP	−4	1	0	11:58	OK	207.5 V −4.8 A
6	Discharge	CP	−8	190	0	13:09		202.5 V −9.8 A
7	Rest	CP	0	1	0			Discharged 23.77 kWh
8	Shutdown	CP	0	1	0			
9	Off	CP	0	1	0			

Run 10

Table	Operation	Mode	Set Point	Min	Sec	Time	Notes	
1	Wake-Up	CP	0	15	0	08:37	OK	OCP 114 v
2	Charge	CP	8	180	0	08:52	OK	222 V 9.0 V
4	Rest	CP	0	1	0	11:52	OK	Charged 23.84 kWh
5	Discharge	CP	−4	240	0	11:53	OK	204.5 V −4.9 A
7	Rest	CP	0	1	0	15:50		Discharged 14.63 kWh
8	Shutdown	CP	0	1	0			DC Alarm 1 & 2 Tripped
9	Off	CP	0	1	0			

Appendix – Table of Recorded Data

Data Log Tag	Parameter Description	Alter	Unit
max_target_power	Maximum request for active power	-	kW
target_active_power	Setpoint active power	-	kW
target_reactive_power	Setpoint reactive power	-	kVAr
Total Active Power	Active power of all phases	-	kW
Total Reactive Power	Reactive power of all phases	-	kVAr
Total Apparent Power	Apparent power of all phases	-	kVAr
Total power factor	Global power factor	-	-
Max charge power	Present maximum charge power	-	kW
Max discharge power	Present maximum discharge power	-	kW
Active power	Present active power at inverter	-	kW
Reactive power	Present reactive power at inverter	-	kVAr
Range	Available discharge or charge at designated power	-	kWh
Charge level	Present charge level	/10	%
V_El_ Temperature	Temperature of electrolyte in the storage tank	/10	°C
DC Bus voltage	Voltage on the DC-bus system	-	V
DC Bus current	Current on the DC-bus system	-	A
Operational status	Operational status register (16 bit) Bit 1: Reserve Bit 2: Normal operation Bit 3: Malfunction causes limited operation Bit 4: Malfunction causes system shut down Bit 5: Emergency stop activated Bit 6: Storage fully charged (CL > 99%) Bit 7: Storage fully discharged (CL < 1%) Bit 8: Battery overheated Bit 9: Grid error - grid disconnected Bit 10-16: Reserve	-	-
Safety Status	Safety status register (16 bit) Bit 1: Reserve Bit 2: Safe operation Bit 3: Smoke detector alarm Bit 4: Increased H2 concentration Bit 5: Critical H2 concentration Bit 6: Electrolyte in containment Bit 7: Critical leakage in fluid circuit Bit 8: Main door open Bit 9: Electrical cabinet open Bit 10-16: Reserve	-	-

Data Log Tag	Parameter Description	Alter	Unit
System status	Present status of CellCube	-	-
	0 = Off		
	1 = On		
	2 = Starting		
	3 = Stopping		
	4 = Emergency		
	5 = Deactivating		
Active Power L1	Active power at phase 1	-	kW
Reactive Power L1	Reactive power at phase 1	-	kVAr
Apparent Power L1	Apparent power at phase 1	-	kVAr
Voltage L1	Voltage at phase 1	/10	V
Apparent Current L1	Apparent current at phase 1	/100	A
Power Factor L1	Power factor at phase 1	-	-
Active Power L2	Active power at phase 2	-	kW
Reactive Power L2	Reactive power at phase 2	-	kVAr
Apparent Power L2	Apparent power at phase 2	-	kVAr
Voltage L2	Voltage at phase 2	/10	V
Apparent Current L2	Apparent current at phase 2	/100	A
Power Factor L2	Power factor at phase 2	-	-
Active Power L3	Active power at phase 3	-	kW
Reactive Power L3	Reactive power at phase 3	-	kVAr
Apparent Power L3	Apparent power at phase 3	-	kVAr
Voltage L3	Voltage at phase 3	/10	V
Apparent Current L3	Apparent current at phase 3	/100	A
Power Factor L3	Power factor at phase 3	-	-
IBS Total active power	Active power of all phases		kW
IBS Total reactive power	Reactive power of all phases		kVAr
IBS Total apparent power	Apparent power of all phases		kVAr
IBS Voltage	Phase voltage		V
IBS apparent current	Apparent current		A
IBS Power factor	Global power factor		-
IBS Active Power L1	IBS power at phase 1		kW
IBS Reactive Power L1	IBS power at phase 1		kVAr
IBS Apparent Power L1	IBS power at phase 1		kVAr
IBS Voltage L1	IBS voltage at phase 1		V
IBS Apparent Current L1	IBS current at phase 1		A
IBS Power Factor L1	IBS factor at phase 1		-
IBS Active Power L2	IBS power at phase 2		kW
IBS Reactive Power L2	IBS power at phase 2		kVAr
IBS Apparent Power L2	IBS power at phase 2		kVAr

Data Log Tag	Parameter Description	Alter	Unit
IBS Voltage L2	IBS voltage at phase 2		V
IBS Apparent Current L2	IBS current at phase 2		A
IBS Power Factor L2	IBS factor at phase 2		-
IBS Active Power L3	IBS power at phase 3		kW
IBS Reactive Power L3	IBS power at phase 3		kVAr
IBS Apparent Power L3	IBS power at phase 3		kVAr
IBS Voltage L3	IBS voltage at phase 3		V
IBS Apparent Current L3	IBS current at phase 3		A
IBS Power Factor L3	IBS factor at phase 3		-

Appendix – Work Sequences

The following is a list of work sequences used throughout this project with stated objectives and results. The first series of sequences was to establish the programs operation. To do this successfully several command functions had to be confirmed.

Date: 17/08/17 Time: Not recorded

Aim: determining the command function SOC as a trigger for limiting extents of charge and discharge within the battery.

Result: No operation within the battery.

Condition	Target Power kW
wait = 0	200
SOC >= 7500	0
wait = 0	−200
SOC <= 2000	0

Date: 17/08/17 Time: Not recorded

Aim: establish the unit associated with the time function.

Result: the number was determined to operate by minutes.

Condition	Target Power kW
wait = 5	0

Date: 17.08/17 Time: Not recorded

Aim: use a defined time range to reach a limiting trigger.

Result: battery operated at 0 kW for duration of run.

Condition	Target Power kW
wait = 100	−200
SOC <= 7200	0

Date: 17.08/17 Time: Not recorded

Aim: to see if limit will alter target power between triggered limits

Result: discharge at –100 kW but disregarded triggered limits and continued to discharge at this level. Triggered state of charge limits are not to be used due to unreliability.

Condition	Target Power kW
wait = 0	−100
SOC <= 6500	0
wait = 0	−50
SOC <= 6000	0

Date: 17.08/17 Time: Not recorded

Aim: ensure that the time function trigger will move to a lower level of discharge.

Result: first ten minutes operated at 0 kW then discharged at –100 kW for the second period before stopping.

Condition	Target Power kW
wait = 10	−100
wait = 10	−50

Date: 17.08/17 Time: Not recorded

Aim: confirm the previous run.

Result: first ten minutes operated at 0 kW then discharged at –50 kW for the second period before stopping.

Condition	Target Power kW
wait = 10	−50
wait = 10	−100

Date: 17.08/17 Time: Not recorded

Aim: ensure problem from previous run is consistent between charge and discharge.

Result: first ten minutes operated at 0 kW then discharged at 100 kW for the second period before stopping.

Condition	Target Power kW
wait = 10	100
wait = 10	−100

Date: 18/08/17 Time: Not recorded

Aim: confirm that the first row time value does not associate with the first row target power.

Result: ran at 0 kW for 5 minutes before stopping. First row targeted power may be associated with second row time value.

Condition	Target Power kW
wait = 5	100

Date: 18/08/17 Time: Not recorded

Aim: confirm that the first row targeted power is associated with second row time value.

Result: this was successfully confirmed as the battery operated at 0 kW for 5 minutes then 100 kW and −100 kW subsequently.

Condition	Target Power kW
wait = 5	100
wait = 5	−100
wait = 5	0

Date: 18/08/17 Time: Not recorded

Aim: ensure the battery can successfully operate between various discharge rates.

Results: the first time row seems to be available to ensure time for the stacks to initiate. The battery successfully changes discharge rates. However, the number of grouped stacks does not decrease for the lower discharge level.

Condition	Target Power kW
wait = 5	−100
wait = 5	−50
wait = 5	0

Date: 18/08/17 Time: Not recorded

Aim: optimise the time required for stacks to be initiated, observed time was three minutes.

Result: three minutes adequate for initiation of required stacks. Stacks to support the maximum target power sustained through the entire sequence.

Condition	Target Power kW
wait = 3	−100
wait = 5	−50
wait = 5	0

Date: 18/08/17 Time: Not recorded

Aim: to see if the number of stacks will initially be lower to support the lower discharge power.

Results: the number of stacks initiated is related to the maximum target power stated.

Condition	Target Power kW
wait = 3	−50
wait = 5	−100
wait = 5	0

Date: 18/08/17 Time: Not recorded

Aim: confirm control between various charge and discharge levels.

Results: successful operation of the stated sequence.

Condition	Target Power kW
wait = 3	−50
wait = 5	−100
wait = 5	−50
wait = 5	50
wait = 5	100
wait = 5	50
wait = 5	0

Date: 18/08/17 Time: Not recorded

Aim: confirm the battery does not go below the charge level of 0%.

Result: power decreases on approach to charge level limit before being set to 0 kW for the remaining time.

Condition	Target Power kW
wait = 108	−100

Date: 21/08/17 Time: 17:20

Aim: charge the battery at the 100 kW to a charge level of 100%.

Result: battery failed to record full data set.

Condition	Target Power kW
wait = 3	100
wait = 1000	0

Date: 22/08/17 Time: 17:20

Aim: charge the battery at the maximum power to a charge level of 100%.

Result: battery did not over charge and is discussed in Battery Characteristics.

Condition	Target Power kW
wait = 3	200
wait = 1000	0

Date: 23/08/17 Time: 14:50

Aim: discharge the battery at the maximum power to a charge level of 100%.

Result: successfully recorded and discussed in Battery Characteristics.

Condition	Target Power kW
wait = 3	−200
wait = 1000	0

Date: 23/08/17 Time: 14:50

Aim: battery left active with no power being supplied to the stacks. Determine the pumps activity.

Result: Pumps showed that they pulse to keep the stacks active and at 0% charge level will also occasionally charge at 20 kW to prevent the state of charge from dropping further.

Date: 24/08/17 Time: 16:50

Aim: charge and discharge the battery at 200 kW.

Result: error in multimeter set-up. 0.00 V for 0 – 400 V range resulted in an overload error for values above 40 V. Resulting errors turns out to be an inconsistency between the multimeter and operations manual. 0.0 V is for the desired range.

Condition	Target Power kW
wait = 3	200
wait = 192	−200
wait = 192	0

Date: 25/08/17 Time: 11:00

Aim: repeat 200 kW cycle

Result: successfully recorded and discussed in System efficiency.

Condition	Target Power kW
wait = 3	200
wait = 192	−200
wait = 192	0

Date: 25/08/17 Time: 17:00

Aim: charge and discharge the battery at 60 kW.

Result: successfully recorded and discussed in System efficiency.

Condition	Target Power kW
wait = 3	60
wait = 745	−60
wait = 745	0

Date: 26/08/17 Time: Weekend

Aim: charge and discharge the battery at 50 kW.

Result: recorder memory reached limit.

Condition	Target Power kW
wait = 3	50
wait = 895	−50
wait = 895	0

Date: 28/08/17 Time: 15:50 (next day)

Aim: charge and discharge the battery at 50 kW.

Result: successfully recorded and discussed in System efficiency.

Condition	Target Power kW
wait = 3	50
wait = 895	−50
wait = 895	0

Date: 29/08/17 Time: 14:40

Aim: charge and discharge the battery at 100 kW.

Result: recorder memory reached limit.

Condition	Target Power kW
wait = 3	100
wait = 448	−100
wait = 448	0

Date: 29/08/17 Time: 17:00

Aim: charge and discharge the battery at 150 kW.

Result: recorder memory reached limit.

Condition	Target Power kW
wait = 3	150
wait = 293	−150
wait = 293	0

Date: 30/08/17 Time: 17:00

Aim: charge and discharge the battery at 100 kW.

Result: successfully recorded and discussed in System efficiency.

Condition	Target Power kW
wait = 3	100
wait = 448	−100
wait = 448	0

Date: 31/08/17 Time: 05:00

Aim: charge and discharge the battery at 150 kW.

Result: successfully recorded and discussed in System efficiency.

Condition	Target Power kW
wait = 3	150
wait = 293	−150
wait = 293	0

Date: 01/08/17 Time: 17:00

Aim: track the state of charge with the OCV.

Result: written values taken, though Siemens recorder reset every two hours as it was operating on the electrolyser settings.

Condition	Target Power kW
wait = 5	200
wait = 20	0
wait = 5	200
wait = 20	0
wait = 5	200
wait = 20	0
wait = 5	200
wait = 20	0
wait = 5	200
wait = 20	0
wait = 5	200
wait = 20	0
wait = 5	200
wait = 20	0
wait = 5	200
wait = 20	0
wait = 5	200
wait = 20	0
wait = 5	200
wait = 20	0
wait = 5	200
wait = 20	0
wait = 5	200
wait = 20	0
wait = 5	200
wait = 20	0

Date: 01/08/17 Time: 23:30 (over weekend)

Aim: record the rate of self-discharge with four active stacks

Result: over the weekend the battery discharged from 100% charge level to 8.3%. However, the problem from the previous run was not discovered until Monday and affected this sequence also.

Condition	Target Power kW
wait = 3	200
wait = 20	0
wait = 0	0

Date: 05/08/17 Time: 13:00

Aim: record the rate of self-discharge with four active stacks

Result: it was observed that wait = 0 does not mean for the row will operate for an infinite time and will rather skip the step. However, upon repeating this sequence to confirm it was noted that setting the time to zero will sometimes crash the program's inbuilt timer. This will result in no data being collected and that the stated target power will continue until the charge level limit is reached.

Condition	Target Power kW
wait = 3	0
wait = 0	0
wait = 1	200

Date: 05/08/17 Time: 13:10

Aim: record the rate of self-discharge with four active stacks

Result: successfully recorded and discussed in Identification of the energy loss.

Condition	Target Power kW
wait = 5760	0
wait = 5760	0
wait = 1	200

Date: 07/09/17 Time: 18:00

Aim: Repeat the 100 kW cycle. The previous data shows to be an outlier possibly due to higher than normal temperature.

Result: successfully recorded and discussed in System efficiency.

Condition	Target Power kW
wait = 3	100
wait = 448	−100
wait = 448	0

Date: 08/09/17 Time: 16:30

Aim: record the pumps power requirements for various rates of charge/ discharge at different states of charge.

Result: the energy consumption from the pumps can be calculated from the powers stated at the given state of charges discussed in Identification of the energy loss section. There was no specified procedure for this section as it had to be controlled and monitored manually.

Date: 09/09/17 Time: 02:00

Aim: record the pumps power requirements for various rates of charge/ discharge at different states of charge.

Result: the energy consumption from the pumps can be calculated from the powers stated at the given state of charges discussed in Identification of the energy loss section. There was no specified procedure for this section as it had to be controlled and monitored manually.

Date: 14/09/17 Time: 14:00

Aim: determine the AC/DC and DC/DC convertor losses.

Result: At a charge level of 50%, the HVP and LVP were recorded as a ratio to determine the DC/DC efficiency. Whereas, the HVP, Self Support P, and P-Grid, were measured to determine the AC/DC efficiency. Discussed in Convertor efficiencies .

Appendix – Active Power/ Charge Level *vs.* Time

200 kW Cycle

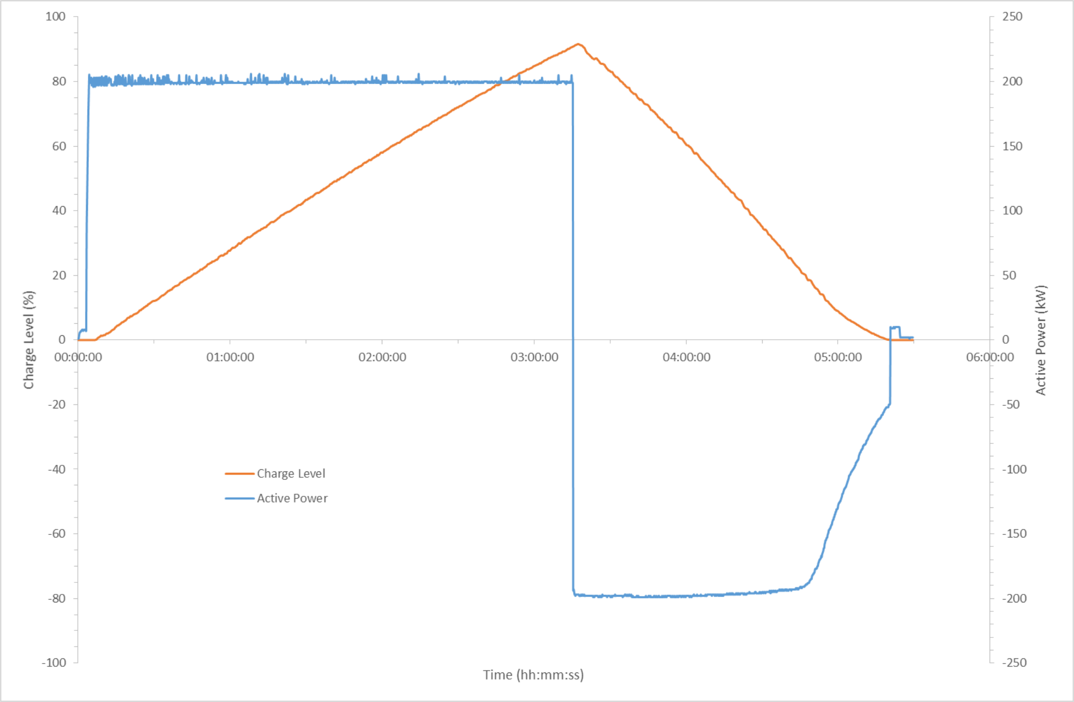

150 kW Cycle

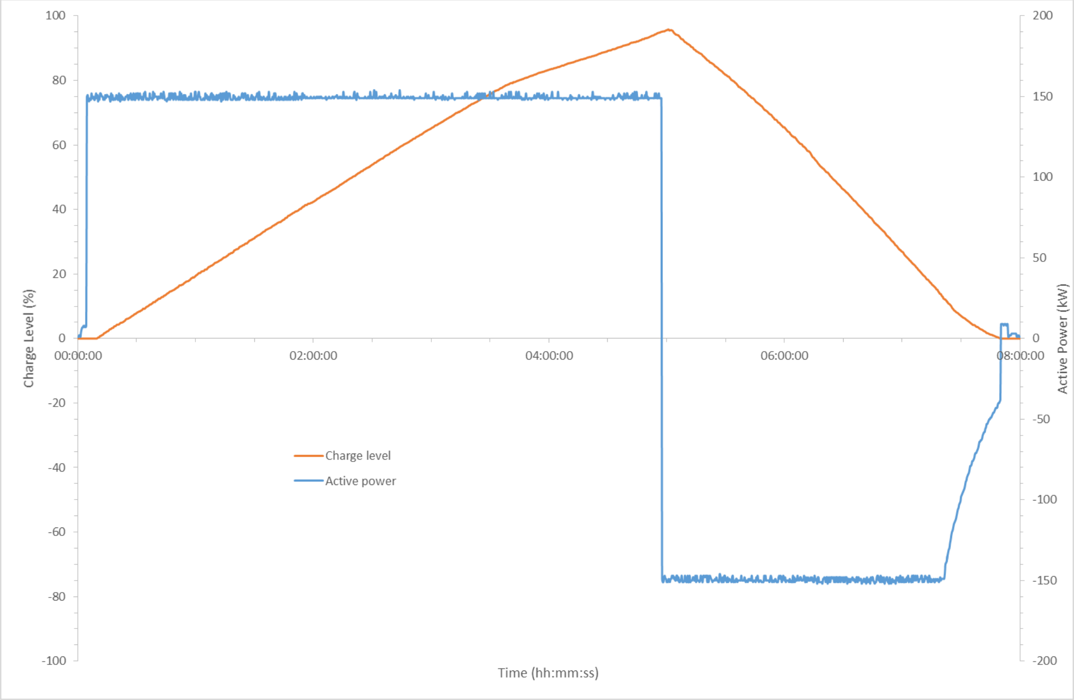

100 kW Cycle (a)

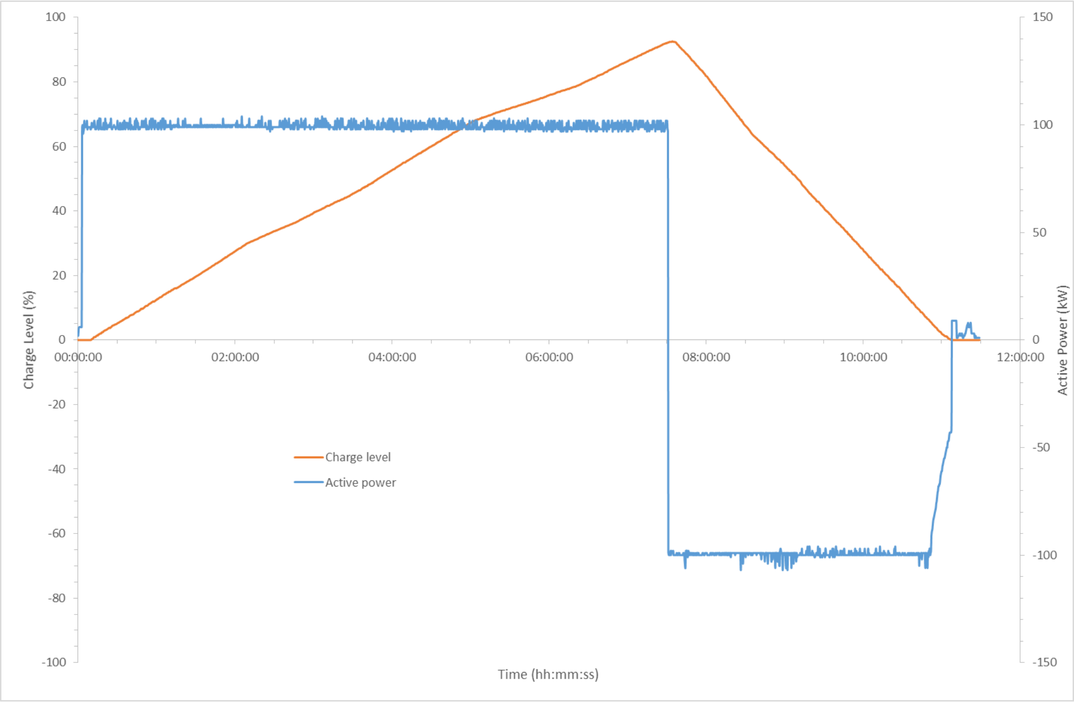

100 kW (b)

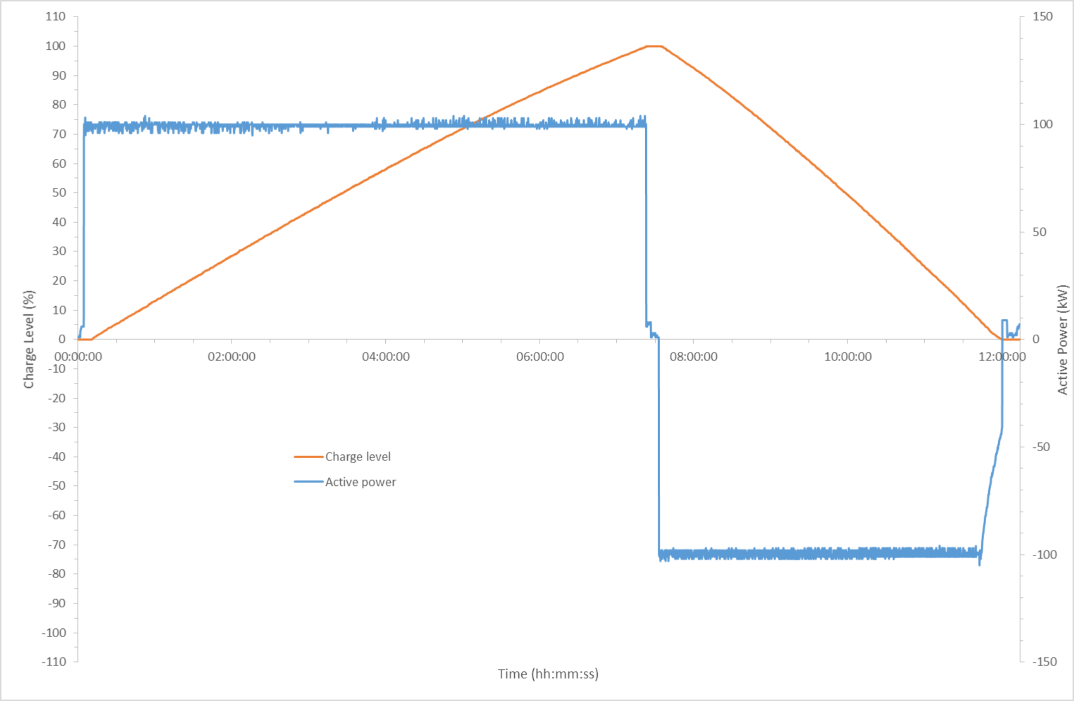

60 kW Cycle

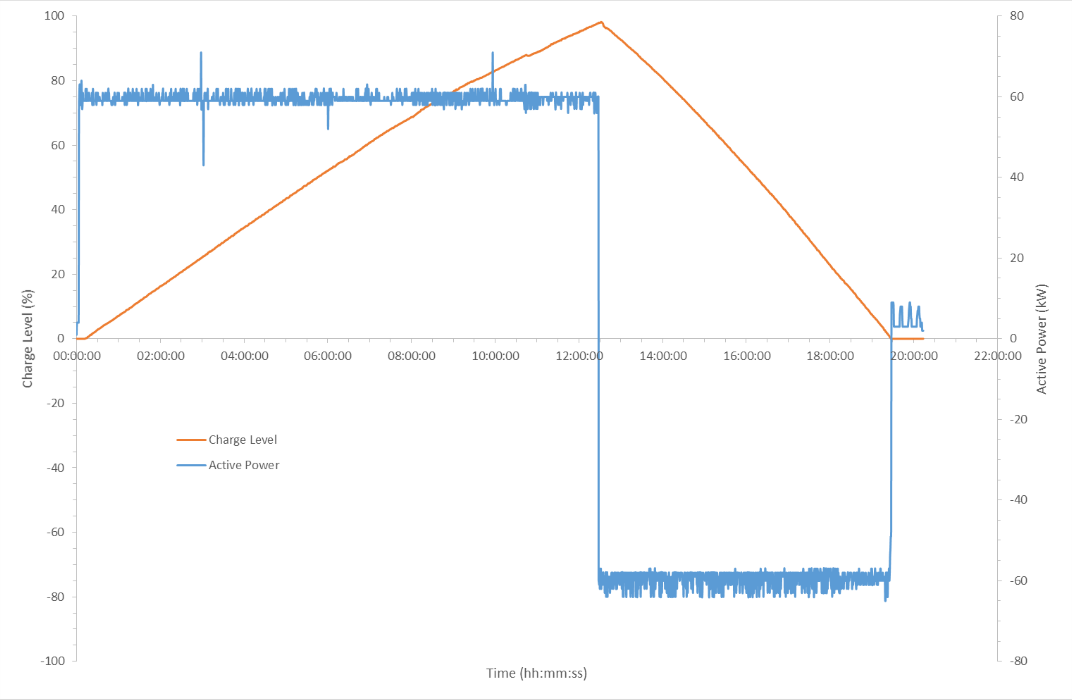

50 kW Cycle

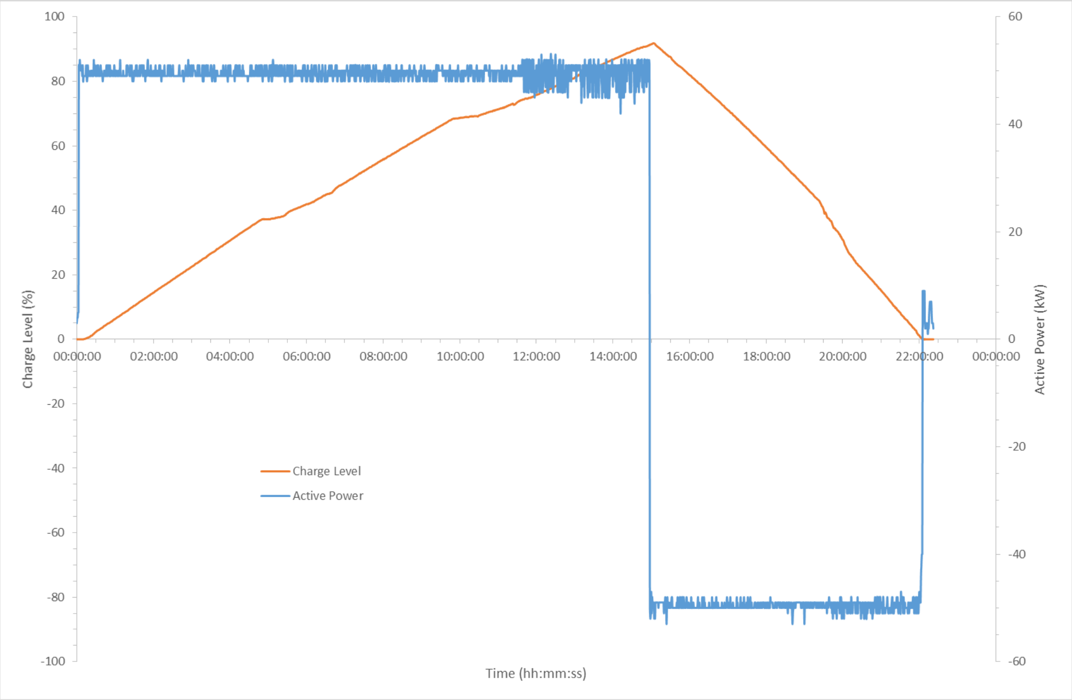

Appendix – Centrifugal Pump Power Consumptions

Charge Level	20%									
Pump	200	-200	150	-150	100	-100	60	-60	50	-50
AP	0.96	0.94	0.95	0.95	0.95	0.94	0.97	0.93	0.95	0.95
AN	0.9	0.88	0.89	0.88	0.9	0.88	0.9	0.88	0.88	0.9
BP	0.94	0.92	0.94	0.93	0.93	0.94	0.94	0.92	0.93	0.92
BN	1.11	1.11	1.11	1.13	1.19	1.13	1.12	1.12	1.14	1.1
CP	0.99	0.99	1.01	1.01	1	1.01	1.01	1.01	0	1.12
CN	1.08	1.09	1.1	1.08	1.08	1.08	1.08	1.07	0	1.08
DP	1.07	1.04	1.04	1.05	1.04	1.03	0	0	0	0
DN	0.97	0.94	0.96	0.94	0.96	0.97	0	0	0	0
Total Power	8.02	7.91	8	7.97	8.05	7.98	6.02	5.93	3.9	6.07

Charge Level	50%									
Pump	200	-200	150	-150	100	-100	60	-60	50	-50
AP	0.96	0.94	0.95	0.95	0.95	0.96	0.95	0.95	0.96	0.95
AN	0.9	0.89	0.9	0.88	0.89	0.89	0.88	0.88	0.88	0.87
BP	0.95	0.92	0.94	0.93	0.94	0.92	0.93	0.93	0.93	0.92
BN	1.13	1.11	1.13	1.11	1.12	1.11	1.1	1.12	1.12	1.12
CP	1.1	1.11	1.1	1.11	1.09	1.1	1.11	1.11	0	0
CN	1.09	1.07	1.09	1.08	1.08	1.07	1.1	1.07	0	0
DP	0.95	0.93	0.97	0.95	0.95	0.94	0	0	0	0
DN	1.07	1.05	1.05	1.04	1.04	1.04	0	0	0	0
Total Power	8.15	8.02	8.13	8.05	8.06	8.03	6.07	6.06	3.89	3.86

Charge Level	80%									
Pump	200	-200	150	-150	100	-100	60	-60	50	-50
AP	0.97	0.97	0.96	0.95	0.96	0.95	0.95	0.95	0.95	0.95
AN	0.89	0.87	0.91	0.88	0.9	0.89	0.89	0.88	0.88	0.87
BP	0.95	0.93	0.93	0.93	0.94	0.93	0.94	0.95	0.94	0.95
BN	1.13	1.12	1.11	1.11	1.11	1.11	1.12	1.12	1.11	1.1
CP	0.99	0.97	0.99	0.98	0.99	0.99	0.99	0.98	0.98	0
CN	0.93	0.93	0.93	0.91	0.93	0.92	0.92	0.92	0.92	0
DP	1.05	1.05	1.05	1.04	1.04	1.04	0	0	0	0
DN	0.98	0.98	0.98	0.98	0.98	0.98	0	0	0	0
Total Power	7.89	7.82	7.86	7.78	7.85	7.81	5.81	5.8	5.78	3.87

Appendix – Active Power/ Voltage/ Temperature *vs.* Time

200 kW Cycle

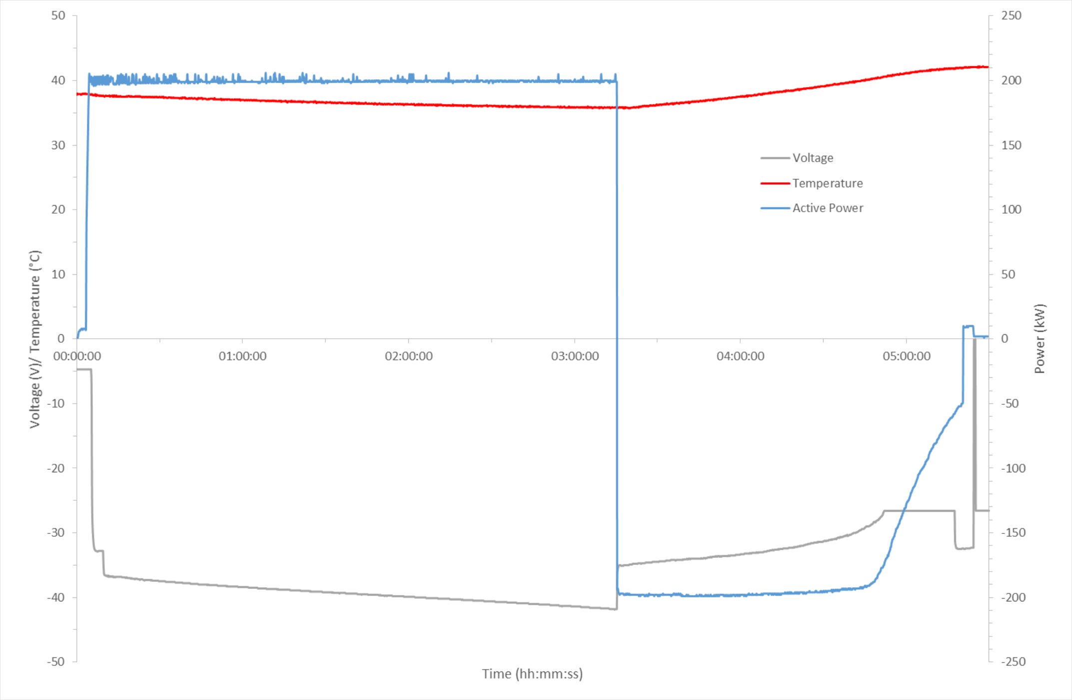

150 kW Cycle

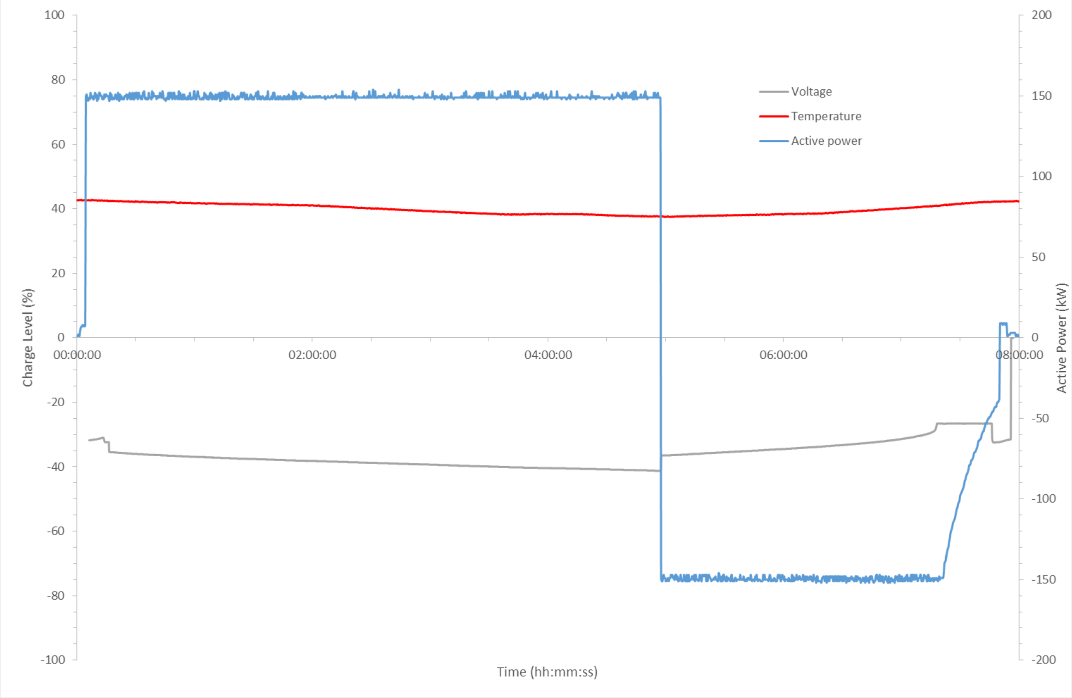

100 kW Cycle (a)

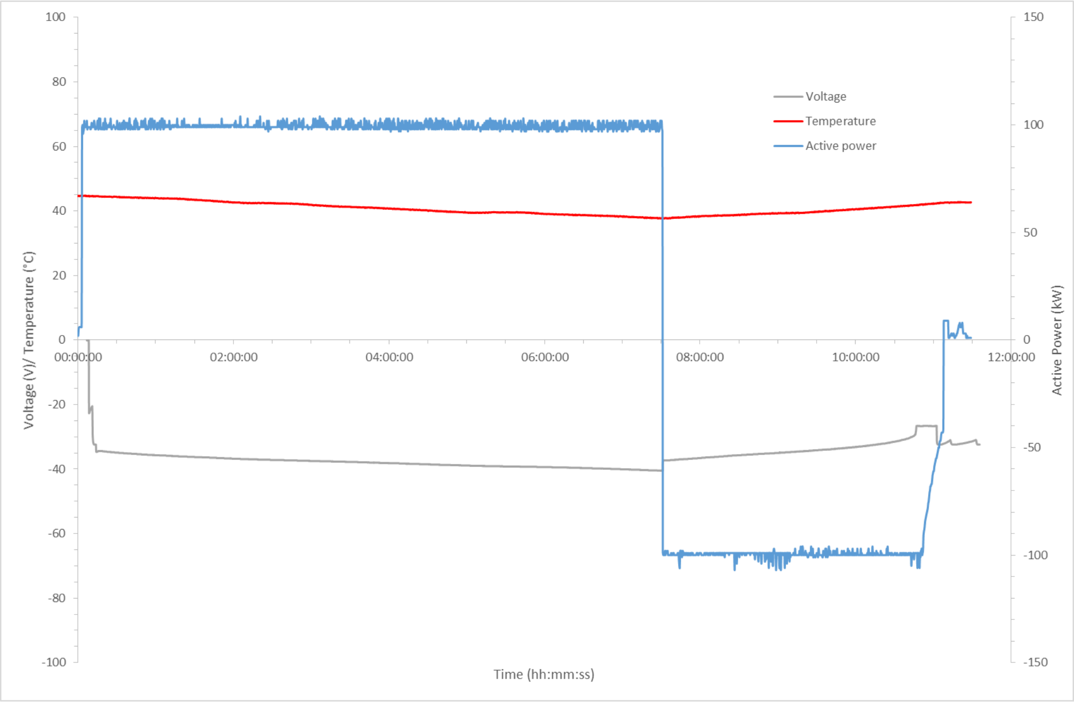

100 kW (b)

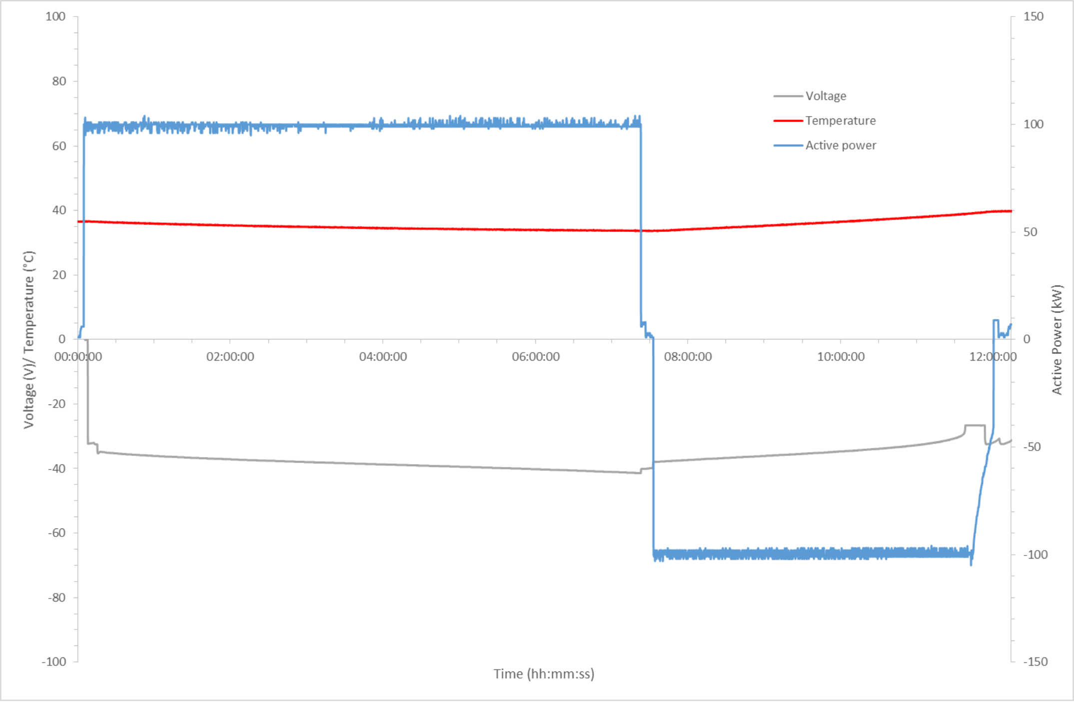

60 kW Cycle

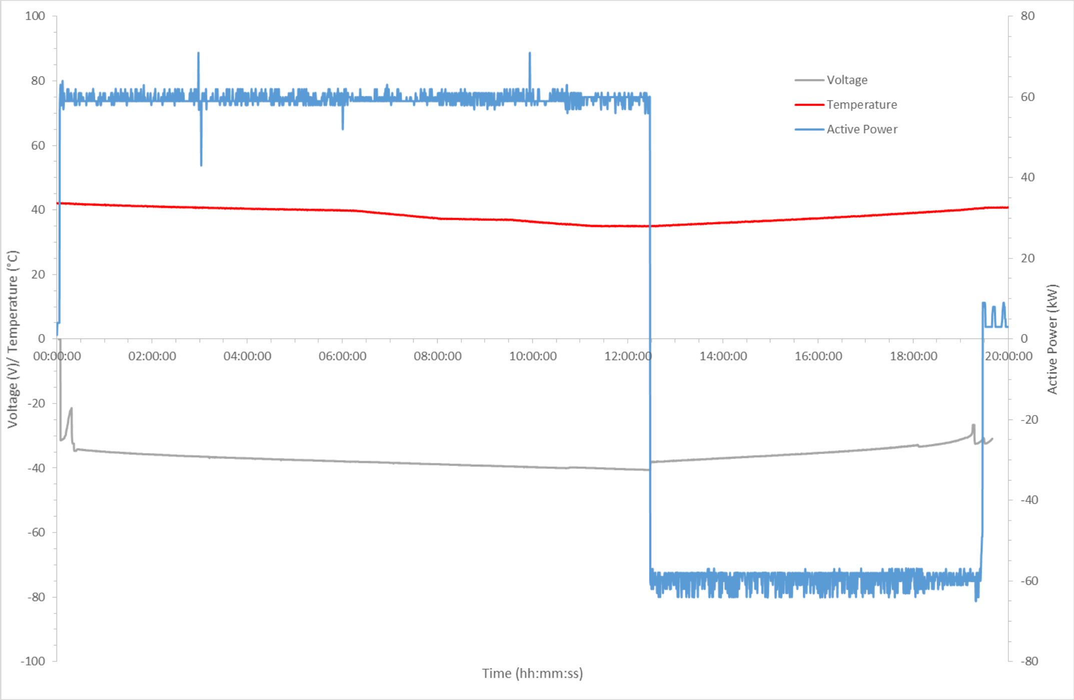

50 kW Cycle